

**STUDY ON THE STRUCTURAL FACTORS AFFECTING  
THE OXIDE IONIC CONDUCTIVITY OF RARE EARTH  
MIXED OXIDES FOR DEVELOPMENT OF NEW OXIDE  
IONIC CONDUCTORS**

*Thesis submitted to*

**THE UNIVERSITY OF KERALA**

*for the award of the degree of*

**DOCTOR OF PHILOSOPHY IN PHYSICS**

*under*

**THE FACULTY OF SCIENCE**

**BY**

**RENJU U. A.**



**MATERIALS SCIENCE & TECHNOLOGY DIVISION  
CSIR- NATIONAL INSTITUTE FOR INTERDISCIPLINARY  
SCIENCE AND TECHNOLOGY (NIIST),  
THIRUVANANTHAPURAM 695 019,  
KERALA  
(Research centre affiliated to University of Kerala)**

**NOVEMBER 2019**



*To my parents...*



## **DECLARATION**

I hereby declare that the PhD thesis entitled "**Study on the Structural Factors affecting the Oxide Ionic Conductivity of Rare Earth Mixed Oxides for Development of New Oxide Ionic Conductors**" is an independent work carried out by me and it has not been submitted anywhere else for any other degree, diploma, or title.

THIRUVANANTHAPURAM

RENJU U.A

Date:



# NATIONAL INSTITUTE FOR INTERDISCIPLINARY SCIENCE AND TECHNOLOGY (NIIST)



**Council of Scientific & Industrial Research  
(Formerly Regional Research Laboratory)  
Industrial Estate P.O., Trivandrum - 695 019  
Kerala, INDIA**



**Dr. P. Prabhakar Rao,  
Emeritus Scientist  
Materials Science and Technology Division**

**Tel: 91-471-2515 311  
E-mail: padala\_rao@yahoo.com**

19-11-2019

## CERTIFICATE

This is to certify that the work embodied in the thesis entitled "**Study on the Structural Factors affecting the Oxide Ionic Conductivity of Rare Earth Mixed Oxides for Development of New Oxide Ionic Conductors**" has been carried out by Mrs Renju U. A. under my supervision and guidance at the Materials Science and Technology Division of National Institute for Interdisciplinary Science and Technology (CSIR-NIIST), Thiruvananthapuram.

THIRUVANANTHAPURAM

Date:

Dr. P. Prabhakar Rao

(Thesis Supervisor)





## ACKNOWLEDGEMENTS

*This thesis has become a reality with the kind support and help of many individuals. I would like to extend my sincere thanks to all of them.*

*Firstly, I would like to express my sincere gratitude to my research supervisor, Dr P. Prabhakar Rao for introducing me to this exciting field of science and for his dedicated help, advice, inspiration, encouragement and continuous support, throughout my PhD. His keen observations and challenging arguments helped me a lot in refining my ideas, and discussions with him gave me a lot more insights. This work would not have been possible without his guidance, support and encouragement.*

*I am grateful to Dr A. Ajayghosh, Director CSIR-NIIST, and former director, Dr Suresh Das, for allowing me to carry out my research in this esteemed laboratory. I owe a great deal to Dr Savithri S, Dr Harikrishna Bhat, Dr P. Prabhakar Rao, Dr M. L. P. Reddy and Dr M. T. Sebastian, present and former Head of Materials Science and Technology Division, for extending the research facilities. Also, I sincerely thank all the scientists and staffs of MSTD for all the help and support extended to me.*

*I am privileged to thank Kerala State Council for Science Technology and Engineering (KSCSTE) for the financial support granted to me to undertake this research work and also for allowing me to attend conferences and meet interesting people. Also, I am thankful to International Centre for Diffraction Data (ICDD) for the financial support during the starting of my research career and Council for Scientific and Industrial Research (CSIR) for providing me all the facilities and infrastructure to perform my research work.*

*Special thanks to Mr M. R. Chandran, Mrs Luci Paul, Mrs Soumya Valsalam and Mr Harish Raj for SEM imaging. I wish to thank Mr N. Pruthiviraj, Mr M. P. Varkey Mr. Shanoj and Ms Haritha A. N for the technical support. I also thank VSSC and Dr K. K. Maiti, CSTD, NIIST-CSIR for the help with Raman analysis.*

*I am most grateful to the senior colleagues Dr Vaisakhan Thampi, Dr Divya S, Dr Sreena T. S., Dr Linda Francis, Dr Sameera S, Dr Mahesh, Dr Sumi S, Dr Athira K. V Raj, and Mrs Vineetha James, for lending me their expertise to my scientific and technical problems. Thanks to my colleagues of Energy Materials Lab in the Materials Science and Technology Division particularly Mrs Parvathi S Babu, Mrs Suchithra V. G, Mrs Aswathi B*

*A and Mrs Aju Thara T. R. Special Thanks to Dr. Subrata Das and his students, Ms. Malini Abraham, Ms Shisina S., Ms Meera Sebastian, Ms Sreevalsa, Mr Ranjith, and Mr Thejas. Completing this work would have been more difficult without the support and friendship provided by these people. I am incredibly indebted to them for their help.*

*I am thankful to library staff and administrative staff of NIIST for their help and services.*

*My special regards to my teachers because of whose teaching at different stages of education has made it possible for me to see this day. Because of their kindness, I feel, was able to reach a stage where I could write this thesis.*

*I feel a deep sense of gratitude for my parents, Ushakumari and Appukuttan Nair who for showing faith in me and giving me the liberty to choose what I desired. Their selfless love, care, sleepless nights, pain and sacrifice will remain my inspiration throughout my life. Although you hardly understood what I researched on, you were willing to support any decision I made. I would never be able to pay back the love and affection showered upon by my parents. Also, I express my thanks to my sister Lekshmi, her husband Ajikumar, for their constant inspiration and encouragement and their little boy Manav Krishna whose smiling face always made me happy.*

*Moreover, most of all, I owe my deepest gratitude to my husband, Mr Vaisakh R. S, for his affection, encouragement, and for sharing my wish to reach the goal of completing this task. He supported me without any complaint or regret that enabled me to complete my PhD thesis. I also wanted to thank my mother in law Sreekumari Amma, grandmother in law Devaki Amma, brother in law Praveen R. S., sister Durga and their son Amarnath.*

*Above all, I praise God, the almighty, whose blessings have made me who I am today.*

**Renju U A**

# CONTENTS

<b>Declaration</b>	<b>i</b>
<b>Certificate</b>	<b>iii</b>
<b>Acknowledgements</b>	<b>v</b>
<b>Contents</b>	<b>vii</b>
<b>List of Tables</b>	<b>xi</b>
<b>List of Figures</b>	<b>xiii</b>
<b>Abbreviations</b>	<b>xvii</b>
<b>Preface</b>	<b>xix</b>
<b>Chapter 1: Introduction</b>	<b>1-40</b>
1.1 Introduction	3
1.2 Materials Science	3
1.3 Energy Crisis and Environmental Pollution	4
1.4 Fuel Cells	5
1.4.1 Types of Fuel cells	6
1.5 Solid Oxide Fuel Cells	8
1.5.1 History of Solid Oxide Fuel Cells	8
1.5.2 Advantages and Disadvantages of Solid Oxide Fuel Cells	9
1.5.3 Applications of Solid Oxide Fuel Cells	10
1.5.4 Working of Solid Oxide Fuel Cells	10
1.6. Components of Solid Oxide Fuel Cells	12
1.6.1 Anode	14
1.6.2 Cathode	15
1.6.3 Interconnect	17
1.6.4 Electrolyte	18
1.7 The State of the Art of Material for Solid Oxide Fuel Cells	18
1.8 Reducing the Operating Temperature of the SOFCs	20
1.9 Solid Oxide Electrolyte	20
1.9.1 Conduction Mechanism	21
1.9.2 General Survey of Electrolyte Materials	23
1.9.2.1 Zirconia Based Electrolytes	23
1.9.2.2 Ceria Based Electrolytes	24
1.9.2.3 Perovskite Structured Oxides	25

1.9.2.4 Brownmillerite Oxides	27
1.9.2.5 Apatite Structured Oxides	27
1.9.2.6 LAMOX ( $\text{La}_2\text{Mo}_2\text{O}_9$ )	28
1.9.2.7 Ruddlesden-Popper Type Oxides	29
1.9.2.8 Aurivillius Type Oxides	30
1.9.3 The Relevance of the Present Work	30
1.9.3.1 Pyrochlore Structured Oxides	31
1.9.3.2 $\text{Bi}_2\text{O}_3$ Based Oxide Ion Conductors	37
1.10 Preface to the Current Thesis	40
<b>Chapter 2: Influence of Phase Transition from Order to Disorder and Phillip's Ionicity on Thermal Expansion Coefficient of Pyrochlore Type Compositions with Multivalent Environment</b>	<b>41-66</b>
2.1 Introduction	43
2.2 Experimental	46
2.3 Results and Discussion	47
2.3.1 Structural analysis using X-ray diffraction methods	47
2.3.2 Raman spectral analysis	51
2.3.3 Electron microscopic studies	54
2.3.4 Fractional ionicity calculation based on theoretical methods	55
2.3.5 High-temperature XRD studies	59
2.3.6 Impedance analysis	63
2.4 Conclusions	66
<b>Chapter 3: Contrasting Anion Disorder Behaviour in <math>\text{Sm}_2\text{Zr}_2\text{O}_7</math> by Simultaneous Aliovalent Cation Substitution and its Structural and Electrical Properties</b>	<b>67-86</b>
3.1 Introduction	69
3.2 Experimental	71
3.3 Results and Discussion	72
3.3.1 Powder X-ray diffraction analysis	72
3.3.2 Raman spectroscopic studies	78
3.3.3 Morphological analysis	80
3.3.4 Impedance spectroscopic analysis	81
3.4 Conclusions	85
<b>Chapter 4: Study on the Introduction of Oxygen Vacancies to the Pyrochlore Type Compositions and its Influence on the Electrical Properties</b>	<b>87-104</b>

4.1 Introduction	89
4.2 Experimental	91
4.3 Results and Discussion	92
4.3.1 X-ray diffraction studies	92
4.3.2 Raman spectroscopic analysis	95
4.3.3 Surface morphological studies	97
4.3.4 Electrical properties	98
4.4 Conclusions	104
<b>Chapter 5: Study of the Ionic Conductivity on the Displaced Pyrochlore Type Compositions</b>	<b>105-126</b>
5.1 Introduction	107
5.2 Experimental	109
5.3 Results and Discussion	110
5.3.1 Powder X-ray diffraction studies	111
5.3.2 Morphological analysis	118
5.3.3 Electrical properties	119
5.4 Conclusions	125
<b>Chapter 6: Structural Stabilization of <math>\delta</math>-phase <math>\text{Bi}_2\text{O}_3</math> in the <math>\text{MgBi}_{1.5}\text{RE}_{0.5}\text{O}_4</math> System through Rare Earth Substitution for improved Ionic Conductivity</b>	<b>127-142</b>
6.1 Introduction	129
6.2 Experimental	131
6.3 Results and Discussion	132
6.3.1 Powder X-ray diffraction studies	132
6.3.2 Scanning electron microscopic studies	134
6.3.3 Thermal stability studies	135
6.3.4 Conductivity studies	136
6.4 Conclusions	141
<b>Chapter 7: Conclusions and Future Scope</b>	<b>143-152</b>
7.1 Conclusions	145
7.2 Future Scope	150
<b>References</b>	<b>153-174</b>
<b>List of Publications</b>	<b>175-176</b>



## LIST OF TABLES

Table No.	Table Captions	Page No.
1.1	Types of fuel cells	7
2.1	Rietveld refined parameters of $\text{RE}_2\text{Y}_{2/3}\text{Zr}_{2/3}\text{Nb}_{2/3}\text{O}_7$ (RE = La, Nd, Sm, Gd, Dy, Y)	50
2.2	Factor group analysis for Pyrochlore Structure	51
2.3	Peak positions and corresponding modes of vibration	54
3.1	Rietveld refined parameters of the $\text{Sm}_2\text{Zr}_{2-x}(\text{YNb})_{x/2}\text{O}_7$ ( $x = 0, 0.25, 0.5, 0.75, 1$ )	75
3.2	The bond length of the compositions obtained from the Rietveld analysis and lattice strain calculated using the W-H Plot	77
4.1	Ionic radii and radius ratio of the prepared compositions	92
4.2	The Rietveld refinement results	94
5.1	The d-spacing and corresponding hkl values of the monoclinic structure	111
5.2	The Wyckoff position and site of occupancies of all the compositions used for the refinement	113
5.3	The refined parameters for the cubic pyrochlore structured compositions	114
5.4	The lattice parameter values of all the prepared compositions	116
6.1	Lattice parameter and volume of the compositions $\text{MgBi}_{1.5}\text{RE}_{0.5}\text{O}_4$ (RE = Nd, Sm, Gd, Dy, Y)	134
6.2	The total conductivity at 1023K and activation energy of the compositions $\text{MgBi}_{1.5}\text{RE}_{0.5}\text{O}_4$ (RE = Nd, Sm, Gd, Dy, Y)	138





## LIST OF FIGURES

Figure No.	Figure Captions	Page No.
1.1	The relationship between the four elements of materials science	4
1.2	The schematic representation of a fuel cell	6
1.3	Working of solid oxide fuel cell	10
1.4	Components of SOFC	13
1.5	The commonly used components of the SOFC	19
1.6	Fluorite and Pyrochlore Crystals	31
1.7	(a) Pyrochlore and (b) Fluorite crystal structure	32
1.8	Different polymorphs of Bi <sub>2</sub> O <sub>3</sub>	37
2.1	(a) Powder X-ray diffraction patterns of the series RE <sub>2</sub> Y <sub>2/3</sub> Zr <sub>2/3</sub> Nb <sub>2/3</sub> O <sub>7</sub> (RE = La, Nd, Sm, Gd, Dy, Y). (b) Zoomed view of 2θ between 14 to 15° (c) 28 to 30°	48
2.2	Variation of the lattice parameter of the compositions RE <sub>2</sub> Y <sub>2/3</sub> Zr <sub>2/3</sub> Nb <sub>2/3</sub> O <sub>7</sub> with the radius ratio	49
2.3	Observed, calculated and difference XRD profiles of (a) Pyrochlore structured La <sub>2</sub> Y <sub>2/3</sub> Zr <sub>2/3</sub> Nb <sub>2/3</sub> O <sub>7</sub> and (b) Fluorite structured Y <sub>2</sub> Y <sub>2/3</sub> Zr <sub>2/3</sub> Nb <sub>2/3</sub> O <sub>7</sub>	50
2.4	Raman spectra of the series of compositions RE <sub>2</sub> Y <sub>2/3</sub> Zr <sub>2/3</sub> Nb <sub>2/3</sub> O <sub>7</sub> . (a) Pyrochlore structured compositions and (b) fluorite structures compositions	53
2.5	High-resolution lattice image and SAED patterns of the compositions La <sub>2</sub> Y <sub>2/3</sub> Zr <sub>2/3</sub> Nb <sub>2/3</sub> O <sub>7</sub> and Dy <sub>2</sub> Y <sub>2/3</sub> Zr <sub>2/3</sub> Nb <sub>2/3</sub> O <sub>7</sub>	55
2.6	(a) The variation of the lattice parameter of Nd <sub>2</sub> Y <sub>2/3</sub> Zr <sub>2/3</sub> Nb <sub>2/3</sub> O <sub>7</sub> with temperature. (b) The corresponding shift in the d-spacing of Nd <sub>2</sub> Y <sub>2/3</sub> Zr <sub>2/3</sub> Nb <sub>2/3</sub> O <sub>7</sub>	60
2.7	The variation of the lattice thermal expansion coefficient with the different lanthanides in the compositions: RE <sub>2</sub> Y <sub>2/3</sub> Zr <sub>2/3</sub> Nb <sub>2/3</sub> O <sub>7</sub> (RE = La, Nd, Sm, Gd, Dy, Y)	61
2.8	The variation of lattice thermal expansion coefficient with ionicity of bonds (a) A-O bond (b) B-O bond and (c) difference in ionicity between A-O and B-O bonds	62

<b>2.9</b>	(a) Cole-Cole plot of the $\text{Nd}_2\text{Y}_{2/3}\text{Zr}_{2/3}\text{Nb}_{2/3}\text{O}_7$ as a representative sample. (b) The Arrhenius plot of the samples fitted with a straight line. (c) The variation of activation energy and pre-exponential factor of the series of samples. (d) The overall conductivity variation of the samples at 1023K.	<b>64</b>
<b>3.1</b>	The powder X-ray diffraction patterns of the $\text{Sm}_2\text{Zr}_{2-x}(\text{YNb})_{x/2}\text{O}_7$ ( $x = 0, 0.25, 0.5, 0.75, 1$ )	<b>72</b>
<b>3.2</b>	The increase in the lattice parameter with an increase in the doping concentration ( $x$ )	<b>74</b>
<b>3.3</b>	Observed, calculated and difference XRD profiles of $\text{Zr}_1$ composition	<b>76</b>
<b>3.4</b>	W-H plot of one representative sample $\text{Zr}_{1.75}$	<b>76</b>
<b>3.5</b>	Raman spectrum of the $\text{Sm}_2\text{Zr}_{2-x}(\text{YNb})_{x/2}\text{O}_7$ ( $x = 0, 0.25, 0.5, 0.75, 1$ ) compositions	<b>78</b>
<b>3.6</b>	The ratio of the intensity of the $E_0$ Raman mode at $\approx 300 \text{ cm}^{-1}$ ( $I_2$ ) and $T_{2g}$ mode at $800 \text{ cm}^{-1}$ ( $I_1$ ) and $48f$ oxygen $x$ parameter of the compositions	<b>80</b>
<b>3.7</b>	Scanning electron microscopic images of the prepared compositions	<b>81</b>
<b>3.8</b>	Cole-Cole plot of the representative $\text{Zr}_1$ sample at different compositions	<b>82</b>
<b>3.9</b>	Arrhenius plot and the linear fit of the samples $\text{Sm}_2\text{Zr}_{2-x}(\text{YNb})_{x/2}\text{O}_7$ ( $x = 0, 0.25, 0.5, 0.75, 1$ )	<b>83</b>
<b>3.10</b>	(a) Variation of the total conductivity of the samples with the compositions (b) Activation energy and pre-exponential factor of the compositions	<b>84</b>
<b>4.1</b>	The powder X-ray diffraction patterns of the prepared compositions $\text{RE}_3\text{Zr}_{0.5}\text{Nb}_{0.5}\text{O}_{6.75}$ (RE = Nd, Sm, Gd, Dy, Y)	<b>93</b>
<b>4.2</b>	The graphical output of the Rietveld refinement of the XRD	<b>94</b>
<b>4.3</b>	Variation of the lattice parameter of the compositions $\text{RE}_3\text{Zr}_{0.5}\text{Nb}_{0.5}\text{O}_{6.75}$ (RE = Nd, Sm, Gd, Dy, Y)	<b>95</b>
<b>4.4</b>	Raman spectra of the compositions $\text{RE}_3\text{Zr}_{0.5}\text{Nb}_{0.5}\text{O}_{6.75}$ (RE = Nd, Sm, Gd, Dy, Y)	<b>96</b>
<b>4.5</b>	The scanning electron microscopic images of the prepared compositions $\text{RE}_3\text{Zr}_{0.5}\text{Nb}_{0.5}\text{O}_{6.75}$ (RE = Nd, Sm, Gd, Dy, Y)	<b>97</b>
<b>4.6</b>	The Nyquist plot of the representative composition	<b>98</b>

Gd<sub>3</sub>Zr<sub>0.5</sub>Nb<sub>0.5</sub>O<sub>6.75</sub> and Y<sub>3</sub>Zr<sub>0.5</sub>Nb<sub>0.5</sub>O<sub>6.75</sub>

4.7	The conductivity of the prepared compositions at 1023K	99
4.8	Arrhenius plot (a) ln( $\sigma T$ ) Vs 1000/T (b) log ( $f_{\max}$ ) Vs 1000/T	99
4.9	The imaginary part of modulus Vs log frequency	100
4.10	The variation of activation energy of the compositions RE <sub>3</sub> Zr <sub>0.5</sub> Nb <sub>0.5</sub> O <sub>6.75</sub> (RE = Nd, Sm, Gd, Dy, Y)	101
4.11	The normalised plot of $M''/M'_{\max}$ vs log ( $f/f_{\max}$ ) for all the compositions	103
5.1	The powder X-ray diffraction patterns of the composition CT <sub>3</sub> N, CT <sub>2</sub> ZN, CTZ <sub>2</sub> N and CZ <sub>3</sub> N	111
5.2	The observed, calculated patterns of the CT <sub>3</sub> N along with the difference plot	115
5.3	The variation of the lattice volume with the Zirconium content	117
5.4	The scanning electron microscopic images of the polished surface of the sintered pellets of all the prepared compositions	119
5.5	The Nyquist plot of the CZ <sub>2</sub> TN composition at various temperatures	120
5.6	The frequency dependence of the real and imaginary part of the samples CT <sub>3</sub> N and CZ <sub>3</sub> N	121
5.7	The plot of the log of the relaxation frequency against 1000/T	122
5.8	Arrhenius plots of the compositions: CZ <sub>3</sub> N, CZ <sub>2</sub> TN, CZT <sub>2</sub> N and CT <sub>3</sub> N	123
5.9	The variation of the conductivity at 1023K and activation energy with compositions	124
6.1	The powder X-ray diffraction patterns of the compositions MgBi <sub>1.5</sub> RE <sub>0.5</sub> O <sub>4</sub> (RE = Nd, Sm, Gd, Dy, Y)	132
6.2	Cross-sectional SEM images of the compositions MgBi <sub>1.5</sub> RE <sub>0.5</sub> O <sub>4</sub> (RE = Nd, Sm, Gd, Dy)	134
6.3	(a) Elemental dot mapping of the composition MBY. (b) EDAX results for composition MBY	135
6.4	DTA curves of the samples MBDy and MBY	136
6.5	The complex impedance spectra of the representative samples of the composition MgBi <sub>1.5</sub> RE <sub>0.5</sub> O <sub>4</sub> (RE = Nd, Sm, Gd, Dy, Y)	137

<b>6.6</b>	Arrhenius plot of the compositions $\text{MgBi}_{1.5}\text{RE}_{0.5}\text{O}_4$ (RE = Nd, Sm, Gd, Dy, Y)	<b>138</b>
<b>6.7</b>	Variation of the total conductivity of the compositions $\text{MgBi}_{1.5}\text{RE}_{0.5}\text{O}_4$ (RE = Nd, Sm, Gd, Dy, Y) at 1023K	<b>139</b>
<b>6.8</b>	The variation of the conductivity of the compositions MBDy and MBY with the temperature	<b>140</b>

## ABBREVIATIONS

AFC	Alkaline Fuel Cell
BSCCu	$\text{Ba}_{0.5}\text{Sr}_{0.5}\text{Co}_{0.8}\text{Cu}_{0.2}\text{O}_{3-\delta}$
CaSZ	Calcium Stabilised Zirconia
CDC	Calcium Doped Ceria
DMFC	Direct Methanol Fuel Cell
GDC	Gadolinium Doped Ceria
GSC	$\text{Gd}_{0.5}\text{Sr}_{0.5}\text{CoO}_3$
HR-TEM	High Resolution Transmission Electron Microscopy
IT-SOFC	Intermediate Temperature Solid Oxide Fuel Cell
LBC	$\text{La}_{0.5}\text{Ba}_{0.5}\text{CoO}_{3-\delta}$
LCM	Ca-doped $\text{LaMnO}_3$
LNC	Lanthanum Nickel Cobaltite
LNF	$\text{LaNi}(\text{Fe})\text{O}_3$
LNO	$\text{LiNiO}_2$
LSC	Lanthanum Strontium Cobaltite
LSCF	$\text{La}_{1-x}\text{Sr}_x\text{Co}_{1-y}\text{Fe}_y\text{O}_3$
LSCF	Lanthanum Strontium Cobalt Ferrite
LSCN	$\text{La}_{0.8}\text{Sr}_{0.2}\text{Co}_{0.8}\text{Ni}_{0.2}\text{O}_{3-\delta}$
LSCr	Sr-doped $\text{LaCrO}_3$
LSCu	$\text{La}_{1-x}\text{Sr}_x\text{CuO}_{2.5-\delta}$
LSF	Sr-doped $\text{LaFeO}_3$
LSFeCo	Sr-Doped Lanthanum Iron Cobalt
LSFN	$\text{La}_{1-x}\text{Sr}_x\text{Fe}_{0.7}\text{Ni}_{0.3}\text{O}_{3-\delta}$
LSGM	Lanthanum Strontium Gallium Magnesium Oxide
LSGMC	$\text{La}_{0.8}\text{Sr}_{0.2}\text{Ga}_{0.8}\text{Mg}_{0.115}\text{Co}_{0.085}\text{O}_{3-\delta}$
LSGMF	$\text{La}_{0.75}\text{Sr}_{0.25}\text{Ga}_{0.8}\text{Mg}_{0.16}\text{Fe}_{0.04}\text{O}_{3-\delta}$
LSM	$\text{La}_{1-x}\text{Sr}_x\text{MnO}_3$
LSMC	$\text{LaSrMnCoO}_{5+\delta}$
LSMCr	$\text{La}_{0.75}\text{Sr}_{0.25}\text{Mn}_{0.5}\text{Cr}_{0.5-x}\text{CuO}_{3-\delta}$
MCFC	Molten Carbonate Fuel Cell

NSC	Novel Structure Cathodes
PAFC	Phosphoric Acid Fuel Cell
PBC	$\text{PrBaCo}_2\text{O}_{5+\delta}$
PCFC	Protonic Ceramic Membrane Fuel Cell
PCM	$(\text{Pr}_{0.7}\text{Ca}_{0.3})_{0.9}\text{MnO}_{3-\delta}$
PEMFC	Proton Exchange Membrane Fuel Cell
PSM	$\text{Pr}_{0.70}\text{Sr}_{0.30}\text{MnO}_{3-\delta}$
SAED	Selected Area Electron Diffraction
SAFC	Sulphuric Acid Fuel Cell
ScSZ	Scandium Stabilised Zirconia
SDC	Samarium Doped Ceria
SEM	Scanning Electron Microscopy
SOFC	Solid Oxide Fuel Cell
SSC	$\text{Sm}_{0.5}\text{Sr}_{0.5}\text{Co}_{3-\delta}$
TEC	Thermal Expansion Coefficient
TEM	Transmission Electron Microscopy
XRD	X-ray Diffraction
YBCu	$\text{YBa}_2\text{Cu}_3\text{O}_7$
YCCF	$\text{Y}_{(1-x)}\text{Ca}_x\text{Co}_y\text{Fe}_{(1-y)}\text{O}_3$
YDC	Yttrium Doped Ceria
YSCF	$\text{Y}_{(1-x)}\text{Sr}_x\text{Co}_y\text{Fe}_{(1-y)}\text{O}_3$
YSZ	Ytria Stabilised Zirconia

## PREFACE

Solid Oxide Fuel Cell (SOFC) is an electrochemical device characterised by the use of solid oxide material as the electrolyte which can find application as an efficient and reliable energy source. The solid oxide electrolyte is known as the heart of the solid oxide fuel cell, as the operating temperature and cell performance depends on the ionic conductivity of the electrolyte material. Since the oxide ion conduction through the material occurs only at very high temperature, the operating temperature of the cell is high. So among the four components, *viz* anode, cathode, interconnect, and electrolyte, electrolyte materials seek much attention from the researchers. An electrolyte material should possess high ionic conductivity as well as should be chemically stable in both oxidising and reducing atmosphere at a very high temperature. Various factors such as crystal structure, composition and constituent atoms, affect the characteristic properties of the electrolyte, and thus, the factors become essential from the researcher's perspective.

Here, in the present work, various structural factors that affect the oxide ion conductivity of the rare earth mixed oxides were studied. In the present work, pyrochlore composition and bismuth-based composition is studied in this aspect. The pyrochlore structure is characterised by the intrinsic oxide ion vacancies, and these vacancies are ordered in the structure. These ordered vacancies provide an easier path for the migration of oxide ions. In the case bismuth-based composition, the high-temperature  $\delta$ -phase is identified as best oxide ion conductor and the present study is an attempt to stabilise these high temperature high conductive phase to the room temperature via the aliovalent and isovalent substitution.

The first chapter of the thesis starts with the importance of the study of Materials Science and then briefly provides an overview of the current scenario of energy sources and environmental problems. The importance and application of the solid oxide fuel cell are presented in this chapter. The basic operation and components and its requirements are also discussed in the chapter highlighting the importance of the electrolyte. A brief literature review of the solid oxide electrolyte is also presented with an emphasis on the pyrochlore oxides and bismuth-based oxides.

In the second chapter, a new series of compositions,  $\text{RE}_2\text{Y}_{2/3}\text{Zr}_{2/3}\text{Nb}_{2/3}\text{O}_7$  (RE = La, Nd, Sm, Gd, Dy, Y) were prepared, and the structural and electrical characterisation of the compositions were done. In this chapter, the interrelationship among the thermal expansion coefficient, ionicity and oxide ion conductivity is studied in detail. The study revealed that

ionicity of the individual bond plays a vital role in determining the thermal expansion coefficient and oxide ion conductivity in the pyrochlore structured composition whereas in the case of the fluorite structured composition the cumulative effect of the A-O and B-O bond takes the dominant role.

The contrasting effects of anion disorder on the system  $\text{Sm}_2\text{Zr}_2\text{O}_7$  via the simultaneous aliovalent cation substitutions in the Zr site is studied in detail in the third chapter. The study revealed that at the initial lower substitution of Y and Nb on the Zr destabilises the system, and the lattice strain in the system is reduced. On further doping, it stabilises the system, and the lattice strain of the whole lattice is increased. After this, the Y and Nb substitution on the system acts as tetravalent substitution with higher ionic radius. In this study, qualitative measurement of the anion disorder is done using the ratio of the intensity of the  $E_g$  peak to that of the peak at around  $800\text{ cm}^{-1}$ .

Anion deficient pyrochlore type compositions,  $\text{RE}_3\text{Zr}_{0.5}\text{Nb}_{0.5}\text{O}_{6.75}$  is studied in the fourth chapter. In this chapter, as the available oxide ion vacancies are increased the cooperative behaviour of the ions takes a significant role in determining the activation energy and thus the conductivity. Here as the lattice volume of the composition decreases the effect of the cooperative behaviour among the ion enhances and thus, the activation energy increases rapidly, which again causes the decrease in ionic conductivity.

In the fifth chapter ionic conductivity of a misplaced displacive pyrochlore system is studied. In this chapter, the compositions:  $\text{Ca}_3\text{Ti}_3\text{Nb}_2\text{O}_{14}$ ,  $\text{Ca}_3\text{Ti}_2\text{ZrNb}_2\text{O}_{14}$ ,  $\text{Ca}_3\text{TiZr}_2\text{Nb}_2\text{O}_{14}$  and  $\text{Ca}_3\text{Zr}_2\text{Nb}_2\text{O}_{14}$  are studied. The series exhibits a phase transition from cubic pyrochlore to monoclinic pyrochlore as the Zr content in the composition increases. This phase transition is attributed to the increased ionicity of the B-O bond as the Zr in the B site of the pyrochlore increases. The conductivity study revealed that the best conductivity is obtained for the cubic pyrochlore system which is an order of magnitude higher than the reported oxide ion conductivity for the displaced pyrochlore.

The sixth chapter is an attempt to stabilise the  $\delta\text{-Bi}_2\text{O}_3$  via the aliovalent and isovalent substitution by synthesising a series of compositions,  $\text{MgBi}_{1.5}\text{RE}_{0.5}\text{O}_4$  (RE = Nd, Sm, Gd, Dy, and Y). A phase transition from rhombohedral to fluorite structure occurs as the ionic radius of the lanthanide cation decreases. The conductivity of the rhombohedral compositions is lesser than that of the fluorite compositions, which decreases with the lattice volume. However, in the case fluorite composition the maximum conductivity is obtained for the Y substituted composition irrespective of the lesser lattice volume and higher activation energy



than the Dy substituted composition. This is due to the phase transformation of the Dy substituted composition from fluorite to rhombohedral at about 773K.

Chapter seven summarises the significant findings and conclusions drawn from the work and gives the scope for further studies.



# Chapter 1

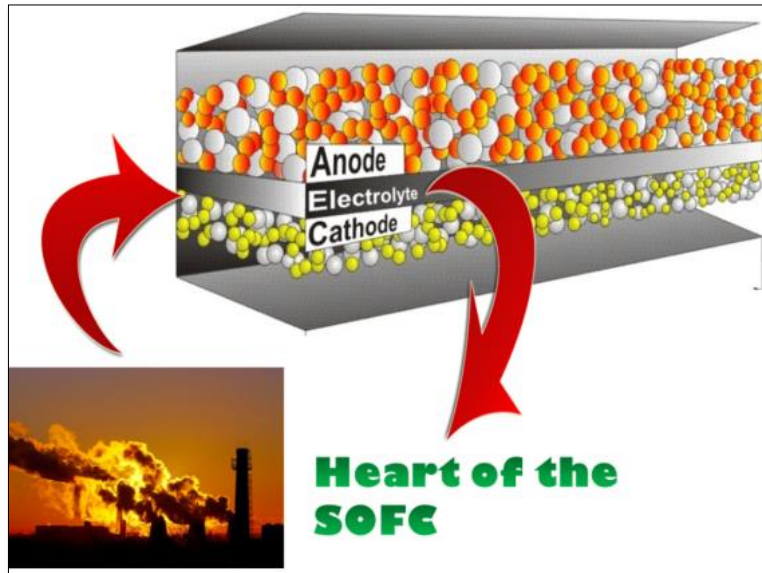
## Introduction

---

---

*This chapter introduces solid oxide fuel cell as a promising and reliable energy source in the near future. The chapter begins with the importance of materials science. The chapter discusses the basic operation, the components of the fuel cell and the material requirements.*

*The importance of the solid oxide electrolyte in determining the cell performance, oxide ion conduction mechanism through the solid oxide materials are also discussed in detail. A general literature survey of oxide ion conducting solid electrolytes belonging to different crystal structures is presented in the chapter.*





## 1.1 Introduction

Energy is an essential and inevitable input to the social and economic growth of the world and the energy resources, and its utilisation makes a significant role in the world's development. Our energy consumption is rising day by day due to the increased population, increased urbanisation and growing economy. At the same time, the use of conventional non-renewable energy resources is causing atrocious effects on the environment, such as the greenhouse effect, global warming, increased atmospheric temperature, and rise in the sea level and further, the sources of fossil fuels are depleting in a rapid rate. Hence alternative eco-friendly sustainable energy resources are needed. Many countries are researching on the development of the new alternative resources known as renewable energy resources. Currently, some of the available alternative energy resources are solar energy, geothermal energy and fuel cells using non-conventional fuels such as hydrogen, biodiesel, methane and biomass source (Panwar *et al.* 2011). The utilisation of these renewable energy sources consist of two steps: (1) converting energy from infinite energy resources such as solar energy and hydrogen to a useful form, (2) storage of energy in high-performance storage devices. The first step mentioned above aims at the development of solar cells, fuel cells etc. and the second one's goal is blooming of lithium-ion batteries and supercapacitors (Sun *et al.* 2011).

## 1.2 Materials Science

Our world is surrounded by different types of materials such as ceramics, glasses, composites, polymers, metal alloys, semiconductors, etc. These materials have always been the keystone in the development and growth of the humankind. The development of these materials began with the man himself, and the designation of the early civilisation is based on the materials development at that time (Stone age, Bronze age and Iron age.). The study of these materials known as materials science, which is an interdisciplinary science concerned with the understanding and application of the properties of materials.

Material science comprises two branches: Material science and Material Engineering. Material scientists investigate the relationship between the structure and property of the materials and the engineers based on these structure-property relations, design the structure of new materials to obtain the predetermined properties. There are four essential components which are involved in the study of materials science and engineering: (1) processing, (2) structure, (3) properties and (4) performance. Structure of a material is the arrangement of the

internal components of the material. The structure of the material depends on the processing techniques used to obtain the final form of the material. The material's response in terms of kind and magnitude to the specific type of stimulus is termed as the property, and the performance of a system depends on the properties. The relation between the four components is shown in Fig. 1.1 (Callister 2001).



**Fig. 1.1** The relationship between the four elements of material science

The materials in the modern world are classified into two categories: Structural materials and Functional materials. As the name implies, the structural materials are used to make structure, bodies, and components. The functional materials perform a particular function in the presence of an external stimulus. This type of materials mainly includes ionic conductors, semiconductors, dielectrics, pyroelectrics, piezoelectrics, ferroelectric, electro-optics and magnetic materials. The discovery of these materials dates back to the nineteenth century, and some of the materials having these properties are used in the Second World War. The properties of these materials mainly depend on the compositions, singularities of the crystallographic structure, and the material processing. The knowledge of the relationships between these factors will help the material world to develop new and improved materials for the current application and new uses. The materials scientists are in search of these relationships to develop and produce new materials that optimise materials to meet tomorrow's needs (Vilarinho 2005).

### 1.3 Energy Crisis and Environmental Pollution

According to World Economic Outlook 2007, fossil fuels will be the primary energy sources and the world's 84% of energy needs will be satisfied by fossil fuels up to 2030. Recent studies on the subject show that fossil fuels will be available only up to 2112 (Sun *et al.* 2011). So the problem of the energy crisis is getting worse, and the diminishing natural resources will take thousands of years to replenish the stores. At the same time, the rate at which the usage of fossil fuels is increasing as the population and wastage of energy increases. In addition to this, the usage of these fossil fuels causes significant damage to the environment surrounding us.

The usage of fossil fuels releases a massive amount of hazardous substances such as

carbon monoxide, sulphur, lead, and other toxic substance to the environment. These gases, which are known as greenhouse gases lead to global warming, increases in atmospheric temperature and rise in sea level. These greenhouse gases act as a blanket to the earth and trap the IR rays from the sun and cause an increase in the temperature. This increase in temperature causes sea level rise and change in the climate. In addition to this, the toxic gases cause detrimental effects to human health. Thus, these two factors (diminishing energy resources and environmental problems) force the researcher to search for new clean, renewable energy resources.

Some of the currently using renewable energy resources are solar energy, wind power, hydroelectric energy, geothermal power, and hydrogen fuel cells. These sources such as solar cells, wind, and hydroelectric power plants in one way or another depends on the sun. Therefore these sources rely on the availability of the sunlight and other facts. That is, these energy resources are variable, and they cannot supply continuous power unless there is no effective storage mediums are present. However, the storage of energy is also a difficult job since the batteries and similar technology performs only for a short period. So in the current scenario, the research is on developing a new clean, sustainable energy resource. One of the solutions to our energy needs is the fuel cell, which is a consistent source of electricity and can rely upon as a sole power source

#### **1.4 Fuel cell**

A fuel cell is an electrochemical device which can directly convert the chemical energy to electrical energy by merely combining hydrogen and oxygen to produce water. The history of fuel cells started with William Grove in 1839. While analysing the electrolysis of water, Grove observed that a small current flowed through the cell, as a result of the reaction between the electrolysis products, hydrogen and oxygen when the external power supply is switched off. Grove combined a number of these cells to form a gaseous voltaic battery (Ormerod 2003). However, the term fuel cell was first used by Mond and Langer in 1889 (Mond and Langer 1890). This fuel cell can provide a continuous supply of energy as the fuel and air are supplied. If hydrogen is used as the fuel, then the products are electricity, water, and heat. The fuel cells almost resemble the batteries, but it does not require electrical charges. Because of this, the fuel cells are used in the space probes, satellites, and spacecraft.

Any fuel cell consists of three components, namely

1. Anode
2. Cathode
3. Electrolyte

Fig. 1.2 is a schematic representation of a fuel cell. The fuel such as the hydrogen is supplied to the anode compartment and the oxygen for oxidation is provided to the cathode compartment. The direct chemical combustion is prevented using the electrolyte in between them. i.e. the electrolyte acts as a barrier to the gas diffusion, but it allows the migration of ions through it. The ions are produced at the electrode compartment. So the oxide ions are supplied to the cathode, and these migrate to the anode to combine with the hydrogen to form water, electrons, and heat.

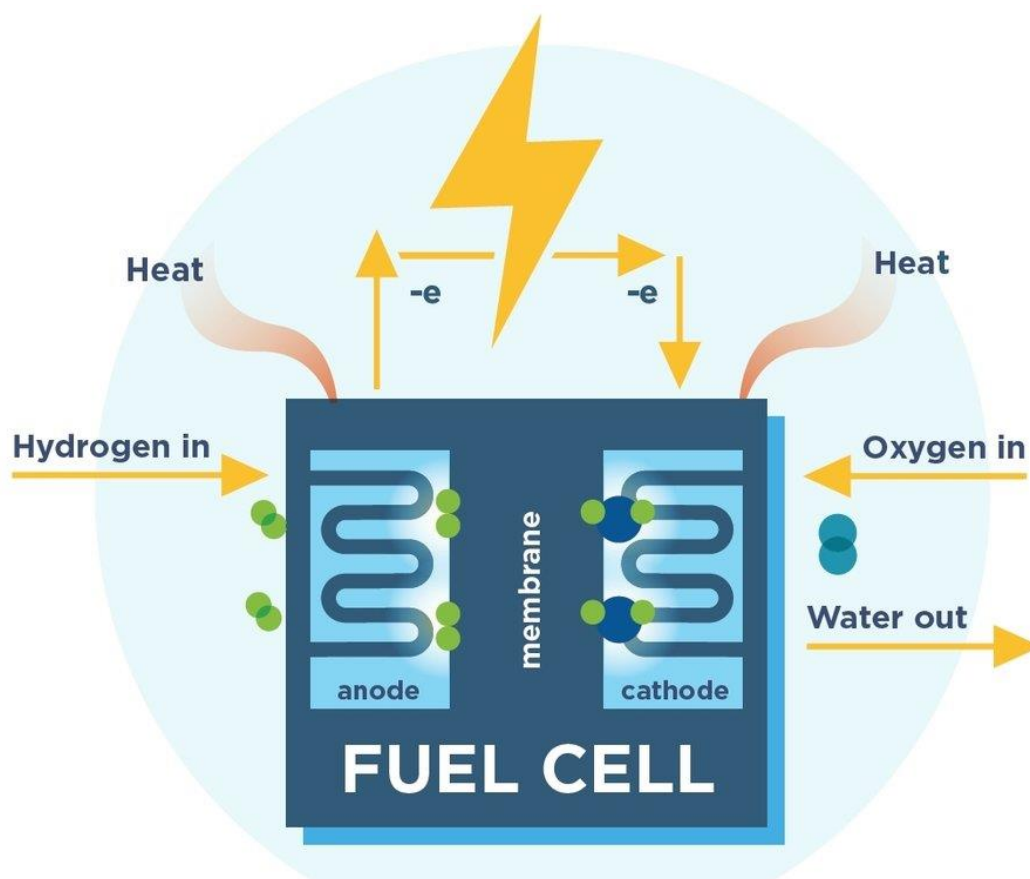


Fig. 1.2 The schematic representation of a fuel cell

#### 1.4.1 Types of fuel cells

Fuel cells are characterised by the electrolyte used in it. Based on the electrolyte, several types of fuel cells have been developed. Table 1.1 shows the different kinds of fuel cells that are currently under development (Stambouli and Traversa 2002).



Table 1.1 Types of fuel cells

Types of fuel cell	Electrolyte	Operating Temperature	Fuel	Oxidant	Efficiency
Alkaline (AFC)	Potassium Hydroxide (KOH)	50-200°C	Pure hydrogen or hydrazine	O <sub>2</sub> /Air	50-55%
Direct Methanol (DMFC)	Polymer	60-200°C	Liquid methanol	O <sub>2</sub> /Air	40-55%
Phosphoric acid (PAFC)	Phosphoric acid	160-210°C	Hydrogen from hydrocarbons and alcohol	O <sub>2</sub> /Air	40-50%
Sulfuric acid (SAFC)	Sulphuric acid	80-90°C	Alcohol or impure hydrogen	O <sub>2</sub> /Air	40-50%
Proton exchange membrane (PEMFC)	Polymer, proton exchange membrane	50-80°C	Less pure hydrogen from hydrocarbons or methanol	O <sub>2</sub> /Air	40-50%
Molten carbonate (MCFC)	Molten salt such as nitrate, sulphate, carbonates	630-650°C	Hydrogen, carbon monoxide, natural gas, propane, marine diesel	CO <sub>2</sub> /O <sub>2</sub> /Air	50-60%
Solid oxide (SOFC)	Ceramic as stabilised zirconia and doped perovskite	600-1000°C	Natural gas or propane	O <sub>2</sub> /Air	45-60%
Protonic ceramic (PCFC)	Thin membrane of barium cerium oxide	600-700°C	Hydrocarbons	O <sub>2</sub> /Air	45-60%

On analysing table 1.1, the first three are characterised by low operating temperature and hydrogen as the fuel. The remaining ones are working at very high temperature and can use hydrocarbons directly as the fuel to the cell and thus possess higher efficiency. The difference in operating temperature implicates the application for which the fuel cell is most suited (Ormerod 2003).

### 1.5 Solid Oxide Fuel Cells

Solid oxide fuel cells, characterised by the use of the solid oxide as the electrolyte material are seeking attention in recent years due to its high efficiency, reliability, fuel adaptability etc. These fuel cells operate at very high temperature, and this high operating temperature allows internal reforming, rapid electrocatalysis with non-precious metals and produces high-quality heat as a byproduct. The efficiency of fuel cell increases to 70% with an additional 20% as heat recovery (Stambouli and Traversa 2002).

#### 1.5.1 History of Solid Oxide Fuel Cells

The first solid oxide electrolyte is discovered in 1899 by Nernst. Nernst reported that conductivity of pure metal oxides increases very slowly with temperature and it remained relatively low, and at the same time, the mixtures of metal oxides show high conductivities. In his patent, Nernst reported a glower in which Zirconium oxide stabilised with 15% yttrium oxide used as a glowing filament. Due to some practical disadvantages and the discovery of the first tungsten lamp in 1905, further research on the subject of ionic conductors was discarded (Nernst 1899).

In 1905 itself the first fuel cell with solid oxide electrolyte (glass and porcelain) is filed for patent. In 1916, Baur and Treadwell filed a patent on fuel cell with ceramic oxides with salt melts in the pores as the electrolyte. In 1937, Baur and Preis demonstrated the solid oxide fuel cell with yttria stabilised zirconia at 1000°C (Nernst 1899). Until the 1960s, the high operating temperature and the reducing nature of the fuel gas held up the development of the solid oxide fuel cell. After the 1960s, advances in the preparation and production of the ceramic materials leads to the development of solid oxide fuel cell. Subsequent developments and advancements in the SOFCs and its components are taking place in the industrial and academic laboratories.

### **1.5.2 Advantages and Disadvantages of Solid Oxide Fuel Cells**

Solid oxide fuel cells have many benefits.

- Higher efficiency, higher power density, highly reliable.
- Fuel flexible since internal reforming can be done on the anode.
- SOFCs produce high-quality heat as a byproduct which can be used in combined heat and power systems which in turn increases the overall efficiency.
- No need for electrolyte loss maintenance and corrosion maintenance.
- SOFCs have extremely low emission as CO is converted to CO<sub>2</sub> at high operating temperature.
- SOFCs have a potentially long life expectancy of more than 40000-80000h since these show higher tolerance to the impurities in the fuel.
- High operating temperature hinders the use of expensive catalysts as platinum.
- They operate quietly, and these are vibration-free since there are no moving parts involved.
- In addition to all these, SOFC stacks can be put together in various ways and some of which are considerably simpler compared to other fuel cell stacks

Even though, the material selection for individual components presents an enormous challenge due to the high operating temperature. Some of the disadvantages of the SOFCs are

- The long startup time, which required to heat the system.
- High operating temperature decreases the cell lifetime.
- Expensive high-temperature alloys are used to house the cell.
- Expensive ceramics for interconnections.
- High operating temperature also needs significant thermal shielding to protect personnel and to retain the heat.

- Also, the high operating temperature induces thermal stress at the electrode-electrolyte interface, and interdiffusion between cell components occurs (Mahato *et al.* 2015).

Thus, for the implementation of low cost SOFCs requires lowering of the operating temperature

### 1.5.3 Applications of Solid Oxide Fuel Cells

SOFC has a broad range of applications from large-scale power plants to smaller home-scale power plants and portable or emergency power generators. The most needed use depends on the following properties of the SOFC

- High power reliability: computer facilities, call centres, communication facilities, data processing centres, high technology manufacturing facilities
- Emission minimisation or elimination: urban area, industrial facilities, airports, zone with strict emission standards
- Limited access to utility grid: rural or remote areas, maximum grid capacity
- Biological waste gases are available: waste treatment plants, SOFC can convert waste gases to electricity and heat with minimal environment intrusion (Stambouli and Traversa 2002).

### 1.5.4 Working of Solid Oxide Fuel Cells

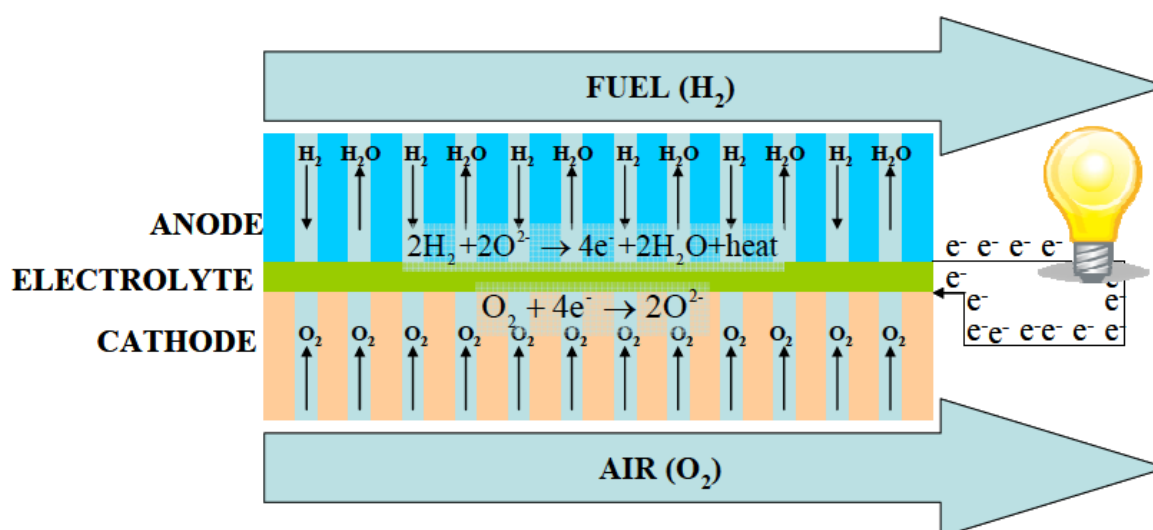


Fig. 1.3 Working of Solid Oxide Fuel Cell

Similar to any other fuel cells, the SOFC also has three components, and a interconnect

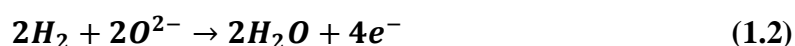
to make a stack of the SOFC. In a typical SOFC, oxide ions move from the cathode to the anode. The air containing oxygen is supplied to the cathode, and the oxygen gets reduced to oxide ions, and the reformed fuel is supplied to the anode. The oxide ions move through the electrolyte to the anode to combine with the fuel and releases electrons to the external circuit and produce water as a byproduct. The chemical reaction occurring at the electrodes are:

At cathode:



An ideal electrolyte offers no electrical conductivity and high ionic conductivity. At the operating temperature, only the oxide ions should flow through the electrolyte to the anode. The oxide ions combine with the fuel at the anode.

At anode:



The overall chemical reaction is (Bove 2007)



The electrons are carried to the external load via the current collector at the anode of the fuel cell. The driving force for the oxide ion movement through the electrolyte is the gradient of the oxide ion concentration at the electrodes or the difference between the oxygen partial pressure ( $P_{O_2}$ ) at the electrodes. Thus the Nernst equation provides the theoretical reversible electromotive force ( $E_{th}$ ) as

$$\mathbf{E_{th} = \frac{RT}{4F} \ln \left( \frac{P_{O_2}^{cathode}}{P_{O_2}^{anode}} \right)} \quad (1.4)$$

where R is the universal gas constant, T is the absolute temperature, and F is the Faraday's constant (96,500 C/mol). The coefficient 4 denotes the number of the electrons transferred when one molecule of the oxygen atom is reacted in the cell. The partial oxygen pressure at the cathode can be taken as that of the air (i.e. 0.21 atm) since air is supplied to the cathode. In laboratory experiments, reformed hydrogen is used as the fuel and is supplied to the anode. Using the overall chemical reaction mentioned above the mass action expression can be represented as

$$\mathbf{K_{eq} = \frac{P_{H_2O}}{(P_{H_2})(P_{O_2})^{\frac{1}{2}}}} \quad (1.5)$$

$K_{eq}$  is the equilibrium constant for fuel gas station. The Gibb's free energy and oxygen partial pressure at the anode side can be calculated using the Eqns (1.4) and (1.5) assuming no water condensation occurs at the anode or the gas delivery system.

$$\Delta G_T = \Delta H_T - T\Delta S_T = -RT \ln (K_{eq}) \quad (1.6)$$

In Eqn (1.6)  $\Delta H_T$  is the heat change, and  $\Delta S_T$  is the entropy change. The oxygen partial pressure at the anode is calculated using Eqn (1.6)

$$P_{O_2} = \left( \frac{P_{H_2O}}{P_{O_2}} \right) \exp \left[ \frac{2(T\Delta S_T - \Delta H_T)}{RT} \right] \quad (1.7)$$

The above mentioned for oxygen partial pressure along with Eqn (1.4) is used to calculate the Nernst potential. The actual cell voltage obtained during the operation of the fuel cell is always lesser than that computed using Eqn (1.4) because of some electrochemical or polarisation losses. This difference between the theoretical and the operating voltages is the cell polarisation or overpotential  $\eta$ , and it arises due to the (i) ohmic resistance, (ii) charge transfer (activation) polarisation and (iii) diffusion concentration.

Ohmic resistance in the cell is due to the resistance offered to the flow of the ions and electrons in ionic and electronic conductors, respectively. It comprises the contact resistances between the cell components. The significant contribution to the ohmic polarisation is due to the electrolyte material, the magnitude of which is directly proportional to the current passing through the cell (Virkar *et al.* 2000). The activation polarisation arises due to the transfer of charges between the electronic and ionic conductors, and therefore, it is also termed as charge transfer polarisation. The concentration polarisation in the cell occurs when the reacting molecules are consumed in a faster rate so that the oxygen partial pressure at the cathode or low fuel partial pressure at the anode decreases and thus the overall voltage from the SOFC drops. The losses due to this polarisation cannot be eliminated, but it can be reduced by using proper components materials and optimised design of the cell (Mahato *et al.* 2015).

### 1.6 Components of Solid Oxide Fuel Cells

The significant components of SOFCs are mentioned earlier on the working of the SOFC. Since the operating temperature is high, the material of the components used in SOFC, should have to perform its function along with the other cell components. Hence the general requirements of the cell components are:

- Chemical stability in fuel cell environments and compatibility with other cell components.
- Phase and microstructural stability.
- Minimum thermal expansion mismatch between the various cell elements.
- Reasonable toughness and strength at the cell operating temperature.
- Moderate thermal shock resistance.
- Low vapour pressure to avoid loss of the material.
- Must allow cost-competitive component fabrication (Badwal and Foger 1996).

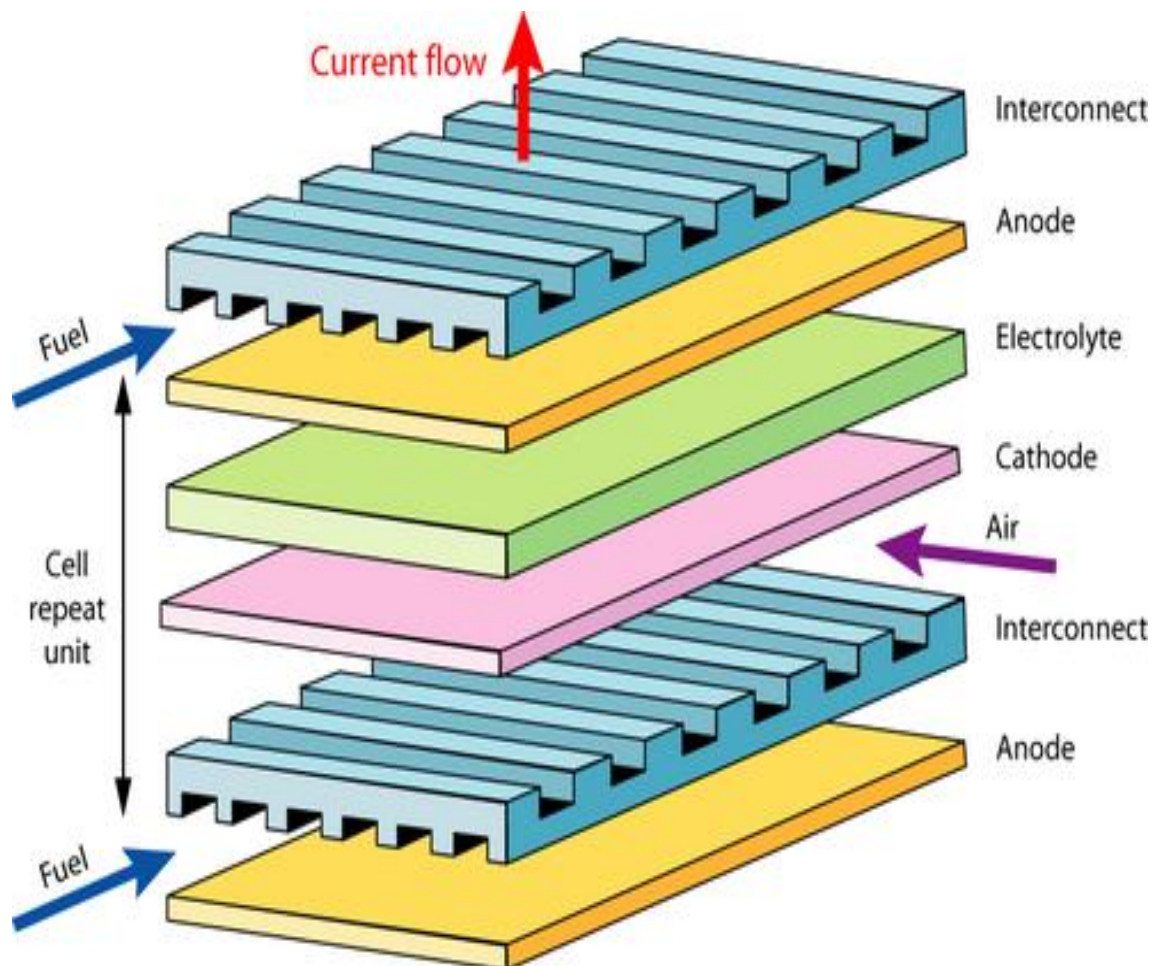


**Fig. 1.4** Components of SOFC

### 1.6.1 Anode

The electrode, through which the fuel is supplied to the fuel cell is the anode, and therefore, it is generally known as fuel electrode. The requirements of an anode are:

- The material should be stable under reducing atmosphere, high operating temperature.
- Should have high electric conductivity.
- High porosity to allow the passage of fuel.
- There should be no thermal expansion mismatch with the other cell components

The fuels used are reducing in nature, and so metals can be used as the anode materials (Singhal 2000). Because of the high operating temperature of the SOFC, the choice of the anode materials is limited to nickel, cobalt and the noble metals. Usually, nickel is preferable due to the low cost compared to cobalt and other noble metals. However, at the operating temperature of the SOFC, the nickel gets sintered and causes a decrease in the porosity, and the thermal expansion of the nickel is high compared to the electrolyte. The problem of thermal expansion mismatch and decline in the porosity can be eliminated using a skeleton of solid oxide electrolyte around nickel particles which is formed by dispersing the nickel with the solid oxide electrolyte material which is used as solid oxide electrolyte.

The electrical conductivity and thermal expansion coefficient of the cermet depend on the nickel content in the cermet. Both the parameters increase as the nickel content in the system increases. The conductivity of the anode also depends on the microstructure, particle size distribution of the solid electrolyte and nickel, and the connectivity of the nickel particles in the cermet. The higher thermal expansion mismatch may cause cracking of the electrolyte or delamination of the anode during the fabrication or in the operating cycle of the fuel cell. Thermal expansion mismatch can be overcome by avoiding any flaws in the processing of the electrolyte, improve in its fracture toughness and using anodes of different compositions and the addition of a third material to the cermet. In addition to all this, sintering of the nickel particles occurs at the high operating temperature of the SOFC, which increases with increase in the nickel content in the cermet (Ormerod 2003). Because of all these facts currently, much interest is put on the development of the alternative anode materials instead of nickel/YSZ cermet. Some of the alternative anode materials are listed here:



- Nickel/Ceria cermet anode for zirconia and ceria-gadolinium based SOFCs. These anodes show excellent performance in ceria based SOFCs (Uchida *et al.* 1998).
- Ceria added Ni/YSZ shows improved electrical performance and resistance to carbon deposition (Tsai and Barnett 1998).
- Cobalt/YSZ and Ruthenium/YSZ has high reforming activity, high sulphur tolerance, high resistance to sintering, and these electrodes are rarely used due to high cost.
- Various dopants such as molybdenum, gold, ruthenium and lithium are incorporated into nickel/zirconia and nickel ceria anodes to modify their reforming activity and tolerance against sulphur and carbon deposition (Finnerty and Ormerod 2000).
- Oxides which are electronic conductors and stable under both oxidising and reducing atmosphere are potential anode materials, and some of them are  $\text{LaCrO}_3$  and  $\text{SrTiO}_3$ . These anode materials offer the potential for direct oxidation of hydrocarbon fuel.

The development of anodes which can also be used for the direct hydrocarbon oxidation is a very active area of current research.

### 1.6.2 Cathode

The electrode known as the air electrode operates in an oxidising environment at approximately  $1000^\circ\text{C}$ . The oxygen in the air is reduced to oxide ions consuming two electrons in the process. The air electrode has to meet the following requirements:

- ❖ High electronic conductivity.
- ❖ Chemical and dimensional stability in environments encountered during cell operation and fabrication.
- ❖ Thermal expansion match and compatibility with the other cell components.
- ❖ Minimum reactivity with the electrolyte and the interconnect with which the electrode comes into contact.
- ❖ To facilitate the transport of molecular oxygen in the air supplied to the electrode, it should have sufficient porosity (Singhal 2000).

Similar to the case of anodes, it should be noble metals or oxides possessing sufficient electronic conductivity which is stable at the elevated temperature and in the oxidising atmosphere. Due to economic reasons, noble metals are precluded, and various oxides materials are studied in this aspect. Strontium doped lanthanum manganite (LSM), a perovskite structured material is the most commonly used material for the cathode.

$\text{La}_{1-x}\text{Sr}_x\text{MnO}_3$  is an intrinsic p-type conductor due to the formation of cation vacancies and electronic conductivity in this material can be enhanced by the use of lower valent cation, as the dopant in the A or B site cation. Magnesium, calcium, strontium, barium etc. are used as the dopants (Kertesz *et al.* 1982). Strontium doped ones are most common for zirconia-based SOFCs. The electronic conductivity of the LSM increases with the strontium content. At the same time, the increased strontium content increases the thermal expansion coefficient and thereby growing the mismatch with the Zirconia electrolyte. In the practical cases two layers are used as the cathode: (i) the first layer is a mixture of LSM and the yttria stabilised zirconia which is used as the electrolyte in the zirconia-based electrolyte so that the thermal expansion mismatching and sintering of the cathode material can be avoided and improved porosity can be achieved, (ii) the second layer used as the current collector is pure LSM. Platinum can be added to the cathodes to increase the cell performance by reducing the resistance loss between the current collector and the cathode (Minh 1993). The use of LSM cathodes with the zirconia-based SOFCs have some chemical compatibility issue above  $1200^\circ\text{C}$ . Above  $1200^\circ\text{C}$ , the LSM diffuses to the YSZ and forms  $\text{La}_2\text{Zr}_2\text{O}_7$  and  $\text{SrZrO}_3$  (in the case of compositions having higher Sr content). The conductivity of  $\text{La}_2\text{Zr}_2\text{O}_7$  is 100 times lower than that of zirconia (Taimatsu *et al.* 1992; Yamamoto *et al.* 1987).

Another perovskite material which is having superior electrical conductivity compared to that of the  $\text{LaMnO}_3$  and studied as the cathode material is  $\text{LaCoO}_3$ . Similar to lanthanum magnetite, the suitable substitution of the divalent cation on the lanthanum site increases the conductivity of the  $\text{LaCoO}_3$ . However, the use of the  $\text{LaCoO}_3$  as the cathode material in the zirconia-based SOFCs is precluded due to its higher reactivity towards YSZ at high temperature, and it is highly reducible at high temperature. Also, the thermal expansion coefficient is high compared to that of  $\text{LaMnO}_3$ , whose thermal expansion coefficient (TEC) is itself higher than YSZ. In order to make a better thermal expansion match and improve the electronic conductivity, a mixture of  $\text{LaCoO}_3$  and  $\text{LaMnO}_3$  is used. Strontium and iron substituted  $\text{LaCoO}_3$  ( $\text{La}_{1-x}\text{Sr}_x\text{Co}_{1-y}\text{Fe}_y\text{O}_3$ : LSCF) which is having improved performance as

cathode material is used in intermediate temperature SOFCs since LSM reduces the cell performance at low temperature. The current research on the field is to develop the cathode materials having better performance at a temperature as low as 500°C (Minh 1993; Ohno *et al.* 1981; Yamamoto *et al.* 1987).

### 1.6.3 Interconnect

The interconnect in the fuel cell provides electrical contact between the adjacent cells and distributes the fuel to the anode and air to the cathode. The requirements of the interconnection are

- It should have high electronic conductivity in both oxidising and reducing atmosphere.
- Should be stable on both oxidising and reducing atmosphere at high temperature.
- Chemical stability with the anode, cathode and electrolyte at high temperature.
- It must be impermeable to avoid mixing of the fuel and air supplied to the respective electrodes.
- Thermal expansion close to that of the electrodes and electrolyte.

LaCrO<sub>3</sub> having perovskite structure is used in the majority of the zirconia-based SOFCs. Doping with a divalent cation such as strontium, calcium and magnesium can improve the electrical conductivity of LaCrO<sub>3</sub>. Since the conductivity of the LaCrO<sub>3</sub> in hydrogen is shown to be around 1000 times lower than that in the air, there is an electrical conductivity gradient across the interconnect. At the high operating temperature, this gradient in the electrical conductivity does not affect the overall cell performance (Minh 1993). However, it is difficult to sinter LaCrO<sub>3</sub> to high density and impermeable due to the volatilisation of chromium under oxidising conditions. The sintering of LaCrO<sub>3</sub> can be facilitated at low oxygen partial pressure with firing temperature above 1600°C. Different methods are extensively studied to reduce the sintering temperature, and the methods include use of dopants, various sintering aids, different synthesis methods and the use of non-stoichiometric LaCrO<sub>3</sub>, which is deficient in chromium (Minh 1993). Calcium doped yttrium chromite is also used as the interconnect because of its better thermal expansion

compatibility. In intermediate temperature SOFCs, ferrite stainless steel composites are used as the interconnect, which offers very substantial cost benefits (Steele and Heinzl 2001). Using metals as the interconnect has the advantages of high electric and thermal conductivities which makes the fabrication easier and minimise the thermal gradients. However, the metal is prone to corrosion, and so corrosion resistant layers are required, and thermal expansion mismatch is significant. Siemens and Plansee AG developed Cr-based alloy with a better match in the thermal expansion of yttria stabilised zirconia over a whole range of temperature. However, much amount of work is still required to establish the suitability of this alloy for interconnects in SOFC (Badwal and Foger 1996).

### 1.6.4 Electrolyte

The operating temperature of the SOFC is determined by the solid oxide electrolyte used in the fuel cell through which the oxides ions starts conducting only at very high temperature and thus the solid oxide electrolyte is called as the “heart of the SOFC” (Zhu 2009). The objective of the present thesis is on the study of the structural factors that affect on the ionic conductivity of the solid oxide electrolyte and so a detailed literature survey on the solid oxide electrolyte is added on the latter section of the current chapter.

## 1.7 The State of the Art of Material for Solid Oxide Fuel Cell

In an attempt to improve the overall cell performance and to reduce to the operating temperature to an intermediate-range (400-700°C), different materials and their combination are developed and are studied in detail. For versatile applications of SOFC, each component with enhanced properties is needed. The commonly used cell components used in the SOFC are pictured in Fig. 1.5 (Abdalla *et al.* 2018).

## SOFC Hardware Alternative Materials

Electrolyte	Anode	Cathode	Interconnect
<ul style="list-style-type: none"> <li>• Zirconia material(YSZ, ScSZ,CaSZ)</li> <li>• Ceria Material (GDC, SDC,YDC, CDC)</li> <li>• Lanthunum materials (LSGM, LSGMC, LSGMF)</li> <li>• Bismuth based oxides</li> <li>• Pyrochlore based oxides</li> <li>• Barium and Stronitum</li> <li>• Brownmillerites</li> </ul>	<ul style="list-style-type: none"> <li>• Nickel based (Ni-O/YSZ, Ni-O/SSZ, Ni-O/GDC, Ni-O/SDC, Ni-O/YDC)</li> <li>• Copper materials (CuO<sub>2</sub>/CeO<sub>2</sub>/YSZ, CuO<sub>2</sub>/YSZ, CuO<sub>2</sub>/YZT, CuO<sub>2</sub>/CeO<sub>2</sub>/SDC)</li> <li>• Lanthunum materials (La<sub>1-x</sub>Sr<sub>x</sub>CrO<sub>3</sub>, La<sub>1-x</sub>Sr<sub>x</sub>Cr<sub>1-y</sub>M<sub>y</sub>O<sub>3</sub>)</li> <li>• Other materials (CeO<sub>2</sub>/GDC, TiO<sub>2</sub>/YSZ)</li> <li>• Cobalt based materials</li> </ul>	<ul style="list-style-type: none"> <li>• Lanthnum materials (LSM,LSF,LS C, LSCF, LSMC, LSMCr, LCM, LSCu, LSFN, LNF, LSCN, LBC, LNC, LNO)</li> <li>• Gadolinium mateials (GSC)</li> <li>• Prasedomium Materials (PCM, PSM, PBC)</li> <li>• Strontium materials (SSC, NSC, BSCCu)</li> <li>• Yttrium materials (YSCF, YCCF, YBCu)</li> </ul>	<ul style="list-style-type: none"> <li>• Metals (base metals, chromium alloys, ferritic stainless steel, austenitic stainless steel, iron alloys)</li> <li>• Coatings ( LSM, LCM, LSC, LSFeCo, LSCr, LaCoO<sub>3</sub>)</li> <li>• Ceramic (lanthunum chromite)</li> </ul>

Fig. 1.5 The commonly used components of the SOFC


### 1.8 Reducing the Operating Temperature of the SOFCs

The high operating temperature causes a limitation in the commercial development of the SOFC and put numerous requirements on the selection of the material and secondary units. Therefore, a sustainable amount of work is doing in reducing the operating temperature of the fuel cell to an intermediate range of 500-700°C. However, as the temperature decreases resistive losses of the solid electrolyte increases and the overpotentials at the air and fuel electrode are magnified. Different strategies are used to reduce the operating temperature, and some of them are listed below:

- \* Reducing the thickness of the electrolyte by using new techniques like dense screen printing.
- \* Development of new electrolyte materials such as LAMOX, BIMEVOX or apatite families and understanding of mass transport properties can improve the ionic conductivity and thus reducing the operating temperature.
- \* Development to new anodes based on oxides to substitute the classical cermets, eg.  $\text{LaSrTiO}_3$ .
- \* Development of new cathodes with layered structures, e.g.  $\text{La}_2\text{NiO}_{4+\delta}$  and  $\text{GdBaCo}_2\text{O}_{5+\delta}$  may reduce the operating temperature
- \* Adaption of the fabrication processes for using interconnects based on metals.
- \* New strategies based on micro- and nanotechnologies are studied to improve the overall cell performance (Zhu 2009).

### 1.9 Solid Oxide Electrolyte

The major challenge in reducing the operating temperature of the solid oxide fuel cell is the development of new oxide ion-conducting materials which can be used as the electrolyte in the cell. In practical application, only a few materials are suitable for function as a solid oxide electrolyte, and this is because many electrical, chemical, mechanical and electrochemical properties should be optimised for a solid oxide electrolyte. Some of them are listed below:

-  An electrolyte should have very high oxide ion conductivity and nearly zero electron conductivity to reduce the leakage current.

- ✚ Excellent thermodynamical stability.
- ✚ The electrolyte should have high chemical compatibility with the anode, cathode and interconnect.
- ✚ Should be highly dense to avoid the mixing of fuel and air.

To reduce the operating temperature, which is governed by the nature of the electrolyte used depends on the two factors: its ionic conductivity and its thickness. In earlier times, SOFC relies on the electrolyte for structural support, and nowadays, the anode supported SOFCs are developed, and the thickness of the electrolyte is reduced to 10-15  $\mu\text{m}$  (Ormerod 2003). Besides all these difficulties, the solid oxide electrolytes have several advantages over the liquid ones, and some of them are listed below:

- \* Easier to handle than the reactive liquid electrolytes and the sealing problems can be avoided.
- \* Discharge is minimized under open-circuit conditions.
- \* It has improved chemical stability under highly reactive conditions.
- \* The miniaturisation of the cell can be achieved through the application of thin-film techniques (Tuller 2017).

For improved ionic conductivity, the search for alternative solid electrolyte has been an active area of research for many years.

### 1.9.1 Conduction Mechanism

In a typical solid, the ionic conduction is in the range of  $10^{-10}$  S/cm at a temperature of  $200^\circ\text{C}$ , since there is a limited number of mobile ions are available for the conduction process. In solids, the ions are trapped in relatively stable potential wells, and hence their motion is hindered thus causes much smaller velocity. However with the increase in temperature, the total thermodynamical free energy gets increased and to minimise the free energy, the system will try to increase entropy which will lead to a creation of more defects in the lattice.

The ionic conduction through the solids occurs through the activated jump process, and the diffusion coefficient corresponding to this conduction is given by

$$D = D_0 \exp\left(\frac{-\Delta G}{k_B T}\right) = \gamma(1 - c) Z a^2 \vartheta_0 \exp\left(\frac{\Delta S}{k_B}\right) \exp\left(\frac{-E_m}{k_B T}\right) \quad (1.8)$$

where  $a$  is the jump distance  $\vartheta_0$  is the lattice frequency, and  $E_m$  is the migration energy. The factor  $(1 - c)Z$  defined the number of neighbouring unoccupied sites, while  $\gamma$  includes geometric and correlation coefficients. The ion mobility  $\mu$  is given by the equation

$$\mu = \frac{qD}{k_B T} \quad (1.9)$$

Using the equation for the diffusion coefficient and the classical equation connecting the conductivity and mobility

$$\sigma = nq\mu = \frac{nq^2}{k_B T} \gamma c(1 - c)Za^2\vartheta_0 \exp\left(\frac{\Delta S}{k_B}\right) \exp\left(\frac{-E_m}{k_B T}\right) \quad (1.10)$$

where  $n$  in the present context is the total number of sites that are available for conduction (Tuller 2017). The equation is in correlation with the Arrhenius equation given by

$$\sigma = \sigma_0 \exp\left(\frac{-E_a}{k_B T}\right) \quad (1.11)$$

where  $\sigma_0$  is the pre-exponential coefficient, which is a measure for the available charge carriers,  $E_a$  is the activation energy required for the hopping of ions through the lattice. The equation for the conductivity reveals that the conductivity is zero when the factor  $c(1-c)$  is zero, which is for highly perfect crystals. However, it implies that ionic conductivity through the solids can be explained in terms of creation and motion of atomic defects, notably vacancies and interstitials.

Ionic defects can be induced to the lattice of the oxides by

1. Thermally causing the intrinsic ionic disorder such as Schottky and Frenkel defect
2. Redox induced defects
3. Impurity caused defects.

The defects such as the Schottky and Frenkel defects left the stoichiometry of the composition intact and the redox induced defects to cause the imbalance of cation to anion ratio, and so causes non-stoichiometry. In the case of the third one, substituting the cation with a lower valent cation induces high charge carrier density to the lattice. The selection for the lower valent cation depends on the following factors:

- The high solid solubility of the substituent with the lower valency.



- Association energies between the oxygen vacancy and dopant should be small.
- No long-range ordering of defects.

Thus the high density of mobile ions, availability of vacancies and a crystal structure that enable the migration of ions much easier are required for a good oxide ion conductor (Tuller 2017).

### 1.9.2 General Survey of Electrolyte Materials

As discussed earlier, one of the essential properties of the solid oxide electrolyte is the ionic conductivity. In the development of oxide ionic conductors; the structure of the materials plays an upper hand role. It has to have some peculiar features such as:

- ✓ Existence of a large number of equivalent sites for the oxide ions and oxygen vacancies.
- ✓ High symmetry for the crystal system (mostly available oxide ion conductors are in cubic).
- ✓ Large specific free volume.
- ✓ High polarizability of the cations in the system to make the transport of oxide ion easier.

Consequently, a limited number of crystal systems are suitable to develop as oxide ionic conductors and some of the reported oxide ion conductors are reviewed here.

#### 1.9.2.1 Zirconia Based Electrolytes

The best-known oxide ion conductor and the solid oxide electrolyte which is used in the commercially available high-temperature SOFC is the acceptor doped  $ZrO_2$ . Pure  $ZrO_2$  is not an oxide ion conductor and exhibit three different crystal polymorphs: monoclinic, tetragonal or cubic respectively depending on the temperature (Boivin and Mairesse 1998). The cubic phase of the  $ZrO_2$  forms only at a temperature of  $2300^\circ C$ . The cubic structure of the  $ZrO_2$  is stabilised to the room temperature by the substitution of acceptor cation in the  $ZrO_2$  lattice, and the substitution with the lower valent cation induces oxygen vacancies to the lattice which causes the oxide ion conductivity through the lattice. The ionic conductivity at a temperature depends on the concentration and nature of the dopant cation. The conductivity is maximum when the dopant has a similar ionic radius as that of the  $Zr^{4+}$ .

Commonly used dopants are cations such as  $\text{Ca}^{2+}$ ,  $\text{Y}^{3+}$  and  $\text{Sc}^{3+}$ . The yttria stabilised zirconia (YSZ) is a good oxide ion conductor at a temperature above  $700^\circ\text{C}$  and has been the subject of intense research to be used in the SOFC (Brett *et al.* 2008; Steele and Heinzel 2001). The high operating temperature makes the use of YSZ difficult for small scale application (Mobius 1997). Scandium Stabilised Zirconia (ScSZ) is a possible substitute for the YSZ one, but the cost of scandium limits its use (Badwal *et al.* 2000; Malavasi *et al.* 2010). The high conductivity of the ScSZ is arising due to the similarity in the ionic radius of the  $\text{Sc}^{3+}$  ( $r = 0.87\text{\AA}$ ) and  $\text{Zr}^{4+}$  ( $0.84\text{\AA}$ ) (for VIII coordination). As the substitution with the lower valent cation increases, the extrinsic conductivity due to the oxygen vacancies created increases, and beyond a particular substitution concentration, the linear increase in the number of oxygen vacancies does not promote the oxide ion conductivity and thereafter it decreases. The decrease in the conductivity is because of the association of point defects, which leads to a reduction in defect mobility and thus conductivity. The optimum concentration of the dopant lies in the range of  $0.08 \leq x \leq 0.12$ . Considering all the requirements of solid oxide electrolyte such as the chemical stability, mechanical stability yttria stabilised zirconia with  $x=0.08$  is used in the practical application of the SOFC (Boivin and Mairesse 1998).

### 1.9.2.2 Ceria Based Electrolytes

$\text{CeO}_2$  doped with acceptor cations are another category of fluorite type compositions which seeks the attention of the researchers in the field of solid oxide electrolyte whose conductivity is higher than that of YSZ typically at a lower temperature ( $500\text{-}700^\circ\text{C}$ ). The common dopants are  $\text{Gd}_2\text{O}_3$  (producing gadolinium doped ceria (GDC) and  $\text{Sm}_2\text{O}_3$  (samarium doped ceria, SDC). In addition to these gadolinium and samarium (Ishihara *et al.* 2005; Yahiro *et al.* 1988; Yahiro *et al.* 1989), other dopants for ceria include lanthanum (Suda *et al.* 2006), yttrium (Kharton *et al.* 2004; Yahiro *et al.* 1989), ytterbium (Yashiro *et al.* 2004) and neodymium (Hong *et al.* 1998). Among these dopants, gadolinium and samarium are suitable because of their similarity in the ionic radius. The high ionic conductivity at the lower temperature makes this electrolyte as a suitable candidate for the IT-SOFC (Intermediate temperature –Solid Oxide Fuel Cell). However, at low oxygen partial pressure and temperature above  $600^\circ\text{C}$ ,  $\text{Ce}^{4+}$  ions get reduced to  $\text{Ce}^{3+}$  and thus increasing the electronic conductivity (Wang *et al.* 1997). This reduction causes non-stoichiometry and lattice expansion which leads to mechanical failure (Kharton *et al.* 2004). The materials

redox stability can be increased via co-doping with the rare earth elements. Although the electronic conductivity does not affect the overall efficiency significantly except for a reduction in the overall voltage.

Increased dopant concentration on the CeO<sub>2</sub> leads to the decrease in ionic conductivity, and atomic simulation and experimental studies show that clustering of dopant ions and oxygen vacancies and defect association causes the decrease in ionic conductivity (Kilner 2000; Seo *et al.* 2006; West *et al.* 1997). Another vital strategy to improve the ionic conductivity properties is to mixing of zirconia along with ceria so that an electrolyte with improved chemical and mechanical properties of zirconia and better ionic conductivity of ceria can be developed (Yeh and Chou 2009) but the system produced is not suitable for long term application since chemical reaction occurs between zirconia and ceria (Boivin and Mairesse 1998).

The chemical stability of the ceria with the cathode materials is high compared to the YSZ. Ceria based electrolytes are compatible with any available cathode electrodes such as LSM, LSC, LSF, LSCF, LNF (Brugnoni *et al.* 1995; Chiodelli and Scagliotti 1994; Yeh and Chou 2009). Because of this excellent chemical stability, it is used as the interface between the YSZ and cathode in the cells, which can improve oxygen transport through the cathode materials. Due to this high ionic conductivity and high chemical stability with the cathode materials makes the ceria based electrolyte as an ideal candidate for the IT-SOFC.

### 1.9.2.3 Perovskite Structured Oxides

Perovskite structured oxides with the general formula ABO<sub>3</sub> are another category of materials that are suitable for use as a solid oxide electrolyte. The structure is composed of two octahedra: A cation coordinated to twelve oxygen ions and the B cation occupying a six-coordinate site and forming BO<sub>6</sub> octahedra. Tilting of these polyhedra results in the deviation from the cubic symmetry (Malavasi *et al.* 2010). The cubic symmetry of the composition lowers as a tolerance factor, defined using the ionic radius of the A and B cations,  $(R_A+R_O)/(R_B+R_O)$  ratio deviates from the ideal  $\sqrt{2}$  value (Boivin and Mairesse 1998). Similar to the fluorite structured oxides, oxygen vacancies are introduced to the lattice by the aliovalent acceptor cation. Samuel *et al.* predicted that lattices with a low mean value of metal-oxygen bonding energy, an open structure (high free volume), and a critical cation bottleneck for O<sup>2-</sup> migration are suitable factors for a perovskite oxide ion conductors, and

this shows that the A and B cation ionic radius and their valence state are determining factors (Takahashi and Iwahara 1971).

LaGaO<sub>3</sub> is one of the highly studied perovskite oxides in this aspect. Ishihara *et al.* in 1994 reported that Sr and Mg-doped LaGaO<sub>3</sub> (La<sub>1-x</sub>Sr<sub>x</sub>Ga<sub>1-y</sub>Mg<sub>y</sub>O<sub>3-δ</sub>) known as LSGM is an oxide ion conductor (Ishihara *et al.* 1994). LSGM shows pure ionic conductivity over a wide range of partial pressure and ionic conductivity is high compared to YSZ at relatively low temperature. However, the practical use of LSGM as an ionic conductor has some difficulties: (i) it is difficult to obtain pure single-phase materials and (ii) the gallium is highly volatile (iii) high reactivity towards Ni (which used as the cathode in the fuel cell) so that ionically insulating LiNiO<sub>3</sub> forms. The high ionic conductivity in LSGM is due to the increased symmetry arises due to the reduction of the tilt of GaO<sub>6</sub> octahedra due to the simultaneous substitution of Sr and Mg (Kajitani *et al.* 2005). The oxide ion migration in these oxides occurs by vacancy hopping mechanism between oxygen sites along a GaO<sub>6</sub> octahedron edge, accompanied by outward relaxation of adjacent cations with a slightly curved trajectory (Ishihara *et al.* 1994). The study on the dopant vacancy association shows that the binding energy for Sr dopant-vacancy clustering is negligible and that of the Mg dopant-vacancy has a significant value resulting two distinct regions or non-linear portion on the Arrhenius plot (Islam and Slater 2009). Thus higher Mg doping level increases the activation energy, and slight replacement Mg with Co or Ni whose binding energy is less improves the overall cell performance (Li and Bergman 2009).

Ishihara *et al.* studied a new series of rare-earth-doped compositions (La<sub>0.9</sub>Ln<sub>0.1</sub>)<sub>0.8</sub>Sr<sub>0.2</sub>Ga<sub>0.8</sub>Mg<sub>0.2</sub>O<sub>3-δ</sub>, with Ln = Y, Nd, Sm, Gd, Yb and the study revealed that the conductivity decreases as Nd > Sm > Gd > Yb > Y. This variation in the conductivity is due to the departure from the cubic symmetry (Ishihara *et al.* 1995). NdGa<sub>0.9</sub>Mg<sub>0.1</sub>O<sub>2.95</sub> (Petri and Huang 1996) and Gd<sub>0.85</sub>Ca<sub>0.15</sub>AlO<sub>2.925</sub> (Sinha *et al.* 2008) are other perovskite structured oxides which can also be used as an oxide ion conductor. Perovskite-related oxides, K<sub>2</sub>NiF<sub>4</sub> (A<sub>2</sub>BO<sub>4+δ</sub>) structure such as Ln<sub>2</sub>NiO<sub>4+δ</sub> (where Ln = La, Nd, Pr) are also studied. The conduction mechanism in this type of oxides is by an interstitial transport mechanism (Chroneos *et al.* 2010).

Perovskite structured oxides exhibit a wide variety of compositions and high solid solution solubility, and thus these are subjected to continued investigation in this aspect.

#### 1.9.2.4 Brownmillerite Oxides

Brownmillerite is closely related to the oxygen-deficient perovskite structure with general formula  $A_2BB'O_5$ . The difference between the two structures is on the oxygen vacancy distribution. The brownmillerite composition exhibit the phase transformation with temperature in which disorder in the lattice increases and it is difficult to distinguish between a disordered brownmillerite structure and an oxygen-deficient perovskite structure. The structure contains 16.66% intrinsic vacancies that are ideally ordered along the 110 direction; some other ordering can also occur. For example, considering the perovskite octahedra linking model, a row of equatorial oxygen is missing every two rows in alternate (001)  $BO_6$  layers, resulting in a new series of alternating  $BO_6$  perovskite octahedra and  $BO_4$  tetrahedral (Boivin and Mairesse 1998).

$Ba_2In_2O_5$  is the first reported brownmillerite structured oxide ion conductor. The composition exhibits an order-disorder transformation at a temperature of about 800°C, and the conductivity increases drastically from  $10^{-3}$  S/cm to  $10^{-1}$  S/cm. In order to stabilise the high temperature highly conductive phase, aliovalent doping strategy is used. The cerium substituted composition  $Ba_2In_{1.75}Ce_{0.25}O_5$  exhibits a break in conductivity at a temperature of 850°C (Shabana and Misak 1990). The decreased ionic conductivity is due to the decrease of the available oxide ion vacancies, and increased activation energy is due to the trapping of the oxide ion vacancies.  $Ba_2(GdIn_{1-x}Ga_x)O_5$  is one of the solid solutions which shows the best ionic conductivity properties. However, the stability of  $Ba_2In_2O_5$  is poor and the compositions degrade in the  $CO_2$  atmosphere and cause the production of  $BaCO_3$  and loss of  $In_2O_3$ . Similar to ceria based electrolyte the doped  $Ba_2In_2O_5$  can be used in the solid oxide fuel cell in the moderate temperatures.

#### 1.9.2.5 Apatite Structured Oxides

In the mid-1990s, the silicate-based apatites  $Ln_{9.33}(SiO_4)_6O_2$  (where Ln is typically larger lanthanide ion such as  $La^{3+}$  or  $Nd^{3+}$ ) were found to be most fascinating oxide ion conductor (Nakayama, Aono, and Sadaoka 1995). The general formula for the apatite oxides is  $M_{10}(XO_4)_6O_{2-y}$ , where M is a rare-earth or alkaline-earth cation, X is a p-block element such as P, Si or Ge, and y is the amount of oxygen non-stoichiometry. Si and Ge based lanthanum apatites are good oxide ion conductors. They exhibit hexagonal symmetry (space group P63/m), with a lattice parameter 9.7–9.9 Å and c parameter around 7 Å, which varies with the dopant (Nakayama, Kageyama, and Sadaokac 1995). In the structure, La occupies

the cavity formed by the  $\text{SiO}_4$  or  $\text{GeO}_4$  tetrahedra with four distinct oxygen sites and on additional oxygen site which forms a channel through the structure.

In contrast, with fluorite structured or perovskite ones the ionic conductivity in these oxides is due to the interstitial oxide ion transport mechanism.  $\text{La}_{9.33+x}(\text{SiO}_4)_6\text{O}_{2+3x/2}$  system shows an increased conductivity as the interstitial oxide ions that are free to conduct through the system increases (Sansom *et al.* 2001). On comparing the Si and Ge based apatites the amount of interstitial oxides that can be contained in the Si-based ones is lower than that in the Ge based apatites (Kendrick *et al.* 2007). However, the Ge based apatites have some practical problems such as high volatilisation, the tendency to glass formation and high costs of  $\text{GeO}_2$  (Kharton *et al.* 2004).

Since the apatites structured oxides are interstitial oxide ion conductors, the conduction path stimulates much debate. The path of oxide ion through the Ge-based apatites is much clear. The oxides ions move close to the  $\text{GeO}_4$  units leading to a five coordinated Ge (Kendrick *et al.* 2008; Kendrick *et al.* 2009). Both neutron diffraction studies and modelling studies support this fact. However, in the case of Si-based ones, the interstitial site is sensitive to the sample composition and synthesis conditions. Much study is needed to clarify this problem (Malavasi *et al.* 2010).

The apatite oxides lent themselves to a wide range of cation dopants on both the La site or on the Si/Ge site. However, there are still many avenues to explore in order to improve the conductive properties of these oxides.

### 1.9.2.6 LAMOX ( $\text{La}_2\text{Mo}_2\text{O}_9$ )

A new family of oxide ion conductors developed by Laccore and his team in 2000 based on a parent compound named LAMOX, whose composition is  $\text{La}_2\text{Mo}_2\text{O}_9$  (Laccore *et al.* 2000). The composition exhibits a phase transition from a non-conductive monoclinic ( $\alpha$ ) to a conductive cubic phase ( $\beta$ ) at about  $580^\circ\text{C}$  whose conductivity is  $5 \times 10^{-2}$  S/cm at  $800^\circ\text{C}$ .

The structure of the low-temperature phase is the most complex structure so far reported and consists of 312 distinct crystallographic sites (Evans *et al.* 2005). The neutron diffraction studies of high-temperature  $\beta$  phase reveal the structure contains three crystallographic distinct oxygen sites, and the two of them are partially occupied (Goutenoire *et al.* 2001; Laccore *et al.* 2000). The presence of strong modulation on the  $\beta$  phase indicated the oxygen sublattice in the cubic phase is highly disordered, which causes high oxygen

mobility. The pair distribution analysis of the neutron diffraction data reveals that as the transition from the monoclinic to the cubic phase occurs the distribution of oxygen lattice changed from the static to dynamic distribution (Malavasi *et al.* 2007). The conduction in these oxides occurs as the fully occupied O<sub>1</sub> jumps to the O<sub>2</sub> and then to O<sub>3</sub> and again to the O<sub>1</sub> site. Thus the pathway is in three dimensional (Wang and Fang 2002).

In order to facilitate the use of LAMOX as the solid oxide electrolyte in the practical SOFC, two more issues are to be solved: (i) the volume strain associated with the phase transformation and (ii) the chemical stability under reducing atmosphere. Alkaline (K, Rb) and alkaline earth (Ca, Sr, Ba) doping on the La site stabilises the LAMOX to the room temperature and the diffusion coefficients of the composition with Gd, Y or Nd dopant on the La site and W dopant on the Mo site are higher than that of YSZ and LSGM (Georges *et al.* 2003; Goutenoire *et al.* 1999; Ishihara *et al.* 1998; Wang *et al.* 2005; Wang and Fang 2002). The chemical stability of the LAMOX is very poor in the presence of hydrogen, and the substitution of Mo with W enhanced the chemical stability. La<sub>1.7</sub>Gd<sub>0.3</sub>Mo<sub>0.8</sub>W<sub>1.2</sub>O<sub>9</sub> is stable under reducing condition with no compromise in the conductivity (Malavasi *et al.* 2010).

Further investigations are needed to find the potential of these materials to be used as the solid oxide electrolyte in the practical applications.

### 1.9.2.7 Ruddlesden-Popper-Type Oxides

Navac *et al.* discovered a highly conductive intergrowth in which perovskite layer(s) alternate(s) with one or several different structure type layers with general formula A<sub>n+1</sub>B<sub>n</sub>O<sub>3n+1</sub> (Navas and Zur Loye 1996). In this oxide nABO<sub>3</sub> perovskite is sandwiched between to AO rock-salt structures. Sr<sub>3</sub>Ti<sub>2</sub>O<sub>7</sub> is an example of n=2. The conductivity studies on Sr<sub>3</sub>Ti<sub>2</sub>O<sub>7</sub> doped with Mg<sup>2+</sup> and Al<sup>3+</sup> were reported by Turillas *et al.* (Turillas *et al.* 1988). Navas *et al.* extended the study to the substitution at the B site as the formula Sr<sub>3</sub>(M<sub>2-x</sub>, M'<sub>x</sub>)O<sub>7-x/2</sub> with M' = Ti<sup>4+</sup>, Zr<sup>4+</sup> and M'' = Al<sup>3+</sup>, Ga<sup>3+</sup>, In<sup>3+</sup>. The best conductivity at 950°C is 1.6x10<sup>-3</sup> S/cm. The lack of precise structural information makes it challenging to decide on the ability of these types of materials as oxide electrolytes.



### 1.9.2.8 Aurivillius Type Oxides

A new family of oxide ion conductors based on  $\text{Bi}_2\text{O}_3$  with parent composition  $\text{Bi}_4\text{V}_2\text{O}_{11}$  which is having a layered material showing a complex polymorphism is also studied. The highly conductive polymorph is stable only at a temperature above  $560^\circ\text{C}$ , and it can be stabilised to room temperature by iso- or aliovalent substitution, and such compositions exhibit conductivities of the order of 0.1 to 1 S/cm at  $600^\circ\text{C}$ . This class of oxides are also known as BIMEVOX, where BI stands for bismuth ME for metal, V for vanadium and OX for oxygen. The structure consists of alternating  $\text{Bi}_2\text{O}_2^{2+}$  and perovskite-like  $\text{VO}_{3.5}^{2-}$  layers, with oxygen vacancies in the perovskite layers facilitating rapid ion migration. The dopant used to stabilise the high-temperature  $\gamma$  phase is Cu, Ni, Co and Mg. This dopant increases the ionic transport number close to 1.0. These oxides are mainly used as an electrochemical catalyst for selective reduction of NO due to its high ionic conductivity at relatively low temperature compared to YSZ. Chemical reactivity, reducibility and low mechanical strength of these oxides are yet to be explored to check the suitability of these oxides as the electrolyte in the SOFC (Malavasi *et al.* 2010).

### 1.9.3 The Relevance of the Present Work

The discussion on the SOFC reveals that the solid oxide electrolyte is the most crucial component of the fuel cell, which determines the operating temperature and overall efficiency of the fuel cell. Thus the name “heart of the SOFC” is most suitable to the electrolyte. In order to get better overall efficiency of the fuel cell, the development of new electrolyte with much-improved properties is essential. One of the possible and suitable candidates for this application is pyrochlore oxides. The structure of these compositions itself contains intrinsic anion vacancies which facilitate an easy pathway for the movement of oxide ions. Several aspects like structure, lattice parameter(s), lattice volume, nature of ions, lattice defects like vacancies and interstitials, bond strength, thermal expansion behaviour and structure transition are reported evidently to affect the properties of a solid electrolyte. Despite the extensive research on these aspects, there still some of the factors which ionic conductivity remains unlearned.

The present thesis focuses on factors that affect the ionic conductivity of the pyrochlore type compositions so that the design of new pyrochlore oxide ionic conductors becomes facile. In addition to these an attempt to stabilise the bismuth compositions were also done.



### 1.9.3.1 Pyrochlore Structured Oxides

Pyrochlore is a mineral group of formula  $(\text{Na}, \text{Ca})_2\text{Nb}_2\text{O}_6(\text{OH}, \text{F})$ . All the crystal systems isostructural with the pyrochlore mineral group is known as pyrochlore. The pyrochlore is closely related to another mineral group  $\text{CaF}_2$  called as fluorite.



**Fig. 1.6** Fluorite and pyrochlore crystals

Pyrochlore structured oxides of general formula  $\text{A}_2\text{B}_2\text{O}_7$  are identified as the potential candidates for Solid Oxide Fuel Cells (Liu *et al.* 2009; Wang *et al.* 2012). The fully ordered or ideal pyrochlore belonging to space group  $\text{Fd}\bar{3}\text{m}$  is described as the superstructure of the ideal defect fluorite structure belonging to  $\text{Fm}\bar{3}\text{m}$ , with twice the cell constant  $a \approx 10\text{\AA}$ . In the fluorite structure with general formula  $\text{AO}_2$  one species usually the cations have an fcc arrangement and the second species occupies all of the available tetrahedral interstices within the array. The arrangement of cations in the pyrochlore structure is such that the larger  $\text{A}^{3+}$  cation is eight coordinated and located at  $16d$  whereas the  $\text{B}^{4+}$  cation is in six coordination located at  $16c$  position. The ordering in pyrochlore results in two structurally different anions at  $48f$  site and  $8b$  site. The  $48f$  site has two  $\text{A}^{3+}$  and two  $\text{B}^{4+}$  cations as neighbours and anion at  $8b$  site have tetrahedral coordination of entirely of  $\text{A}^{3+}$ . Additionally, there is another anionic tetrahedral site  $8a$  co-ordinated to four  $\text{B}^{4+}$  ions, which is symmetrically vacant in ordered pyrochlore (Wuensch *et al.* 2000).

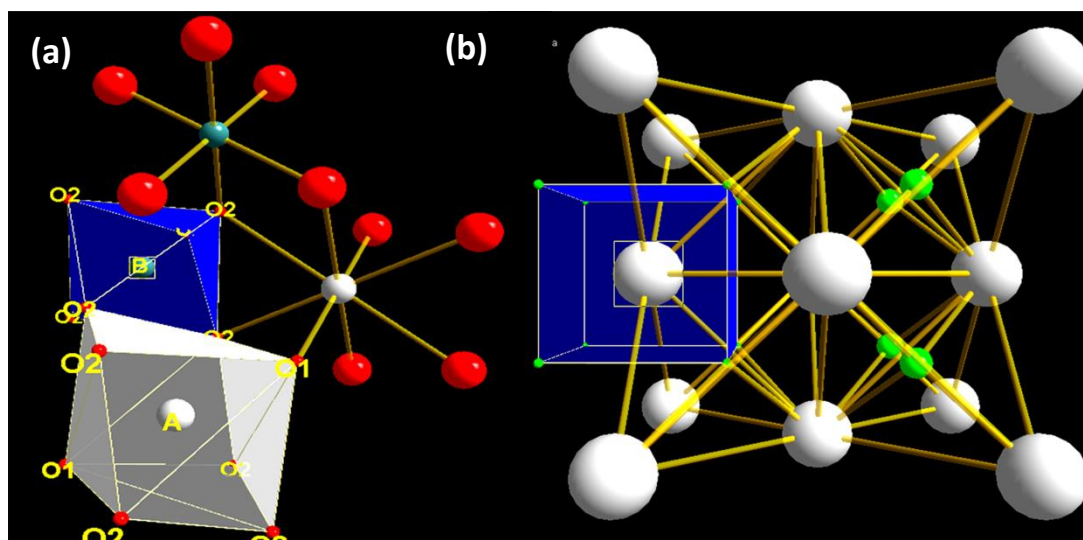


**Fig. 1.7** (a) Pyrochlore and (b) Fluorite crystal system

Pyrochlore Oxides have considerable importance in both the basic science and engineering and become a point of attraction for researchers, especially in materials science. This is because pyrochlore provide themselves to a wide variety of substitution at the A and B site provided the ionic radius ratio ( $r_A/r_B = 1.46$  to  $1.78$ ) and charge neutrality are satisfied (Radhakrishnan *et al.* 2012) and exhibit large variety of physical and chemical properties depending on the chemical composition and the existing order/disordering of the A and B site cations and oxygen vacancies. As a solid oxide electrolyte, the pyrochlore oxide structure itself contains intrinsic anionic vacancies and exhibit significant ionic conductivity at a lower temperature. An important problem in the case of the fuel cell is the compatibility of the electrolyte with the electrode material. Appropriate doping can induce hole, electronic and ionic conductivity in same pyrochlore material and the same material can be used as cathode, anode and electrolyte in the fuel cell. Another characteristic of these oxides is its structural transition from ordered pyrochlore to defect fluorite structure depending on the composition, temperature, and by applying pressure. In a pyrochlore lattice, ordered oxide ion vacancies provide a low energy pathway and low mobility of oxide ions because of its ordered structure (Kiruthika *et al.* 1998). As the lattice transforms to defect fluorite structure, the increased number of Frenkel defect gives a high energy continuous pathway for oxide ion motion and an increase in the number of mobile oxide ions. Therefore, it is noted that the conductivity varies drastically during this order-disorder transition (Sayed *et al.* 2012). The final atomic arrangement adopted by the pyrochlore oxides and the ionic conductivity depends not only on chemical composition but also on the method chosen to process the powder under study.

Oxygen ion conduction in pyrochlores, like in fluorites, proceeds via oxygen vacancy mechanism. An ordered pyrochlore structure has an intrinsic oxygen vacancy at the  $8a$  site, and the migration mechanism of oxide ions occurs via jumps from  $48f$  and  $8b$  into these vacant sites, leaving behind vacancies at their original sites (Tuller 1994). In the pyrochlore lattice, continuous pathways for oxygen ion migration are provided by jumps from a  $48f$  site to a vacant  $48f$  site along with both  $\langle 100 \rangle$  and  $\langle 110 \rangle$  directions. An alternate pathway is from  $48f$  site to vacant  $8b$  site followed by a jump from  $8b$  site to vacant  $48f$  site, but only along the  $\langle 110 \rangle$  direction (van Dijk *et al.* 1985; Wilde 1998). Previous computational studies have found that the  $48f$ - $48f$  mechanism is a more energetically favourable pathway than the  $48f$ - $8b$  mechanism. Experimental results also provide a clear indication that the  $48f$ - $48f$  mechanism is the dominant mechanism for oxide ion conduction in pyrochlore oxides. The B cation at  $16c$  in pyrochlore is surrounded only by  $48f$  O atoms. Hence the study shows that B site doping and B-O bonding has a prominent effect on the oxide ionic conductivity and activation energy (Radhakrishnan *et al.* 2012).

The ionic conductivity of pyrochlore oxides can be improved by increasing the charge carrier concentration and decreasing the activation energy. As has been demonstrated experimentally, the high ionic conductivity by increasing the concentration of free charge carriers can be achieved through extrinsic doping with lower valence cation impurities that cause a local charge imbalance and drives the formation of charge compensating positive oxygen vacancies. However, for aliovalent doped materials, an important parameter that can increase activation energies is the binding of an oxygen vacancy to an aliovalent dopant (Pirzada *et al.* 2003). The activation energy is influenced by the effect of cation disorder and anion disorder in the lattice. Computational studies suggest that a higher degree of cation disorder in a pyrochlore decreases the transport of oxygen ions even though cation disorder has associated with it a degree of anion disorder (Minervini *et al.* 2000). At the same time, anionic disorder decreases the activation energy. The aliovalent ion substitution induces anion disorder in the pyrochlore lattice, which leads to a slight lowering of the activation energy for oxygen migration. Hence decoupling of anion disorder from cation disorder through aliovalent doping may be a significant factor in making pyrochlore materials useful. Hence the study of aliovalent and co-doping on B site of the pyrochlore oxide becomes essential.

Many research works were done on the aliovalent substitution at the A site, and it proved that aliovalent substitution could enhance the ionic conductivity (Kramer 1995; Kramer *et al.* 1994). Tuller and co-workers have synthesised pyrochlores in which either the A or B site was doped with an aliovalent cation. Substitution of  $\text{Ca}^{2+}$  at the A site of gadolinium titanate,  $(\text{Ca}_z\text{Gd}_{(1-z)})_2\text{Ti}_2\text{O}_7$  increased the ionic conductivity by more than two orders of magnitude with an increase in  $z$  value. Similar increases in conductivity were seen upon doping the B site with  $\text{Al}^{3+}$ , but the solubility limit extended  $y= 0.01$  (Kramer *et al.* 1994). Kiruthika *et al.* studied the effect of aliovalent substitution on the oxide ionic conductivity of rare-earth pyrohafnates. With Sr substitution at the A site, the values of activation energy and the pre-exponential factor are lower compared to the parent phase. Aluminium substitution at the B site increases both the  $E_a$  and the pre-exponential factor. This difference may be due to a significant difference in the solubilities of the dopants. The ionic conductivity of doped pyrohafnates is lower than the pyrozirconates. The decrease in conductivity of the present system compared to pyrozirconates can be attributed to the difference in the bond lengths of the Zr-O and Hf-O bonds. The degree of covalency being higher for Hf-O bond leads to an increase in the bond strength, and hence, the oxide ion migration becomes less probable (Kiruthika *et al.* 1998).

Sayed *et al.* studied the  $\text{Sc}^{3+}$  substitution for  $\text{Zr}^{4+}$  in  $\text{NdGdZr}_2\text{O}_7$ . The  $\text{Sc}^{3+}$  substitution increases both the activation energy and pre-exponential factor. The increase in the activation energy results from the disordering arises due to the substitution of larger cation at the B site. On the other hand, the creation of additional oxygen vacancies in the crystal lattice to increase the conductivity. The overall oxide ionic conductivity increases and then decrease as the  $\text{Sc}^{3+}$  concentration increases. Therefore an optimum substitution at B site of a pyrochlore to a limited concentration can result in improvement in ionic conductivity (Sayed *et al.* 2012). The influence of pentavalent Nb substitution for Zr on the electrical property of oxide ion conductor  $\text{Gd}_2\text{Zr}_2\text{O}_7$  was studied by Xia *et al.*  $\text{Nb}^{5+}$  substitution decreases the charge carrier concentration and activation energy. With the substitution of pentavalent Nb cations for Zr cations in Fluorite type  $\text{Gd}_2\text{Zr}_2\text{O}_7$ , the number of oxide ion vacancies decreases in order to maintain the charge balance. In this study, the oxide ionic conductivity increases and then decreases with concentration (Xia *et al.* 2010).

Role of bond strength on the oxide ion conductivity and lattice thermal expansion in quaternary pyrochlore solid solutions were investigated by Radhakrishnan *et al.* The tantalum

is substituted in place of Nb at the B site of  $\text{CaGdZrNb}_{1-x}\text{Ta}_x\text{O}_7$  ( $x = 0, 0.2, 0.4, 0.6, 0.8, 1$ ). Lattice thermal expansion coefficients of the samples show that the thermal expansion coefficient decreases with the substitution of Ta. Oxide ion conductivity also shows the same trend with the substitution of Ta, and this is due to the high bond strength of the Ta–O bond compared to that of the Nb–O bond. This makes the diffusion of oxide ions difficult in two ways: because of the reduction of the pathway for oxygen migration and because of the high activation energy required for breaking of the metal-oxygen bond. The studies established the role of chemical bonding in deciding the conductivity of pyrochlore oxides and confirmed that the  $48f$ – $48f$  hopping mechanism and the B–O bond strength plays a vital role in determining the oxide ion conductivity of pyrochlore oxides. The above results would allow prediction of the oxide ion conductivity and lattice thermal expansion of the pyrochlore-type compounds depending on the nature of the element substituted at the B site. Doping of an element with high ionisation energy increases the bond strength, and consequently, both the oxide ion conductivity and thermal expansion coefficient decrease (Radhakrishnan *et al.* 2012).

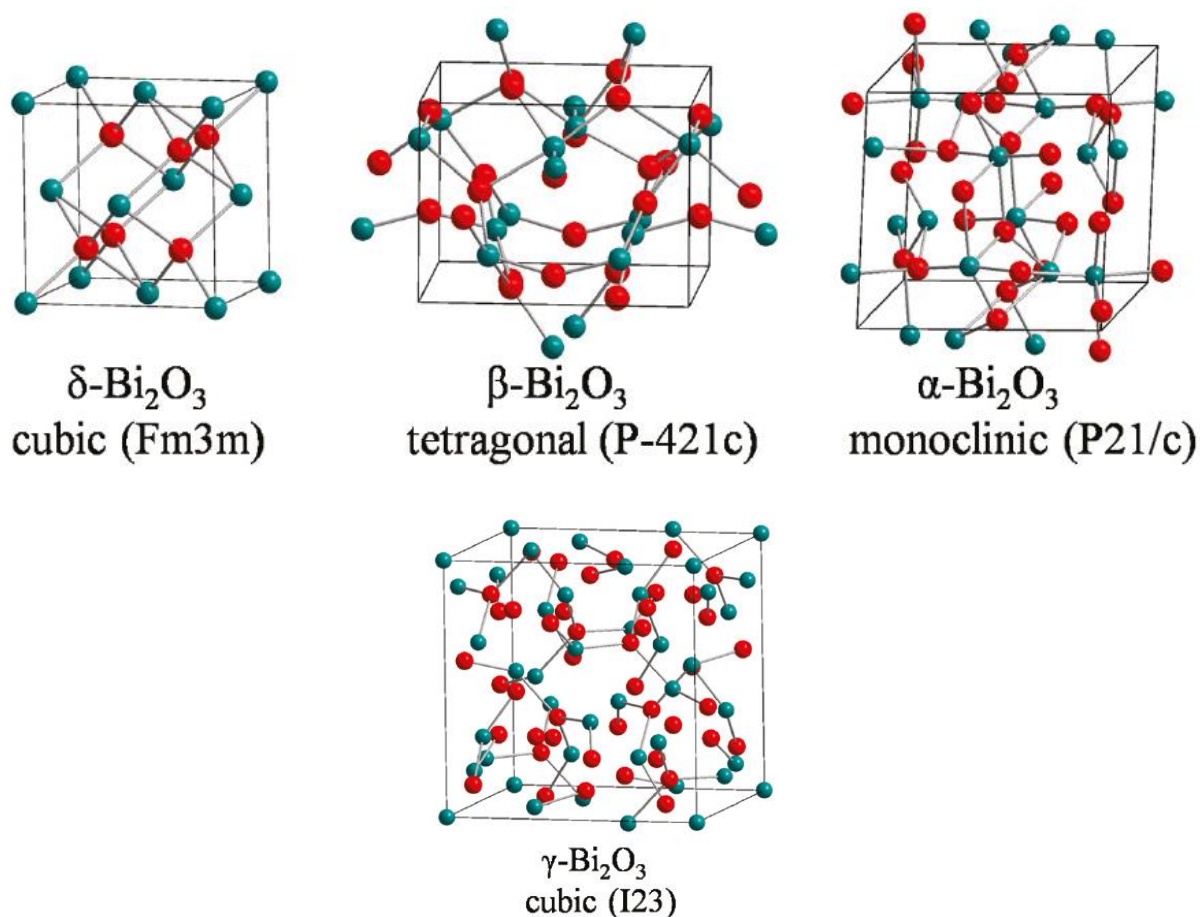
The influence of B-site substitution and B–O binding energy is studied by substitution of Ce cations in  $\text{Sm}_2\text{Zr}_2\text{O}_7$  by Vaisakhan Thampi *et al.* Addition of Ce ions into the lattice induced structural disorder to both cationic and anionic sublattices, gradually transforming the unit cell from an ordered pyrochlore to a defect fluorite structure. The ionic disorder led to a decreased energy barrier for the thermally activated conduction process, thereby increasing the overall conductivity of the materials. The maximum value of the total conductivity observed in this study is higher than the recently reported values in a similar  $\text{Sm}_2\text{Zr}_2\text{O}_7$  system. As the concentration of Ce in  $\text{Sm}_2\text{Zr}_2\text{O}_7$  increases the ion-ion interaction in the disordered lattice began to dominate, leading to increased activation energy and decreased total conductivity (Vaisakhan Thampi *et al.* 2014).

Influence of disorder-order transition on lattice thermal expansion and oxide ion conductivity in  $(\text{Ca}_x\text{Gd}_{1-x})_2(\text{Zr}_{1-x}\text{M}_x)_2\text{O}_7$  ( $\text{M} = \text{Nb}, \text{Ta}$ ) pyrochlore solid solutions were investigated by Radhakrishnan *et al.* The defect fluorite structure of  $\text{Gd}_2\text{Zr}_2\text{O}_7$  progressively changed to more ordered pyrochlore structure by simultaneous substitution at the A and B site. The lattice expansion coefficient in these pyrochlore oxides was found to decrease with decrease in the  $48f$  oxygen  $x$  parameter (decrease in disorder) in pyrochlore oxides. Hence lattice thermal expansion coefficient is a good indicator of disordering in pyrochlore type

oxides. The conductivity studies reveal that Nb-doped compositions show a considerable change in conductivity near the phase boundary of disordered pyrochlore and defect fluorite phases, whereas the Ta doped compositions show almost constant ionic conductivity with doping. This variation in the conductivity is because Ta–O bond strength is higher than that of the Nb–O bond, as evident from the lattice expansion coefficients, which is higher for Nb doped samples than Ta doped ones. Hence from the study of impedance spectroscopy, it is found that not only structural disorder but also the bond strength is a crucial parameter in deciding the conductivity of pyrochlore type solid solutions (Radhakrishnan *et al.* 2011).

The study on oxide ion conductivity on a non-stoichiometric compositions  $\text{Nd}_{2-x}\text{Zr}_{2+x}\text{O}_{7+x/2}$  ( $-0.2 \leq x \leq 0.4$ ) which are in the perfect pyrochlore lattice shows that they exhibit high conductivity of  $1.78 \times 10^{-2}$  S/cm which is attributed to the optimised hybrid structure consisting of fluorite-type disordered zones interspersed in the ordered pyrochlore structure obtained under suitable annealing conditions. Hence non-stoichiometry in a composition can also be utilised to tailor the ionic conductivity (Anithakumari *et al.* 2016). The study of simultaneous substitution of Scandium and Cerium to  $\text{Sm}_2\text{Zr}_2\text{O}_7$  suggests that in addition to the lattice disordering the co-operating behaviour of oxides ion and the individual bond strength plays a vital role in determining the ionic conductivity of the pyrochlore oxides (Vaisakhan Thampi *et al.* 2017). The same authors also revealed that cooperative behaviour is disadvantageous for long-range conduction and smaller lattice volume enhances the effect (Vaisakhan Thampi *et al.* 2015). Srinivasan *et al.* studied the effect of substitution of  $\text{Ti}^{4+}$  and  $\text{Ru}^{4+}$  cation on the  $\text{Gd}_2\text{Sn}_2\text{O}_7$ , and the ionic conductivity is good compared to the undoped  $\text{Gd}_2\text{Sn}_2\text{O}_7$ . Highly polarisable Ti–O and Ru–O bonds are the causes of the enhanced ionic conductivity (Srinivasan and Kiruthika 2019).



1.9.3.2 Bi<sub>2</sub>O<sub>3</sub> Based Oxide ion Conductors

**Fig. 1.8** Different polymorphs of Bi<sub>2</sub>O<sub>3</sub>

Bi<sub>2</sub>O<sub>3</sub> based oxide ion conductors are an essential class of material in the fluorite structured electrolytes whose ionic conductivity is 1-2 orders higher than the YSZ at relatively low temperature. The Bi<sub>2</sub>O<sub>3</sub> compositions exhibit in four polymorphs:  $\alpha$ -Bi<sub>2</sub>O<sub>3</sub> (monoclinic),  $\beta$ -Bi<sub>2</sub>O<sub>3</sub> (tetragonal),  $\gamma$ -Bi<sub>2</sub>O<sub>3</sub> (cubic, bcc),  $\delta$ -Bi<sub>2</sub>O<sub>3</sub> (cubic, fcc)  $\epsilon$ -Bi<sub>2</sub>O<sub>3</sub> (orthorhombic),  $\omega$ -Bi<sub>2</sub>O<sub>3</sub> (triclinic) and with two non-stoichiometric phases (Bi<sub>2</sub>O<sub>2.33</sub> and Bi<sub>2</sub>O<sub>2.75</sub>). On heating the monoclinic  $\alpha$ -Bi<sub>2</sub>O<sub>3</sub> transforms to the  $\delta$ -phase which is stable only at a high temperature above 730°C and it is stable up to the melting point of Bi<sub>2</sub>O<sub>3</sub> at 825°C. On cooling the high-temperature  $\delta$  phase to room temperature, the  $\gamma$  and  $\beta$  phase forms. Slow cooling results in the formation of  $\beta$ -Bi<sub>2</sub>O<sub>3</sub> at ~ 650°C and at ~ 640°C the  $\gamma$ -Bi<sub>2</sub>O<sub>3</sub>. Below 500°C, these metastable phase transforms to stable  $\alpha$ -Bi<sub>2</sub>O<sub>3</sub> (Medernach and Snyder 1978). Among these, the fluorite structured  $\delta$ -Bi<sub>2</sub>O<sub>3</sub> exhibit high ionic conductivity. The factors that account for high oxide ion conductivity in Bi<sub>2</sub>O<sub>3</sub> oxides which is listed below:

- ✓ 1/4 of the oxygen sites are vacant in the fluorite-type lattice.

- ✓ The electronic structure of  $\text{Bi}^{3+}$  is characterised by the presence of  $6s^2$  lone pair electrons, leading to high polarisability of the cation network, which in turn leads to oxide ion mobility;
- ✓ The ability of the  $\text{Bi}^{3+}$  to accommodate highly disordered surroundings (Mairesse 1993).
- ✓ Weaker Bi-O bonds promote greater mobility of the oxygen vacancies in the lattice (Mairesse 1993).

Although these oxides have some disadvantages too. The high thermal expansion coefficient (TECs), thermodynamic instability and low mechanical strength are some of them. In addition to all these, the high conductive  $\delta\text{-Bi}_2\text{O}_3$  is stable only on a narrow range of temperature (730-825°C). Several studies were done on the  $\text{Bi}_2\text{O}_3$  in order to stabilise the high temperature high conductive  $\delta\text{-Bi}_2\text{O}_3$  to room temperature. Addition of the several dopants stabilised the  $\delta\text{-Bi}_2\text{O}_3$  to the room temperature, and some of them result in the formation of the rhombohedral structure also.

Mainly used dopants are rare earth elements. The substitution of the rare earth to the bismuth oxides results in the  $\delta\text{-Bi}_2\text{O}_3$  and rhombohedral structured composition. Rare earth elements with higher ion radius up to gadolinium results in the rhombohedral structure and remaining ones form in the fluorite structured ones. Among the rare earth doped  $\text{Bi}_2\text{O}_3$  the Er-doped composition  $(\text{Bi}_2\text{O}_3)_{0.8}(\text{M}_2\text{O}_3)_{0.2}$  exhibit maximum conductivity of 0.4 S/cm at 973K and the high ionic conductivity is explained using the low dopant concentration that is required for the stabilisation of the  $\delta$ -phase of  $\text{Bi}_2\text{O}_3$  (Sammes *et al.* 1999; Verkerk *et al.* 1980). The study of Meng *et al.* showed that instead of using a single rare earth element, using a couple of rare elements, it is possible to stabilise  $\delta$ -phase down to room temperature with lower dopant concentration. This is due to the increased entropy of the resulting ternary system. Study of such systems shows that a smaller concentration of the second dopant stabilises the fcc structure and causes an increased ionic conductivity. At the same time, an increase in the concentration of the second dopant causes a decrease in the ionic conductivity (Meng *et al.* 1988).

The structural stabilisation of  $\text{Bi}_2\text{O}_3$  substituted with alkaline earth oxides,  $\text{Bi}_2\text{O}_3\text{-MO}$  (M=Ca, Sr, Ba) was studied by Levin *et al.* (Levin and Roth 1964), Roth *et al.*, Takahashi *et al.* (Takahashi *et al.* 1972) and Conflant *et al.* (Conflant *et al.* 1976). The conductivity studies on the Ca-stabilised  $\text{Bi}_2\text{O}_3$  show that the rhombohedral structured composition exhibit higher



oxide ion conductivity. Strontium shows a wide range of solid solution solubility with  $\text{Bi}_2\text{O}_3$  (Sillén and Aurivillius 2014). The conductivity of the Sr doped rhombohedral phase is higher than that of the Ca-stabilised  $\text{Bi}_2\text{O}_3$ , and this is due to the large cation size of the  $\text{Sr}^{2+}$  than  $\text{Ca}^{2+}$ . This variation in conductivity with ionic radius led to the assumption that the Ba doping may lead to higher oxide ion conductivity and among these Ba doped composition shows maximum conductivity. The study reveals that the alkaline earth stabilised  $\text{Bi}_2\text{O}_3$  has superior conductivity properties compared to pure  $\text{Bi}_2\text{O}_3$  and Sr stabilised rhombohedral phase is much more stable (Fung *et al.* 1992) than others.

Pentavalent cation stabilised  $\text{Bi}_2\text{O}_3$  ( $\text{Bi}_2\text{O}_3\text{-M}_2\text{O}_5$ ,  $\text{M} = \text{V, Nb, Ta}$ ) also studied. The amount of dopant needed to stabilise the  $\delta$ -phase is 12.5 mol% for  $\text{V}_2\text{O}_5$ , 15 mol% for  $\text{Nb}_2\text{O}_5$  18 mol% for  $\text{Ta}_2\text{O}_5$ . It is to note that the threshold amount needed to stabilise the delta phase is a function of the atomic number of the pentavalent cation. Takahashi *et al.* reported that the maximum conductivity is obtained for the compositions  $(\text{Bi}_2\text{O}_3)_{0.85}(\text{Nb}_2\text{O}_5)_{0.15}$  (Takahashi *et al.* 1978; Takahashi *et al.* 1977). Hexavalent doped  $\text{Bi}_2\text{O}_3$  were also studied in this aspect (Hoda and Chang 1974; Takahashi and Iwahara 1973).

We mentioned earlier that the co-doping could enhance the stability and conductivity properties of the  $\text{Bi}_2\text{O}_3$ .  $\text{Er}_2\text{O}_3\text{-PbO}$  co-doped  $\text{Bi}_2\text{O}_3$  oxides were studied in detail, and the conductivity increases with increasing  $\text{Pb}^{2+}/\text{Er}^{3+}$  ratio and decreasing  $(\text{Er}^{3+} + \text{Pb}^{2+})/\text{Bi}^{3+}$  ratio. The neutron diffraction data shows that the oxygen sublattice in the fcc structure is completely disordered (Webster *et al.* 2007). The total doping concentration required to stabilise the  $\delta$ -phase in  $\text{Bi}_2\text{O}_3$  doped with  $\text{Er}_2\text{O}_3$  and  $\text{Nb}_2\text{O}_5$  reduces from 20 mol% to 10 mol% (Chou *et al.* 2011). The study on the system  $\text{Bi}_{0.76}\text{Y}_{0.24-x}\text{M}_x\text{O}_{1.5+\delta}$  ( $\text{M} = \text{Gd}_2\text{O}_3, \text{Nb}_2\text{O}_5, \text{Sc}_2\text{O}_3, \text{ZrO}_2, \text{and BaO}$ ) shows that the co-dopant stabilised  $\text{Bi}_2\text{O}_3$  ceramics outperforms their single-dopant stabilised counterparts in terms of conductivity (Wang *et al.* 2012). Thus co-doping improves the structural stabilisation and conductivity properties of the  $\text{Bi}_2\text{O}_3$  based oxides and suitability of these oxides to use in the IT-SOFC is high.

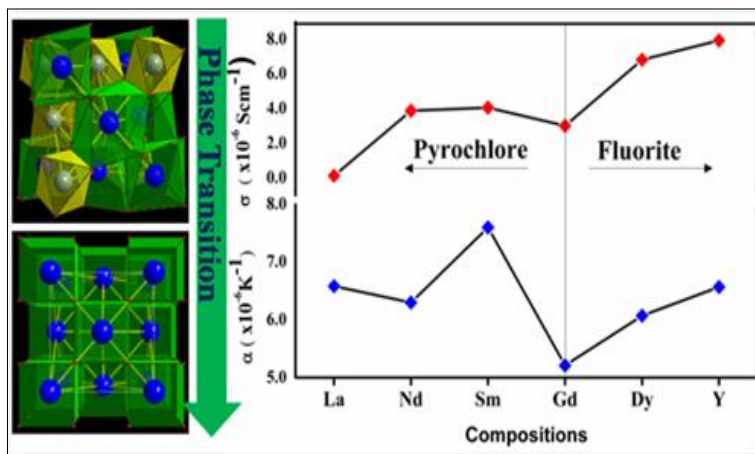
### 1.10 Preface to the current thesis

The intense research on the oxide ion conductivity of the pyrochlore structured composition shows that there is still plenty of information to be understood on the factors that affect the oxide ion conductivity of these oxides that are not unveiled. The present thesis is an attempt to study some of the factors that affect the conducting properties of the rare earth mixed oxides. The focus is on the pyrochlore structured rare earth mixed oxides. On the second chapter of the thesis, the analysis of crystal chemistry of the pyrochlore structure composition is done, and its effect on the thermal expansion coefficient and ionic conductivity is also done in detail. The third chapter comprises the study with varied substitution concentration of Y and Nb on the Zr site of the  $\text{Sm}_2\text{Zr}_2\text{O}_7$  keeping the oxygen stoichiometry same and its effect on the conductivity and structural parameter. Then  $\text{RE}_3\text{Zr}_{0.5}\text{Nb}_{0.5}\text{O}_{6.75}$ , in which additional oxygen vacancies are introduced, is also studied in detail. Then study on the oxide ion conductivity of the displaced pyrochlore is also done. In the last part of the work, the study of oxide ion conductivity of the bismuth-based oxide ion conductors is also done.

# Chapter 2

## Influence of Phase transition from Order to Disorder and Philip's Ionicity on Thermal Expansion Coefficient of Pyrochlore Type Compositions with Multivalent Environment

The present study involves a detailed investigation on interrelationships among Philip's ionicity, thermal expansion coefficient and ionic conductivity. The system undergoes a structural transition from an ordered pyrochlore structure to a disordered defect fluorite structure in the series with a phase boundary



at Gd substitution. Ionicity calculation for the pyrochlore type composition is done. The study demonstrates that individual bond ionicity and ionicity difference plays a significant role in determining the thermal expansion and ionic conductivity of pyrochlore based materials with structural dependence.

*New J. Chem., 2017, 41, 245-255*



## 2.1 Introduction

Pyrochlore oxides find innumerable applications in materials science, from highly insulating materials to metallic materials, dielectric, piezo/ferroelectric and magnetic materials, and fluorescence and phosphorescence host materials, (Subramanian *et al.* 1983) ionic conductor, gas sensors and nuclear waste immobilization (Minervini *et al.* 2000) due to its high chemical stability, high catalytic activity, high melting temperature, and excellent oxide ion conductivity. The pyrochlore structure is consisting of octahedra of highly charged cations with an ionic radius of 0.6 to 0.7 Å (B at 16c) coordinated by oxygen ions (48f). These octahedra share corners to form  $(B_2O_6)_\infty$ . The larger A cations (16d) of ionic radius 0.9 to 1.2 Å occupies the holes formed by the octahedral network of B cations. The remaining one extra anion at (8b) is placed in the structure one to every  $B_2O_6$  octahedra (Aleshin and Roy 1962). Pyrochlore is also considered as a superstructure of a simple cubic fluorite structure, (Wuensch and Eberman 2000) with a general formula  $A_2B_2O_6O'$ , belonging to a space group Fd3m ( $a \approx 10\text{Å}$  (twice that of the Fluorite),  $Z = 8$ ) (Subramanian *et al.* 1983). Mostly, A is a trivalent rare earth oxide, but can be mono- or divalent cations and B is 3d, 4d or 5d transition metal ion with appropriate valence to maintain the stoichiometry of the composition  $^{VIII}A_2^{VI}B_2^{IV}O_6^{IV}O'$  (Radhakrishnan *et al.* 2012) (The Roman letters in superscript shows the coordination number of each species). The pyrochlore oxide lends themselves to a wide variety of substitutions at the A, B and O sites, and it can tolerate vacancies at the A and O sites (Radhakrishnan *et al.* 2012). Another significant factor which makes the pyrochlore a prime candidate in the field of material science is its inclination to show disordering effects, i.e. to randomising the distribution of two cations (16d and 16c to 4a) and corresponding redistribution of two anion lattice sites (48f and 8b to 8c), to transform to more disordered fluorite structure (Ubic *et al.* 2008).

The additional ordering in pyrochlore oxides (compared to the fluorite structure) arises due to the ionic radius mismatch between the A and B cations (Wuensch and Eberman 2000). The stability of the pyrochlore oxides is defined using the tolerance factor defined by

$$\text{tolerance factor} = \frac{\text{radius of A cation}}{\text{radius of B cation}} \quad (2.1)$$

and using the  $x$ - parameter ( $x$ -coordinate of 48f oxide ions). The radius ratio of lanthanide pyrochlore oxides is within ( $1.4 < R_A/R_B < 1.9$ ) (Sayed *et al.* 2012). The  $x$ -value ranges between ( $0.309 \leq x \leq 0.355$ ) for pyrochlore while in fluorite, it is equal to 0.375 (Ubic

*et al.* 2008). Also, the  $x$ -parameter determines the polyhedral shape associated with A and B cations. For  $x = 0.3125$ , the B ions have perfect octahedral coordination of 48f oxide ions, and A cations are eight coordinated in the form of the distorted hexagon of six oxygen (48f) and whose plane is perpendicular to the O'-A-O' axis. When  $x = 0.375$ , the A cation will be at the centre of regular cubic eight coordination and B cations at the centre of highly distorted octahedron (Subramanian *et al.* 1983). The disorder in pyrochlore compounds seeks much attention since it governs the structural properties, which in turn affect the electrical and other properties. The order-disorder transition is not merely carried out by a change in the compositions but can also occur by increasing the temperature, by applying pressure and by high energy ion irradiation (Sayed *et al.* 2012). The unique property of pyrochlore oxides is the disordering of anion, and cation sublattice occurs simultaneously and independently (Radhakrishnan *et al.* 2011).

Among various pyrochlore type oxides, lanthanide zirconates,  $\text{Ln}_2\text{Zr}_2\text{O}_7$  are extensively studied due to its complex crystal chemistry, low thermal conductivity, high thermal expansion coefficient, and high chemical stability and find applications in the field of ionic conductors, superconductivity, catalyst, luminescence, dielectric, gas sensors, ferromagnetism, thermal barrier coating, and immobilization hosts of actinides in nuclear waste (Feng *et al.* 2012). The lanthanide zirconates garb in pyrochlore structure when the ions lighter than the  $\text{Gd}^{3+}$  occupies the A site and the heavier ones in fluorite structure (Subramanian *et al.* 1983). Due to its immense applications and a wide range of compositions, a considerable number of investigations have been taking place to optimise the property, which is suitable for the applications. Similar to other pyrochlore oxides, lanthanide zirconates also exhibit phase transition from pyrochlore to fluorite structure with increase in temperature, and the transition temperature is found to reduce as  $\text{Ln}^{3+}$  ionic radius decreases (Michelet *et al.* 1974). The studies on the oxide ion conducting property of the lanthanide zirconates show that the conductivity is maximum in the vicinity of the pyrochlore to fluorite transition (Shlyakhtina *et al.* 2005). The dielectric studies of Solomon *et al.* showed that  $\text{Ln}_2\text{Zr}_2\text{O}_7$  (Ln = Ce, Pr, Nd, Sm, Gd, Dy, Er and Yb) prepared via auto-ignition methods exhibit an increasing impedance as the radius ratio decreases from 1.588 to 1.463 and then decreases on further decreasing the ionic radius ratio. The study indicates that at the phase boundary from pyrochlore to defect fluorite, there is a distortion in the structural symmetry (Solomon *et al.* 2015). The molecular dynamics calculation of lanthanide zirconates for thermal expansion coefficient shows that the thermal expansion coefficient increases as the

lanthanide ion radius decreases (Schelling *et al.* 2004). The experimental support for this fact is given by Kutty *et al.* and reported that the thermal expansion coefficient of the  $\text{Ln}_2\text{Zr}_2\text{O}_7$  lies in the range of  $8\text{-}11 \times 10^{-6} \text{ K}^{-1}$  (Kutty *et al.* 1994). The studies show that lighter lanthanide zirconates are suitable for thermal barrier coating applications (Bolech *et al.* 1997), and heavier zirconates are for oxide ion conducting applications (Shlyakhtina *et al.* 2005). The phase transformation from pyrochlore to fluorite structure introduces disorder and new paths for oxide ion movement and thus increasing ionic conductivity and thermal conductivity.

In this work, the correlation of structural properties and thermo-physical properties of lanthanide zirconates with multivalent (trivalent and pentavalent) ions on the zirconium site will be investigated based on the crystal chemistry of the pyrochlore oxides. The study of Wuensch *et al.* (Wuensch *et al.* 2000) on the oxide ion conductivity and structural changes of pyrochlore with the composition and temperature shows that the disorder cannot be induced merely by reducing the ionic radius ratio of the A and B cations. However, bonding characteristic also plays a significant role in determining the structural stability, which in turn influences the thermal expansion coefficient and oxide ion conductivity. In pyrochlore oxides, the selection of B-site cations needs more important than that of A site due to smaller size and higher ionic charge of the B cation which results in much stronger B-O bond than A-O bond. Hence the B-O bond energetics dramatically affects the properties of the pyrochlore lattice (Schelling *et al.* 2004). The studies of Radhakrishnan *et al.* also showed that the B-O bond energy plays a significant role in determining the ionic conductivity of the pyrochlore system (Radhakrishnan *et al.* 2012). However, the effect of multivalent ion in the B-site of pyrochlore oxides is yet to be explored. Here in this work the structural aspects of simultaneous substitution of the  $\text{Y}^{3+}$  and  $\text{Nb}^{5+}$  ions in the  $\text{Zr}^{4+}$  site are studied. Irvine *et al.* assumed the  $\text{Nb}^{5+}$  ions are oppositely charged when comparing with  $\text{Y}^{3+}$  since it has higher charge and smaller ionic radius. Thus simultaneous substitution of the  $\text{Y}^{3+}$  and  $\text{Nb}^{5+}$  to the  $\text{Zr}^{4+}$  site might reduce both the vacancy association and strain induced in the lattice and hence an increase in the oxide ion conductivity can be expected (Norberg *et al.* 2009). The paper is focussed on the explanation for the thermal expansion coefficient, oxide ion conductivity and structural stability based on chemical bond point of view for the pyrochlore system. The pyrochlore system is yet to be explored in this aspect. The fractional ionicity of individual bonds ( $f_i^{\mu}$ ) is calculated theoretically for A-O and B-O bonds. In the case of perovskite systems, the oxygen ionic conductivity and thermal expansion coefficient decrease with the difference in ionicity  $\Delta f_i$  between A-O and B-O bond (Taniguchi and Aniya 2010). In this

paper influence of the simultaneous substitution of the trivalent and pentavalent ion on the B site ion on thermal expansion coefficient and ionic conductivity will be discussed based on the chemical point of view.

### 2.2 Experimental

Compositions,  $\text{RE}_2\text{Y}_{2/3}\text{Zr}_{2/3}\text{Nb}_{2/3}\text{O}_7$  (RE = La, Nd, Sm, Gd, Dy, Y) were prepared by the conventional ceramic route using  $\text{La}_2\text{O}_3$  (Sigma Aldrich, 99.99%),  $\text{Nd}_2\text{O}_3$  (Alfa Aesar, 99.9%),  $\text{Sm}_2\text{O}_3$  (Alfa Aesar, 99.9%),  $\text{Gd}_2\text{O}_3$  (Alfa Aesar, 99.9%),  $\text{Dy}_2\text{O}_3$  (Sigma Aldrich, 99.9%),  $\text{Y}_2\text{O}_3$  (Aldrich, 99.99%),  $\text{ZrO}_2$  (99%), and  $\text{Nb}_2\text{O}_5$  (Aldrich) as starting materials. The precursor chemicals were dried in an air oven before taking the weights. The stoichiometric raw materials were mixed in an agate mortar in a wet medium using acetone. Then, the mixture was dried in an air oven at  $100^\circ\text{C}$  for 1h. This procedure of mixing and subsequent drying was repeated thrice to get a homogenous mixture. The powdered samples are then calcined at  $1500^\circ\text{C}$  for 12h. The calcined product was ground into a fine powder and pressed into cylindrical pellets of 10mm diameter and 2-3 mm height using a hydraulic press. Pellets were sintered at  $1600^\circ\text{C}$  for 6h.

Powder X-ray diffraction patterns were recorded to identify the crystalline phase of the sintered samples using a Ni filtered  $\text{CuK}\alpha$  radiation by a Philips X'pert Pro diffractometer operating at 45kV and 30mA. Scans recorded over a  $2\theta$  range of  $10-90^\circ$  with a step size of 0.02 and a scan time of 30 seconds using X'pert highscore software. The unit cell parameters were calculated by a least square method, and Rietveld analysis using high score plus software. The lattice thermal expansion studies were done using Philip's X'pert Pro unit equipped with Anton Paar HTK attachment and taking the XRD pattern of the sample for  $2\theta=10-90^\circ$  in the temperature range of 298-1273K at a regular interval of 200K in static air. The Raman spectra of the prepared samples were taken using the WITec alpha 300R confocal Raman microscope analysis. The Raman confocal microscope is equipped with 100x oil immersion objective and 300/600 grooves grating. 532nm laser source was used for the excitation, and CCD detector operating at room temperature was used as the detector. The number of accumulations and the integration time used were five and 1s, respectively. The high-resolution transmission electron microscopy and selected area electron diffraction (SAED) of the prepared samples were taken using a TECNAI 30G2 S-TWIN transmission electron microscope (FEI, The Netherlands). The samples for the TEM analysis were prepared by drop-casting of the samples on to the carbon-coated copper grids which are



dispersed in acetone medium by ultra-sonification. The copper grids are then dried. For impedance measurement, silver paste is applied on the flat faces of the pellets. The silver-coated pellets were cured in an oven at 473K for 6h. Also, the measurements were carried out from room temperature to 1023K in the frequency range from 1 Hz to 1MHz by applying the ac signal with an amplitude of 100mV using the computer-controlled impedance analyser (Solatron, SI 1260). The complex impedance plots were made with SMART software.

## 2.3 Results and Discussion

The compositions,  $\text{RE}_2\text{Y}_{2/3}\text{Zr}_{2/3}\text{Nb}_{2/3}\text{O}_7$  (RE = La, Nd, Sm, Gd, Dy, and Y) were prepared via the conventional solid-state reaction methods. In this system, it is expected that the rare earth elements RE = La, Nd, Sm, Gd, Dy, and Y occupied the A site of the pyrochlore structure and the B site is equally taken up by trivalent Yttrium, tetravalent Zirconium, and pentavalent Niobium ions based on their ionic size and co-ordination requirement. These compositions maintain the metal to oxygen ratio for a pyrochlore type structure with a variation of lanthanides on the A site leading to a phase transition in the system.

### 2.3.1 Structural analysis using X-ray diffraction methods

Powder X-ray diffraction patterns of the compositions,  $\text{RE}_2\text{Y}_{2/3}\text{Zr}_{2/3}\text{Nb}_{2/3}\text{O}_7$  are shown in Fig. 2.1. The XRD patterns are indexed with the pyrochlore structure for compositions having RE = La, Nd, Sm, and the remaining ones are indexed to the fluorite structure. Pyrochlore structure is a superstructure of fluorite type of lattice. The sharp reflections in the pyrochlore structure correspond to the fluorite array of atoms and the additional ordering in pyrochlore structure is shown by the weak reflections which are indexed as (111), (331) and (731). The intensity of the weak reflection in the XRD gives information about oxygen scattering length, distribution of oxygen vacancies, and the  $x$ -parameter of the  $48f$  oxygen (Heremans *et al.* 1995). Dickson *et al.* showed that the (111) reflection is more sensitive to the oxygen  $x$ -parameter (Dickson *et al.* 1989). From the Fig. 2.1(b) it can be seen that the intensity of superstructure peaks diminishes as the radius of the lanthanide ion in the A site decreases. This decreasing intensity of the superlattice peaks indicates a phase transition from a more ordered pyrochlore crystal structure to a more disordered fluorite structure. In Fig. 2.1(c) shift of the principal peak with the lanthanide ion is shown.

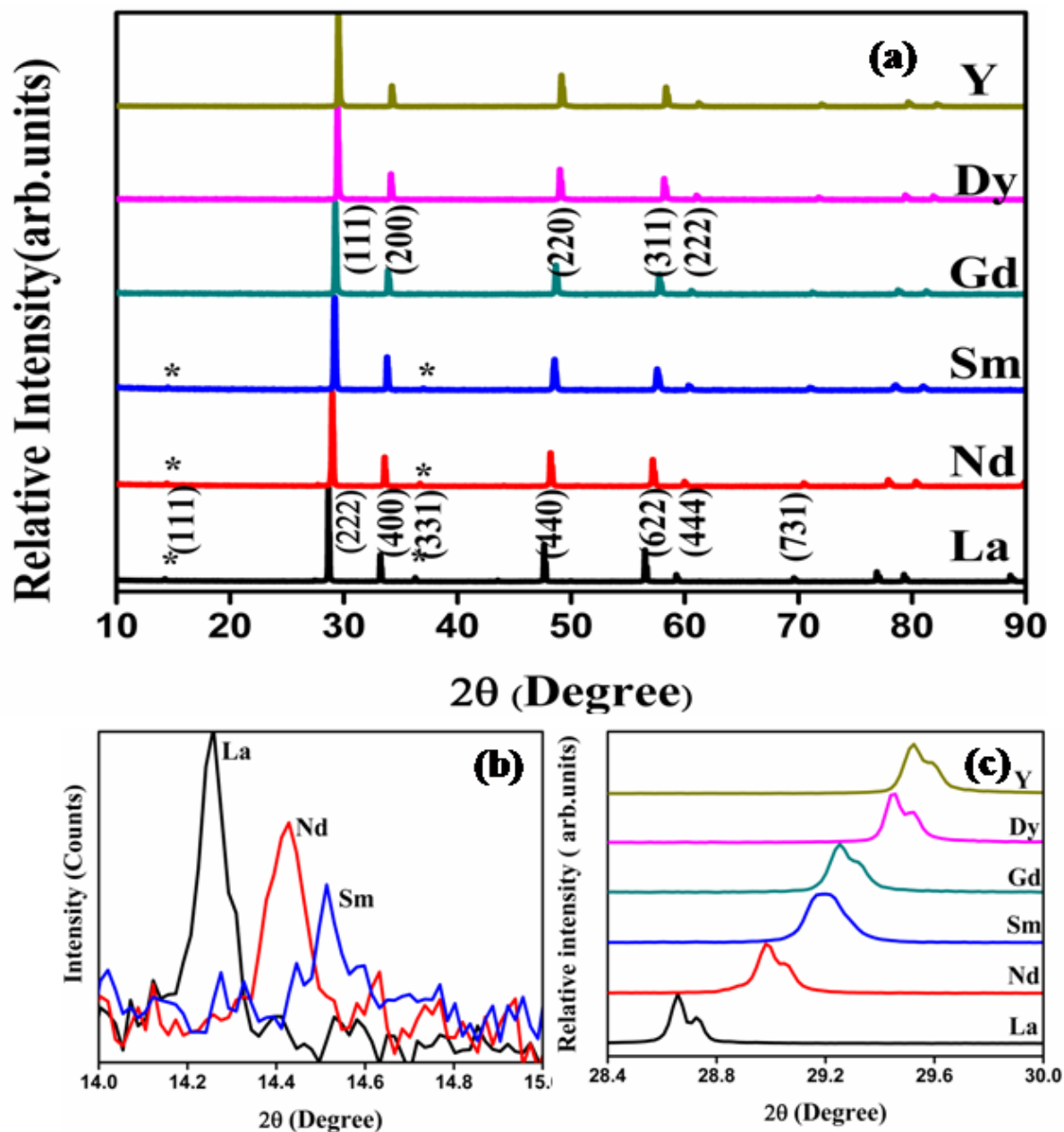


**Fig. 2.1** (a) Powder X-ray diffraction patterns of the series  $RE_2Y_{2/3}Zr_{2/3}Nb_{2/3}O_7$  (RE = La, Nd, Sm, Gd, Dy, Y). (b) Zoomed view of  $2\theta$  between 14 to 15° and (c) 28 to 30°

The order-disorder phase transition occurs with decreasing the tolerance factor defined using the radius ratio of the cations at the A site (eight coordinated) to that at the B site. The ordered pyrochlore structure is favoured within the range of tolerance factor of 1.46 to 1.78 (Whittle *et al.* 2009). Here for the current series of compounds, the radius ratio varies between 1.35 and 1.54. (The ionic radius of rare-earth ions and the used transition metals are obtained from Shannon's table (Shannon *et al.* 1976). Fig. 2.2 shows the variation of the lattice parameter against the radius ratio of A and B cations. The lattice parameters of the fluorite compositions are doubled to compare with the pyrochlore structure. The lattice

parameter varies linearly with the ionic radius ratio of the A and B cations in pyrochlore type compositions (Yamamura *et al.* 2003). An abrupt change in the lattice parameter occurs as the  $Gd^{3+}$  ion replaces the  $Sm^{3+}$  and this may be due to transition from the ordered pyrochlore structure to the more disordered defect fluorite structure.

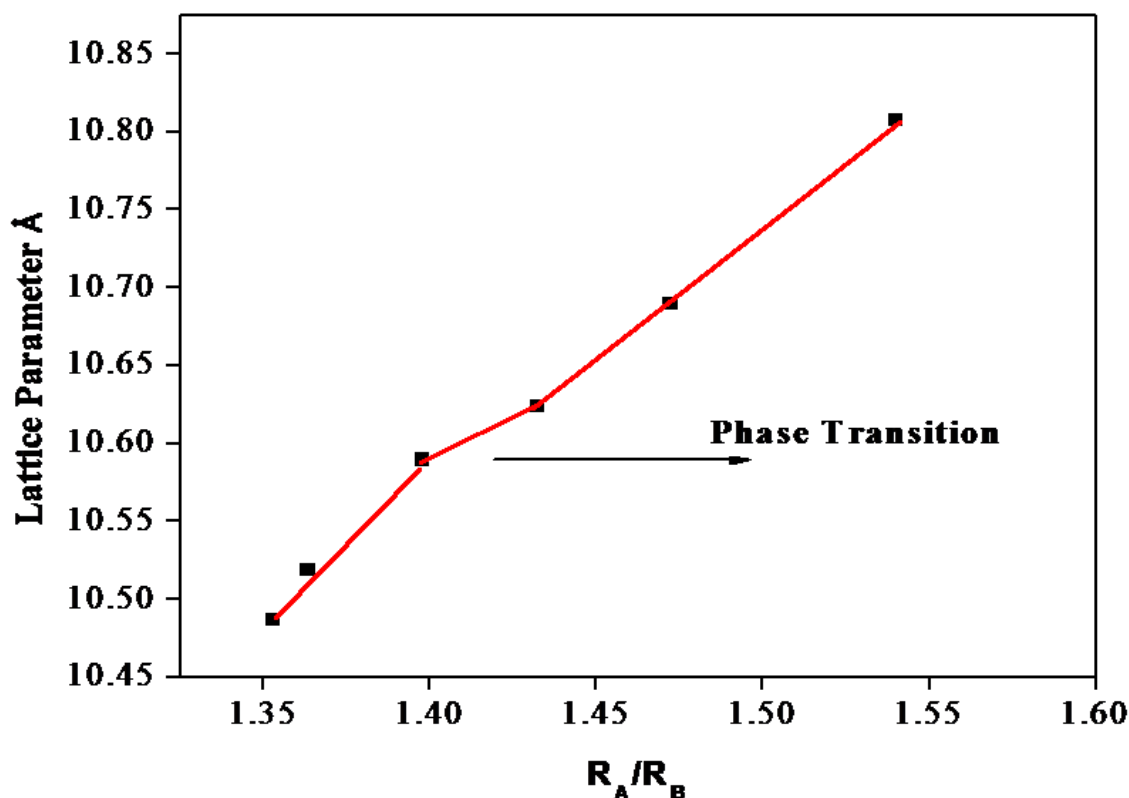


**Fig. 2.2** Variation of the lattice parameter of the compositions  $RE_2Y_{2/3}Zr_{2/3}Nb_{2/3}O_7$  with the radius ratio.

Structural analyses of the XRD patterns are carried out by Rietveld analysis using Fullprof software. The initial crystal structure is modelled with that of the pyrochlore (Space Group  $Fd\bar{3}m$ ), and the occupancies are assigned as in the stoichiometric ratio. The A cation ( $A = La, Nd, Sm$ ) is at  $16d$  ( $1/2, 1/2, 1/2$ ) sites and the B cations ( $B = Y, Zr, Nb$ ) are equally and simultaneously distributed at the  $16c$  ( $0, 0, 0$ ) and the anions are distributed at two distinct positions namely  $48f$  ( $x, 1/8, 1/8$ ) and  $8b$  ( $3/8, 3/8, 3/8$ ) and for the fluorite structure also the occupancies of the cations sites are assigned according to the stoichiometry. In the Rietveld process, the scale factor, flat background, specimen displacement and unit cell parameters are refined, and the peak profile is fitted using Pseudo-Voigt profile function. The Caglioti parameters are also refined. The refined XRD pattern of pyrochlore

$\text{La}_2\text{Y}_{2/3}\text{Zr}_{2/3}\text{Nb}_{2/3}\text{O}_7$  and fluorite  $\text{Y}_2\text{Y}_{2/3}\text{Zr}_{2/3}\text{Nb}_{2/3}\text{O}_7$  patterns are shown in Fig. 2.3 a&b, and the results of the refined parameters are shown in Table 2.1.

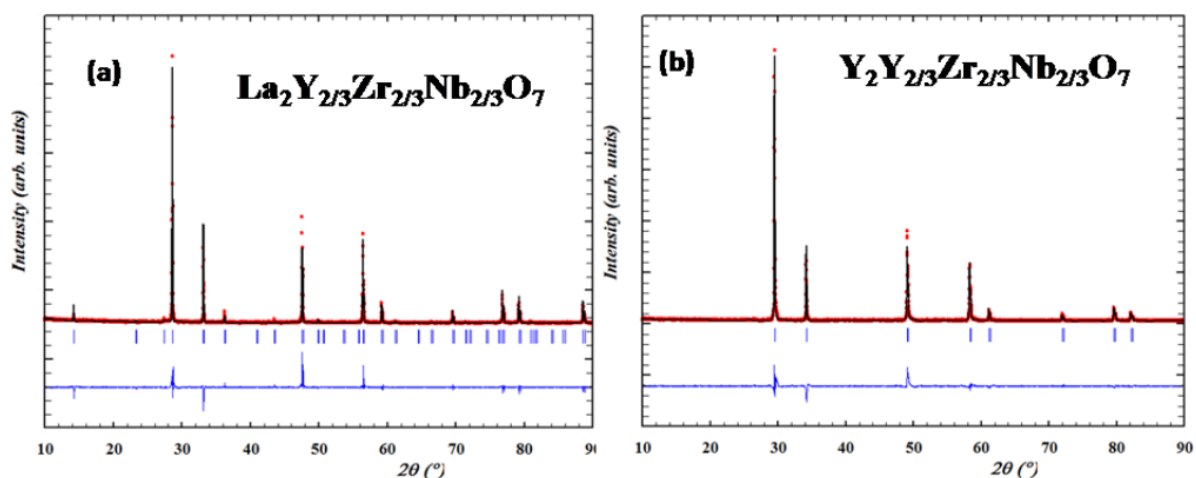


**Fig. 2.3** Observed, calculated and difference XRD profiles of (a) Pyrochlore structured  $\text{La}_2\text{Y}_{2/3}\text{Zr}_{2/3}\text{Nb}_{2/3}\text{O}_7$  and (b) Fluorite structured  $\text{Y}_2\text{Y}_{2/3}\text{Zr}_{2/3}\text{Nb}_{2/3}\text{O}_7$ .

**Table 2.1** Rietveld refined parameters of  $\text{RE}_2\text{Y}_{2/3}\text{Zr}_{2/3}\text{Nb}_{2/3}\text{O}_7$  (RE = La, Nd, Sm, Gd, Dy, Y)

Sample	La	Nd	Sm	Gd	Dy	Y	
Phase	Pyrochlore	Pyrochlore	Pyrochlore	Fluorite	Fluorite	Fluorite	
Unit cell	Cubic	Cubic	Cubic	Cubic	Cubic	Cubic	
Space group	Fd3m	Fd3m	Fd3m	Fm3m	Fm3m	Fm3m	
Total number of independent reflections	36	36	36	36	36	36	
Lattice constant, (Å)	10.80698	10.68908	10.62310	5.29740	5.25950	5.24329	
Fwhm parameters	U	0.00538	0.13101	0.16337	0.08600	0.04132	0.05322
	V	-0.00277	-0.09092	-0.10004	-0.04589	-0.01814	-0.01815
	W	0.00071	0.01924	0.01623	0.01260	0.00619	0.00690
Zero	0.0668	0.0694	0.0794	0.0612	0.0618	0.0409	
Oxygen x-parameters	0.31726	0.32217	0.33557				
R-factors (%)	$R_p$	11.0	9.75	8.82	5.47	5.63	8.19
	$R_{wp}$	15.2	13.0	11.9	7.02	7.19	11.1
	$R_{exp}$	10.2	10.1	9.04	7.31	6.83	5.24
$\chi^2$	2.23	1.602	1.73	0.922	1.11	2.16	
GOF	1.5	1.3	1.3	0.90	1.11	2.16	

### 2.3.2 Raman spectral analysis

The distribution of degrees of freedom around cation equipoint is zero, which shows that the Raman spectrum of pyrochlore type compounds arises due to the vibration of the anion sublattice. The A and B site occupies equipoints with the centre of symmetry so that the displacement coordinate is zero during vibration (Scheetz and White 1979). Therefore Raman spectroscopy is more sensitive to  $O^{2-} - M^{n+}$  vibration and therefore can be used as an excellent tool to determine the order-disorder arising due to anions in these materials (Sayed *et al.* 2012). There are six Raman active modes in pyrochlore given by

$$\Gamma = A_{1g} + E_g + 3T_{2g}(1) + 1T_{2g}(2) \quad (2.2)$$

**Table 2.2** Factor group analysis for pyrochlore structure

Modes	Distribution of degrees of freedom			Number of normal modes		
	A and B cations	X anion $D_{3d} C_2$	O anion $48f T_d$	Acoustic modes	Lattice modes	Selection rules
		$16c, 16d$				
$A_{1g}$	0	1	0	0	1	Raman
$A_{2g}$	0	0	0	0	0	Inactive
$E_g$	0	1	0	0	1	Raman
$T_{1g}$	0	2	0	0	2	Inactive
$T_{2g}$	0	3	1	0	4	Raman
$A_{1u}$	0	0	0	0	0	Inactive
$A_{2u}$	2	1	0	0	3	Inactive
$E_u$	2	1	0	0	3	Inactive
$T_{1u}$	4	3	1	1	7	Infrared
$T_{2u}$	2	2	0	0	4	Inactive

The factor group analysis of pyrochlore structured compositions is shown in Table 2.2. The factor group analysis itself shows that the Raman spectrum can be used as an assured tool to study the phase transition from ordered pyrochlore to more disordered fluorite. The Raman spectra of the current system  $RE_2Y_{2/3}Zr_{2/3}Nb_{2/3}O_7$  is shown in Fig. 2.4a and b. Table 2.3 shows the peak positions and the corresponding modes of vibration. The  $E_g$  mode of vibration at  $\approx 330 \text{ cm}^{-1}$  corresponds to the O-RE-O bending modes (Begg *et al.* 2001). The peaks at  $\approx 350 \text{ cm}^{-1}$  corresponding to combination band of  $E_g$  and  $T_{2g}$  shift towards the higher

wavenumber and the shift corresponds to the decreasing of the lattice parameter of the compositions. The wavenumber shifts from 333 to 380  $\text{cm}^{-1}$  corresponding to the decrease in lattice parameter from 10.81 to 10.62 Å. A larger lattice parameter corresponds to softening of the forces in the crystal lattice and which in turn shifts the phonon band to the lower energy. Thus the shift in Raman peaks and the lattice parameter are in good harmony (Scott 2007) for both pyrochlore and fluorite structured compositions. The  $A_{1g}$  vibration modes due to the O-B-O bending and A-O stretch occurs at  $\approx 500 \text{ cm}^{-1}$ . The  $A_{1g}$  mode of vibration for the composition with RE = Nd is not visible since the sample is coloured. For a perfect pyrochlore, the four  $T_{2g}$  modes occur at 400, 507, 585 and 765  $\text{cm}^{-1}$  (Mandal *et al.* 2010). The  $T_{2g}$  band corresponding to 765  $\text{cm}^{-1}$  is shown in the spectrum with considerable intensity. Other  $T_{2g}$  modes are too weak to be visible.

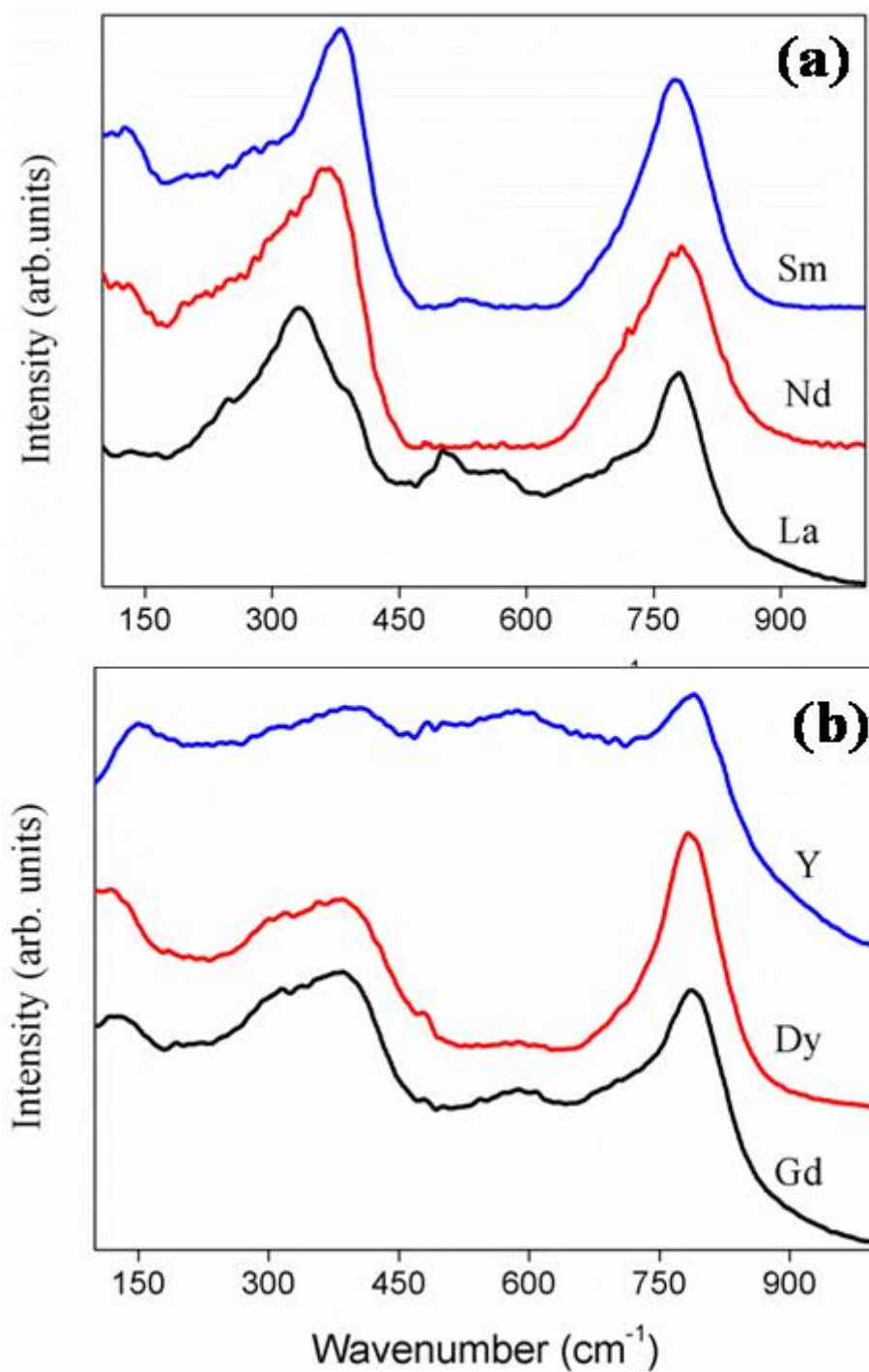


**Fig. 2.4** The Raman spectra of the series of compositions  $RE_2Y_{2/3}Zr_{2/3}Nb_{2/3}O_7$ . (a) Pyrochlore structured compositions and (b) fluorite structured compositions

**Table 2.3** Peak positions and corresponding modes of vibration

Compositions	Modes of vibration and peak position (cm <sup>-1</sup> )		
	E <sub>g</sub>	A <sub>1g</sub>	T <sub>2g</sub>
<b>La</b>	333	503	782
<b>Nd</b>	363	508	781
<b>Sm</b>	380	527	779
	T <sub>2g</sub>	Due to seven coordinated cations	
<b>Gd</b>	384		785
<b>Dy</b>	387		782
<b>Y</b>	399		788

The factor group analysis of fluorite structure predicts only one Raman active vibration mode (Keramidas and White 1973), which involves the vibration of oxygen atoms which is tetrahedrally caged by the cations (Zhou *et al.* 2016).

$$\Gamma = T_{2g} \quad (2.3)$$

Fig. 2.4b is the Raman spectrum of fluorite structured compositions. It shows a vast peak around  $\approx 400$  cm<sup>-1</sup> and an extra band at 780 cm<sup>-1</sup>. The broad peak at 400 cm<sup>-1</sup> corresponds to T<sub>2g</sub> mode. According to literature (Zhou *et al.* 2016), the absence of A<sub>1g</sub> mode around 500 cm<sup>-1</sup> and the broadening of the peak between 300 to 400 cm<sup>-1</sup> confirms the absence of additional ordering of pyrochlore structure. The other band around 780 cm<sup>-1</sup> corresponds to the seven coordinated cations (Radhakrishnan *et al.* 2009). Therefore Raman spectrum can be used as a sublime rule for analysing the order-disorder transitions.

### 2.3.3 Electron microscopic studies

Transmission electron microscopy has emerged as a convincing tool to study the structure of materials in nano and micro scale because of its capability to reveal the morphological information, crystallographic details, and chemical composition of phases distributed on a magnificent scale in a given microstructure (Neogy *et al.* 2006). Fig. 2.5 shows the high-resolution image of the two representative samples, La<sub>2</sub>Y<sub>2/3</sub>Zr<sub>2/3</sub>Nb<sub>2/3</sub>O<sub>7</sub> and Dy<sub>2</sub>Y<sub>2/3</sub>Zr<sub>2/3</sub>Nb<sub>2/3</sub>O<sub>7</sub>. The La<sub>2</sub>Y<sub>2/3</sub>Zr<sub>2/3</sub>Nb<sub>2/3</sub>O<sub>7</sub> sample shows a lattice spacing corresponding to the (111) plane as in the case of pyrochlore structure compositions and the second one shows the plane having the same miller indices but corresponding to fluorite structure. The



selected area electron diffraction patterns of the same compositions are also shown in the figure. The SAED patterns are indexed using the ratio method. The transmission electron microscopy studies also confirm the phase transition from ordered pyrochlore to disordered fluorite structure.

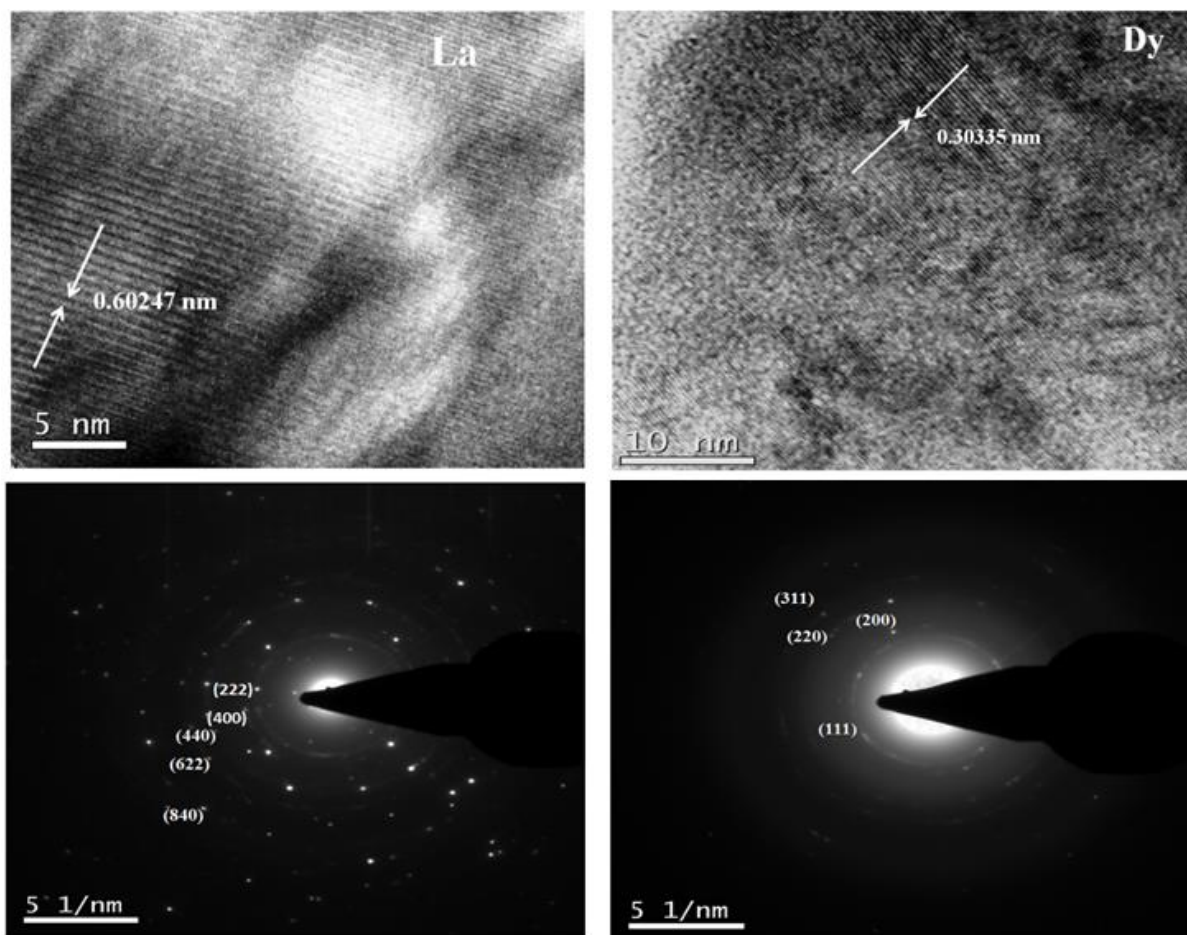


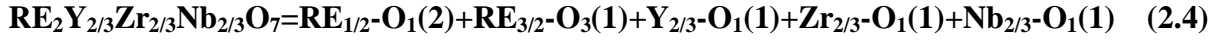
**Fig. 2.5** High-resolution lattice image and SAED patterns of the compositions  $\text{La}_2\text{Y}_{2/3}\text{Zr}_{2/3}\text{Nb}_{2/3}\text{O}_7$  and  $\text{Dy}_2\text{Y}_{2/3}\text{Zr}_{2/3}\text{Nb}_{2/3}\text{O}_7$ .

### 2.3.4 Fractional ionicity calculation based on theoretical methods

Most of the physical properties of the materials can be sensitively described based on the chemical nature of the bond between the atoms. Pauling (Linus Pauling 1960) and Philip (Philip 1970) had made many contributions to the theoretical concepts of the nature of chemical bonding. In the case of complex crystal structure, each bond is characterised by an average energy gap  $E_g$  composed of the bonding  $E_b^\mu$  and antibonding  $C^\mu$  of hybridised molecular orbitals resulting in both ionic and covalent character for each bond. The calculation of the fractional ionic and covalent behaviour can provide a lot of qualitative and

quantitative explanations based on the coordination number, nearest neighbour distances, effective number of valence electrons on the cation and anion (Srivastava and Fermi 1984).

The calculations of ionicity for the compositions  $\text{RE}_2\text{Y}_{2/3}\text{Zr}_{2/3}\text{Nb}_{2/3}\text{O}_7$  were done as follows. The chemical bonding in the multi-component material can be decomposed in the binary crystal as follows for  $\text{RE}_2\text{Y}_{2/3}\text{Zr}_{2/3}\text{Nb}_{2/3}\text{O}_7$  as



According to generalised P-V-V theory, (Philips 1970), the bond ionicity  $f_i^\mu$  and bond covalency  $f_c^\mu$  of an individual bond  $\mu$  can be defined as follows:

$$f_i^\mu = \frac{(C^\mu)^2}{(E_g^\mu)^2} \quad (2.5)$$

$$f_c^\mu = \frac{(E_h^\mu)^2}{(E_g^\mu)^2} \quad (2.6)$$

$$(E_g^\mu)^2 = (E_h^\mu)^2 + (C^\mu)^2 \quad (2.7)$$

$E_g^\mu$  is the average energy gap for the  $\mu$  type of bond and  $E_h^\mu$  and  $C^\mu$  is the covalent or homopolar and ionic or heteropolar energy gaps which comprise the total average energy gap. The homopolar energy of the bond is given by

$$E_h^\mu = \frac{39.74}{(d^\mu)^{2.48}} \quad (2.8)$$

For any binary crystals  $\text{A}_m\text{B}_n$  type compounds, the heteropolar  $C^\mu$  parts can be calculated as follows:

$$C^\mu = 14.4b^\mu \exp(-k_s^\mu r_0^\mu) \left[ Z_A^\mu - \frac{n}{m} Z_B^\mu \right] \frac{1}{r_0^\mu} \quad (2.9)$$

when  $n > m$

$$C^\mu = 14.4b^\mu \exp(-k_s^\mu r_0^\mu) \left[ \frac{m}{n} Z_A^\mu - Z_B^\mu \right] \frac{1}{r_0^\mu} \quad (2.10)$$

when  $m > n$

$$b^\mu = b(N_C^\mu)^2 \quad (2.11)$$

where

$$k_s^\mu = \left( \frac{4k_f^\mu}{\Pi a_B} \right)^{\frac{1}{2}} \quad (2.12)$$

$$k_f^\mu = (3\Pi^2 N_e^\mu)^{\frac{1}{3}} \quad (2.13)$$

$$r_0^\mu = \frac{d^\mu}{2} \quad (2.14)$$

$a_B$  is the Bohr radius (in Å), and  $d^\mu$  is the bond distance (in Å). The units of  $E_H^\mu$  and  $C^\mu$  are in electron volts. The heteropolar energy gives a measure for the difference of screened Coulomb potentials of the two atoms composing the bond or interaction of the point charges while the homopolar energy is a measure of the interaction of dipole and other multiple moments (Wu and Zhang 1999).  $\exp(-k_s^\mu r_0^\mu)$  is the Thomas-Fermi screening factor.  $k_f^\mu$  is the Fermi wave vector.  $b^\mu$  is the correction factor proportional to the square of the average coordination number  $N_c^\mu$ .

$$b^\mu = \beta (N_c^\mu)^2 \quad (2.15)$$

$$N_c^\mu = \frac{m}{m+n} N_{CA}^\mu + \frac{n}{m+n} N_{CB}^\mu \quad (2.16)$$

$\beta$  is 0.089 (Levine, 1973).  $N_{CA}^\mu$  is the coordination number of the  $\mu$  type of bond for cation A, and  $N_{CB}^\mu$  is the coordination number of the bond for anion B.  $N_e^\mu$  is the number of valence electrons of the  $\mu$  type of bond per cubic centimetre.

$$N_e^\mu = \frac{n_e^\mu}{\vartheta_b^\mu} \quad (2.17)$$

$$n_e^\mu = \frac{Z_A^\mu}{N_{CA}^\mu} + \frac{Z_B^\mu}{N_{CB}^\mu} \quad (2.18)$$

where  $n_e^\mu$  is the number of effective valence electrons per  $\mu$  bond and  $\vartheta_b^\mu$  the bond volume.

$$\vartheta_b^\mu = \frac{(d^\mu)^3}{\sum_v (d^v)^3 N_b^v} \quad (2.19)$$

$N_b^\vartheta$  is the number of bonds per cubic centimetre, which is obtained from the crystal structure.

Table 2.4 shows the calculated results for the system  $RE_2Y_{2/3}Zr_{2/3}Nb_{2/3}O_7$ . The values show that ionicity of the A-O bond is always higher than that of the B-O bond which implies that B-O bond has larger covalency caused by the overlap of orbitals resulting in short bond length than that of A-O bond (Taniguchi and Aniya 2010). Further, the ionicity of A-O bond decreases with decreasing of the ionic radii except for Nd composition. In the case of the Nd compound, the ionicity of the A-O bond shows an anomalous trend showing a much lower value compared to the other pyrochlore structured compositions. That is the A-O bond is more covalent in the  $Nd_2Y_{2/3}Zr_{2/3}Nb_{2/3}O_7$ . This higher covalency may be due to the very high polarizability value of  $Nd^{3+}$  (14.519635) compared to other lanthanides in the series. Polarizability is the ease of deforming the valence electron cloud of the chemical species (Ghosh and Biswas 2002). High polarizability value of  $Nd^{3+}$  causes a more covalent character to the Nd-O bond. At the same time, B-O bond shows a gradual increase in ionicity, which decreases the covalency and this lessens the bond strength. The difference in ionicity also exhibits the same trend just like that of the ionicity of the A-O bond. For the defect fluorite structured compositions the ionicity of both A-O and B-O bond decreases gradually hence strengthens the bond. This can be explained as the effect of shorter bond length with a decrease in the lattice parameter. The shorter bond length increases the bond strength which can be attributed to the increased covalency. Also, it is visible that the ionicity of the B-O bond has more role in the phase transition, which reaches a maximum at the phase boundary, then decreases.

**Table 2.4** The ionicity of the A-O, B-O bonds and the ionicity difference of the compositions  $RE_2Y_{2/3}Zr_{2/3}Nb_{2/3}O_7$

Compositions	Ionicity of A-O bond	Ionicity of B-O bond	Ionicity Difference
<b>La</b>	0.9028	0.8237	0.0791
<b>Nd</b>	0.8779	0.8282	0.0497
<b>Sm</b>	0.9584	0.8303	0.1281
<b>Gd</b>	0.9385	0.8472	0.0913
<b>Dy</b>	0.9188	0.8469	0.0719
<b>Y</b>	0.8917	0.8467	0.0450

### 2.3.5 High-Temperature XRD Studies

For the high-temperature application of the pyrochlore oxides, the structure stability and variation of crystallographic properties are to be studied. On the microscopic level, it can be done by using the high-temperature XRD. The lattice thermal expansion coefficient stated by the equation

$$\alpha_a = \frac{1}{a_{298}} \left( \frac{da}{dT} \right) K^{-1} \quad (2.20)$$

$\alpha_a$  is an excellent nominee to represent the structural stability, influence of bond strength on the oxide ion conductivity (Radhakrishnan *et al.* 2012). The XRD patterns of each sample were measured in the temperature range of 298K to 1273K with an interval of 200K. The obtained XRD patterns were analysed by Le-Bail fitting method of the software X'pert High Score Plus. The plot of lattice parameter Vs absolute temperature was done for each sample and the slope of the sample  $\left( \frac{da}{dt} \right)$  divided by the lattice parameter at the room temperature gives the value of lattice thermal expansion coefficient. The variation of lattice parameter with the temperature for  $Nd_2Y_{2/3}Zr_{2/3}Nb_{2/3}O_7$  is shown in Fig. 2.6a. Also, the shift in the d-spacing of the same is shown in Fig. 2.6b.

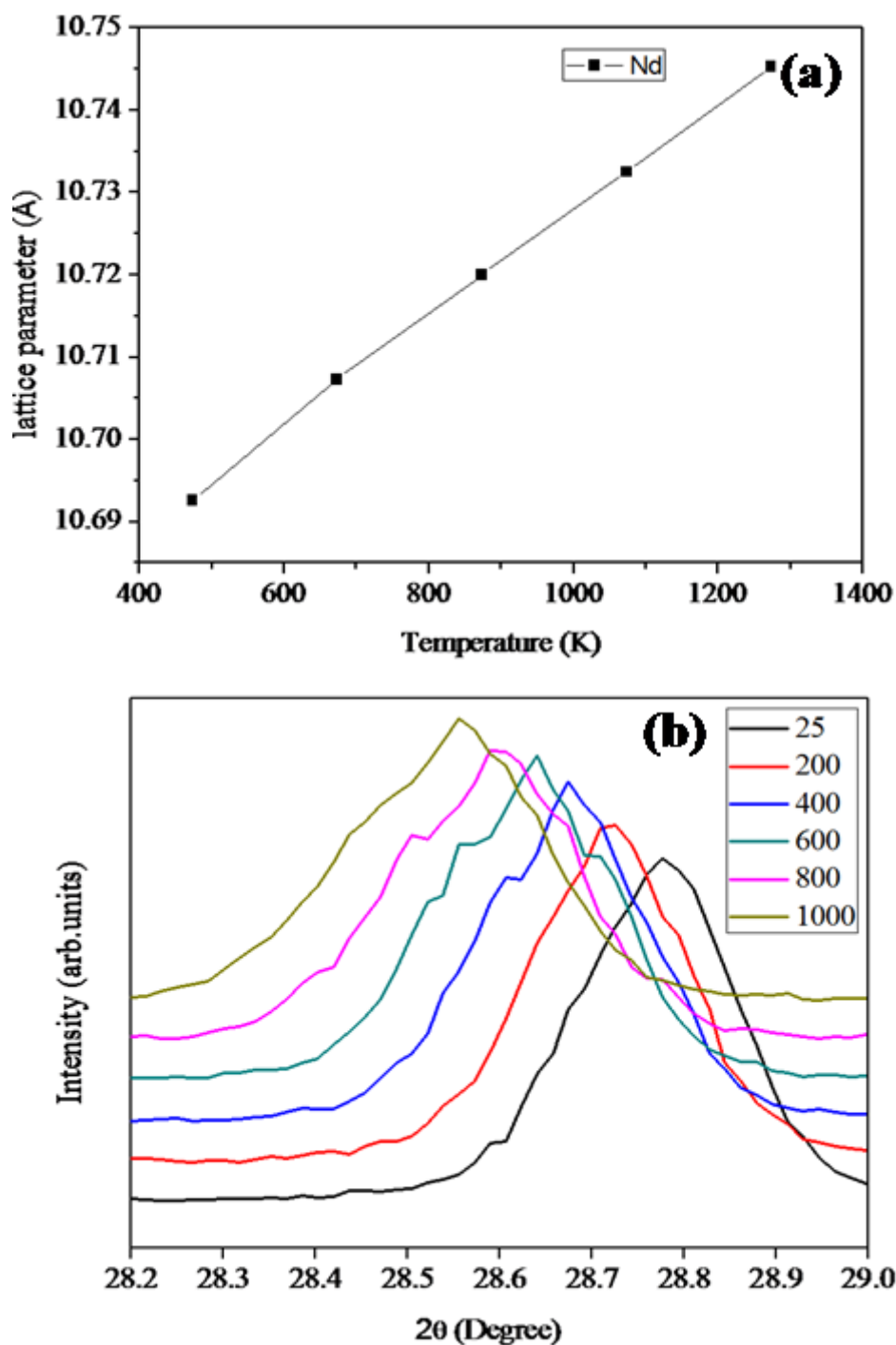


**Fig. 2.6** (a) The variation of the lattice parameter of  $\text{Nd}_2\text{Y}_{2/3}\text{Zr}_{2/3}\text{Nb}_{2/3}\text{O}_7$  with temperature.

(b) The corresponding shift in the d-spacing of  $\text{Nd}_2\text{Y}_{2/3}\text{Zr}_{2/3}\text{Nb}_{2/3}\text{O}_7$

Fig. 2.7 shows the lattice thermal expansion coefficient of each sample. In the case of the pyrochlore structured compound, the lattice thermal expansion coefficient shows an anomalous behaviour. The lattice thermal expansion coefficient of  $\text{Sm}_2\text{Y}_{2/3}\text{Zr}_{2/3}\text{Nb}_{2/3}\text{O}_7$  shows an abnormal increase. The thermal expansion coefficient for the fluorite structured compositions shows a steady increase.

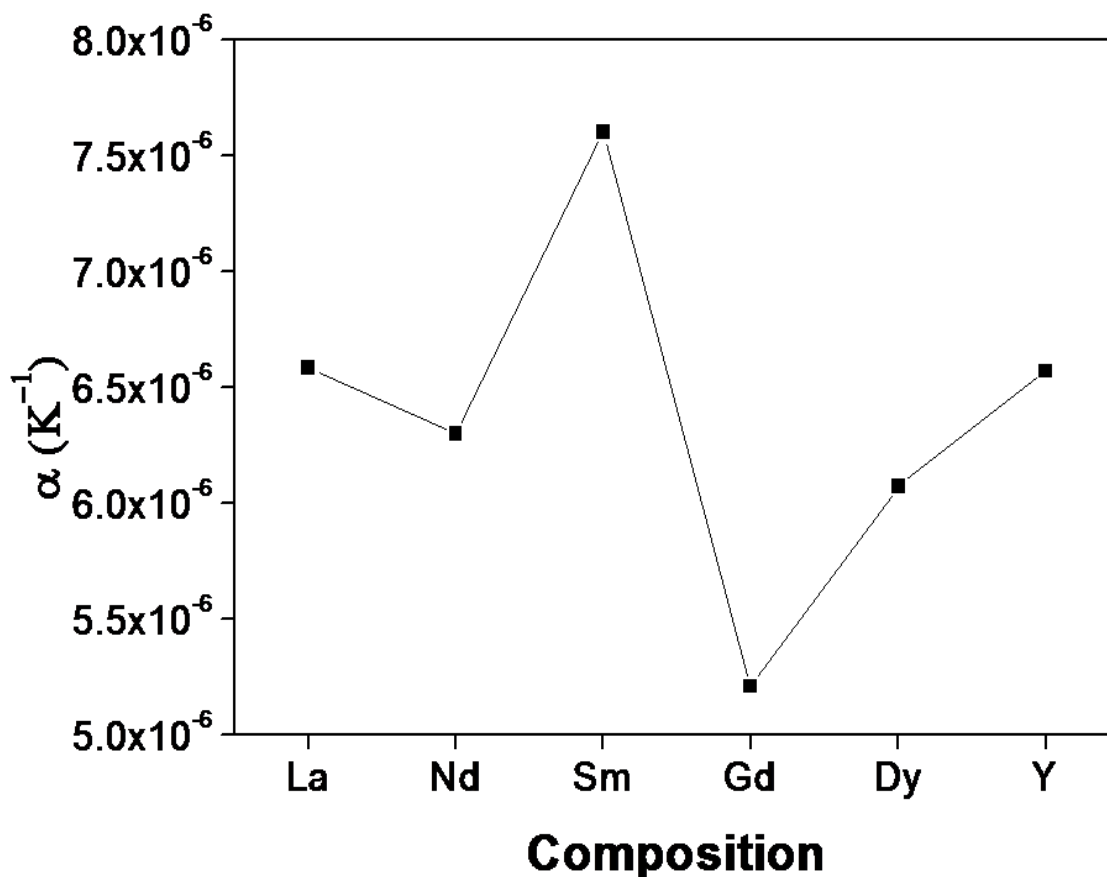


**Fig. 2.7** The variation of the lattice thermal expansion coefficient with the different lanthanides in the composition:  $RE_2Y_{2/3}Zr_{2/3}Nb_{2/3}O_7$  (RE = La, Nd, Sm, Gd, Dy, Y)

The studies on the relationship between the thermal expansion coefficient and ionic conduction in perovskite-type oxides by Taniguchi *et al.* shows a small difference between the ionicities of the A-O and B-O bond results in more significant value of the thermal expansion coefficient due to the instability in the position of the oxygen (Taniguchi and Aniya 2010). However, in the case of pyrochlore oxides, the structure itself contains two crystallographically different oxides ions. The A cation is eight coordinated with six  $48f$  oxygen ions and two  $8a$  ions with different bond length, and the B cation is six coordinated with  $48f$  oxide ions only. The plot of ionicity of A-O bond ( $f_{i A-O}^{\mu}$ ), B-O bond ( $f_{i B-O}^{\mu}$ ) and  $|f_{i A-O}^{\mu} - f_{i B-O}^{\mu}|$  with the thermal expansion coefficient is shown in Fig. 2.8. Here in the case of pyrochlore compounds, A-O and B-O bonds has to be treated separately unlike in the case of perovskites. The ionicity of A-O and B-O bond for the compositions with RE= Nd shows better covalent character due to high polarizability (from the calculated values also). Higher covalency, in other words lower ionicity results in strong bonds. The stronger bond results imply increasing rigidity of the system, which in turn instigates smaller thermal

expansion (Radhakrishnan *et al.* 2012). In the case of composition with RE = Sm, both the A-O and B-O bond has a higher percentage of ionic character compared to other compositions. Therefore the bonds are weaker and hence show a high value of thermal expansion coefficient. From the studies, it is shown that at least in the case of pyrochlore compounds, the chemical characteristics of each bond has its contribution. The studies of the Wuensch *et al.* show that the A<sup>3+</sup>-O bond expands more rapidly than the B<sup>4+</sup>-O bonds (Wuensch *et al.* 2000). Hence higher contribution to the thermal expansion arises from the A-O bond. From this study also it is clear that the lattice thermal expansion coefficient is in line with the ionicity of the A-O bond.

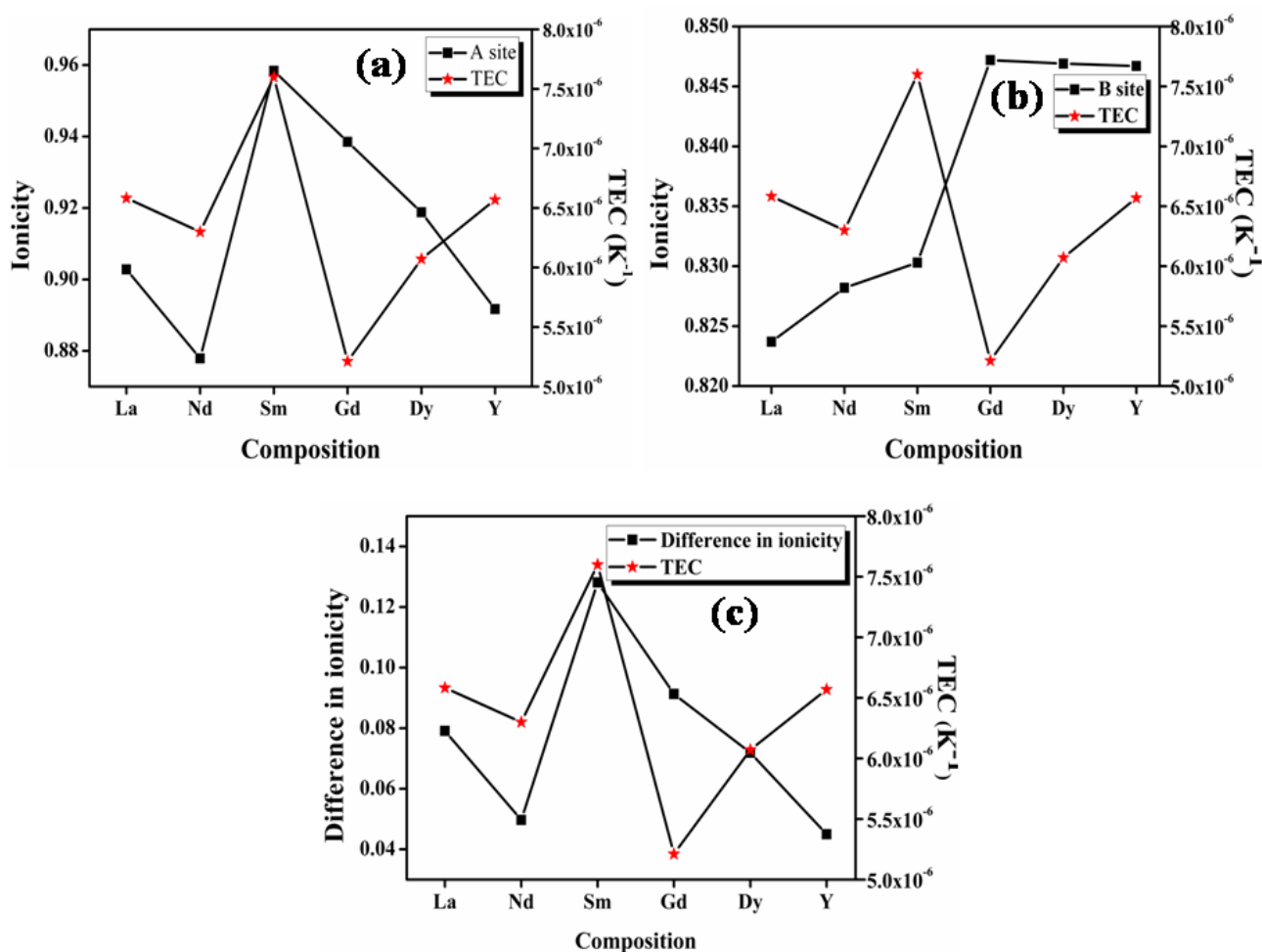


**Fig. 2.8** The variation of lattice thermal expansion coefficient with ionicity of bonds (a) A-O bond (b) B-O bond and (c) Difference in ionicity between A-O and B-O bonds

In the case of fluorite oxides, the 48*f* and 8*b* oxide ions randomise to form the 4*c* oxygen positions. Here just like the perovskite-type oxides A and B cations are coordinated by only one type of oxide ions. Hence here, individual bonds do not play an essential role in



determining the thermal expansion coefficient. Here the thermal expansion coefficient increases with a decrease in the difference in the ionicity of the A-O and B-O bonds. Just like the radius ratio as the difference decreases the disorder in the fluorite structure increases and hence results in higher lattice thermal expansion coefficient. Hence in the case of Fluorite related structure cumulative effects of the bonds take part in determining the thermal expansion coefficient rather than the effects of individual bonds.

### **2.3.6 Impedance Analysis**

The ionic conductivity of the samples was measured using the two probe ac-conductivity measurement method. Impedance spectroscopy is the study of sample resistivity over a wide range of frequencies. Each spectrum provides information about resistive, inductive or capacitive elements which together constitutes the electrical behaviour of the sample. Impedance spectrum taken over a wide range of frequencies is capable of resolving total impedance into three components namely, impedance for the bulk (high-frequency spectrum), grain boundary (middle of the spectrum) and electrode process (low-frequency arc). The conductivity measurements were done on a wide range of temperature from room temperature to 1073K at an interval of 50K. The Cole-Cole plot of the representative sample  $\text{Nd}_2\text{Y}_{2/3}\text{Zr}_{2/3}\text{Nb}_{2/3}\text{O}_7$ , Arrhenius plot, activation energy and pre-exponential constant and the overall conductivity of all the compositions were plotted in Fig. 2.9.

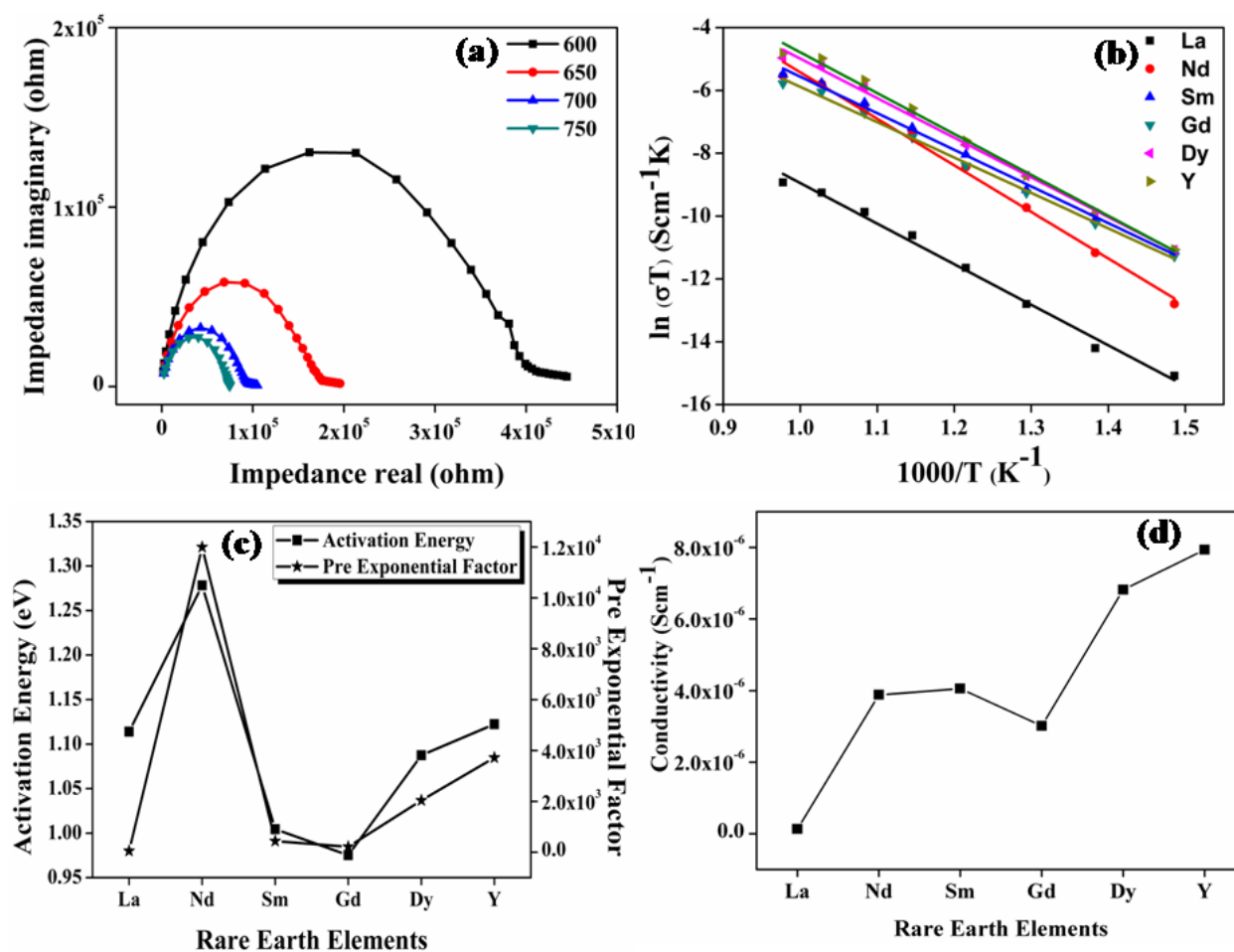


**Fig. 2.9** (a) Cole-Cole plot of the  $\text{Nd}_2\text{Y}_{2/3}\text{Zr}_{2/3}\text{Nb}_{2/3}\text{O}_7$  as a representative sample. (b) The Arrhenius plot of the samples fitted with a straight line. (c) The variation of activation energy and pre-exponential factor of the series of samples. (d) The overall conductivity variation of the samples at 1023K.

Fig. 2.9a shows the Cole-Cole (Nyquist) plot of the sample  $\text{Nd}_2\text{Y}_{2/3}\text{Zr}_{2/3}\text{Nb}_{2/3}\text{O}_7$  at 873, 923, 973, 1023K. It is observed in Fig. 2.9a that the radius of the semicircle of the Cole-Cole plot decreases as the temperature increases, which implies that the conductivity of the samples increases as the temperature increases. Therefore it is understood that the conduction mechanism is thermally activated. The Nyquist plot ends with a small spike at the low-frequency region. This spike is either due to the diffusion of ions through the electrode or the electrode polarisation. The capacitance value corresponding to this spike is the same as those expected for the blocking of ionic charge carriers at the electrode sample interface (Abram *et al.* 2001). Hence this spike confirms the oxide ion conduction in the samples.

The temperature dependence of conductivity is shown in Fig. 2.9b and is found to follow the Arrhenius behaviour given by the equation

$$\sigma(T) = \sigma_0 \exp(-E_a / K_B T) \quad (2.21)$$

where  $\sigma_0$  is the pre-exponential factor, which is a measure of the actual number of mobile oxide ions,  $E_a$  denotes the activation energy for the conduction process,  $K_B$  is the Boltzmann constant, and  $T$  is the absolute temperature. The activation energy and pre-exponential factor are calculated from the Arrhenius plot using the slope and y-intercept of the straight line for each sample. The plot of activation energy and the pre-exponential values are plotted in Fig. 2.9c. The variation of overall conductivity with the composition is also in Fig. 2.9d.

The trend in conductivity with the compositions can be viewed as a competing effect of the trends of activation energy and preexponential factor. The activation energy in the case of  $\text{Nd}_2\text{Y}_{2/3}\text{Zr}_{2/3}\text{Nb}_{2/3}\text{O}_7$  increases drastically compared with the other pyrochlore structured compositions. This high activation energy is due to the highly polarizable Nd ion due to which the covalency of the A-site composition increases and the bonds in the structure became rigid. This causes high activation energy required for the breaking of the metal-oxygen bond. The rigidity of the bonds in the  $\text{Nd}_2\text{Y}_{2/3}\text{Zr}_{2/3}\text{Nb}_{2/3}\text{O}_7$  was proved by the thermal expansion coefficient, which is low compared to the other pyrochlore structured compositions. Hence the activation energy of the sample with Nd is very high. However, the conductivity trend is in the opposite direction since the conductivity increases, disregarding the influence of the activation energy. The explanation for this phenomenon can be done using the concept of ionicity for this composition; the difference in ionicity of the A-O and B-O bonds is shallow. When the difference in ionicity is small the bonding nature in A-O and B-O becomes closer, and the oxygen might bind to the A-site or B-site ion, and hence the position of the oxygen ion becomes unstable (Taniguchi and Aniya 2010). This introduces more anion disordering to the lattice, which in turn enhances the concentration of charge carriers which is also shown in Fig. 2.9c where the pre-exponential which is a measure of the concentration of charge carriers increases rapidly for the sample with RE=Nd. Then the conductivity of the sample  $\text{Sm}_2\text{Y}_{2/3}\text{Zr}_{2/3}\text{Nb}_{2/3}\text{O}_7$  remains the same since the more considerable value of ionicity difference reduces the concentration of charge carriers even though the activation energy is very much reduced. In the case of compositions with the fluorite structure the conductivity follows the same trend with the difference in ionicity. Hence the ionicity calculation in pyrochlore type oxides plays a vital role in determining the ionic conductivity. It can also be concluded that small difference in ionicity also introduces cation disorder in the lattice, which in turn increases the activation energy and the oxygen

position becomes unstable and hence anion disordering also. Cation disorder increases the activation energy, and anion disorder increases the concentration charge carriers in pyrochlore (Munshi 1995). The conductivity hence arises as the result of these competing effect in these compositions.

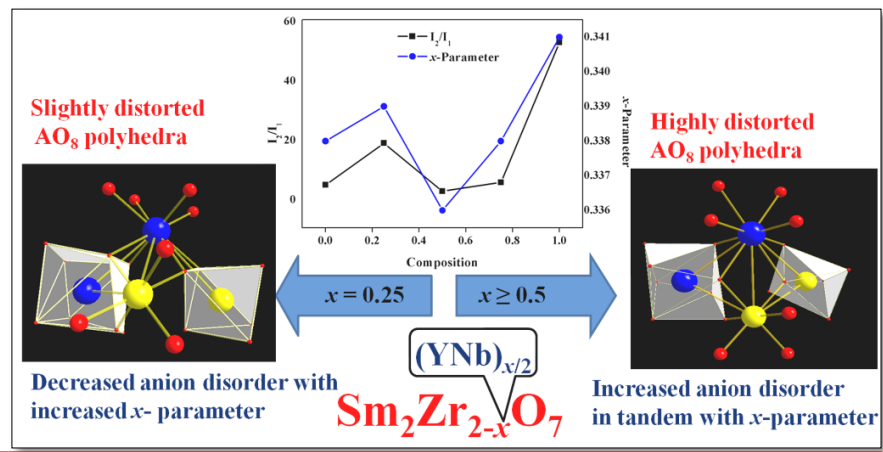
### 2.4 Conclusions

A series of new compositions,  $RE_2Y_{2/3}Zr_{2/3}Nb_{2/3}O_7$  were prepared via solid-state reaction route successfully. The structural analysis using powder X-ray diffraction pattern, Raman analysis, and transmission electron microscopy studies showed a phase transition from an ordered pyrochlore to a defect fluorite type structure with a phase boundary at Gd substitution. The analysis of thermal expansion coefficient, ionicity and oxide ionic conductivity of the system indicated an interrelationship among these parameters with structure-dependent. The decrease in difference in ionicity in metal-oxygen bonds increases the ionic conductivity in both phases. However, the influence of ionicity difference of M-O bond on thermal expansion is dependent on phase as well as ionicity of A-O bond. The best conductivity obtained in the series is  $7.9 \times 10^{-6}$  S/cm for  $Y_2(Y_{1/3}Zr_{1/3}Nb_{1/3})_2O_7$  at 1023K. The minimum thermal expansion coefficient is obtained at the phase boundary for  $Gd_2Y_{2/3}Zr_{2/3}Nb_{2/3}O_7$ , and the value is  $5.2 \times 10^{-6} K^{-1}$ . The present study demonstrated that the ionicity difference of metal-oxygen bonds plays a crucial role in determining the thermal expansion coefficient and ionic conductivity which may help design oxide ionic conductors.

# Chapter 3

## Contrasting anion disorder behaviour in $\text{Sm}_2\text{Zr}_2\text{O}_7$ by simultaneous aliovalent cation substitutions and its structural and electrical properties

In the present study, the effect of simultaneous aliovalent cation substitutions on B site of the pyrochlore type compositions has been attempted to understand the anion disorder and its influence on the electrical properties. The structural analysis studies reveal that the concentration of aliovalent cation substitution has a distinct effect on the structure; the lower concentration of the Y and Nb ( $x \leq 0.25$ ) destabilises the system lowering the distortion and at higher concentration ( $x \geq 0.5$ ) it stabilises the system. The degree of anion disorder is evaluated by the intensity ratio of the Raman intense  $E_g$  mode and  $T_{2g}$  mode around  $800\text{ cm}^{-1}$  from the Raman spectrum whose trend is in line with the oxygen  $x$ -parameter variation with different concentration of the aliovalent cation substitution. The electrical properties follow the same trend of anion disorder and lattice strain in the system.



*J. Appl. Phys.* 2019, 126, 045110



### 3.1 Introduction

Oxide ionic conducting materials draw a lot of attention due to its diverse technological applications such as oxygen sensors and pumps, ceramic membranes for oxygen separation and in solid oxide fuel cells (SOFCs), where they act as electrolytes transporting  $O^{2-}$  ions to react with a fuel such as hydrogen in the clean direct conversion of chemical to electrical energy (Skinner and Kilner 2003). Oxide ion conduction through solids is discovered more than a century ago by Nernst. Due to the small conductivity of the materials at a low temperature, the application of the oxide ion conductors is reduced to the high-temperature application. The small conductivity of these materials arises due to the interaction of the significant double-charged oxide ion with the cation network (Boivin and Mairesse 1998). Therefore some of the highly specified structural compositions will exhibit high ionic conductivity. Pyrochlore structured compositions are one of the relevant class of materials suitable for these applications

Pyrochlore oxides having a general formula  $A_2B_2O_7$  shows a vast range of electrical and physical properties depending on the compositional variations and ordering of the atoms and oxygen vacancies (Moreno *et al.* 2007). This structure has Fd3m space symmetry and is ordered superstructure of the fluorite structure  $AO_2$  (having space symmetry Fm3m) with an ordered absence of the  $1/8^{\text{th}}$  oxygen in the fluorite (Ashbrook *et al.* 2015). Generally, two classes of pyrochlore type compositions are present viz.  $A_2^{3+}B_2^{4+}O_7$  and  $A_2^{2+}B_2^{5+}O_7$ . In these compositions, III-IV type compositions are more favoured due to the ionic radius ratio of A and B cations (Subramanian *et al.* 1983). Fixing the origin at B cation, the Wyckoff position of the pyrochlore type compositions are: the A cation at  $16d$  and the B is at  $16c$ . These cations form an FCC lattice with an alternative arrangement along the  $\langle 110 \rangle$  direction. The crystal lattice consists of three different anion positions, and oxide ion occupies two sites ( $8b$  and  $48f$ ), and one is vacant at  $8a$ . The anion vacancies are ordered in the lattice (Radhakrishnan *et al.* 2011).

Among the pyrochlore zirconates,  $Sm_2Zr_2O_7$  has been extensively studied due to its good ionic conductivity which is comparable to the other oxide ion conductors at low-temperature ranges. The time-independent ionic conductivity and low activation energy make the  $Sm_2Zr_2O_7$  a promising oxide ion conductive material (Shinozaki *et al.* 1979). Xia *et al.* study the aliovalent substitution effect on the  $Sm_2Zr_2O_7$  in the A site, and reported that conductivity increases with the CaO substitution until the secondary phase emerges (Xia *et*

*al.* 2009). Studies of substitution of  $\text{Ce}^{4+}$  on the B site substitution and simultaneous substitution of  $\text{Sc}^{3+}$  and  $\text{Ce}^{4+}$  on  $\text{Sm}_2\text{Zr}_2\text{O}_7$  were carried out (Vaisakhan Thampi *et al.* 2014; Vaisakhan Thampi *et al.* 2017). Both the substitutions increase the ionic conductivity as the disorder increases and then decreases with further increase in the disorder. Acceptor and donor doping on the  $\text{Sm}_2\text{Zr}_2\text{O}_7$  compositions were also reported. MgO on the A-site composition reduces the ionic conductivity, and the  $\text{ZrO}_2$  on the same site slows down the decrease in the ionic conductivity when compared to the acceptor doping on the B site substitution of  $\text{Sm}_2\text{Zr}_2\text{O}_7$  (Shlyakhtina *et al.* 2014; Xia *et al.* 2010). Zirconia stabilisation study using Y and Nb as the dopants reveals some interesting results and these results show that at lower doping concentration, the dopants destabilise the system and as the concentration increases, it stabilises the system but the distortion increases among the neighbouring cation network (Li *et al.* 1994).

The study on the factors that affect ionic conductivity reveals that lattice strain is a prominent parameter in determining the structural and functional properties of the oxide materials. Computational studies on the fluorite structured oxides show that the conductivity increases to several orders of magnitude in a strained system (Kushima and Yildiz 2010). Recent research studies show that in the case of ionic conduction in which the crucial part is played by the site to site hopping (e.g., oxide ions and alkali ion conductors) lattice strain modulates the conductivity (Ferrara *et al.* 2016). This site to site hopping is more favoured by creating anion disorder in the lattice. So far, many pieces of research have been carried out to achieve more disorder either by smaller cation substitution on the A site or bigger ion substitution on the B site of the  $\text{Sm}_2\text{Zr}_2\text{O}_7$  (Vaisakhan Thampi *et al.* 2014; Wan *et al.* 2011). However, these approaches have some drawbacks, such as control of anion disorder and increased activation energy in the highly disordered system. The present investigation is substituting two aliovalent cations on the B site with higher average ionic radius than zirconium and studies its influence on the crystal structure, anion disorder and electrical properties.

Therefore, the present work attempted to study aliovalent cation substitutions (Y and Nb) on the B-site of  $\text{Sm}_2\text{Zr}_2\text{O}_7$  by maintaining the charge neutrality. The study reveals insight of anion disorder and its influence on the electrical properties, which provides a scope in designing and developing new pyrochlore structure-based oxide ionic conductors. To the best of our knowledge, simultaneous substitution on the B site of the  $\text{Sm}_2\text{Zr}_2\text{O}_7$  is not yet studied



in detail. The B site substitution has more influence on the properties of the pyrochlore type composition, and therefore such a study can reveal much understanding of the anion disorder and lattice strain that influence on the electrical properties. The present chapter comprises some of these results studied on this aspect.

### 3.2 Experimental

The compositions,  $\text{Sm}_2\text{Zr}_{2-x}(\text{YNb})_{x/2}\text{O}_7$  ( $x = 0, 0.25, 0.5, 0.75, 1$ ) were prepared via conventional solid-state reaction route. The chemicals  $\text{Sm}_2\text{O}_3$  (Alfa Aesar, 99.998%),  $\text{ZrO}_2$  (Aldrich 99%),  $\text{Y}_2\text{O}_3$  (Aldrich 99.999%) and  $\text{Nb}_2\text{O}_5$  (Aldrich 99.995%) were weighed stoichiometrically. The weighed compositions were mixed using agate and mortar in a wet medium using acetone. The mixed compositions were dried in an oven at 373K for 1h. The process is repeated thrice to make a uniform mixture. Thoroughly mixed samples were calcined at 1573K for 6h and then further calcined at 1873K for 12h with intermittent grinding. The samples were ground into fine powders, and the powder was uniaxially compressed at 25Mpa and sintered at 1923K for 12h. Then the sintered samples were used for further characterisation.

Crystal structure analyses of the prepared compositions were done using X-ray powder diffractometer (X'pert Pro, PANalytical) under Ni-filtered  $\text{CuK}\alpha$  radiation using a Philips X'pert Pro diffractometer operating at 45 kV and 30 mA. Scans were recorded over a  $2\theta$  range of  $10\text{--}90^\circ$  with a step size of 0.02 and a scan time of 30 s using X'pert software. The unit cell parameters were calculated using a least-square method and Rietveld analysis using high score plus software. The Raman spectra of the prepared samples were recorded using a WITec alpha 300R confocal Raman microscope. The Raman confocal microscope was equipped with a 100\_ oil immersion objective and 300/600 groove grating. A laser source of wavelength 532 nm was used for excitation, and a CCD detector operating at room temperature was used for detection. The number of accumulations and the integration time used were 5 and 1 s, respectively. For impedance measurement, a silver paste was applied to the flat faces of the pellets. The silver-coated pellets were placed in an oven at 473 K for 6h, and the measurements were carried out from 573K to 1023 K in the frequency range from 1 Hz to 1 MHz by applying an ac voltage of 100 mV using a computer-controlled impedance analyser (Solatron, SI 1260). The complex impedance plots were made using SMART Software.

### 3.3 Results and Discussion

The compositions,  $\text{Sm}_2\text{Zr}_{2-x}(\text{Ynb})_{x/2}\text{O}_7$  ( $x = 0, 0.25, 0.5, 0.75, 1$ ) prepared via solid-state reaction route are characterised using powder X-ray diffraction, Raman Spectroscopy, SEM and impedance microscopy. The samples are termed as  $\text{Zr}_2$ ,  $\text{Zr}_{1.75}$ ,  $\text{Zr}_{1.5}$ ,  $\text{Zr}_{1.25}$ , and  $\text{Zr}_1$  for brevity.

#### 3.3.1 Powder X-ray diffraction analysis

Fig. 3.1 shows the powder X-ray diffraction patterns of the prepared samples. The XRD patterns of the compositions are indexed to the pyrochlore crystal structure. Pyrochlore is the superstructure of the fluorite structure, so the X-ray diffraction data in Fig. 3.1 consists of all the fluorite peaks plus the less intense superlattice peaks corresponding to the ionic radius difference between the A and B cations.

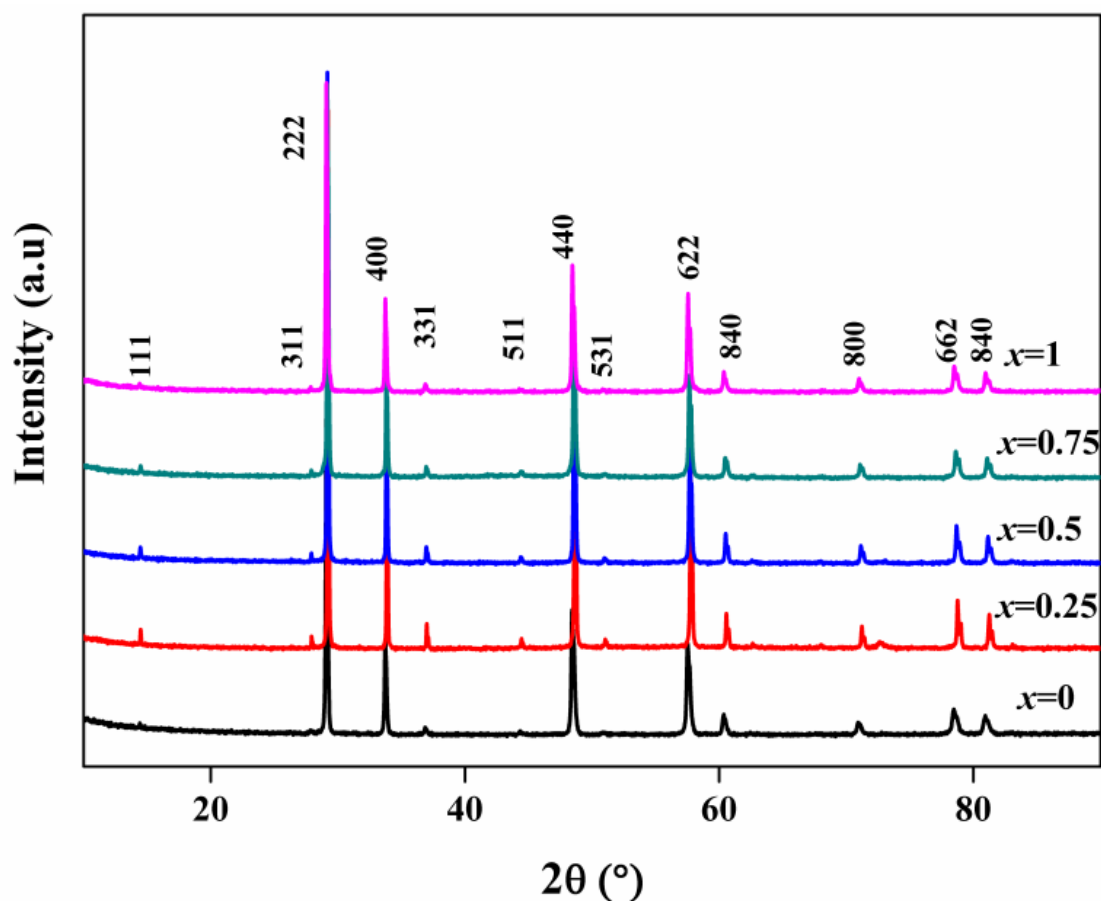


**Fig. 3.1** The powder X-ray diffraction patterns of the  $\text{Sm}_2\text{Zr}_{2-x}(\text{Ynb})_{x/2}\text{O}_7$  ( $x = 0, 0.25, 0.5, 0.75, 1$ ).

The fluorite structure peaks easily satisfy the conditions:

$$h + k = 4n \quad (3.1)$$

$$k + l = 4n \quad (3.2)$$

$$l + h = 4n \quad (3.3)$$

Where (hkl) is the Miller indices of the planes (Heremans *et al.* 1995). The superlattice peaks do not satisfy the above equations.  $\text{Sm}^{3+}$  cation occupies the A site (16d) site which is eight coordinated.  $\text{Zr}^{4+}$  at 16c is co-doped with  $\text{Y}^{3+}$  and  $\text{Nb}^{5+}$  cations. The radius of the cations is 1.079Å, 0.72Å, 0.9Å and 0.64Å for  $\text{Sm}^{3+}$  (VIII coordination),  $\text{Zr}^{4+}$ ,  $\text{Y}^{3+}$  and  $\text{Nb}^{5+}$  (VI coordination) respectively (Shannon 1976). The pyrochlore structure stability depends mainly on the radius ratio  $R_A/R_B$ . The average radius of the B cation is calculated using the formula

$$R_B = \frac{(2-x)R(\text{Zr}^{4+}) + \frac{x}{2}R(\text{Y}^{3+}) + \frac{x}{2}R(\text{Nb}^{5+})}{2} \quad (3.4)$$

The present radius ratio decreases with the incorporation of Y and Nb on the B site ranging from 1.50 to 1.45. Therefore all the compositions are expected to form in the pyrochlore structure. The variation of the lattice parameter with the substitution is shown in Fig. 3.2. The lattice parameter of the compositions increases with increase in the Y, and Nb concentration and the increase in the lattice parameter obeys the Vegard's law as the effective ionic radius of Y and Nb is high compared to that of Zr at the B site. The variation in the lattice parameter also further evidences the effective substitution of Y and Nb into the lattice.

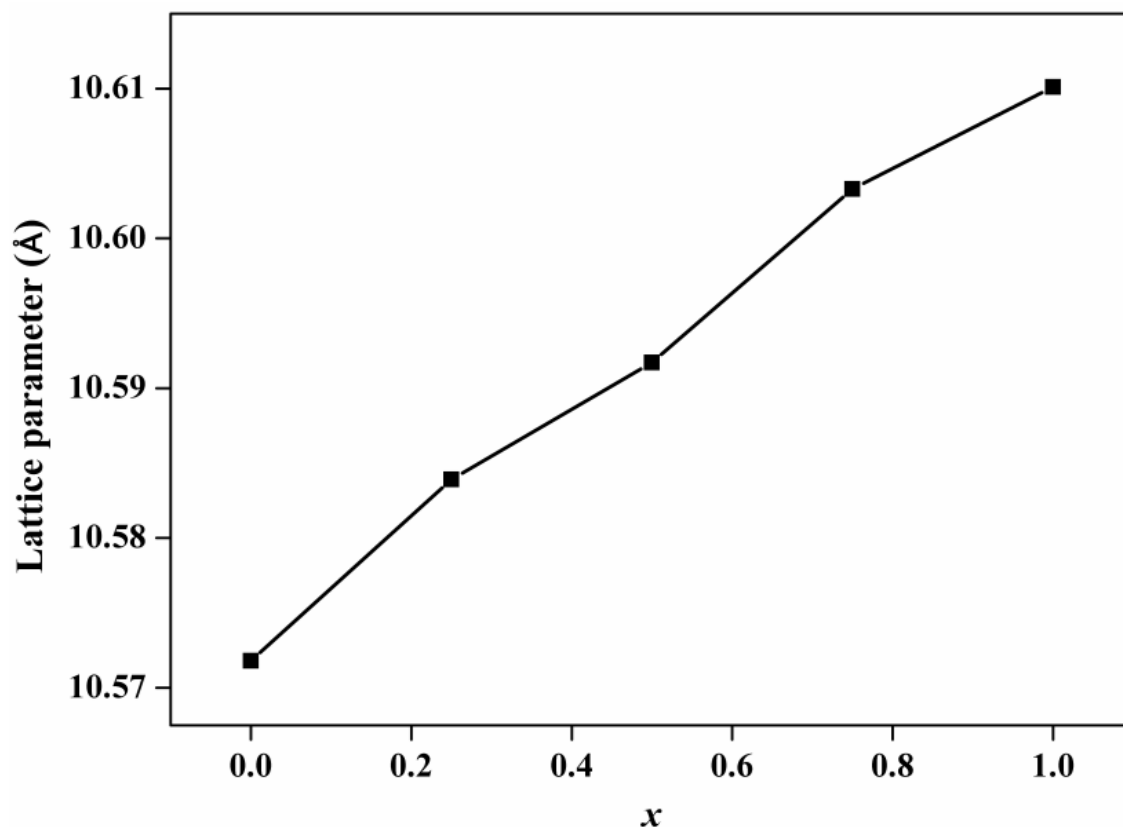


**Fig. 3.2** The increase in the lattice parameter with an increase in the doping concentration  $x$

Rietveld analyses of the samples were done on the X-ray powder diffraction data of the samples in order to study the structural changes with the increase in the substitution. The idea of the Rietveld refinement is to calculate the entire powder diffraction data with the given refinable parameter and to minimise the weighted sum of the square of the difference between the calculated pattern and the observed pattern using the least square methods (Dinnebier 2001). All the compositions are assumed to be in the pyrochlore structure. The  $\text{Sm}^{3+}$  cations occupy the  $16d$  site and  $\text{Zr}^{4+}$ ,  $\text{Y}^{3+}$  and  $\text{Nb}^{5+}$  occupy the  $16c$  site according to the stoichiometric ratio of the compositions. Pseudo Voigt profile function is used to define the pattern. The lattice parameters, oxygen  $48f$   $x$  parameter along with other factors such as scale factor, Caglioti functions, flat background and peak shape functions are refined. The refined parameters are shown in Table 3.1, and the graphical output is shown in Fig. 3.3. The R factors and goodness of fit values suggest that proper fit is achieved.

**Table 3.1** Rietveld refined parameters of the  $\text{Sm}_2\text{Zr}_{2-x}(\text{Ynb})_{x/2}\text{O}_7$  ( $x = 0, 0.25, 0.5, 0.75, 1$ ) compositions

	<b>Zr<sub>2</sub></b>	<b>Zr<sub>1.75</sub></b>	<b>Zr<sub>1.5</sub></b>	<b>Zr<sub>1.25</sub></b>	<b>Zr<sub>1</sub></b>
<b>Unit cell</b>	Cubic	Cubic	Cubic	Cubic	Cubic
<b>Space group</b>	Fd3m	Fd3m	Fd3m	Fd3m	Fd3m
<b>Lattice parameter (Å)</b>	10.5716(1)	10.5840(1)	10.5917(1)	10.6029(9)	10.6101(3)
<b>x- parameter (Å)</b>	0.338(1)	0.339(1)	0.336(9)	0.338(1)	0.341(1)
<b>R<sub>p</sub> (%)</b>	6.40	8.60	9.15	10.22	10.08
<b>R<sub>exp</sub> (%)</b>	5.94	9.11	9.36	9.62	9.93
<b>R<sub>wp</sub> (%)</b>	8.22	10.77	11.19	12.63	12.71
<b>R<sub>Bragg</sub> (%)</b>	10.21	6.95	8.15	9.20	9.07
<b>GoF</b>	1.92	1.40	1.43	1.72	1.64

The bond length of the prepared compositions can also be derived from the Rietveld analysis. The calculated values of the A-O<sub>1</sub>, A-O<sub>2</sub>, B-O<sub>1</sub> compositions are reported in Table 3.2. The lattice strain due to the Y and Nb doping is calculated using Williamson–Hall (W–H) method where both size-induced and strain-induced broadening is deconvoluted by considering the peak width as a function of  $2\theta$ . The width of the individual peaks in the XRD diagram is expressed as

$$\beta \cos\theta = \frac{k\lambda}{d} + 4\varepsilon \sin\theta \quad (3.5)$$

where  $\beta$  is the width of the peaks,  $d$  is the crystallite size,  $\lambda$  is the wavelength of X-ray used, and  $\varepsilon$  is the lattice strain. A plot is drawn with  $4\varepsilon \sin\theta$  along the x-axis and  $\beta \cos\theta$  along the y-axis, and the plot is called Williamson–Hall (W–H plot) plot. From the slope of the linear fit of the plot, the lattice strain can be derived. One representative W–H plot is shown in Fig. 3.4.

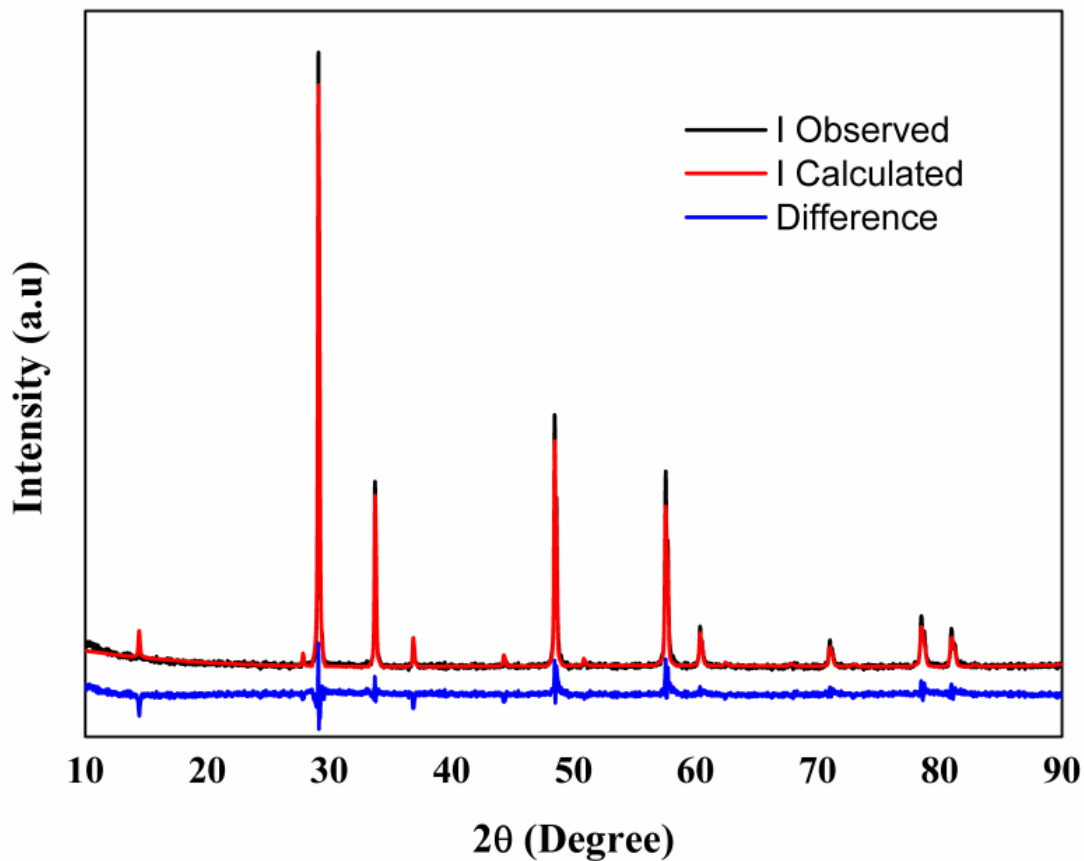


Fig. 3.3 Observed, calculated, and difference XRD profiles of  $Zr_1$  composition

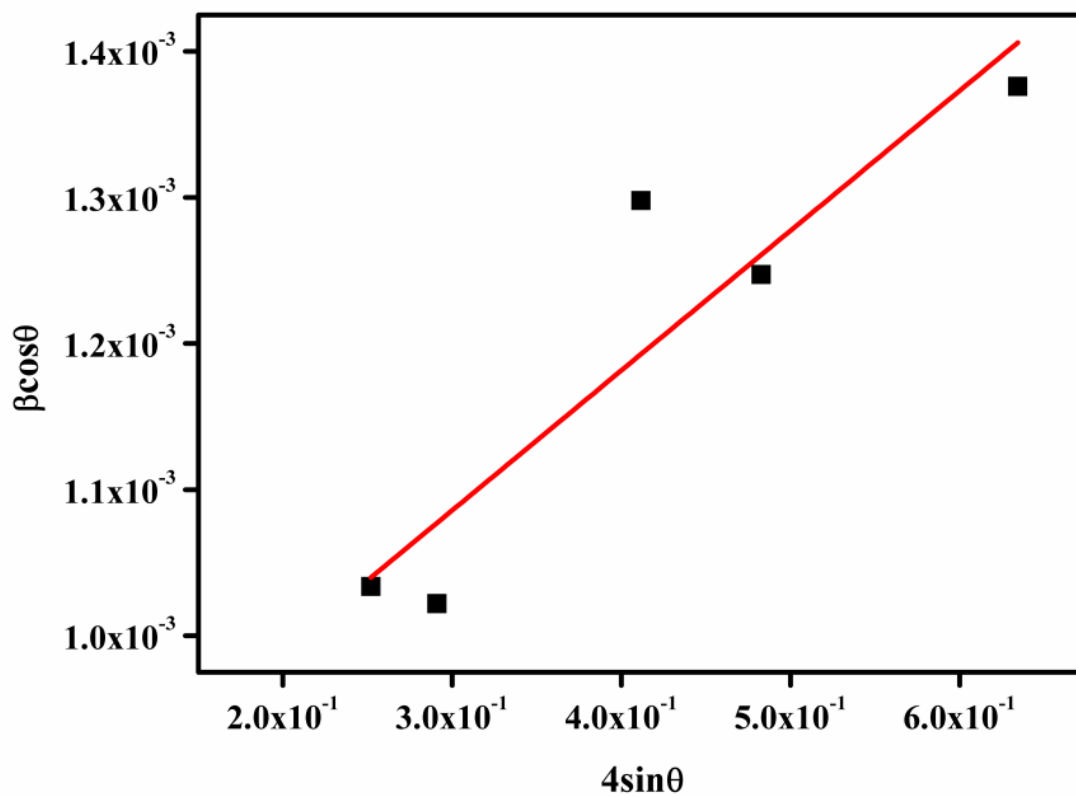


Fig. 3.4 W-H plot of one representative sample  $Zr_{1.75}$

**Table 3.2** The bond length of the compositions obtained from the Rietveld analysis and the lattice strain calculated using W-H plot

Compositions	Sm-O <sub>1</sub> (Å)	Sm-O <sub>2</sub> (Å)	Zr/Y/Nb-O <sub>1</sub> (Å)	Lattice Strain (%)
Zr <sub>2</sub>	2.535	2.289	2.088	0.07835
Zr <sub>1.75</sub>	2.530	2.291	2.095	0.07393
Zr <sub>1.5</sub>	2.552	2.293	2.084	0.142
Zr <sub>1.25</sub>	2.544	2.296	2.092	0.143
Zr <sub>1</sub>	2.525	2.297	2.108	0.144

The variation of the bond length of A-O<sub>1</sub>, A-O<sub>2</sub> and B-O<sub>1</sub> bonds and the  $x$  parameter of the compositions shows some abnormal variation with the substitution. Some of the earlier studies show that the A-O<sub>2</sub> bonds dependence only on the lattice parameter ( $a$ ) and the A-O<sub>1</sub> and the B-O<sub>1</sub> bonds depend on both the lattice parameter and the variable oxygen  $x$ -parameter (Kennedy *et al.* 1997). In this study also, the Sm-O<sub>2</sub> bond length increases with the lattice parameter. The  $48f$  oxygen  $x$  parameter varies from 0.3125 for a perfect octahedral of the BO<sub>6</sub> polyhedra to 0.375 for perfect cubic coordination for A, and an intermediate value is for distortion on both polyhedra (Chakoumakos 1984). For the pyrochlore structure, the distortion of the polyhedra around the B site cation is minor since all the B-O bonds are equal. However, the distortion of the A site polyhedra is significant (Gardner *et al.* 2010). The Y and Nb substitution ( $x = 0.25$ ) on the B site of the present compositions increase the B-O<sub>1</sub> bond length which is evident since the combined radius of the Y and Nb is higher than that of the Zr. Also, it shifts the AO<sub>8</sub> polyhedra towards perfect cubic coordination since the difference of the bond length decreases. That is the distortion of the AO<sub>8</sub> polyhedra decreases, and the distortion of the BO<sub>6</sub> octahedra increases, causing higher  $x$  value (Rittman *et al.* 2017). Also, the strain in the lattice is reduced due to the reduction of the distortion of the AO<sub>8</sub> polyhedra.

A study of co-doping of Y and Nb on the ZrO<sub>2</sub> shows that at low dopant concentration, it destabilises the cubic zirconia. However, at higher concentration, some ordering occurs among the cations, and it stabilises the zirconia and causes severe distortion to the surrounding cation network. Here also at  $x = 0.5$  doping with Y and Nb, the calculated strain on the pyrochlore lattice is very high, and the increased distortion occurs for both

$\text{AO}_8$  and  $\text{BO}_6$  polyhedra. Due to this, the  $x$  parameter of the system reduces to 0.336. Also at this composition the attained strain is maximum and after that increase in Y, and Nb concentration does not cause much more variation in the lattice strain. After this, the substitution merely acts as an isovalent cation with a higher ionic radius than that of the zirconium. It merely increases the cation disorder in the system by reducing the difference between  $\text{A-O}_1$  and  $\text{A-O}_2$  bond length and increase in the  $\text{B-O}_1$  bond length.

### 3.3.2 Raman spectroscopy studies

X-ray diffraction studies are much more sensitive to the disorder in the cationic sublattice in comparison to that of the anionic sublattice, whereas Raman spectroscopy is an excellent tool to determine the cation-anion vibrations and thus to identify the local disorder in the lattice (Advances in Solid Oxide Fuel Cells VI © WILEY). Glerup *et al.* (Glerup *et al.* 2001) used Raman spectroscopy as an effective tool to differentiate the ordered pyrochlore from disordered defect fluorite structure.

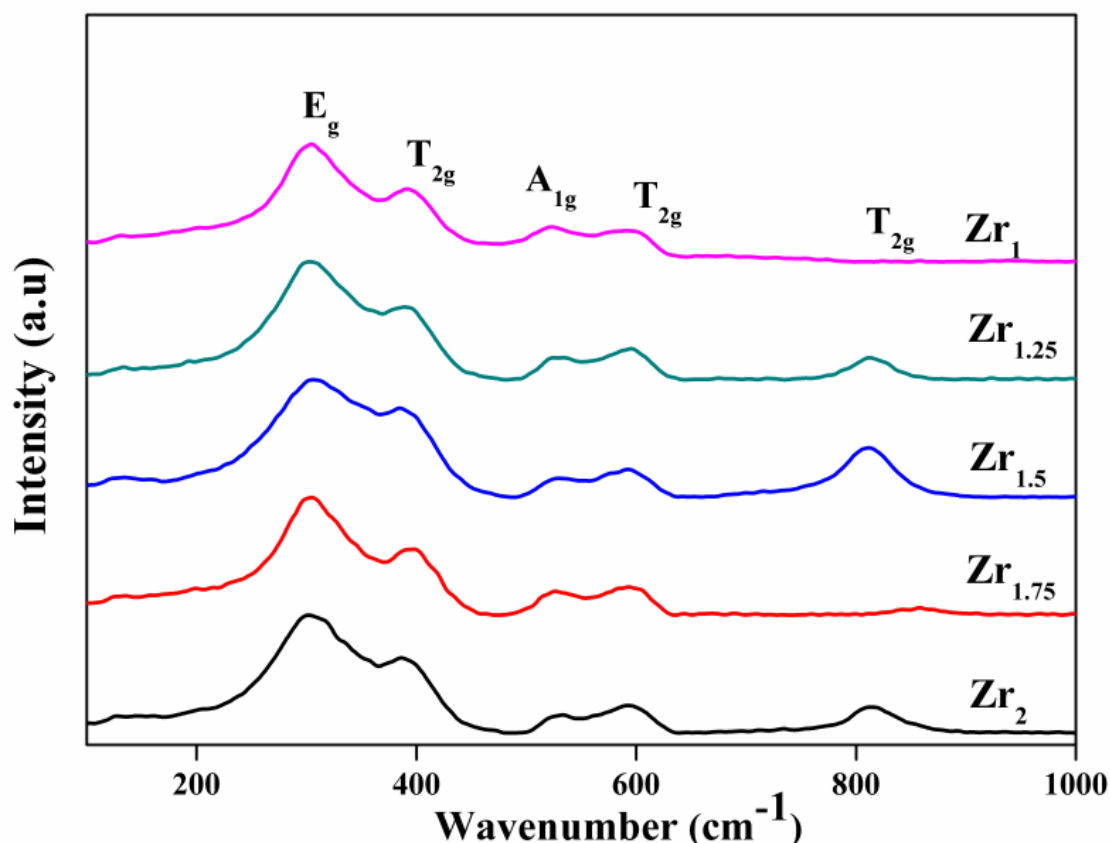


**Fig. 3.5** Raman spectrum of the  $\text{Sm}_2\text{Zr}_{2-x}(\text{Ynb})_{x/2}\text{O}_7$  ( $x = 0, 0.25, 0.5, 0.75, 1$ ) compositions.

The factor group for the cubic pyrochlore  $\text{A}_2\text{B}_2\text{O}_7$  which contain two molecular units in the unit cell is  $\text{O}_h$ . The site symmetry for the A and B cation is  $\text{D}_{3d}$ ,  $\text{C}_{2v}$  for the  $\text{O}_1$  anion



and  $T_d$  for the  $O_2$  anion (McCauley 1980). Factor group analysis of the pyrochlore crystal systems using the above assumptions predicted 26 vibrational modes, out of which only six are Raman active and the Raman active modes of vibration are (Rousseau *et al.* 1981; Vandendorre *et al.* 1983):

$$\Gamma = A_{1g} + E_g + 4T_{2g} \quad (3.6)$$

The Raman spectra of the samples are shown in Fig. 3.5. All the spectra show the characteristic modes of the pyrochlore system as reported in the literature (Qu *et al.* 2007; Singh *et al.* 2008) and this confirms the pyrochlore structure. Only five of the six Raman active modes of vibration are present in the figure. Other modes of vibrations are very weak in intensity and hence are not observable. The most intense peak on the  $\approx 300 \text{ cm}^{-1}$  corresponds to the  $E_g$  mode. The mode corresponding to the  $400 \text{ cm}^{-1}$  is  $T_{2g}$  mode that arises due to the  $8b$  site oxygen ion.  $A_{1g}$  mode appearing about  $525 \text{ cm}^{-1}$  correspond to O-B-O bending. The other two modes at around  $600 \text{ cm}^{-1}$  and  $800 \text{ cm}^{-1}$  are assigned to the  $T_{2g}$  mode corresponds to the  $48f$  oxygen vibration. However, the  $T_{2g}$  mode at  $800 \text{ cm}^{-1}$  shows distinct variation in intensity with the increasing of the B site substitution. On inspection, the appearance and intensity variation of this mode can be correlated to the oxygen  $x$ -parameter, which is more related to the distortion of the  $BO_6$  octahedra. To evaluate this, we have taken the ratio of the highest intensity mode around  $300 \text{ cm}^{-1}$  and the mode under observation.

The ratio of the intensity of the  $E_g$  Raman mode at  $\approx 300 \text{ cm}^{-1}$  ( $I_2$ ) and  $T_{2g}$  mode at  $800 \text{ cm}^{-1}$  ( $I_1$ ) is calculated and is shown in Fig. 3.6 along with oxygen  $x$ -parameter. As expected, this ratio goes in line with the oxygen  $x$ -parameter. This ratio is maximum for the higher concentration of substitution having the highest oxygen  $x$ -parameter that suggests higher amount of anion disorder. Hence anion disordering induces a transformation of the octahedral coordination of the B cation into more distorted octahedron. Further, it can be explained that as the distortion in the  $BO_6$  polyhedra increases, the anion disorder increases, which in turn increases the oxygen  $48f$   $x$ -parameter. However, the aliovalent substitution of Y and Nb on the B site does not show linear trend of anion disorder but dependant on the concentration. Hence Raman spectrum also supports the information obtained from the X-ray diffraction data. i.e., Y and Nb substitution on the B site of the pyrochlore structure first destabilises the crystal system and then stabilises the system.

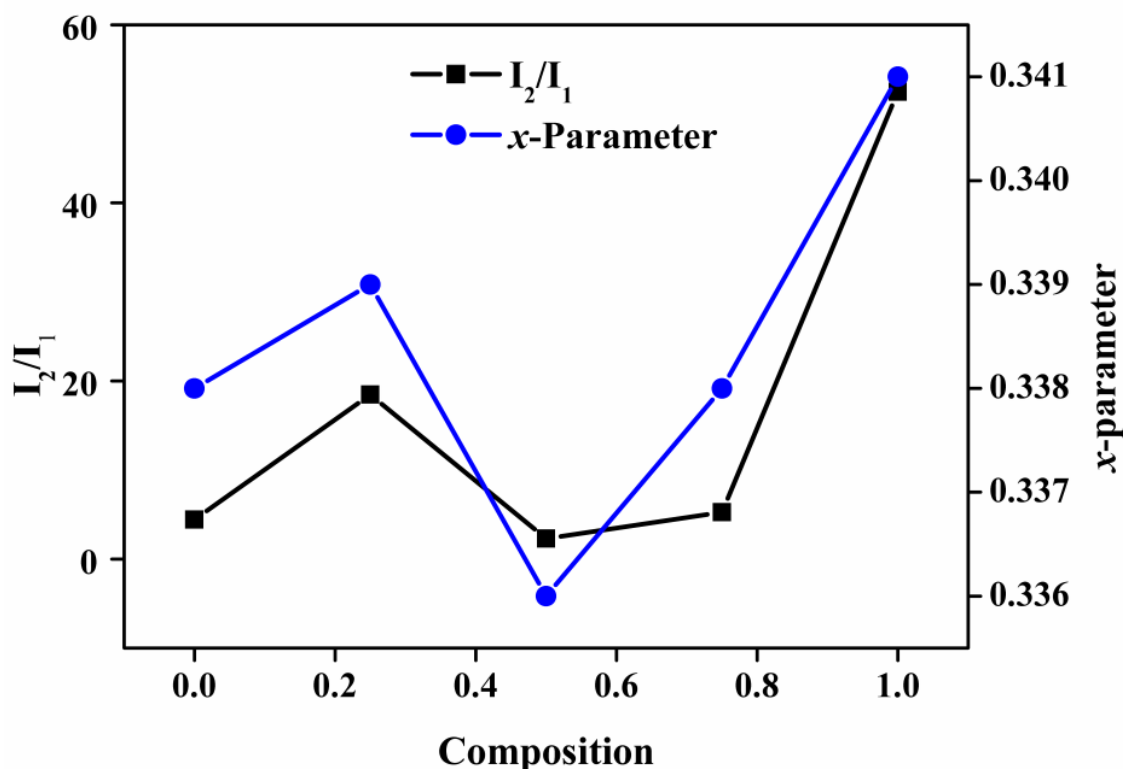


**Fig. 3.6** The ratio of the intensity of the  $E_g$  Raman mode at  $\approx 300 \text{ cm}^{-1}$  ( $I_2$ ) and  $T_{2g}$  mode at  $800 \text{ cm}^{-1}$  ( $I_1$ ) and  $48f$  oxygen  $x$  parameter of the compositions

### 3.3.3 Morphological Analysis

The morphology of the sintered samples was analysed using a scanning electron microscopic technique. The typical SEM images of the four samples are shown in fig. 3.7. The image shows clear grain boundaries with distinguishable grains. The grain size decreases as the substitution increases and attains a minimum size and then increases. The grain size can be related to the strain as the strain increases with decrease in grain size (Zhao and Zhang 2008). Therefore the SEM images also confirm the lattice strain is arising as a result of the Y and Nb substitution on the pyrochlore crystal system

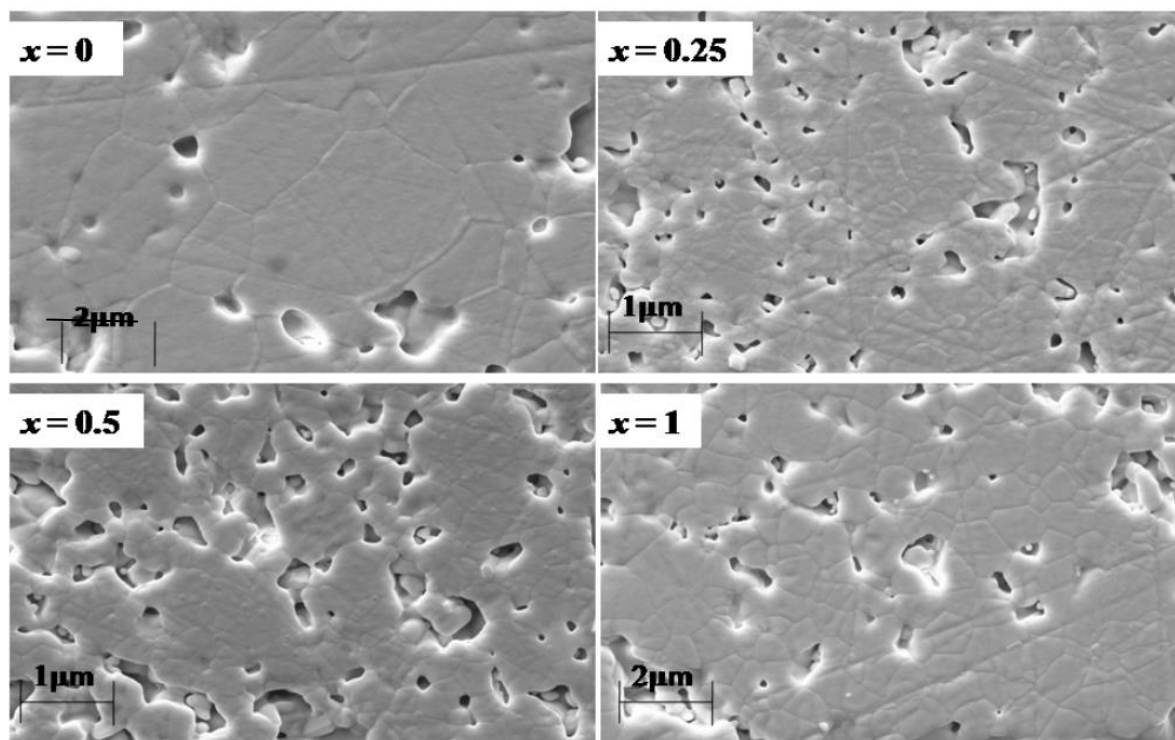


Fig. 3.7 Scanning electron microscopic images of the prepared compositions

### 3.3.4 Impedance spectroscopic studies

The electrical behaviour of the sintered samples of the prepared compositions subjected to an ac signal of 100 mV and frequency ranging from 1Hz to 1MHz was measured using two probe complex impedance spectroscopy. The impedance spectrum comprises of inductive, capacitive and resistive behaviour of the samples. In the case of a polycrystalline material, the system can be regarded as a series of RC circuits in which the resistor I deals with the conduction and the capacitor I is associated with the charge accumulation effects (Vaisakhan Thampi *et al.* 2015). The significance of the impedance spectroscopy lies in the fact that it can uniquely identify the individual reaction/ migration steps in a multistep process since each migration steps have a distinct time constant it can be easily separated in the frequency domain (Lai 2007). Thus in the case of polycrystalline sintered pellets, the impedance spectrum consists of three semicircles due to the impedance for the bulk (high-frequency spectrum), grain boundary (middle of the spectrum) and the electrode process (low-frequency arc). The conductivity measurements were done over a temperature range from 573K to 1023K.

The Nyquist plot impedance spectra of the  $Zr_1$  samples at different temperature are shown in Fig. 3.8a and Fig. 3.8b. For better analysis, the impedance variation of all the

samples at 873K is also shown in Fig. 3.8c. The figure here shows two semicircles which are contributed to the grain and grain boundaries of the system. As the temperature increases, the radius of the semicircles decreases, indicating increased conductivity. This can be due to the thermal agitation and increased hopping rate of the conducting ions (Anithakumari *et al.* 2016). Hence thermally activated conduction mechanism is confirmed. As mentioned in the previous work, here also there is a spike at the lowest frequency region, emerges as a result of the capacitance value for the blocking of the ionic charge carriers at the electrode interface (Abram *et al.* 2001; Renju *et al.* 2017).

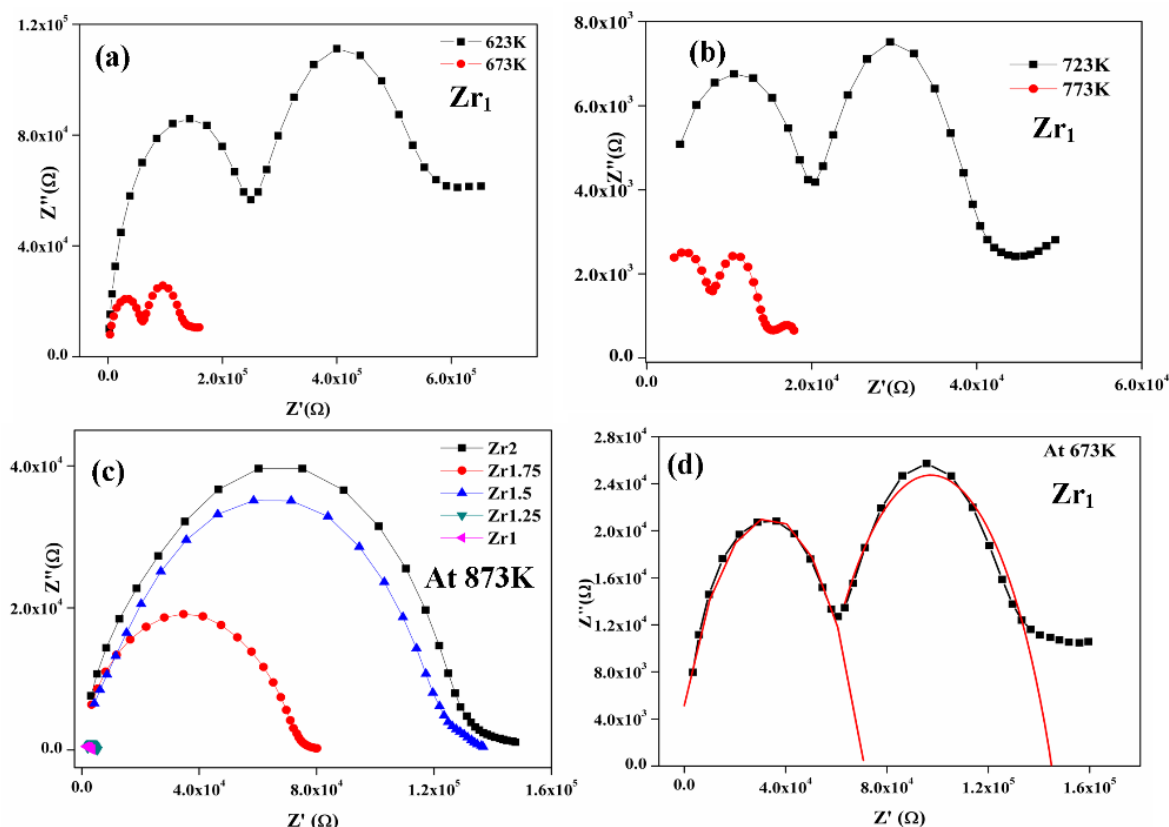


**Fig. 3.8** Cole-Cole plot of the representative  $Zr_1$  sample at different temperatures.

The total conductivity of the samples is calculated by extrapolating the semicircles to make an intercept with the x-axis, and this intercept is taken as the resistance  $l$  of the samples from which the conductivity can be calculated using the formula

$$\sigma = \frac{l}{RA} \quad (3.7)$$

where  $\sigma$  is the conductivity of the sample,  $l$  is the length, and  $A$  is the area of the sintered pellets whose conductivity is measured, and the method of semicircle fit is illustrated in the Fig. 3.8d. The temperature dependence of the samples was studied using the Arrhenius

equation for conductivity given by

$$\ln(\sigma T) = \ln(\sigma_0) - \frac{E_a}{kT} \quad (3.8)$$

The equation is the logarithmic form of the Arrhenius equation. Here the  $\sigma_0$  is the pre-exponential factor which is a measure of the concentration of the charge carriers in the samples,  $T$  is the temperature,  $E_a$  is the activation energy, and  $k$  is the Boltzmann constant. The linearly fitted Arrhenius plot of the samples is shown in Fig. 3.9

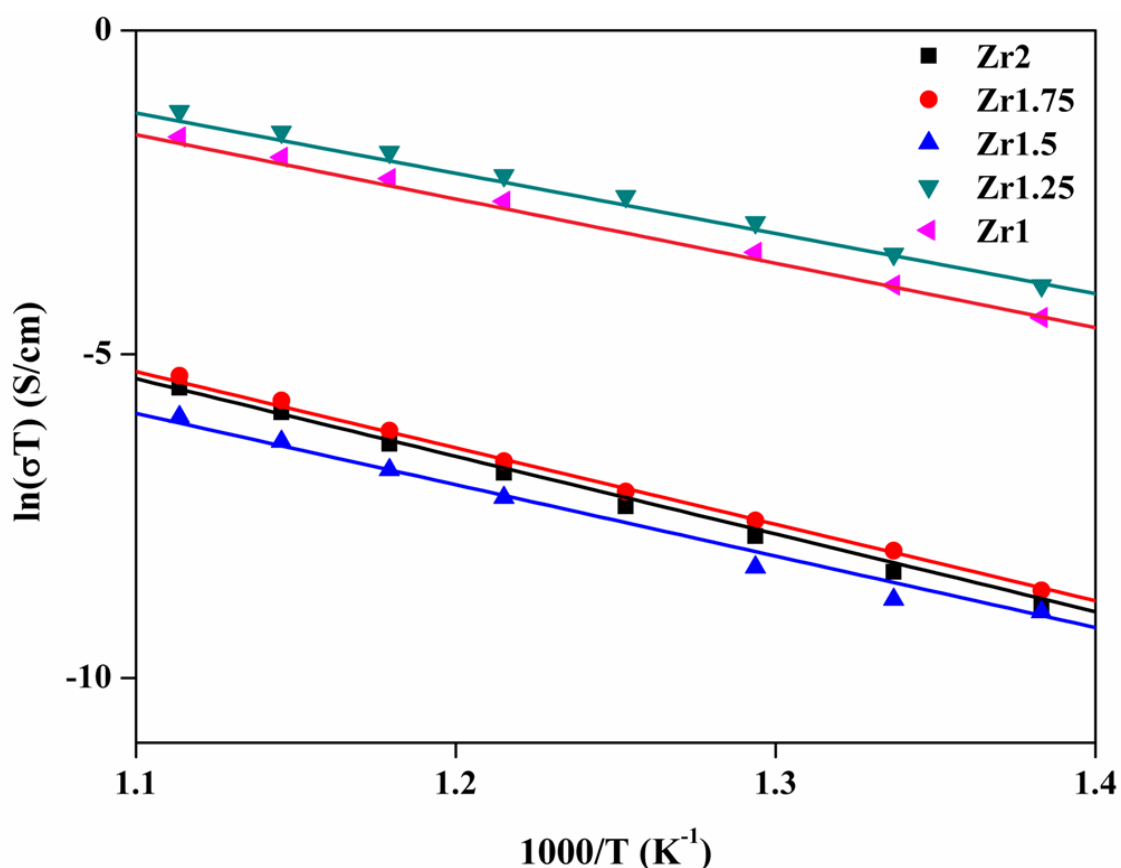


**Fig. 3.9** Arrhenius plot and the linear fit of the samples  $\text{Sm}_2\text{Zr}_{2-x}(\text{Ynb})_{x/2}\text{O}_7$  ( $x = 0, 0.25, 0.5, 0.75, 1$ ).

The linear behaviour of the Arrhenius plot supports for the thermally activated conduction. The slope and intercept of the graphs yield activation energy and the pre-exponential factor of the samples. The variation of the activation energy and pre-exponential factor and the conductivity of the samples with the composition are shown in Fig. 3.10. The conductivity of the samples at 1023K decreases with the substitution of trivalent and pentavalent ion on the B site of the  $\text{Sm}_2\text{Zr}_2\text{O}_7$  compositions up to  $x=0.5$  and further increases with the substitution. The variation of the conductivity with the Y and Nb substitution can be

explained based on the calculation of the activation energy and the pre-exponential constant.

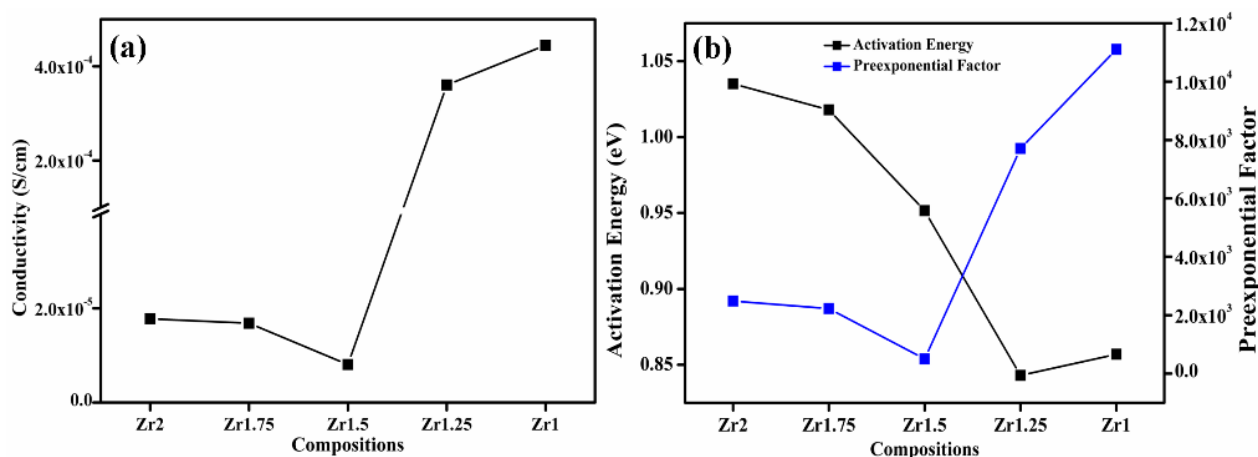


**Fig. 3.10** (a) Variation of total conductivity of the samples with the compositions

(b) Activation energy and pre-exponential factor of the compositions

Analysis of the figures reveals that the conductivity of the prepared samples goes in line with the pre-exponential factor of the samples. The Raman spectra analysis qualitatively quantified the anion disorder in the prepared compositions. The analysis conveys that the Zr<sub>1.5</sub> samples exhibit a much more ordered anion sublattice. Studies on anion disorder in the pyrochlore lattice shows that anion disorder involves in the generation of  $48f$  oxygen vacancies which in turn serves as the charge carriers in the pyrochlore lattice (Yu 1996). Thus the sample with highest anion disorder Zr<sub>1</sub> has the highest value for the pre-exponential factor. The study on the lattice strain reveals the crystal lattice having considerable strain has small activation energy for ion migration. The small activation energy of the lattice is explained by the additional driving force caused by the strain for ion migration because the ion migration process relaxes the lattice strain and thus reduces the free energy of the system (Zhao *et al.* 2017). The small increase in the activation energy of the Zr<sub>1</sub> composition arises due to the increased disorder in the anion lattice, which is confirmed by the X-ray diffraction and Raman spectrum analysis of the prepared compositions. Thus lattice strain and anion disorder in the pyrochlore crystal lattice can significantly influence the ionic conductivity in the lattice.

### 3.4 Conclusions

The  $\text{Sm}_2\text{Zr}_{2-x}(\text{Ynb})_{x/2}\text{O}_7$  ( $x = 0, 0.25, 0.5, 0.75, 1$ ) pyrochlore type compositions are prepared via solid-state reaction route and the structural, morphological and electrical characterisation of the compositions were done using X-ray diffraction, Raman spectrum, scanning electron microscopy and impedance spectroscopy. All the prepared samples are in pure phase and form in the pyrochlore crystal lattice. The lattice strain and oxygen x parameter calculation show that the Y and Nb initial substitution destabilise the pyrochlore system and then it stabilises the system just as the same doping stabilise the  $\text{ZrO}_2$  in earlier studies. The degree of anion disordering is confirmed by the Raman spectra of the samples. The oxide ion conductivity of the prepared compositions also shows that samples are strained and the conductivity decreases to a minimum value due to the decreased pre-exponential factor of the samples and then increases by order of magnitude to the maximum conductivity of  $4.44 \times 10^{-4}$  S/cm. In summary, the conductivity of  $\text{Sm}_2\text{Zr}_2\text{O}_7$  can be primarily influenced by the simultaneous aliovalent cation substitution on the B site through anion disorder and lattice strain.

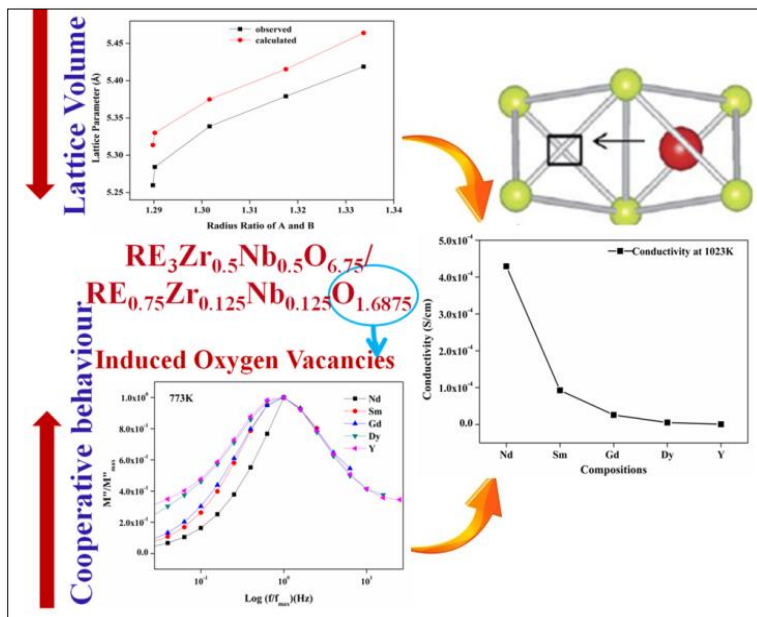




# Chapter 4

## Study of the Introduction of Oxygen Vacancies to the Pyrochlore Type Compositions and its Influence on the Electrical Properties

Anion deficient pyrochlore type compositions were synthesised and analysed in this work. All the compositions prepared via the conventional solid-state reaction method have the defect fluorite structure. The modulus spectrum analysis shows that as the lattice volume decreases the cooperative behaviour of the oxide ions increases, which causes an



increase in activation energy. The increase in activation energy occurs rapidly and thus, the conductivity also decreases. Thus in such cases of systems having high charge oxygen vacancies, the cooperative behaviour among the ions increases and it is further increased by decrease in the lattice

volume.



## 4.1 Introduction

Solid oxide ion conductors have always been the centre of attraction of researchers due to its various practical applications such as in solid oxide fuel cells for generating the electrical power, oxygen separation membranes, membranes which convert methane to syngas and the behaviour of these compositions are tunable by controlling structural and synthetic parameters (Anithakumari *et al.* 2016; Skinner and Kilner 2003). A good oxide ion conductors require partial occupancy of the energetically equivalent sites of oxide ions and lesser activation energy (Goodenough 2000). Oxygen vacancies for oxide ion transport in this material are introduced in two ways: one is to select the crystal systems having intrinsic anion vacancies, and the other is to substitute the compositions with lower valent cation (Goodenough 2000). Therefore the available oxide ion conductors are confined to a small group of oxides which are mainly related to fluorite structure (Lacerda *et al.* 1988).

Pyrochlore oxide ion conductors are an essential class of materials which finds significant application in the field of oxide ion conductivity, dielectrics, magnetic materials multiferroic materials and superconductivity (Gomez-Perez *et al.* 2015). These oxide materials are derivative of basic fluorite structure and possess intrinsic oxygen vacancies. Pyrochlore structure has general formula  $A_2B_2O_7$  belongs to the space group  $Fd-3m$  ( $a \approx 10\text{\AA}$ ,  $Z = 4$ ) whereas the fluorite has general formula  $AO_2$  structure belongs  $Fm3m$  ( $a \approx 5\text{\AA}$ ,  $Z = 4$ ). The fluorite structure has an fcc array of the cation in which all the tetrahedral interstices are occupied by the anions. Pyrochlore structured compositions are retained its fcc array of the cation in non-equivalent sites. Furthermore, anions are located in the tetrahedral interstices just as in the fluorite structured compositions but in two non-equivalent independent sites (Maczka *et al.* 2018). In addition to these two anion sites, there is an additional anion site which is vacant in the pyrochlore structure which makes pyrochlore structured compositions a better candidate as the oxide ion conductors. The A cations in the pyrochlore compositions are eight coordinated and located at  $16d$ , and the B cations which is six coordinated occupies the Wyckoff position  $16c$  taking the B cations at the origin. The anions are at  $48f$  and  $8b$  Wyckoff positions. The additional oxygen vacancy is at  $8c$

(Yang *et al.* 2015). In fluorite structured compositions the cations occupy  $4a$  and anions are at  $8c$  positions. The determination of the structure of these type of compositions mainly depends on the radius ratio of the compositions ( it is in between 1.46 to 1.78) (Subramanian *et al.* 1983) and these compositions often exhibit phase transformation from

ordered pyrochlore to more disordered defect fluorite structure. This phase transformation depends on the compositions, calcination temperature, the pressure applied and ion irradiation.

Pyrochlore zirconates whose structure is either pyrochlore or defect fluorite can be treated as an ideal candidate for the application in the field of oxide ionic conductors since these are treated as an extension of stabilised zirconia which is the currently using as the solid electrolytes in solid oxide fuel cell (Govindan Kutty *et al.* 1995; Zhang *et al.* 2017). In the case of lanthanide zirconates, the zirconates with lesser atomic number than Gadolinium forms into pyrochlore structure and others are in the fluorite structure and the transition temperature of these oxides from pyrochlore to defect fluorite decreases as the ionic radius of the lanthanides decreases (Blanchard *et al.* 2012). Study on the activation energy for  $O_{48f} \rightarrow O_{48f}$  conduction mechanism in  $Gd_2Ti_2O_7$  and  $Gd_2Zr_2O_7$  revealed that a small amount of cation antisite defects on pyrochlore zirconates creates a more tranquil path for oxide ion migration (Gunn *et al.* 2012). The long range migration of the ions through the lattice results in a conductivity given by

$$\sigma_T = \sigma_0 \exp\left(\frac{-E_a}{kT}\right) \quad (4.1)$$

where  $\sigma_0$  is the pre-exponential factor, and  $E_a$  is the activation energy. On analysing the equation, it is seen that the conductivity can be increased by increasing  $\sigma_0$  and decreasing the activation energy. However, the increase in the pre-exponential factor causes an undesired increase in the activation energy and thus limits the oxide ion conductivity (Chadwick 2000). This increase in the activation energy is the result of the increased cooperativity among the oxide ions and thus increases the activation energy for the long-range conduction in the lattice (Moreno *et al.* 2005). In addition to the concentration of vacancies and the activation energy, the cooperative behaviour of the oxides ions plays a crucial role in determining the ionic conductivity (Moreno *et al.* 2005, 2009; Vaisakhan Thampi *et al.* 2015).

Here in this study, a new series of pyrochlore type compositions are prepared in which the oxygen vacancies are introduced to the system by aliovalent and non-stoichiometric substitution on the B site of the compositions. In our previous work, we have studied the effects of aliovalent cation at the B site with preserved oxygen stoichiometry, and it revealed some remarkable results (Renju *et al.* 2017). The literature studies on this subject reveal that anti-site disorder in the pyrochlore type compositions favours oxygen disorder and the

disordering of the oxygen increases the oxygen ionic conductivity (Wuensch *et al.* 2000). So here in this work, we have studied non-stoichiometric pyrochlore type composition with excess oxygen vacancies and thereby an understanding of the increased cooperative behaviour of the oxide ions and its variation with the lattice volume can be done.

## 4.2 Experimental

Powder samples of the compositions  $\text{RE}_3\text{Zr}_{0.5}\text{Nb}_{0.5}\text{O}_{6.75}$  (RE = Nd, Sm, Gd, Dy, Y) were prepared via a solid-state reaction method. The starting materials used are  $\text{Nd}_2\text{O}_3$  (Sigma Aldrich 99.9%)  $\text{Sm}_2\text{O}_3$  (Alfa Aesar 99.998%),  $\text{Gd}_2\text{O}_3$ ,  $\text{Dy}_2\text{O}_3$ ,  $\text{Y}_2\text{O}_3$  (Sigma Aldrich 99.9%),  $\text{ZrO}_2$  (Aldrich 99%) and  $\text{Nb}_2\text{O}_5$  (99.99%). The mentioned chemicals are weighed stoichiometrically and mixed in agate using acetone as the medium. The mixed composition is dried in an oven at a temperature of 373K. The process is repeated thrice to make a uniform mixture. The mixed powder is then calcined at 1573K for 6h. The calcined samples are recalined at 1673K for 6h with intermittent grinding. The prepared powder is uniaxially pressed to make green cylindrical pellets, compaction at 25Mpa. These cylindrical pellets are sintered at 1823K for 18h.

The crystal structure of the prepared samples is analysed using X-ray powder diffractometer (X'pert Pro, Analytical). The analysis was carried out on a two theta range of 10-90° using  $\text{CuK}\alpha$  X-ray radiation of wavelength 1.5406Å. Rietveld refinement of the X-ray diffraction spectrum was done on the X'pert high score plus software. Further structural analysis was employed using the Raman Spectroscopy. Raman spectroscopic measurements were carried out in a Renishaw InVia Raman microscope with a laser beam directed to the sample through 50× and 20× objective lens and a Peltier cooled charge-coupled device (CCD) detector. Samples were excited with a 532 nm excitation wavelength laser, and Stokes shifted Raman spectra were collected with  $1\text{ cm}^{-1}$  resolution. Before every measurement, a calibration with a silicon standard (Raman peak centred at  $520\text{ cm}^{-1}$ ) was performed. WiRE 3.2 software package was used for data acquisition. The surface morphology of the sintered pellet was pictured via electron microscopic imaging using a scanning electron microscope (JEOL, JSM-5600L). The electrical characterisation of the samples were done by electroding the sintered pellets with high temperature curing silver paste then cured at 600°C for 30 min. Impedance analyser (Solatron SI 1260) with a dielectric interface (Solatron 1296) is used to study the electrical properties of the 91 ctahedra pellets, and the study is done in the temperature range of 473-1023K within the frequency range of 1MHz to 1Hz.

### 4.3 Results and Discussion

The compositions  $RE_3Zr_{0.5}Nb_{0.5}O_{6.75}$  (RE = Nd, Sm, Gd, Dy and Y) will be labelled as REZN (NdZN, SmZN, GdZN, DyZN and YZN ) throughout the paper.

#### 4.3.1. X-ray diffraction studies

Fig. 4.1 shows the powder X-ray diffraction patterns of the prepared series of compositions. All the compositions are in the fluorite structure, and the peaks are indexed to the fluorite structure. The radius ratio of these compositions is below 1.34, and the compositions are in the fluorite structure as expected. The ionic radius of the ions used and the radius ratio is shown in Table 4.1. In the fluorite structured compositions, each cation is in tetrahedral coordination with four oxide ions, and the Wyckoff position of each cation and anions are  $4a$  (0,0,0) and  $8c$  (0.25,0.25,0.25) respectively. As the ionic radius of the lanthanide cations in the compositions decreases, there is a shift of the intense peak (111) in the X-ray diffraction pattern towards the higher angle, which further indicates a decrease in the lattice parameter is visible.

**Table 4.1:** Ionic radii and radius ratio of the prepared compositions

	RE( $R_A$ )	$R_B$ ( $\text{\AA}$ )				$R_A/R_B$
	$\text{\AA}$	RE	Zr	Nb	$R_B$ ( $\text{\AA}$ )	
NdZN	1.109	0.983	0.72	0.64	0.8315	1.3337
SmZN	1.079	0.958	0.72	0.64	0.819	1.3175
GdZN	1.053	0.938	0.72	0.64	0.809	1.3016
DyZN	1.027	0.912	0.72	0.64	0.796	1.2902
YZN	1.019	0.900	0.72	0.64	0.790	1.2898

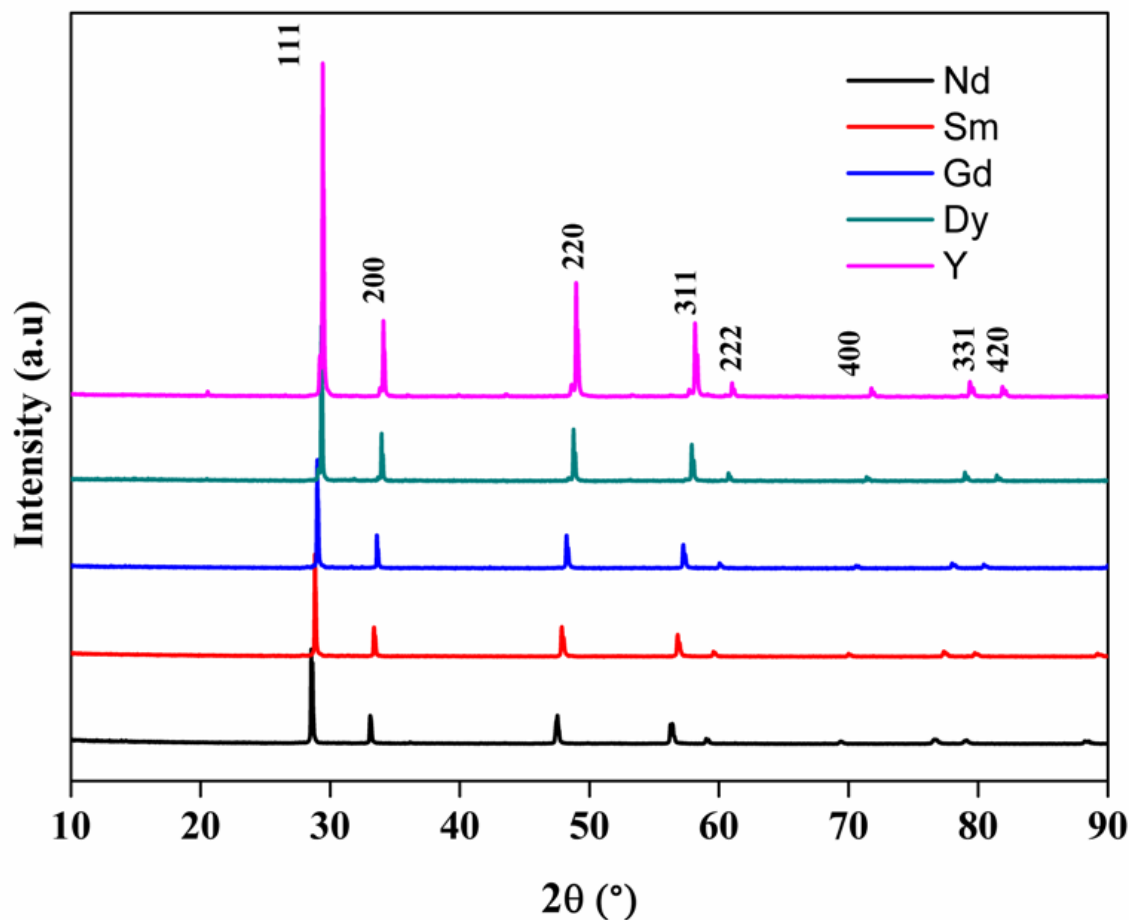
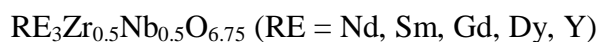


**Fig. 4.1** The powder X-ray diffraction patterns of the prepared compositions



The more detailed structural analysis of the XRD pattern was done by the Rietveld analysis using the commercially available X'pert Highscore plus software. The refinement was done by assuming the fluorite structure for all the compositions. The site of occupancy of all the compositions was deduced from converting  $\text{RE}_3\text{Zr}_{0.5}\text{Nb}_{0.5}\text{O}_{6.75}$  to  $\text{RE}_{0.75}\text{Zr}_{0.125}\text{Nb}_{0.125}\text{O}_{1.675}$ . The fitting function used for the peaks is Pseudo-Voigt profile function. The Caglioti parameters, flat background and two background function coefficients were refined for obtaining a better match between the observed and the calculated XRD pattern. The results of the Rietveld refinement of all the compositions are given in Table 4.2, and the fitted pattern is shown in Fig. 4.2. The variation of the lattice parameter (deduced from the refinement) with the lanthanide ions is shown in Fig. 4.3. As expected, the lattice parameter of the composition decreases following Vegard's law (Vegard 1921).

Table 4.2 The Rietveld refinement results

	NdZN	SmZN	GdZN	DyZN	YZN
<b>Unit cell</b>	Cubic	Cubic	Cubic	Cubic	Cubic
<b>Space group</b>	Fm3m	Fm3m	Fm3m	Fm3m	Fm3m
<b>Scale factor</b>	0.000207	0.000112	0.000138	0.000406	0.000382
<b>Lattice</b>					
<b>parameter</b>	5.4188(2)	5.3790(1)	5.33870(9)	5.28428(7)	5.25980(9)
(Å)					
<b>Rp(%)</b>	9.41662	6.52322	4.58162	4.48375	8.59268
<b>Rexp(%)</b>	7.84612	6.61146	5.15993	4.63807	5.02230
<b>Rwp(%)</b>	12.08039	8.75227	6.12275	6.49887	14.16575
<b>GOF</b>	2.37057	1.75246	1.40800	1.96336	1.95561

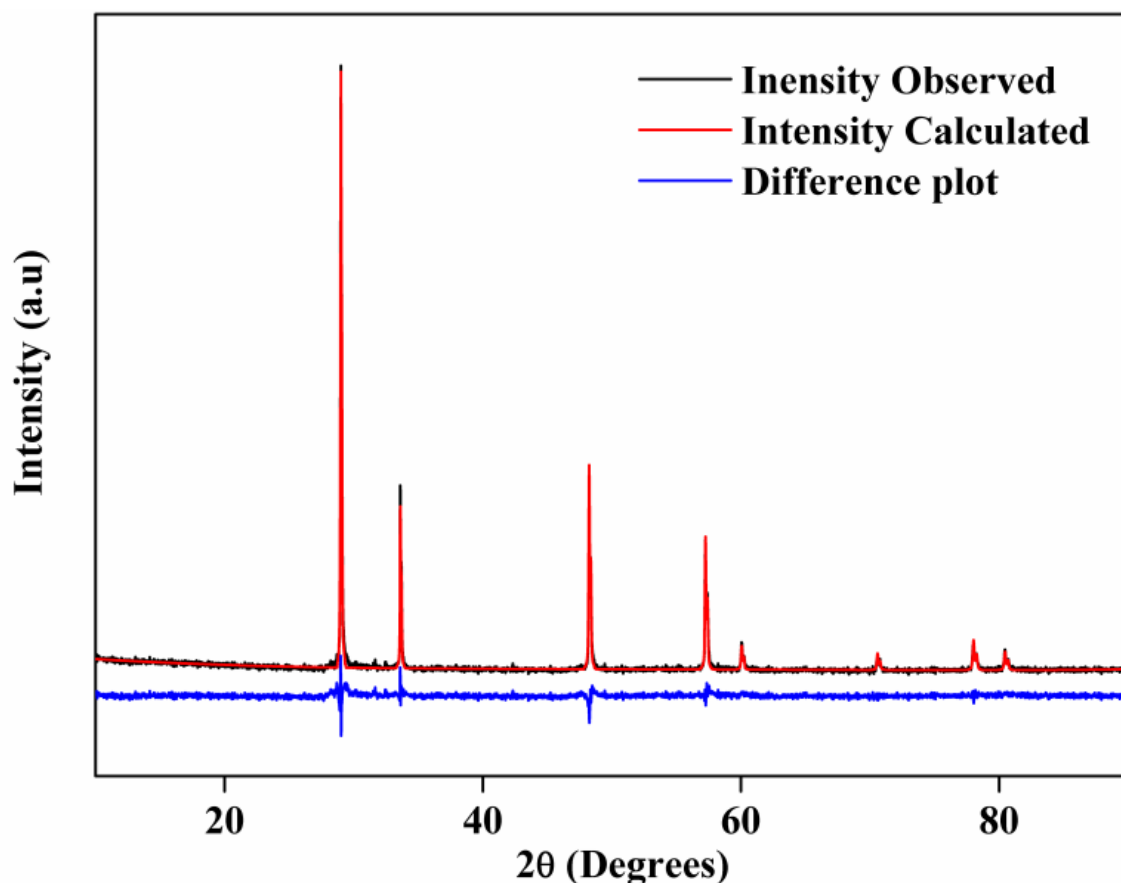


Fig. 4.2 The graphical output of the Rietveld refinement of the XRD

Fig. 4.3 shows the variation of the lattice parameter with the radius ratio of A and B cation. In the figure, the lattice parameter calculated using equation 4.2 is also shown (Mouta



*et al.* 2013). The lattice parameter shows a sharp decrease in the lattice parameter and the similar decrease in the calculated value shows that the sudden variation arises merely due to the ionic radius of the lanthanides cation in the system. The difference between the observed and calculated lattice parameter remains constant. The explanation for the difference in the observed and calculated parameter is that the calculation of the lattice parameter using equation 4.2 does not account the oxygen vacancies and the disorder in the lattice, and the constant difference indicates that same type of the defects are occurring in all the compositions.

$$a = \frac{8}{3^{\frac{1}{2}}} \left[ 1.43373(R_A + R_O) - 0.42931 \left( \frac{(R_A + R_O)^2}{(R_B + R_A)} \right) \right] \quad (4.2)$$

Here  $R_A$ ,  $R_B$  and  $R_O$  are the ionic radii of the A, B and O ions.

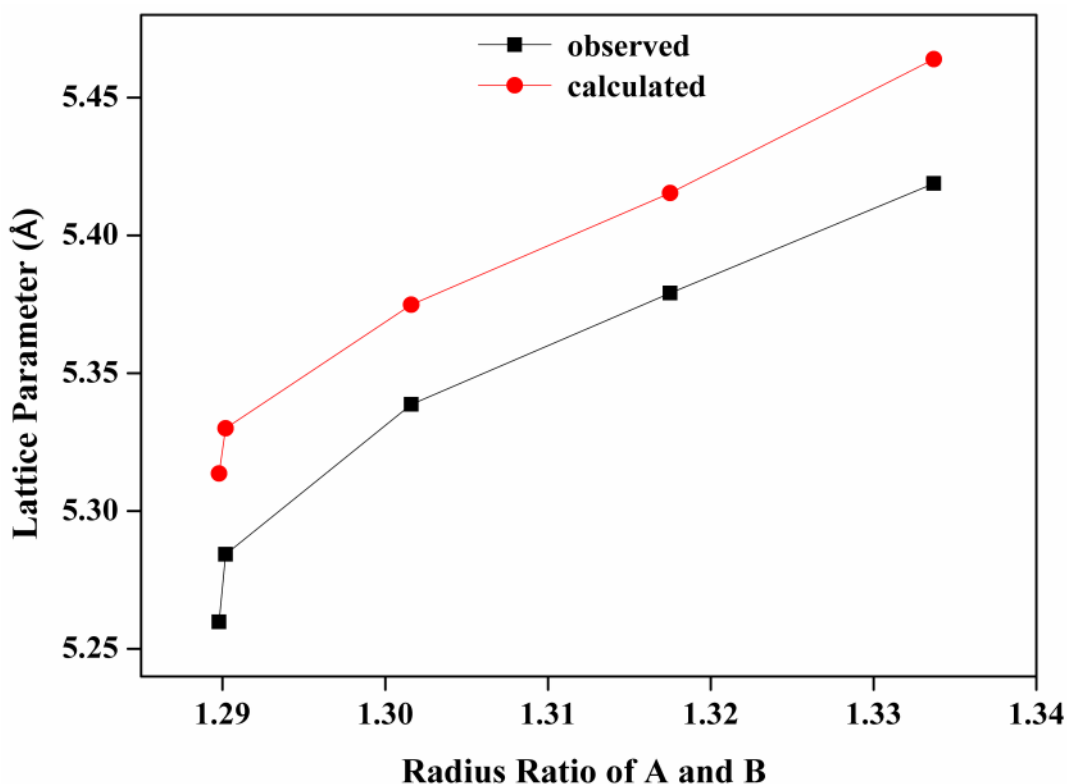
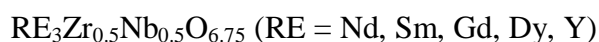


**Fig. 4.3** Variation lattice parameter of the compositions



#### 4.3.2. Raman spectroscopic analysis

For further analysis of the structure of the prepared compositions, the Raman spectra were recorded. The Raman spectra of the prepared compositions are shown in Fig. 4.4. In the cubic fluorite structure, the  $4a$  site in which the cation is occupied has a site symmetry  $O_h$  and

8c has a site symmetry  $T_d$ . According to the Factor group analysis, the ideal fluorite structure has only one Raman active mode  $T_{2g}$ , which is active around  $470\text{cm}^{-1}$  (Vaisakhan Thampi *et al.* 2015).

The spectra in Fig. 4.4 show two peaks around  $360\text{cm}^{-1}$  and  $800\text{cm}^{-1}$ . The observed peaks are very broad. The broad nature is the result of the inherent deviation of the translational periodicity in the lattice of the disordered fluorite structure (Mandal *et al.* 2007; Moriga *et al.* 1990; Wan *et al.* 2011). The additional peak in the Raman spectra indicates a deviation from the fluorite structure. The crystal system has an additional ordering in the lattice due to the presence of different cations in the same crystal lattice. The peak around  $800\text{cm}^{-1}$  arises due to the seven coordinated cations, and it confirms the defect fluorite (Rittman *et al.* 2017). The wavenumber shift towards the higher wavenumber, indicating a decrease in the lattice parameter. A decrease in the lattice parameters indicates a hardening of the bonds in the crystal systems, and it causes an increase in the phonon energy. Thus the shift in the Raman peaks is in line with the decrease of lattice parameter from the XRD.

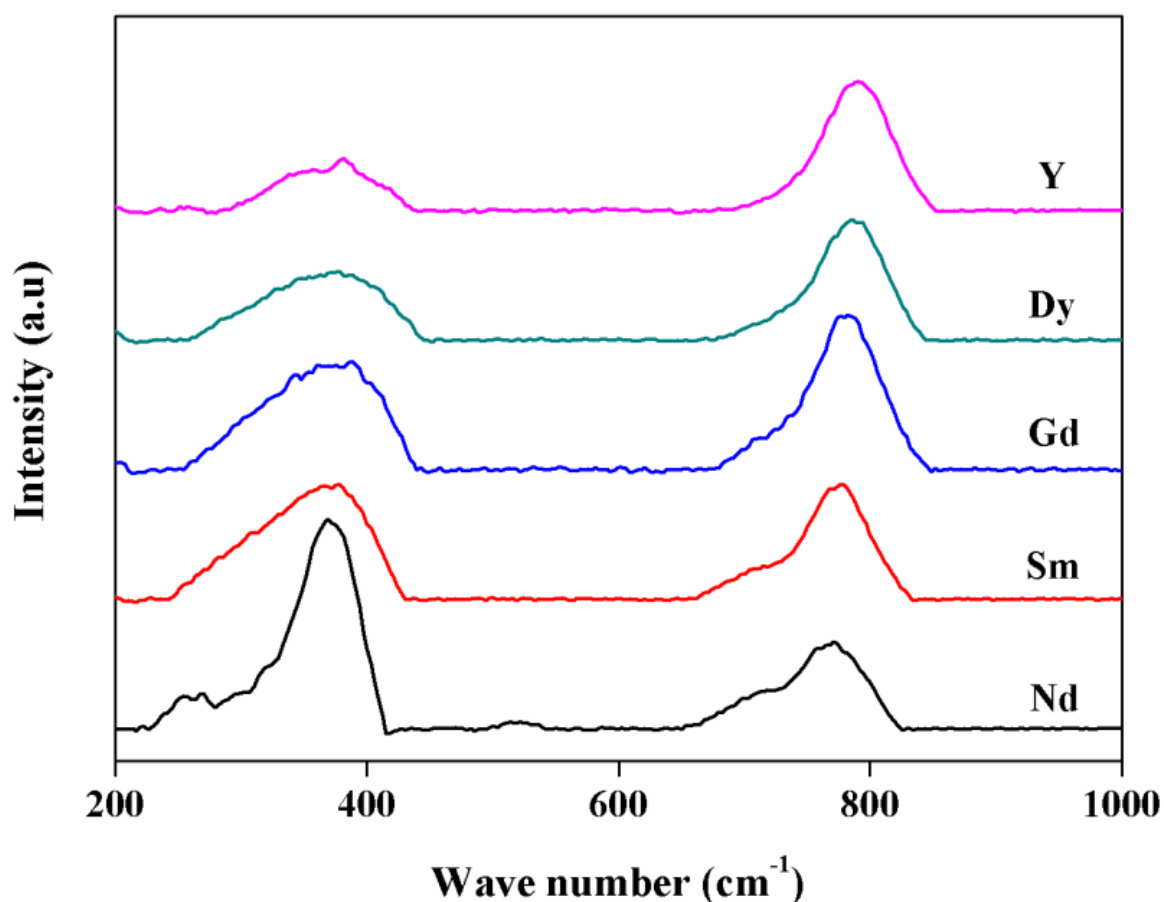


**Fig. 4.4** Raman spectra of the compositions  $\text{RE}_3\text{Zr}_{0.5}\text{Nb}_{0.5}\text{O}_{6.75}$  (RE = Nd, Sm, Gd, Dy, Y)

The peaks broaden as the ionic radius of the substituent ions decreases, which indicates increased disorder in the lattice. The radius ratio  $R_A/R_B$  is a measure for disorder in the disordered fluorite lattice. In the present study, the ratio ranges from 1.33 to 1.29, i.e. as the ionic radius of the substituent ions decreases the disorder in the compositions decreases. Thus the XRD results and Raman spectra confirm the defect fluorite structure of the prepared compositions.

#### 4.3.3. Surface morphological studies

The surface morphology of the sintered pellets was pictured using the scanning electron microscopy. The scanning electron microscopic images of the pellets are shown in Fig. 4.5. The figure shows an improvement in the grain structure as the ions goes from Nd to Dy.

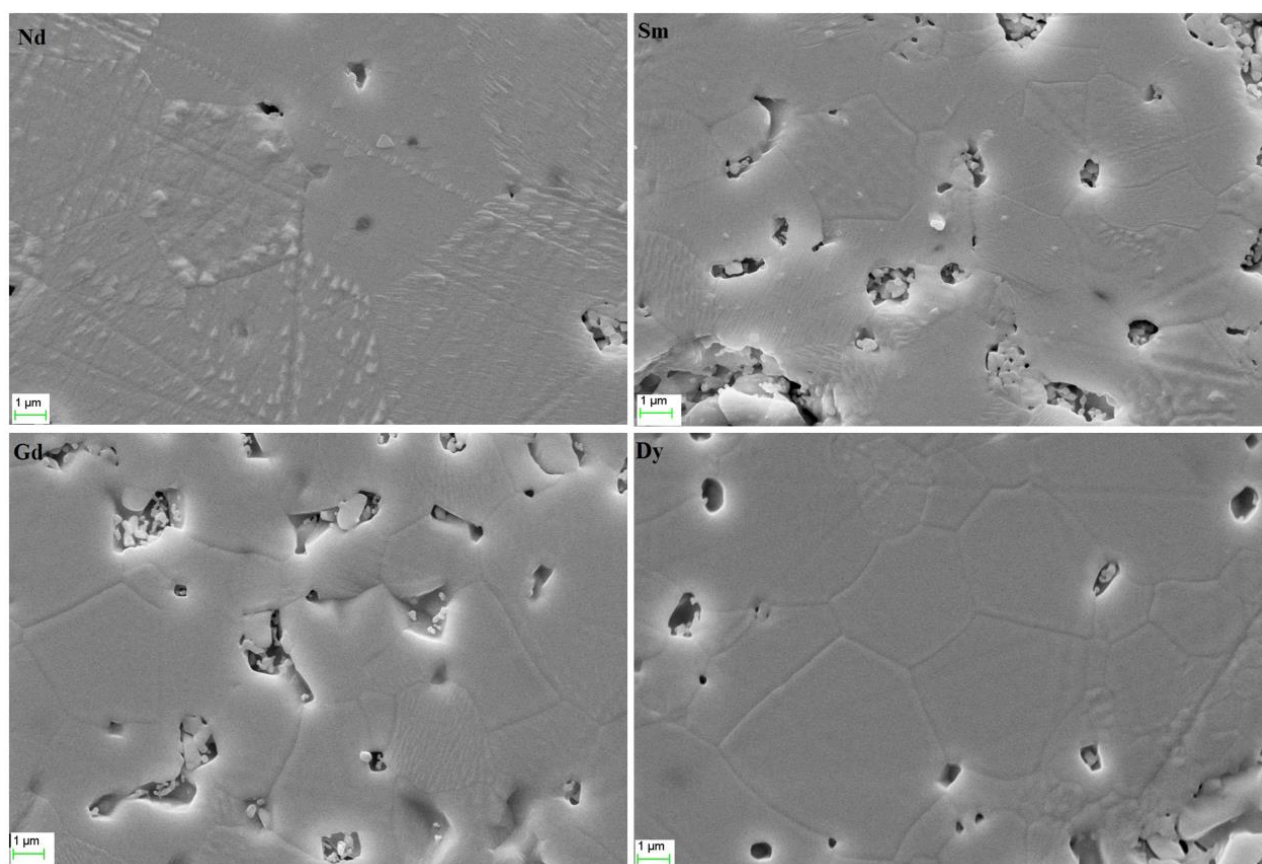


**Fig. 4.5** The scanning electron microscopic images of the prepared compositions



#### 4.3.4. Electrical Properties

The electrical properties of the sintered pellets were recorded using the impedance analyser by giving the pellets a small ac signal of 100mV with varying frequency from 1MHz

to 1Hz. The measurements were done in the temperature range from room temperature to 1023K. In the case of polycrystalline samples, the Nyquist plot contains three semi-circles, corresponding to bulk contribution from grains at the higher frequency; second one corresponding to the grain boundary and the last one at the lower frequency corresponds to the electrode-electrolyte interfaces.

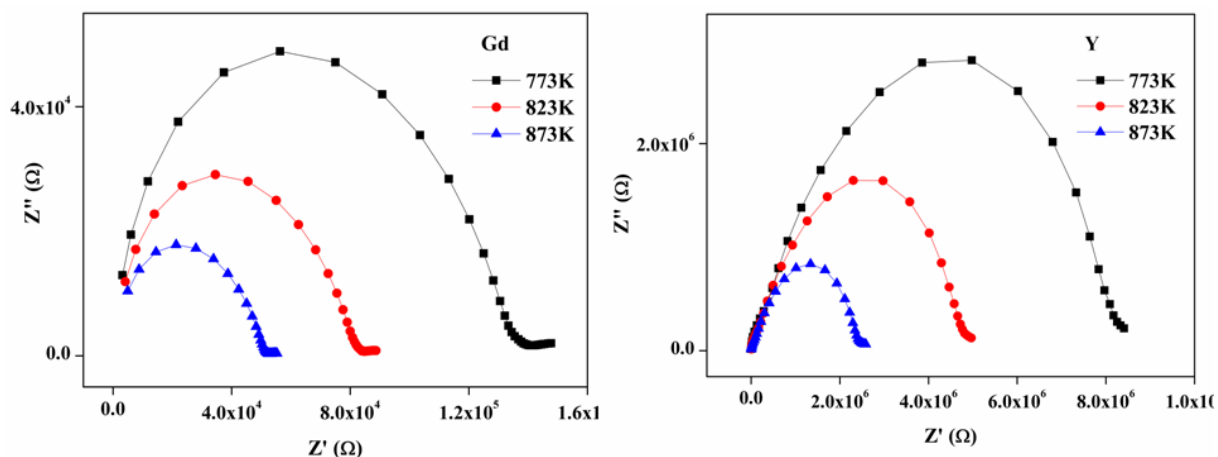


**Fig. 4.6** The Nyquist plot of the representative composition  $Gd_3Zr_{0.5}Nb_{0.5}O_{6.75}$  and  $Y_3Zr_{0.5}Nb_{0.5}O_{6.75}$

Fig. 4.6 shows the Cole-Cole plot of the representative samples  $Gd_3Zr_{0.5}Nb_{0.5}O_{6.75}$  and  $Y_3Zr_{0.5}Nb_{0.5}O_{6.75}$ . The figure shows a spike-like structure at the low frequencies and the peaks are due to the blocking effect of the electrode-electrolyte interface (Barsoukov and Macdonald 2005). The blocking resistance at the electrolyte electrode interfaces proves that the conduction in these samples is due to ions. The resistance of the samples is calculated from the Cole-Cole plot by fitting semicircles and then extrapolating to meet the x-axis, and the x value corresponding to the intersection gives the resistance of the samples. The conductivity of the samples is calculated from the resistance using the formula

$$\sigma = \frac{l}{RA} \quad (4.3)$$

where  $l$  the height of the cylindrical pellets is,  $R$  is the resistance obtained from the Nyquist plot, and  $A$  is the area of the cylindrical pellets. The variation of the conductivity with the ionic radius of the lanthanide cations is shown in Fig. 4.7.

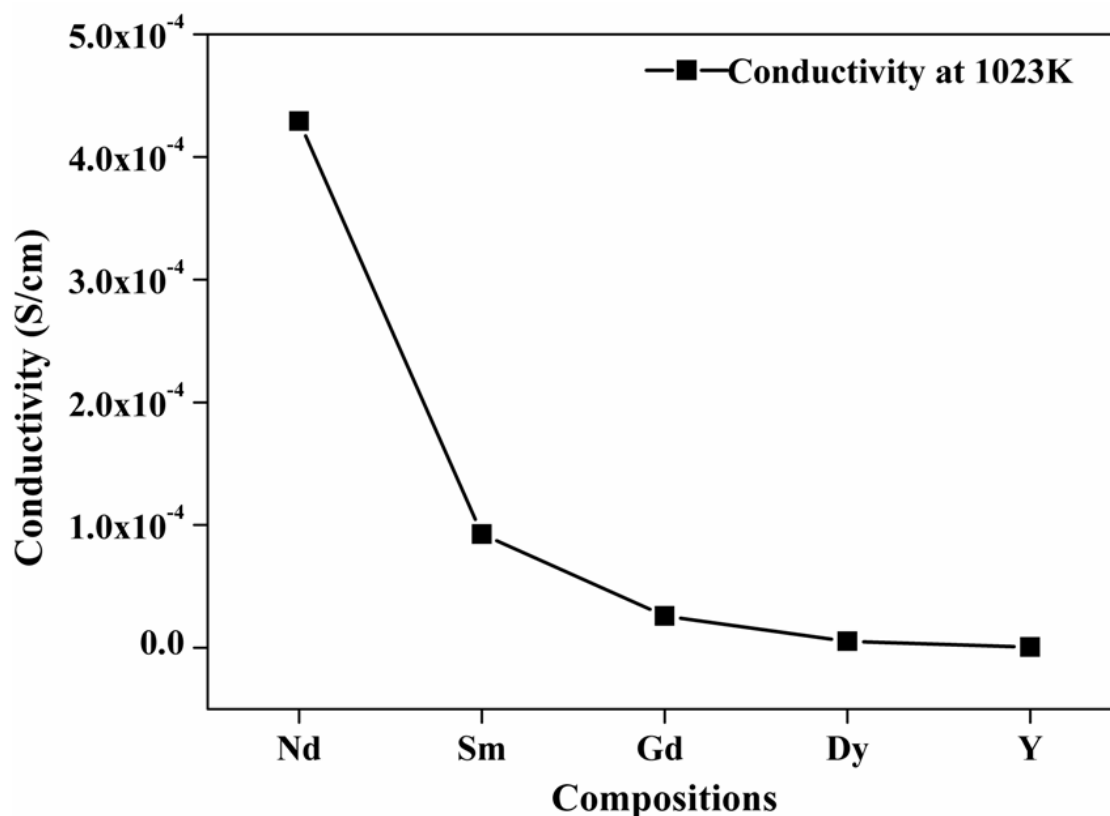


Fig. 4.7 The conductivity of the prepared compositions at 1023K

The conductivity of the compositions decreases as the ionic radius of lanthanide ions decreases. Fig. 4.8 shows the temperature dependence of the conductivity and the lines are linearly fitted using Arrhenius equation given below.

$$\sigma = \sigma_0 \exp\left(\frac{-E_{dc}}{KT}\right) \quad (4.4)$$

The figure shows that the conduction is thermally activated. Activation energy can be calculated from the slope of the linear fit in the Fig. 4.8.

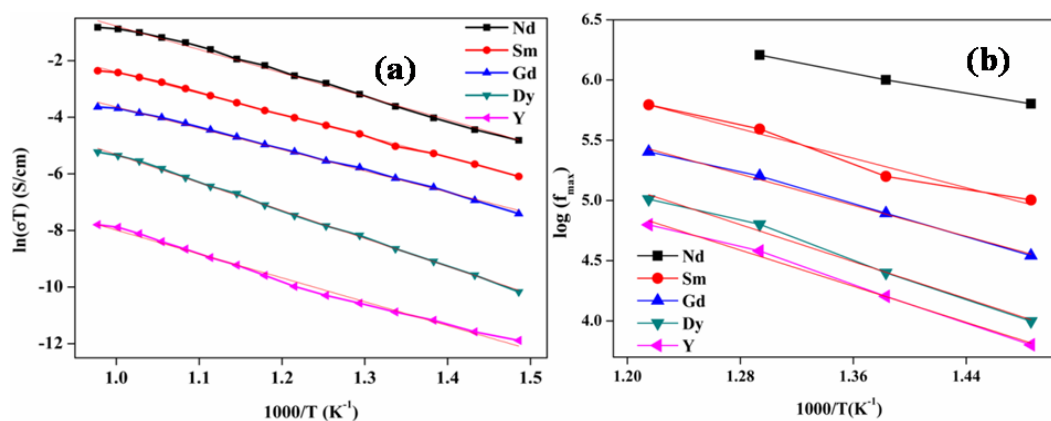
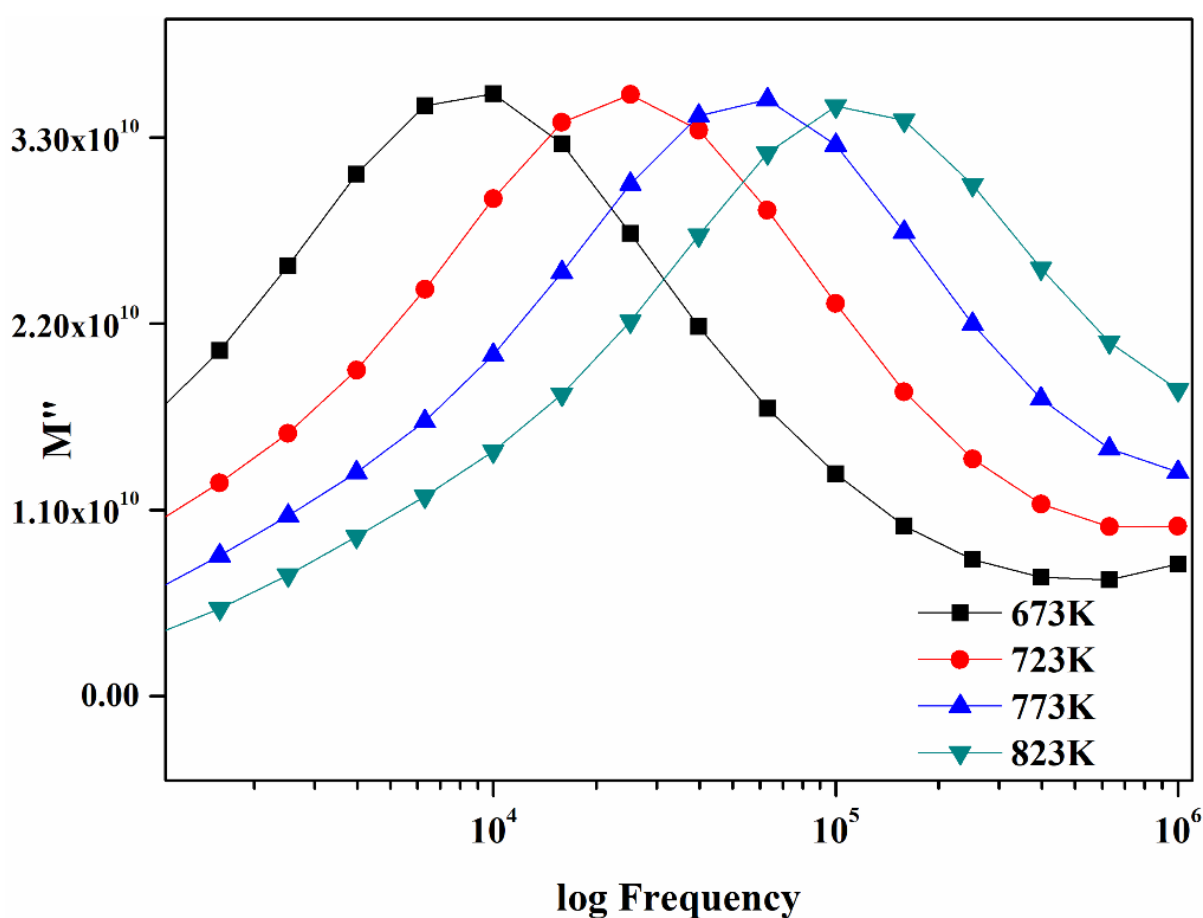


Fig. 4.8 Arrhenius plot (a)  $\ln(\sigma T)$  Vs  $1000/T$  (b)  $\log(f_{max})$  Vs  $1000/T$

A better analysis of the electrical properties of the compositions can be done using the concept of electric modulus function which is the reciprocal of the dielectric permittivity and is given by the equation

$$M^* = j\omega C_0 Z^* \quad (4.5)$$

where  $C_0$  is the vacuum cell capacitance, and  $\omega$  is the frequency. The modulus formulation highlights the bulk process in the conductivity, and it reduces the contribution from the electrode polarisation effects and is complementary to the complex impedance spectra.



**Fig. 4.9** Imaginary part of modulus Vs log frequency

Fig. 4.9 shows the plot of the imaginary part of the modulus against log frequency on the DyZN sample. The peaks in Fig. 4.9 are asymmetric to the peak maxima, and the shape of the peaks is the same irrespective of the temperature. However, the peaks shift towards higher frequency as the temperature increases, and the peak height is constant, which indicates the dielectric constant remains the same. The region to the left of the peak maximum corresponds to the ions which are mobile over a long-range, and the right of the peak corresponds to the

ones which are confined to the potential wells (Padmasree *et al.* 2006). i.e. at the frequency in which the  $M''$  maxima occurs, the reorientation of the ions involving oxide ion vacancies occurs. The activation energy for these charge re-orientation can be calculated by plotting the Arrhenius plot of  $\log f_{\max}$  versus  $1000/T$  (Reau *et al.* 1994), and the plot is in Fig. 4.8(b).

The activation energy calculated from both the Arrhenius plot is the same, and this confirms the conduction through the lattice occurs via the hopping mechanism (Reau *et al.* 1994; West *et al.* 1997). Fig. 4.10 shows the activation energy of the composition. The activation energy shows a rapid increase as the lattice volume of the composition increases. The sudden increase in the activation energy is due to the cooperative behaviour of the ions, which can be confirmed by the broadening of the peak in the normalised modulus against normalised log frequency.

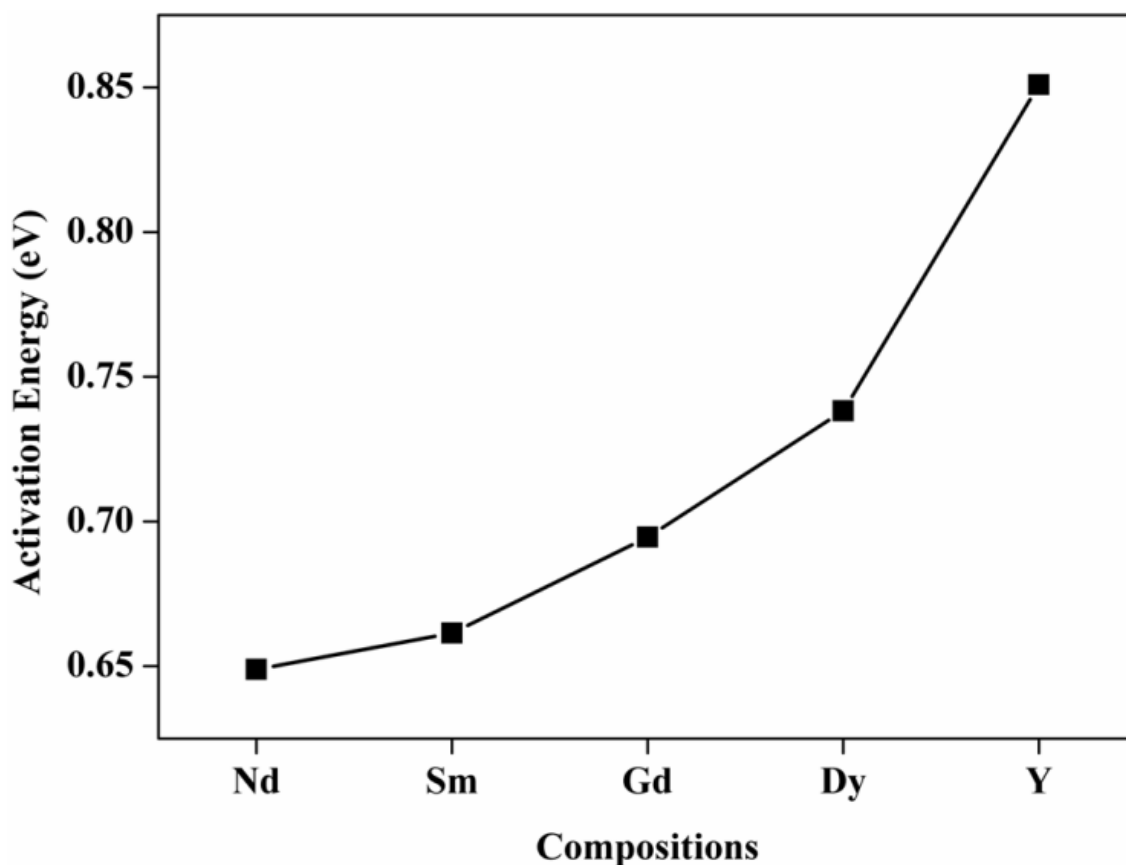


**Fig. 4.10** The variation of activation energy of the composition  $\text{RE}_3\text{Zr}_{0.5}\text{Nb}_{0.5}\text{O}_{6.75}$  (RE = Nd, Sm, Gd, Dy, Y)

The plot of the normalised  $M''/M''_{\max}$  vs  $\log(f/f_{\max})$  is plotted on the Fig. 4.11. The peaks in the plot are unsymmetrical, and this peak proves that these composition exhibit non-

Debye relaxation. The fitting function of the Debye relaxation is purely exponential and symmetric to the maxima given by equation 4.6.

$$\varphi(t) = \exp\left(\frac{-t}{\tau_0}\right) \quad (4.6)$$

The fitting function for the non-Debye relaxation is non-exponential and is represented below

$$\varphi(t) = \exp\left(\frac{-t}{\tau}\right)^\beta \quad 0 < \beta < 1 \quad (4.7)$$

$\tau$  is the relaxation time which is the inverse of the angular frequency corresponding to the peak in the imaginary part of the modulus vs log frequency ( $\omega_p$ ), and  $\beta$  is the Kohlrausch parameter whose value is less than 1 for a practical solid oxide electrolyte. The Kohlrausch parameter decreases when there is an increase in the distribution of the relaxation time (Moreno et al. 2005). The  $\beta$  value can be calculated using the FWHM value of the normalised  $M''/M''_{\max}$  plot.

$$\beta = \frac{1.14}{FWHM} \quad (4.8)$$



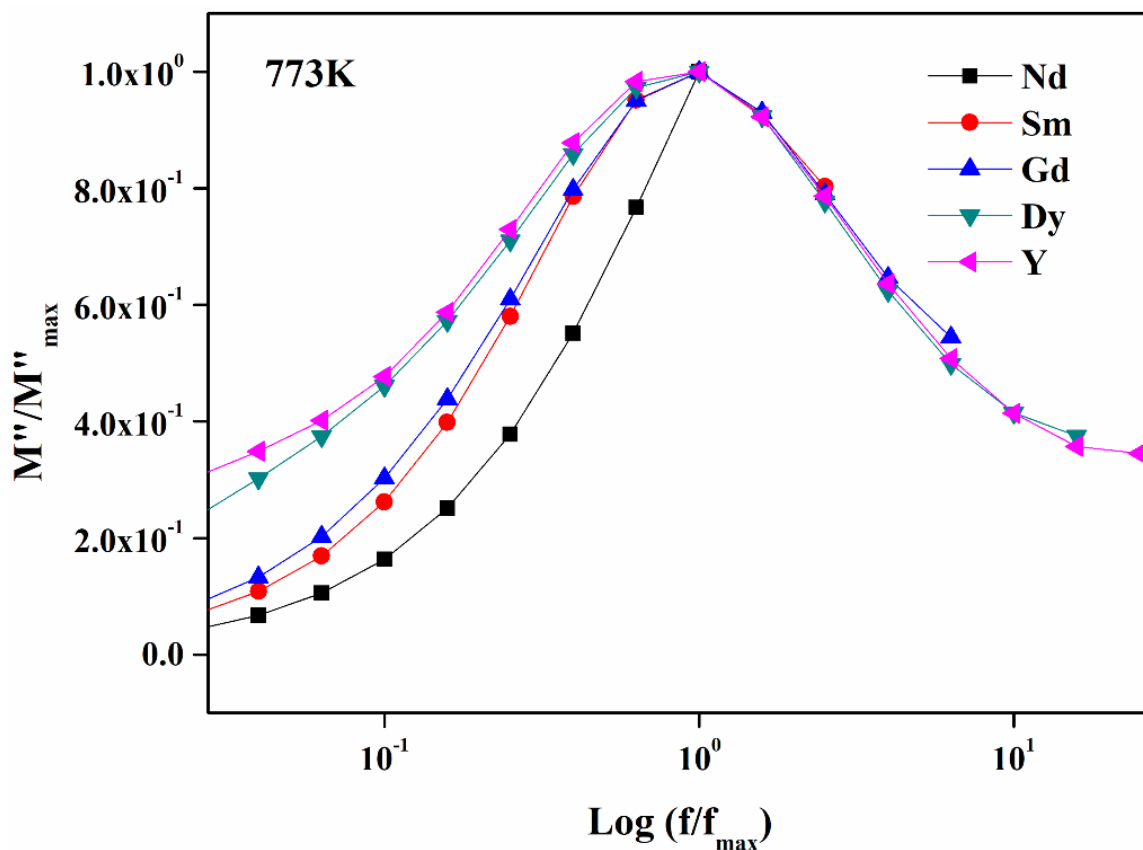


**Fig. 4.11** The normalised plot of  $M''/M''_{\max}$  vs  $\log(f/f_{\max})$  for all the composition

The Fig. 4.11 shows that as the lanthanide ions in the composition become smaller the peak width increase which in turn decreases the  $\beta$  value and the deviation from the Debye relaxation increases. The coupling model for the ion transport shows that the hopping of ions to an adjacent vacant site occurs with an exponential relaxation function represented by equation 4.6 (Ngai and Leon 2002; Ngai and León 2003; Ngai and Tsang 1999). However, because of ion-ion interaction the independent hopping does not occur, and this ion-ion interaction slows down the ion hopping thus increasing the relaxation time and thus the exponential correlation function changes to Kohlrausch equation. Thus the ion-ion interaction causes increased cooperative behaviour of the mobile charge carriers, and thus the activation energy for the long-range conduction and that for individual hopping differs, and the relation between them is given by the equation below.

$$E_a = \frac{E_{ai}}{\beta} \quad (4.9)$$

The smaller value of  $\beta$  causes an increase in the activation energy for long-range conduction. In addition to this, studies on the systems having higher charge carrier concentration this cooperative behaviour increase as thus activation energy increases and in

the present system due to the increased availability of the oxygen vacancies (Moreno et al. 2005) this effect becomes prominent. Lattice volume also takes a role in the enhancement of the cooperative behaviour of the present series. All these effects thus cause an exponential decrease in the conductivity as the ionic radius of the lanthanide ion present in the system decreases, as shown in Fig. 4.7.

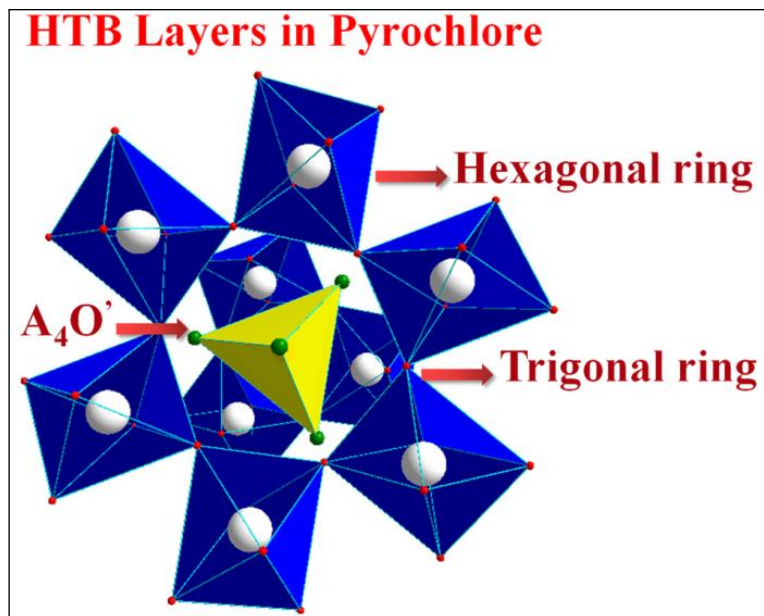
### 4.4 Conclusions

A new series anion vacant pyrochlore composition  $RE_3Zr_{0.5}Nb_{0.5}O_{6.75}$  was synthesised by conventional solid state reaction method. All the prepared composition are characterised by powder X-ray diffraction, Raman spectroscopy, scanning electron microscopy and impedance spectroscopy. The compositions are in pure phase with a fluorite crystal structure as predicted using the radius ratio. The Raman analysis also confirmed the formation defect fluorite structure. The impedance spectrum analysis on the prepared composition reveals that the conductivity decreases rapidly as the lattice volume of the prepared composition decreases. The activation energy calculated from the Arrhenius plot also increases sharply. This sharp increase in the activation energy and decrease in the conductivity is explained using the cooperative behaviour of the mobile charge carriers in the compositions. The modulus spectrum analysis of the composition shows that as the lattice volume of the composition decreases the ion-ion interaction in the lattice increases thus it enhances the cooperative behaviour of the ions which in turn causes an increase in the activation energy and thus decreases in the conductivity. Thus the study reveals that in addition to the no of oxygen vacancies and activation energy, the cooperative behaviour of the oxide ion also plays a crucial role in determining the ionic conductivity. The effect of the induced oxygen vacancies on the ionic conductivity is maximum only when the lattice volume is maximum on which the ion-ion interaction is minimum.

# Chapter 5

## Study of the Ionic Conductivity on the Displaced Pyrochlore Type Compositions

*Electrical properties of the displaced pyrochlore compositions were done in the present chapter. A series of compositions in which the Zr replaced the Ti in the displaced pyrochlore composition  $\text{Ca}_3\text{Ti}_3\text{Nb}_2\text{O}_{14}$  were prepared and the series exhibit the phase transition from cubic to the monoclinic pyrochlore as the Zr content in the composition increases. The phase transition takes place due to the increase ionicity of the B-O in the composition. The conductivity studies show that the composition with the fluorite structure have the maximum conductivity, which is an order of magnitude higher than the reported oxide ion conductivity value for the displace pyrochlore.*





## 5.1 Introduction

Pyrochlore oxides are an essential class of oxide materials that find enormous application in the field of ionic and electronic conductors, magnetic materials, phosphor host nuclear waste immobilisation and spin ice (Ewing *et al.* 2004; Morris *et al.* 2009; Pirzada *et al.* 2001; Wuensch *et al.* 2000) due to its lattice stiffness, high chemical stability, ability to tolerate both cation and anion sublattice disorder independently and to accommodate a diverse range of cations on the A and B sites (Sreena *et al.* 2015). These oxides with general formula  $A_2B_2O_7$  belong to  $Fd\bar{3}m$  space group are closely related to fluorite structure which belongs to  $Fm\bar{3}m$  space group. The A cation is eight coordinated to the oxide ion, and the B cation is six coordinated. The addition ordering in the pyrochlore structure due to the A and B cation with different ionic radii causes two crystallographic different oxide ions: one is at  $48f$  and second one is at  $8b$ . The formation of pyrochlore structure occurs for the composition having radius ratio of A and B cations in the range of 1.46 to 1.78 (Nishino *et al.* 2004). An oxygen vacancy at  $8c$  is also contained in the structure. The  $x$ -parameter of the  $48f$  oxide ion is another factor characterising the pyrochlore structure. The  $x$  value ranges from 0.3125 to 0.375. The value of  $x$ -parameter determines the A-O and B-O bond distance and the shape of the  $AO_8$  and  $BO_6$  polyhedra. When  $x = 0.3125$ ,  $BO_6$  polyhedra become perfect octahedra and thus a perfect pyrochlore structure forms.  $AO_8$  becomes perfect cubic polyhedra when  $x = 0.375$ , and thus the structure becomes fluorite (Shlyakhtina *et al.* 2018).

The A cation in the  $AO_8$  polyhedra is at the centre of a puckered hexagonal ring of six oxide ions ( $48f$ ) and normal to the mean plane of this puckered hexagonal there is a pair of oxide ion ( $O'$ ) at  $8b$ . The A-O bond length is longer compared to the A- $O'$  bond and neglecting the A-O interaction the framework of the pyrochlore structure can be treated as interpenetrating  $B_2O_6$  and  $A_2O'$  chains (Subramanian *et al.* 1983). The stability field for the several substitutions on the A and B cation of the pyrochlores depends on the simple parameters such as the radius ration of A and B cations and electronegativity (Subramanian *et al.* 1983; Vanderah *et al.* 2005). However, in a recent study, the stability field is extended for composition that can tolerate a cation displacement and maintain the microscopic cubic symmetry of pyrochlore (Avdeev *et al.* 2002; Hector and Wiggin 2004; Radosavljevic *et al.* 1998). One of such composition is bismuth-containing pyrochlore composition. The bismuth is a bigger cation reducing the stability region that causes displacive disorder on both the A and  $O'$  ions (Withers *et al.* 2004). IR reflectance study on the bismuth-based

pyrochlores also confirmed this displacement (Chen *et al.* 2005). In the case of ideal pyrochlore structure, only  $O_{48f}$  can relax to the oxygen vacancy and thus the variables that characterise an ideal pyrochlore structure is the  $x$ -parameter of the  $O_{48f}$  and the lattice parameter. However, here in the case of these bismuth-based pyrochlore, the lone pair of electrons is the reason for the cation displacement and hence the disorder in the  $A_2O'$  network (Hinojosa *et al.* 2008). Such pyrochlores are commonly termed as misplaced-displace pyrochlores. Since the  $A_2O'$  network weakly interacts with the rigid  $B_2O_6$  network, the disorder or vacancies in this network does not affect the whole pyrochlore structure (Sreena *et al.* 2016). Thus the pyrochlore structure is highly tailorable, for example, the identities and oxidation state of the B cation which play an essential role in determining the electrical properties of the oxides can be controlled through deliberate choices of the A and  $O'$  by maintaining the electrical neutrality (Vanderah *et al.* 2005).

As mentioned in the previous paragraph displacive structure is observed for bismuth-containing composition. Levin *et al.* studied the structure and the stoichiometry of the pyrochlore structured bismuth zinc niobate as  $Bi_{1.5}Zn_{0.92}Nb_{1.5}O_{6.92}$  with partial zinc occupancy in both the A and B position. The displacement of the cation occurs along  $\langle 112 \rangle$  direction perpendicular to the  $O'-A-O'$  axis and the  $O'$  ions displaces through the  $\langle 110 \rangle$  directions. These displacements cause the appearance of some weak forbidden reflection (eg:442) which violate special reflection conditions for  $8b$ ,  $16c$ ,  $16d$ , and  $48f$  positions occupied in the ideal arrangement (Levin *et al.* 2002). In the ideal pyrochlore structure, the intensity of this reflection is zero, and this arises to the displacement of the A cation to a lower symmetry position such as g, h, i, e. Also the bismuth titanate with pyrochlore structure was prepared for the first time by Radosavljevic *et al.* which cannot exist based on the  $Bi_2O_3/TiO_2$  phase diagram, and the composition of the sample is  $Bi_{1.74}Ti_2O_{6.62}$ . The refinement studies confirmed the displacement of the Bi cations (Radosavljevic *et al.* 1998).

Crystal chemical study on the pyrochlore structure reveals that the displacive disorder becomes a structural feature for compositions that allows the formation of cubic pyrochlores in which the smaller B cation occupies ca 25% of the A cations (Vanderah *et al.* 2005). The off-centre displacement is because of the larger A-site cavity which is too big for the smaller ones (Avdeev *et al.* 2002). The phase equilibria study of  $CaO: TiO_2:Nb_2O_5$  by Roth *et al.* revealed that a pyrochlore structured solid solution is formed for the composition  $3CaO: 3TiO_2: Nb_2O_5$  or  $Ca_{1.5}Ti_{1.5}NbO_7$ . The refinement studies show that the structure has an

intrinsic displacive disorder. The Ca and Ti occupy the  $16d$  and  $96g$  Wyckoff position respectively. The O' ions shifts from the ideal  $8b$  to tetrahedral  $32e$  position. The similarities of the electrical properties of this composition with the Bi-based pyrochlores confirms that the properties arise due to the displacive disorder in the system and not due to the presence of the polarizable lone pair of electrons in the bismuth (Roth *et al.* 2008). Thus it is confirmed that the displacive disorder in the pyrochlore phase can tune the properties of the system.

In a recent study on metastable  $\text{Bi}_2\text{Zr}_2\text{O}_7$  revealed that these displaced pyrochlore oxides could exhibit oxide ion conductivity. In the currently mentioned study, the ionic conductivity obtained is  $3.071 \times 10^{-6}$  S/cm at 773K. Activation energy and other electrical properties confirmed the charge carrier for this conductivity is oxide ions (Pandey, Shrivastava, and Nagarajan 2018). Also, the bismuth titanate doped with Cu, Mg, and Sc identified as mixed electron- ionic conductor, exhibit high oxygen mobility at a temperature above  $400^\circ\text{C}$  and it depends on the doped cation radius and the oxygen vacancies formed (Pandey *et al.* 2018).

Despite all these facts, the study on ionic conductivity of the misplaced displacive pyrochlore is not explored in detail. Here in the present work, we have tried to study the ionic conductivity of  $\text{Ca}_3\text{Ti}_3\text{Nb}_2\text{O}_{14}$  composition in which the titanium is gradually replaced by zirconium which is having the high ionic radius than titanium. From the literature survey on this pyrochlore, it is revealed that the Ti is small to occupy the A cation site  $16d$  in the ideal pyrochlore structure and that is why the  $\text{Ti}^{4+}$  ion occupies the  $96g$  position. So in the present study, replacement of Ti with Zr may seriously affect the structure and ionic conductivity properties of the composition. The present work analyses these structural and conductivity properties changes.

## 5.2 Experimental

The powder samples of the present series of compositions  $\text{Ca}_3\text{Ti}_3\text{Nb}_2\text{O}_{14}$ ,  $\text{Ca}_3\text{Ti}_2\text{ZrNb}_2\text{O}_{14}$ ,  $\text{Ca}_3\text{TiZr}_2\text{Nb}_2\text{O}_{14}$  and  $\text{Ca}_3\text{Zr}_3\text{Nb}_2\text{O}_{14}$  were prepared by conventional solid-state reaction method. The starting material  $\text{CaCO}_3$  (99.9%, Sigma Aldrich),  $\text{TiO}_2$  (99.9995%, Sigma Aldrich),  $\text{ZrO}_2$  (99.99%, Sigma Aldrich) and  $\text{Nb}_2\text{O}_5$  (99.995%, Sigma Aldrich) were dried for 1h and then weighed stoichiometrically. The weighed chemicals were ground in agate and mortar using acetone as the medium. The mixture is dried in a microwave oven for 1h. The process is repeated thrice to get a uniform mixture of the composition. Thus obtained uniform mixture is then calcined at  $1300^\circ\text{C}$  for 6h and at  $1400^\circ\text{C}$  for 6h with intermittent

grinding. The prepared powder is uniaxially pressed to make green cylindrical pellets, compaction at 25 Mpa. These cylindrical pellets are sintered at 1450°C for 18h.

The samples prepared via solid-state reaction method is characterised for structural and conductivity properties. The crystal structure of the composition was analysed using X-ray powder diffractometer (X'pert Pro, Analytical) operating at 45kV and 30mA. The analysis was carried out on a two theta range of 10-90° using Ni filtered CuK $\alpha$  radiation of wavelength 1.5406 Å. Scans recorded over a 2 $\theta$  range of 10-90° with a step size of 0.02 and a scan time of 30 seconds using X'pert highscore software. The structural analysis of the prepared composition was done using the least square method, and Rietveld analysis using high score plus software. The surface morphology of the composition in the form of the pellet is done using a scanning electron microscopy. Here the scanning electron microscope (JEOL, JSM-5600L) is used to picture the surface morphology of the sintered pellet. The electrical properties of the pellets were done by Impedance analyser (Solatron SI 1260) with a dielectric interface (Solatron 1296). High temperature curing silver paste was coated on both sides of sintered pellets then cured at 600°C for 30 min. The conductivity measurements were carried out from room temperature to 1023K in a frequency range of 1Hz to 1MHz. The impedance plots were made with SMART software.

### 5.3 Results and Discussion

The compositions Ca<sub>3</sub>Ti<sub>3</sub>Nb<sub>2</sub>O<sub>14</sub>, Ca<sub>3</sub>Ti<sub>2</sub>ZrNb<sub>2</sub>O<sub>14</sub>, Ca<sub>3</sub>TiZr<sub>2</sub>Nb<sub>2</sub>O<sub>14</sub> and Ca<sub>3</sub>Zr<sub>3</sub>Nb<sub>2</sub>O<sub>14</sub> were abbreviated as CT<sub>3</sub>N, CT<sub>2</sub>ZN, CTZ<sub>2</sub>N, and CZ<sub>3</sub>N throughout the text.



## 5.3.1 Powder X-ray Diffraction Studies

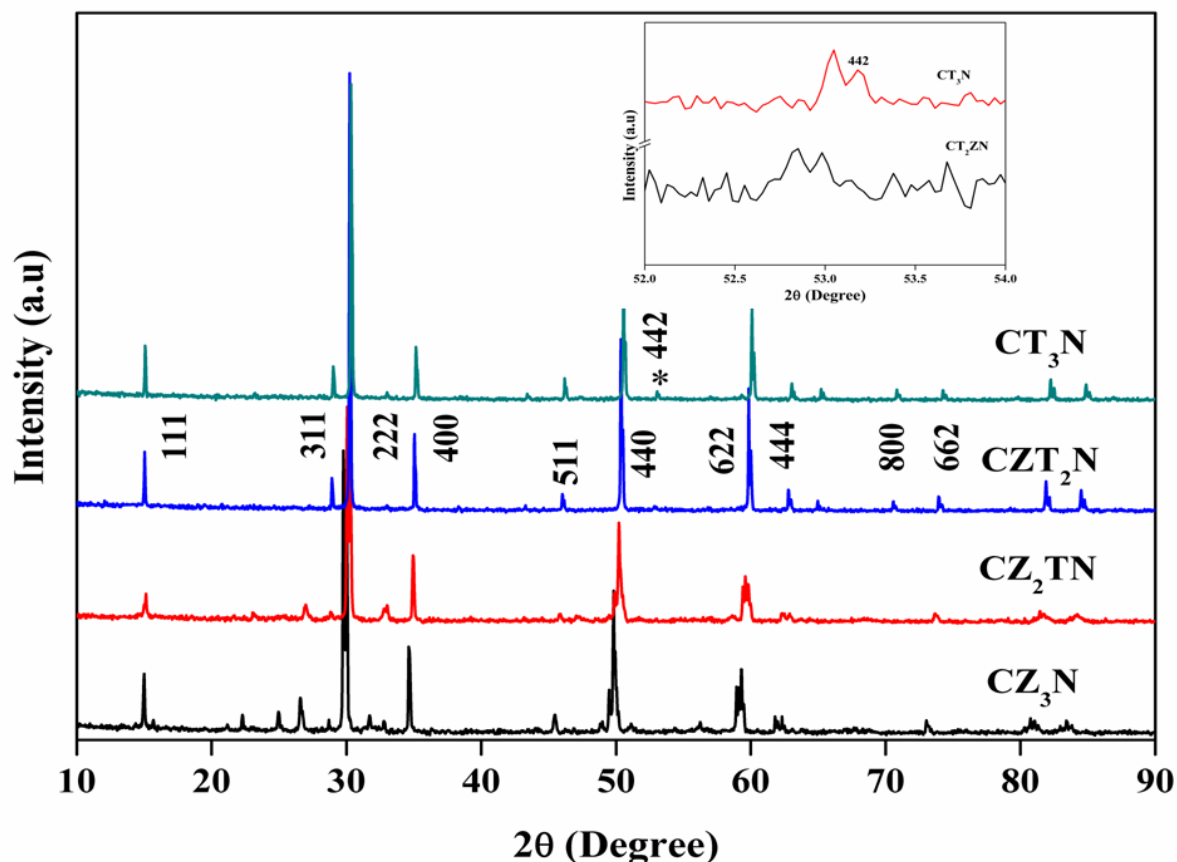


**Fig. 5.1** The powder X-ray diffraction patterns of the compositions  $CT_3N$ ,  $CT_2ZN$ ,  $CTZ_2N$  and  $CZ_3N$

The powder X-ray diffraction patterns of the compositions  $CT_3N$ ,  $CT_2ZN$ ,  $CTZ_2N$  and  $CZ_3N$  are shown in Fig. 5.1. The series of composition exhibit a phase transition from cubic pyrochlore to monoclinic zirconolite ( $CaZrTi_2O_7$ ) like structure as the zirconium content in the composition increases. In Fig. 5.1 only cubic pyrochlore is indexed. The table of d-spacing and the hkl values corresponding to the monoclinic is shown in Table 5.1.

**Table 5.1** The d-spacing and corresponding hkl values of the monoclinic structure

d-spacing ( $\text{\AA}$ )	h	k	l
5.91191	2	0	0
5.64838	0	0	2
3.98794	2	0	2
3.56565	0	2	1
3.35342	3	1	1

2.99885	2	2	1
2.97590	0	0	4
2.73066	2	2	3
2.58865	4	0	2
1.99459	4	0	4
1.86230	4	0	6
1.84270	2	2	5
1.83115	0	4	2
1.78640	6	2	1
1.63595	4	4	2
1.56612	2	2	7
1.55841	4	4	2
1.50114	4	4	4
1.49014	0	0	8

Pyrochlore oxide is a member of the oxygen octahedron family in which the structural stability of the composition is determined by using radius ratio and  $x$ -parameter of the  $48f$  oxygen. However, recently, some of the composition that resides outside the region of structural stability by radius ratio were synthesised, and the compositions are characterised by displacement of the A and O' ions. In earlier studies, such compositions with pyrochlore structure and non-cubic symmetry are found in the composition in which the A cation is possessed with an inert lone pair of electrons such as  $\text{Bi}^{3+}$ ,  $\text{Pb}^{2+}$  and so on (Shannon *et al.* 1980; Vetter 1978; Wang *et al.* 2005). Avdeev *et al.* and some of the recent research works on these misplaced displacive pyrochlore reveals that the doping of smaller transition metal ions on the A site of the pyrochlore structure can also induce some structural disorder in the  $\text{A}_2\text{O}'$  network and thus form the displacive pyrochlore (Sreena *et al.* 2015, 2016). Here in the present work also such a disorder in the  $\text{A}_2\text{O}'$  causes the formation of displaced disorder in the system. In the present composition much smaller Ti cation occupies the  $16d$  site which is too big for the Ti ions. Thus the  $\text{Ti}^{4+}$  cation is shifted to lower symmetry position  $96g$  or  $96h$ . Such a displacement affect the position of the O' and shift to  $32e$  position.

**Table 5.2** The Wyckoff position and site of occupancies of all the compositions used for the refinement

CT <sub>3</sub> N	CT <sub>2</sub> ZN	CTZ <sub>2</sub> N	CZ <sub>3</sub> N
(Ca <sub>1.5</sub> Ti <sub>0.5</sub> )(TiNb)O <sub>7</sub>	(Ca <sub>1.5</sub> Zr <sub>0.5</sub> )(TiNb)O <sub>7</sub>	(Ca <sub>1.5</sub> Zr <sub>0.5</sub> )(Zr <sub>0.5</sub> Ti <sub>0.5</sub> Nb)O <sub>7</sub>	(Ca <sub>1.5</sub> Zr <sub>0.5</sub> )(ZrNb)O <sub>7</sub>
16d→0.75Ca+0.25Ti	16d→0.75Ca+0.25Zr	8f→0.75Ca+0.25Zr	8f→0.75Ca+0.25Zr
16c→0.5Ti+0.5Nb	16c→0.5Ti+0.5Nb	8f→0.125Zr+0.125Ti+0.25Nb	8f→0.25Zr+0.25Nb
48f→1O <sub>1</sub>	48f→1O <sub>1</sub>	4e→0.125Zr+0.125Ti+0.25Nb	4e→0.25Zr+0.25Nb
8b→1O <sub>2</sub>	8b→1O <sub>2</sub>	8f→O <sub>1</sub>	8f→O <sub>1</sub>
		8f→O <sub>2</sub>	8f→O <sub>2</sub>
		8f→O <sub>3</sub>	8f→O <sub>3</sub>
		8f→O <sub>4</sub>	8f→O <sub>4</sub>
		8f→O <sub>5</sub>	8f→O <sub>5</sub>
		8f→O <sub>6</sub>	8f→O <sub>6</sub>
		8f→O <sub>7</sub>	8f→O <sub>7</sub>

The X-ray diffraction pattern of the cubic pyrochlore structured composition is refined using X'pert high score plus software. The refinement was done assuming the ideal pyrochlore structure. The Wyckoff positions and site of occupancy based on the stoichiometry used is shown in Table 5.2. The observed, calculated patterns and difference plot of the cubic pyrochlore are shown in the Fig. 5.2. The refined parameters are tabulated in Table 5.3. The isotropic temperature parameter obtained from the refined data in Table 5.3 and 442 reflections peak shown as the inset in the Fig. 5.1. confirms the displaced pyrochlore structure (Levin *et al.* 2002). The isotropic temperature parameter values for the ions which are prone to displacement are high compared to the ions that are fixed as in the ideal pyrochlore structured composition. This high-value isotropic temperature parameter indicates the displacement of the respective ions from the ideal higher symmetric position to lower symmetry position.

Table 5.3. The refined parameters for the cubic pyrochlore structured composition

Composition		CT <sub>3</sub> N	CT <sub>2</sub> ZN
<b>Refined parameters</b>			
<b>Phase</b>		Pyrochlore	Pyrochlore
<b>Unit cell</b>		Cubic	Cubic
<b>Space group</b>		Fd-3m	Fd-3m
<b>Lattice parameter (Å)</b>		10.2180(8)	10.2554(1)
<b>Flat absorption correction</b>		0.0027	0.000392
<b>FWHM parameter (Å)</b>	U	-0.015490	-0.007096
	V	0.020928	0.015636
	W	0.000891	0.0016286
<b>R-factors (%)</b>	R <sub>p</sub>	12.32052	11.29987
	R <sub>wp</sub>	10.44868	9.34402
	R <sub>exp</sub>	13.83089	12.09797
<b>x-parameter (Å)</b>		0.330607	0.323471
<b>Biso Ca</b>		0.506903	0.854905
<b>Biso Ti</b>		2.496859	1.321170
<b>Biso Ti</b>		0.001000	0.001021
<b>Biso Nb</b>		0.002000	0.001042
<b>Biso O<sub>1</sub></b>		0.000668	0.000000
<b>Biso O<sub>2</sub></b>		8.9(5)	0.3(7)

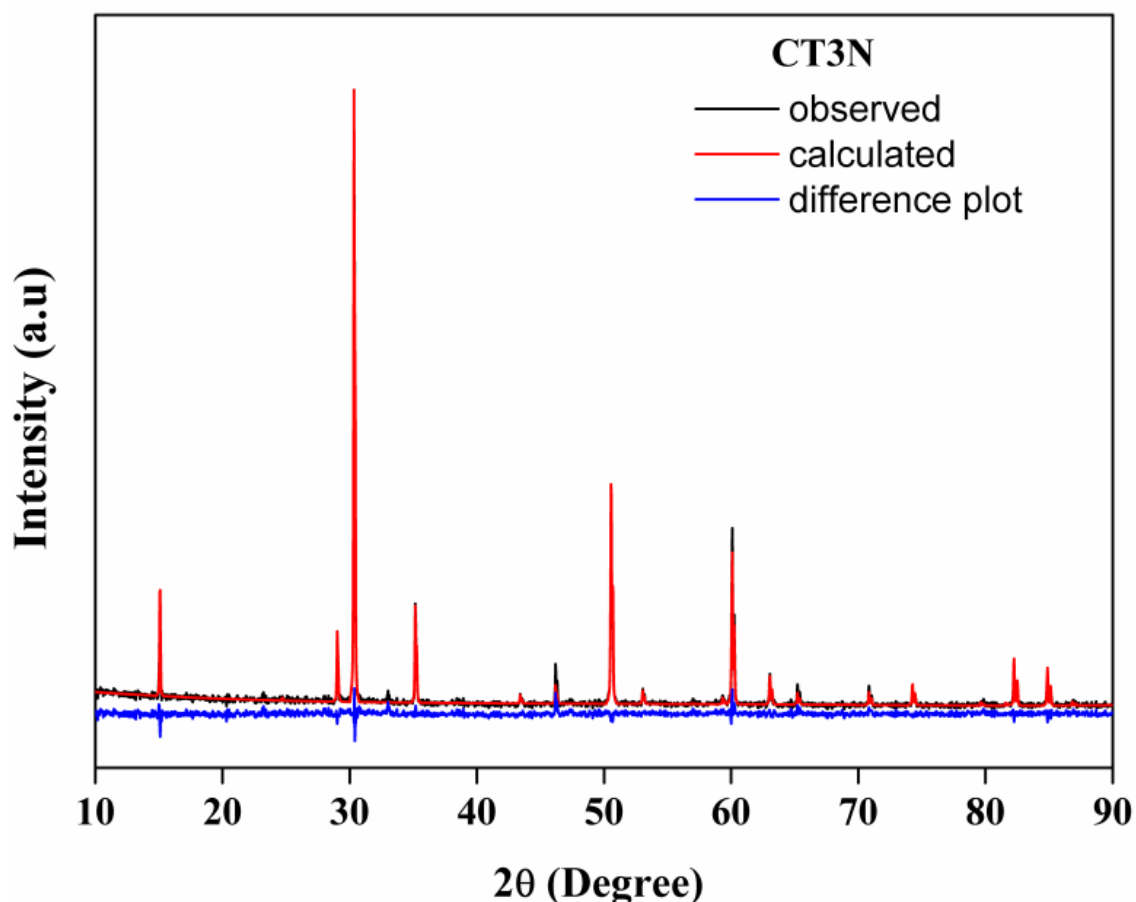


**Fig. 5.2** The observed, calculated patterns of CT<sub>3</sub>N along with the difference plot.

The lattice parameter of the monoclinic pyrochlore structured composition was calculated using the formula

$$\frac{1}{d_{hkl}} = \frac{1}{\sin^2\beta} \left[ \frac{h^2}{a^2} + \frac{k^2 \sin^2\beta}{b^2} + \frac{l^2}{c^2} - \frac{2hc \cos\beta}{ac} \right] \quad (5.1)$$

$$V = abc \sin\beta \quad (5.2)$$

The refinement of the lattice parameter of these compositions was done on the X'pert highscore plus software using Le bail fit (since the high-quality XRD diffraction data is needed to refine) and the obtained lattice parameter from the refinement and using equation were in agreement. The lattice parameter values of all the composition are listed in Table 5.3. The variation of the lattice volume with the Zr substitution is shown in Fig. 5.3.

**Table 5.4** The lattice parameter values of all the composition

Composition	Lattice parameters (Å)	Lattice volume (Å <sup>3</sup> )	Electronegativity difference in B-O bond
<b>CT<sub>3</sub>N</b>	$a=10.2180(8)$	1066.8306	1.96
<b>CT<sub>2</sub>ZN</b>	$a=10.2554(1)$	1078.5935	1.96
<b>CTZ<sub>2</sub>N</b>	$a=13.0871(5)$ $b=7.5155(2)$ $c=11.29676(8)$ $\beta=101.2365^\circ(3)$	1089.8105	2.0225
<b>CZ<sub>3</sub>N</b>	$a=13.1223(4)$ $b=7.5557(1)$ $c=11.3364(9)$ $\beta=102.365^\circ(5)$	1097.9105	2.125

The Fig. 5.3 indicates that as the Zr content in the composition increases the lattice volume increases as can be predicted from the Vegard's law irrespective of the structural changes.

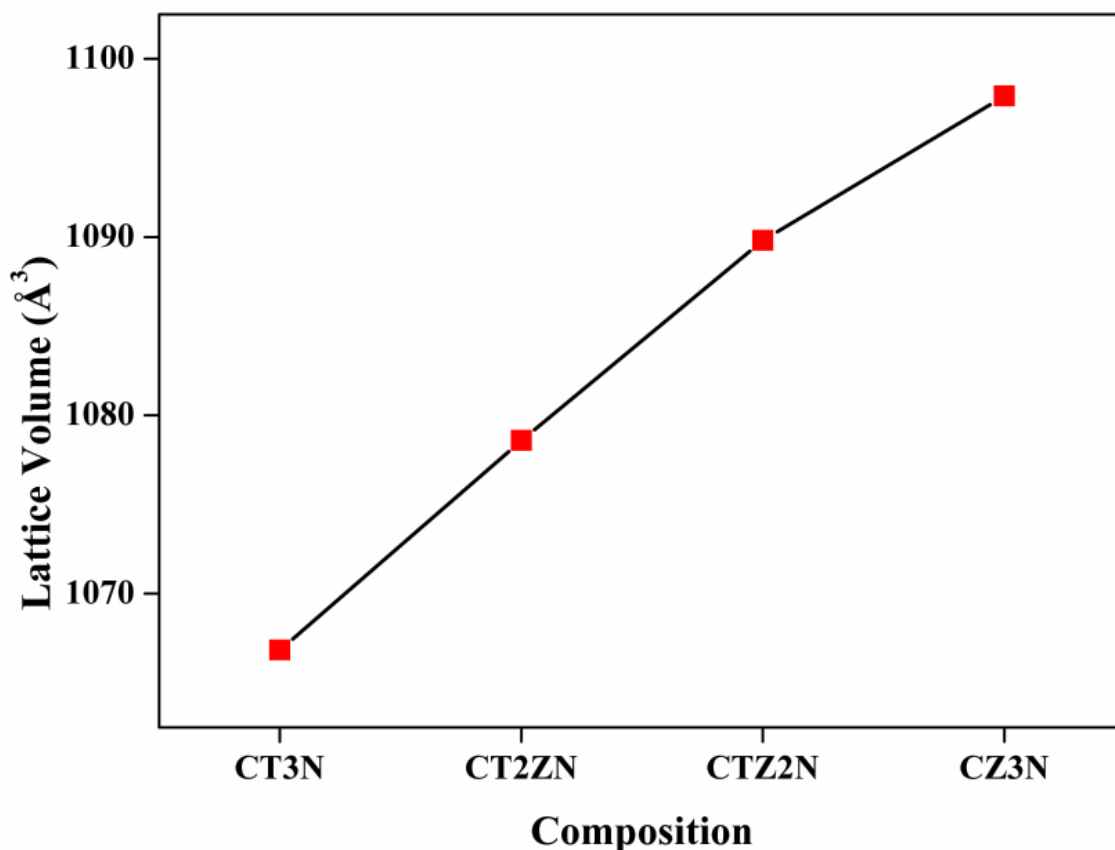


**Fig. 5.3** The variation lattice parameter with the Zirconium content

Most of the compositions with  $A_2B_2O_7$  composition are reported to be in the cubic pyrochlore structure. However, several compositions such as tetragonal  $Bi_2FeVO_7$  and  $Bi_2AlVO_7$ , trigonal  $Er_2Mn_{2/3}Re_{4/3}O_7$ , orthorhombic  $Y_2YbSbO_7$  or monoclinic  $Y_2FeMoO_7$  and  $Bi_2Zn_{2/3}Nb_{4/3}O_7$  were reported with crystal structure other than ideal cubic pyrochlore depending on the A and B substitutions (Torres-Martínez *et al.* 2012). A phase transformation similar to the present work is reported earlier in the bismuth zinc niobate system (BZN). The mentioned compositions are  $Bi_{1.5}ZnNb_{1.5}O_7$  and  $Bi_2(Zn_{2/3}Nb_{4/3})O_7$ . The structure of the latter composition was the subject to discussion in earlier times. In the earlier studies, the structure is described as distorted pyrochlore with pseudo-orthorhombic pyrochlore with  $a = 7.202\text{Å}$ ,  $b = 7.603\text{Å}$  and  $c = 10.64\text{Å}$  (Wang *et al.* 2005). In a detailed structural analysis of the composition  $Bi_2(Zn_{2/3}Nb_{4/3})O_7$  by Levin *et al.* using the neutron diffraction data and refinement studies revealed that the structure is monoclinic similar to zirconolite  $CaZrTi_2O_7$  (Levin *et al.* 2002) with space group  $C2/c$ . The monoclinic zirconolite structure cannot be derived from the pyrochlore structure but like in the case of pyrochlore structure can be described as an anion deficient derivative of fluorite structure with the distinct distribution of cations over the metal sites.

In the pyrochlore structured composition, the  $\text{BO}_6$  octahedra –sharing vertices forms a three-dimensional octahedra forming a three-dimensional network  $\text{B}_2\text{O}_6$  leaving large cavities in which the A and O' ions reside and forms  $\text{A}_2\text{O}'$  tetrahedral network. The  $\text{B}_2\text{O}_6$  network consists of 111 sheets of octahedra sharing vertices to form six and three-membered rings often referred to as hexagonal tungsten bronze layer (HTB). The sequential arrangement of these HTB layers causes a difference in the structure (Torres-Martínez *et al.* 2012). Pyrochlore structure is a 3D arrangement of these HTB blocks while monoclinic is a 2D arrangement with different sequence of arrangement. In the case of monoclinic structure the interstices formed by the six-membered  $\text{BO}_6$  octahedra is occupied by the smaller B cations. Also, in the ideal pyrochlore structure the A cation remains in the ring centre and are eight coordinated whereas in the case of the zirconolite compositions the smaller B cation are displaced from the ring centre and reside on both sides of the two-fold symmetry axis resulting six coordination (Levin *et al.* 2002). Thus on increasing the Zr content on the composition the Zr ions enter into the A sites. On further increasing the part of the Zr resides on the  $\text{B}_2\text{O}_6$  octahedra and thus the interstices of this network are also occupied by the Zr ion, and thus the system transforms from the cubic to the pyrochlore structure. In addition to this electronegativity also plays an important role in the determination of the phase in the displaced pyrochlore. In the case of the displaced pyrochlore increased ionic character of the B-O bond causes a distorted pyrochlore structure. The cubic pyrochlore is formed when the B-O bond has high covalent character. Here in this study also the increase in the amount of Zr causes increased ionic behaviour in the B-O bond and thus causes the formation of monoclinic pyrochlore (Wang *et al.* 2005). The difference in electronegativity is included in Table 5.4

### 5.3.2 Morphological analysis

The morphological analyses of the sintered pellets were done using the scanning electron microscopy. Fig. 5.4. shows the surface morphology of the sintered pellets. The images show the polycrystalline nature and the grain size of the composition containing zirconium is in the range of 1-3  $\mu\text{m}$ , and that of the  $\text{CT}_3\text{N}$  is ranging from 2-5  $\mu\text{m}$ . All the samples possess some porosity.



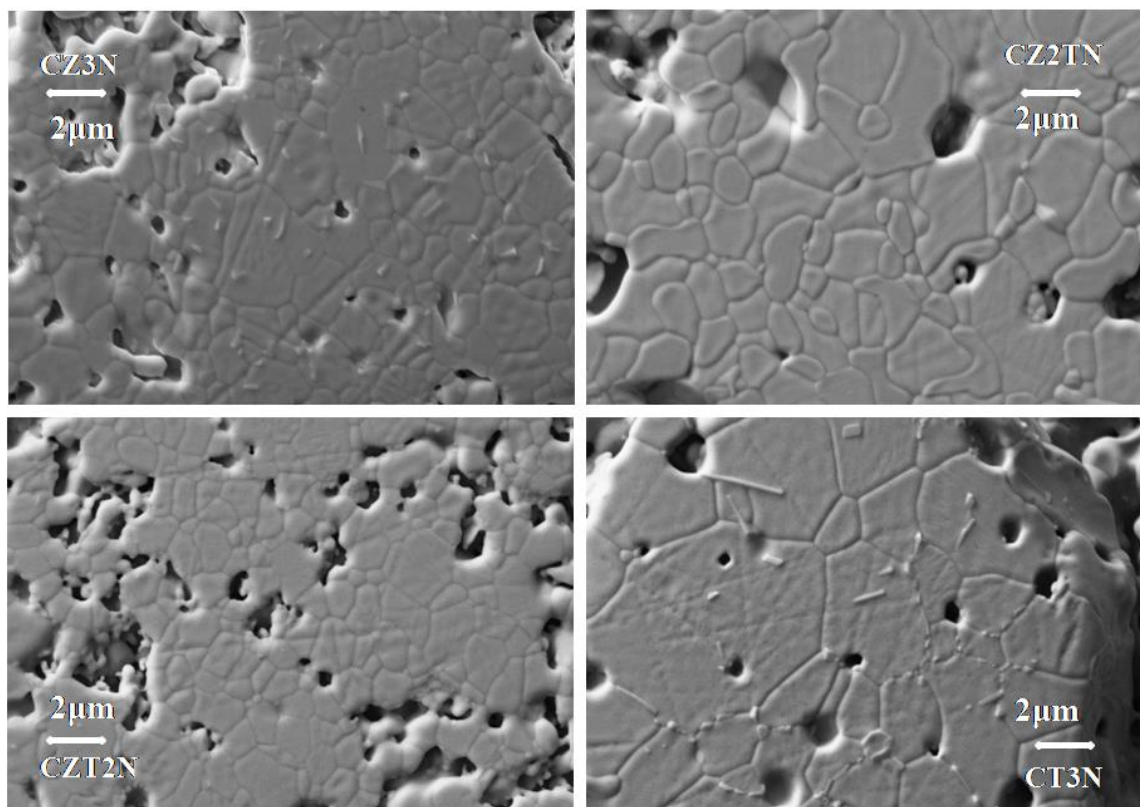


**Fig. 5.4** The scanning electron microscopic images of the polished surface of the sintered pellets of all the prepared composition

### 5.3.3 Electrical properties

In the case of a polycrystalline solid, the resistance to the charge flow occurs via two mechanisms: the first one arises from the pure ohmic resistance part, and the other is the accumulation charge in somewhere thereby causing capacitive reactance to the charge flow. The accumulation of charges occurs mainly in the bulk, grain boundary and the sample-electrode interfaces. Depending on the sites where charge accumulation occurs, the capacitance differs. In the bulk of the material the capacitance falls in the pico farad range and that for grain boundary and sample electrode interface happen to be in the nano farad and microfarad range respectively. Thus the polycrystalline sample is analogous to a series of three RC parallel circuits.

The impedance spectroscopy studies on the polycrystalline samples can throw some light on the physical aspects of the charge carriers' conduction. An ac stimulus of 100mV is applied to the silver-coated flat surface of the cylindrical pellets. Analysis of the impedance spectra was done using the Smart software.

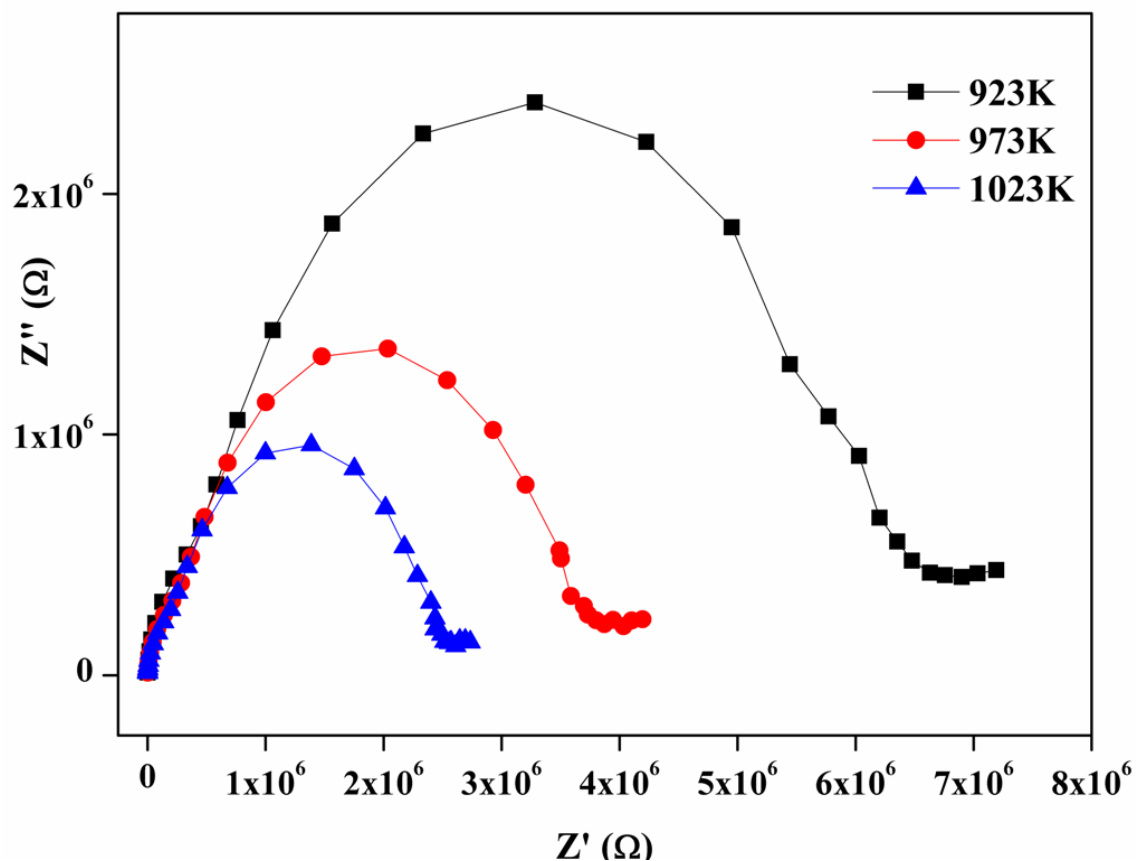


**Fig. 5.5** The Nyquist plot of the  $\text{CZ}_2\text{TN}$  composition at various temperature

Fig. 5.5 shows the Cole-Cole plot of the sample  $\text{CZ}_2\text{TN}$  at temperature 923K, 973K, 1023K. Three semicircles are not seen in the Fig. 5.5. Due to the difference in the distribution of relaxation frequencies, the semicircles may appear merged or incomplete, and some portions of the semicircles may lie outside the frequency range used in the measurement. At high temperature, the accumulation of charge carriers at the sample electrode interface may give rise to spikes in the complex plane instead of semicircles due to the high capacitance. Such spikes also confirm that the conduction occurs due to the oxide ions (Sibi *et al.* 2009).

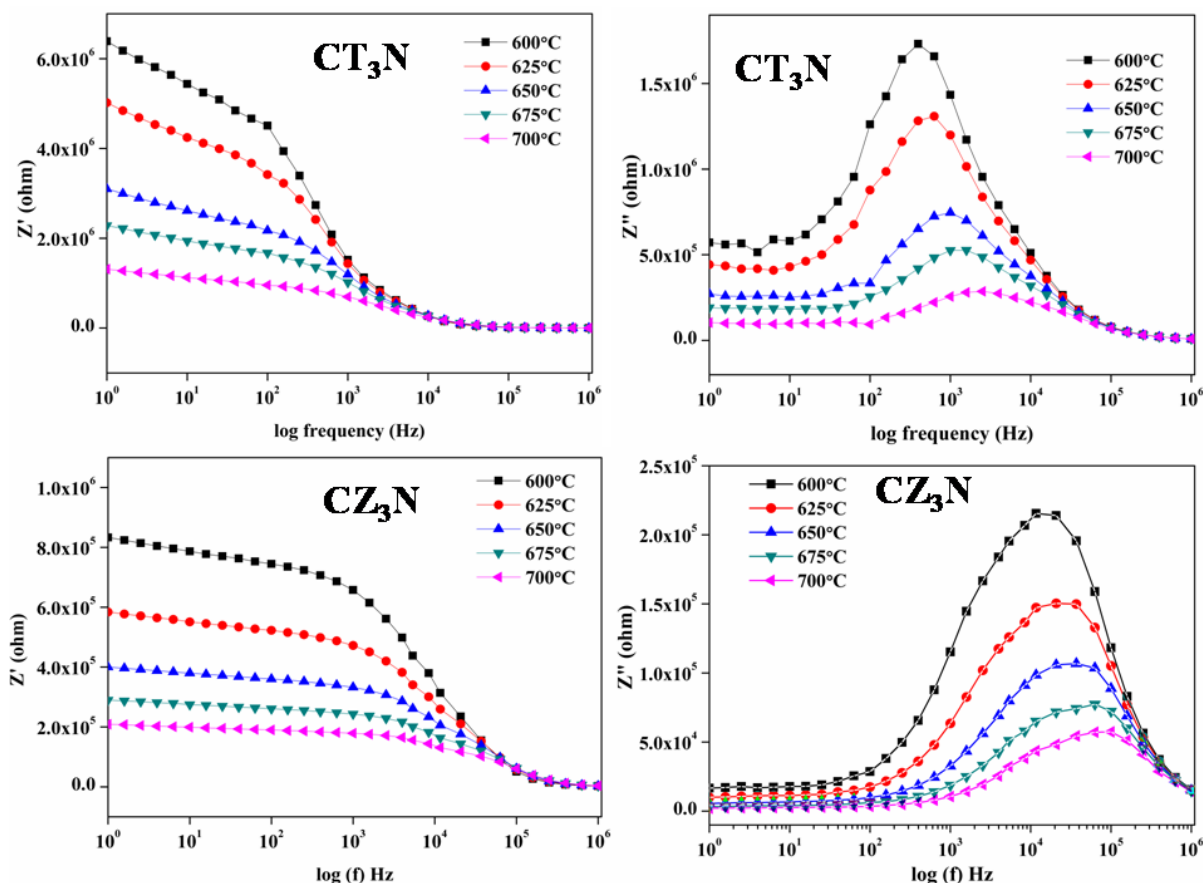


**Fig. 5.6** The frequency dependence of the real and imaginary part of the samples  $CT_3N$  and  $CZ_3N$

Fig. 5.6 represents the frequency dependence of the real and imaginary part of the impedance of two representative samples  $CT_3N$  and  $CZ_3N$  at various temperatures. The jump  $Z'$  and peak of the  $Z''$  shifts towards higher frequency as the temperature increases. The real part of the impedance decreases as the temperature increases. The coincidence of  $Z'$  at high frequencies and high impedance value at low frequencies indicates the possible release of the space charge. This confirms the relaxation of oxide ions. In the case of imaginary part of the impedance, when the temperature increases, the relaxation peaks shift towards the higher frequency, and the peaks get broadens. The relaxation frequency in the Nyquist plot corresponds to the apex of the semicircle satisfying the relation

$$\omega RC = 1 \quad (5.3)$$

where  $\omega = 2\pi f_r$  where  $f_r$  is the relaxation frequency. The bulk capacitance of the samples was calculated using the equation. The relaxation frequency is independent of the geometrical measurements of the samples and is related to the conductivity via the relation

$$f_{\tau} = \frac{\sigma}{2\pi\epsilon_r\epsilon_0} \quad (5.4)$$

The temperature dependence of the relaxation frequency is shown in the Fig. 5.7. The figure shows the dependence follows the Arrhenius equation

$$f_{\tau} = f_{\tau 0} \exp\left(\frac{-E_a}{k_B T}\right) \quad (5.5)$$

$f_{\tau 0}$  is the pre-exponential term,  $E_a$  is the activation energy,  $k_B$  is the Boltzmann constant and  $T$  is the temperature. The slope of the straight line gives the activation energy.

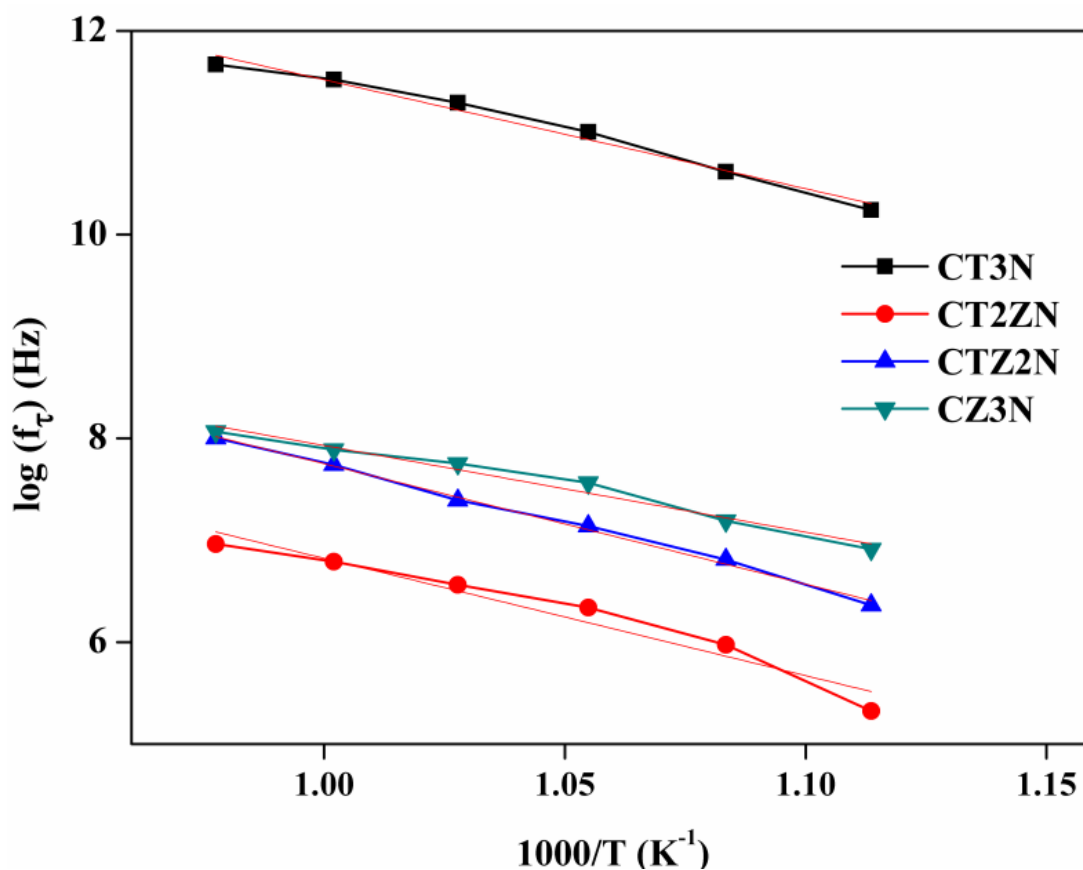


Fig. 5.7 The plot of the log of the relaxation frequency against  $1000/T$

The intercept of the semicircle with the real axis gives the resistance of the samples associated with the particular mechanism. The conductivity of the samples is calculated using the formula

$$\sigma = \frac{l}{RA} \quad (5.6)$$

$A$  and  $l$  are the area and height of the cylindrical pellets and  $R$  is the resistance value obtained from the intercept of the semicircle. The temperature dependence of the conductivity was

analysed by plotting  $\ln(\sigma T)$  against  $1000/T$ . Fig. 5.8 shows the plot. All the samples obey the Arrhenius equation and show linear behaviour. The linear fit of the data points also shown in the figure. This linearity confirms the thermally activated conduction

$$\sigma = \sigma_0 \exp\left(\frac{-E_a}{k_B T}\right) \quad (5.7)$$

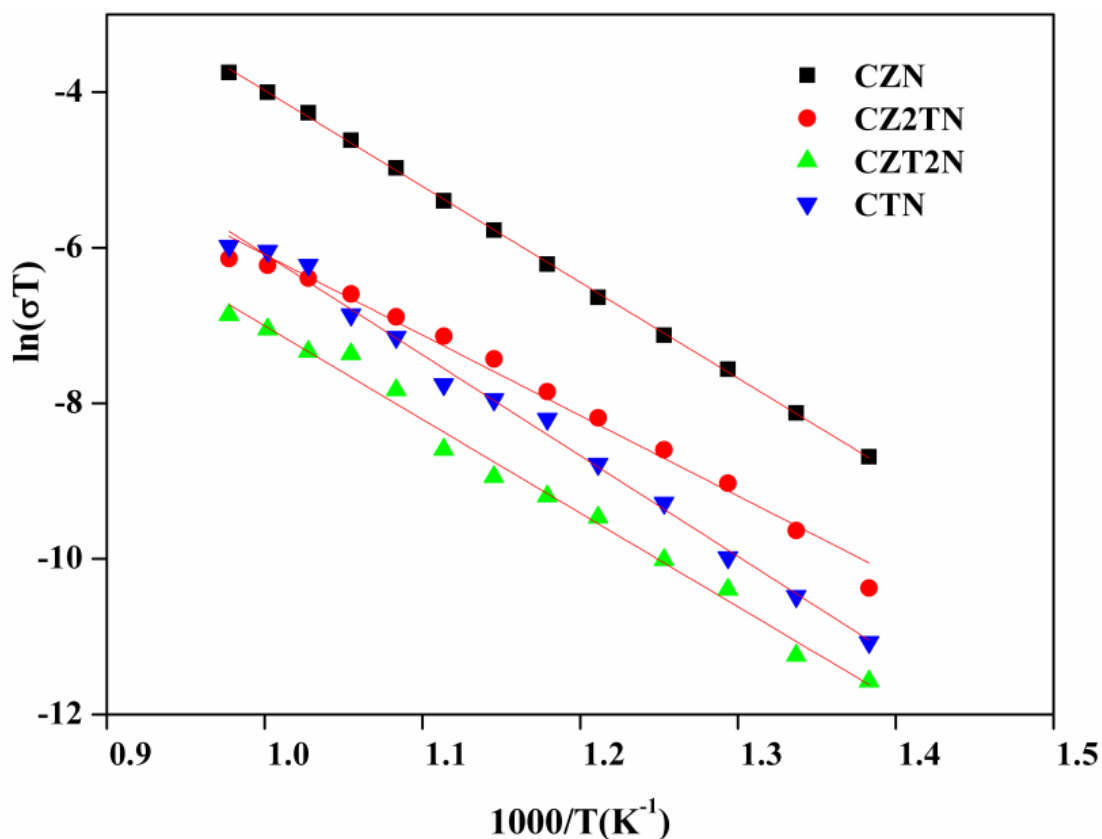


**Fig. 5.8** Arrhenius plot of the composition  $\text{CZ}_3\text{N}$ ,  $\text{CZ}_2\text{TN}$ ,  $\text{CZT}_2\text{N}$  and  $\text{CT}_3\text{N}$

The slope of the Arrhenius plot gives the activation energy for the conduction, and the intercept of the straight line gives the pre-exponential factor, which is a measure for available charge carriers. The variation of activation energy and conductivity is shown in Fig. 5.9. The activation energy calculated here is almost in agreement with the activation energy calculated from the frequency plot. The agreement in these values shows that the conduction and relaxation have the same origin.

The Fig. 5.9 shows that the activation energy increase with the Zr substitution as observed in the case of the ideal pyrochlore structure (Gunn *et al.* 2012). However, for the composition containing only zirconium the activation energy decreases and this effect may be due to the presence of single B cation in the monoclinic structure whose B cation is much

more ordered compared to the pyrochlore (Bazuev and Chupakhina 2009). The conductivity of the composition also goes in hand with the activation energy. The conductivity decreases by order as the Zr content increases. The maximum conductivity is obtained for CT<sub>3</sub>N composition with cubic pyrochlore structure which is an order of magnitude higher than the reported conductivity for displaced pyrochlore (Pandey *et al.* 2018).

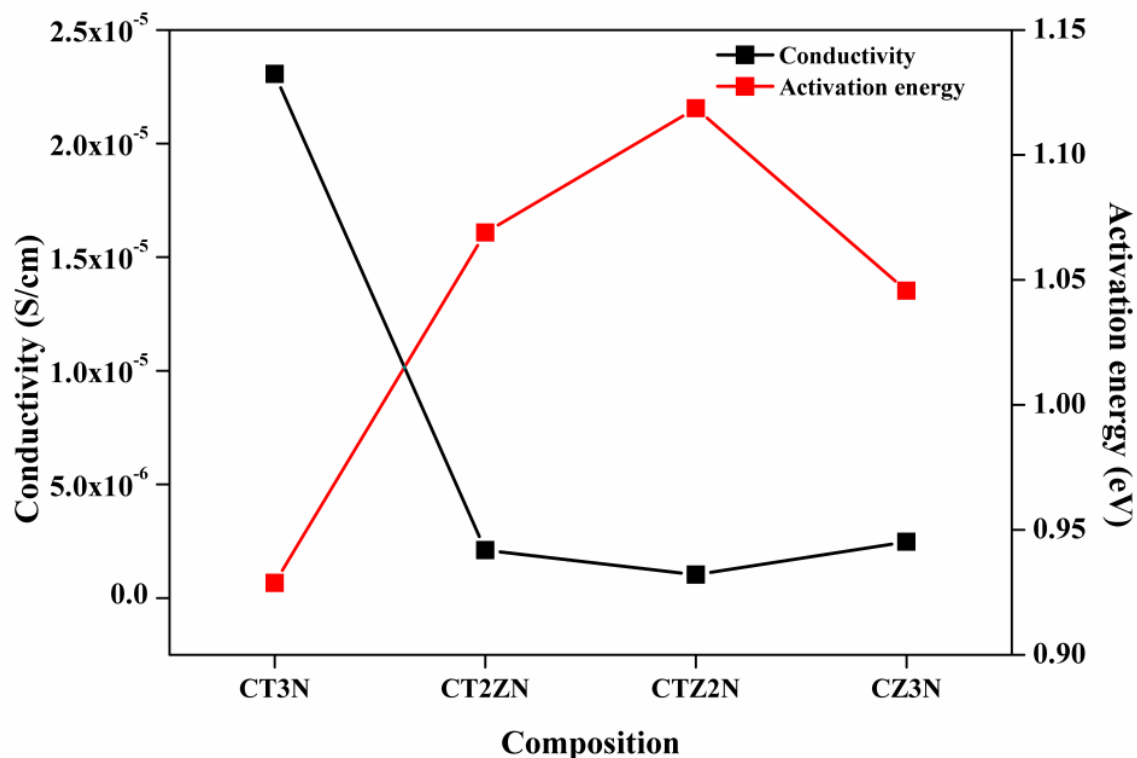


Fig. 5.9 The variation of conductivity at 1023K and activation energy with compositions

## 5.4 Conclusions

A series of displaced pyrochlore structured compositions  $\text{Ca}_3\text{Ti}_3\text{Nb}_2\text{O}_{14}$ ,  $\text{Ca}_3\text{Ti}_2\text{ZrNbO}_{14}$ ,  $\text{Ca}_3\text{TiZr}_2\text{Nb}_2\text{O}_{14}$  and  $\text{Ca}_3\text{Zr}_3\text{Nb}_2\text{O}_{14}$  were synthesised via conventional solid state reaction method. The structural studies on the series confirmed the transition from the cubic pyrochlore to the monoclinic pyrochlore as the zirconium doping in the series increases. The transition occurs from the cubic to the monoclinic due to the placement of smaller transitional cation on the interstices of the  $\text{B}_2\text{O}_6$  octahedra. The conductivity also varies as Zr content increases. The activation energy increases for the composition with Zirconium content. A small decrease in the activation energy occurs when the Zr content fully replaces the Ti in the composition. The conductivity also goes in line with the change in the activation energy. Maximum ionic conductivity is obtained for the composition  $\text{Ca}_3\text{Ti}_3\text{Nb}_2\text{O}_{14}$ , which is an order of magnitude higher than the reported ionic conductivity for the displaced pyrochlore.

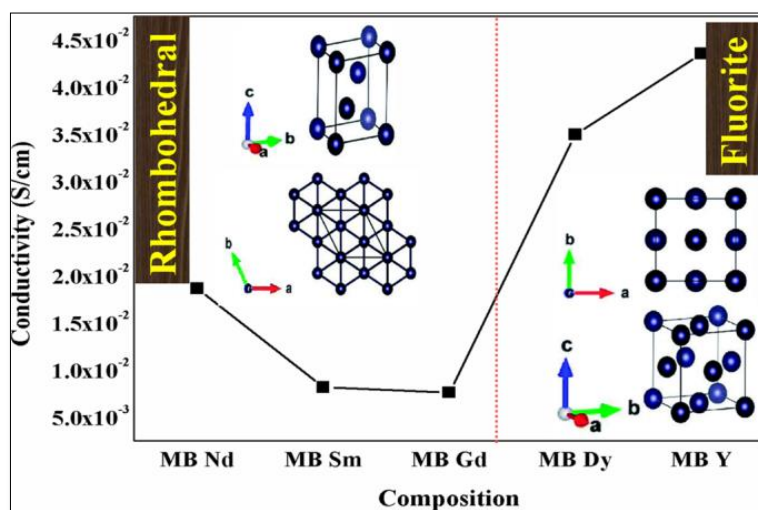




# Chapter 6

## Structural Stabilization of $\delta$ -phase $\text{Bi}_2\text{O}_3$ in the $\text{MgBi}_{1.5}\text{RE}_{0.5}\text{O}_4$ System through Rare Earth Substitution for Improved Ionic Conductivity

*The present study is an attempt to stabilise the highly conductive  $\delta$ -phase of the  $\text{Bi}_2\text{O}_3$  via aliovalent and isovalent substitution. The series of the composition exhibits a phase transition from rhombohedral to fluorite structure depending on the ionic radius of the rare-earth ion substituted. The conductivity of the rhombohedral composition is lower than that of the fluorite ones. In the rhombohedral composition, the conductivity decreases with a decrease in the lattice volume and in the case of the fluorite composition conductivity increases with a decrease in the lattice volume. The variation in the trend of the conductivity is due to the transformation of Dy substituted composition from cubic to rhombohedral*



*at a temperature of 773K. The maximum conductivity and better stability are obtained for Y substituted composition.*

*Ionics (communicated)*



## 6.1 Introduction

Oxide ion conductors have become the subject of intense research over the last century because of their varied applications in the field of solid oxide fuel cell (SOFC), oxygen sensors, dense ceramic membranes for oxygen separation, membrane reactors for oxidative catalysis etc. (Boivin 2001). In these materials, the conductivity of oxide ions occurs mainly through the vacancy mediated transport mechanisms. Some other types of transport mechanisms are also involved in a few numbers of oxide ion conductors. Therefore, in the development of oxide ionic conductors, the structure of the materials plays a crucial role. It has to have some peculiar features such as the existence of a large number of equivalent sites for the oxide ions and oxygen vacancies, high symmetry for the crystal system (most of the best oxide ion conductors are cubic), large specific free volume, and high polarizability of the cations in the system to make the transport of oxide ion easier (Boivin 2001; Hayashi *et al.* 1999; Sammells *et al.* 1992). Consequently, a limited number of crystalline systems are suitable to develop as oxide ionic conductors.

Fluorite structured oxides are one of the crystalline systems that exhibit high oxide ion conductivity and hence have been extensively studied. The general formula for the fluorite structure is  $AO_2$  where A is a tetravalent cation. The cations are eight coordinated by anion and anions are in tetrahedral coordination with the cations (Navrotsky 2010). An additional oxygen vacancy for the conduction oxide ions can be generated by doping the system with acceptor cations. One of the most studied, oldest and currently using and commercially viable oxide ion conductors for SOFC applications is yttria stabilised zirconia (YSZ) in which zirconia is stabilised in the fluorite structure by doping with yttria (Malavasi *et al.* 2010; Scott 1975). However, the high operating temperature (1000°C) makes the price of YSZ based fuel cells high, and small scale usage is impractical. Another type of fluorite type structured composition is  $CeO_2$ . Trivalent cations are introduced into  $CeO_2$  to generate oxide vacancies in the system (Scott 1975). Commercially used dopants for  $CeO_2$  are  $Gd_2O_3$  and  $Sm_2O_3$ , and the resulting systems are known as Gadolinium-Doped Ceria (GDC) and Samarium Doped Ceria (SDC) (Malavasi *et al.* 2010). These compositions have higher ionic conductivity compared to the YSZ at a lower temperature range of 500-700°C. However, they suffer from electronic conduction at higher temperatures and low oxygen partial pressure, which limits their commercial use.

$\text{Bi}_2\text{O}_3$  based oxides are an important class of materials that exhibit good oxide ion conductivity. These oxides find applications in the field of paint formulations, photovoltaic cells, oxygen sensors and oxygen pumps.  $\text{Bi}_2\text{O}_3$  exhibit many polymorphs:  $\alpha$ -  $\text{Bi}_2\text{O}_3$  (monoclinic),  $\beta$ -  $\text{Bi}_2\text{O}_3$  (tetragonal),  $\gamma$ -  $\text{Bi}_2\text{O}_3$  (cubic, bcc),  $\delta$ -  $\text{Bi}_2\text{O}_3$  (cubic, fcc)  $\varepsilon$ -  $\text{Bi}_2\text{O}_3$  (orthorhombic),  $\omega$ -  $\text{Bi}_2\text{O}_3$  (triclinic) with two non-stoichiometric phases ( $\text{Bi}_2\text{O}_{2.33}$  and  $\text{Bi}_2\text{O}_{2.75}$ ).  $\delta$ -  $\text{Bi}_2\text{O}_3$  possesses a defect fluorite structure and is known to have the best oxide ion conductivity. (However,  $\delta$ -  $\text{Bi}_2\text{O}_3$  is stable only above  $\approx 730^\circ\text{C}$  and exists up to its melting point, which is approximately  $825^\circ\text{C}$  (Yilmaz *et al.* 2011).

$\delta$ -  $\text{Bi}_2\text{O}_3$  is characterised by an oxygen sublattice with a high fraction of oxygen vacancies which causes the high oxide ion conductivity in the system which is two orders of magnitude higher than that of zirconia (Fung and Virkar 1991). Other factors that account for high oxide ion conductivity of this phase are high mobile of oxide ions due to weaker Bi-O bonds and the high polarizability of  $\text{Bi}^{3+}$  with its lone pair of  $6s^2$  electrons. Much research is being carried out to stabilise  $\delta$ -  $\text{Bi}_2\text{O}_3$  to room temperature by partially replacing bismuth by isovalent and aliovalent cation in the systems.  $\text{Y}_2\text{O}_3$ ,  $\text{Nb}_2\text{O}_5$ ,  $\text{WO}_3$ ,  $\text{Er}_2\text{O}_3$  etc. have been identified as suitable dopants maintaining good ionic conductivity in stabilised  $\delta$ -phase (Meng *et al.* 1988). The stabilisation of  $\text{Bi}_2\text{O}_3$  in the cubic phase depends on the particular dopant ion, dopant concentration, heat treatment to make the compositions and cooling rate in the preparation methods (Yilmaz *et al.* 2011). Studies involving  $\text{Eu}_2\text{O}_3$  on the  $\text{Bi}_2\text{O}_3$  causes a phase transformation only at a higher temperature and the conductivity of the composition increases with increase in the  $\text{Eu}_2\text{O}_3$  doping (Yilmaz *et al.* 2011). In the composition involving double stabilizers, it can be seen that overall amounts of dopant which are needed to stabilise the  $\delta$  phase down to the room temperature are reduced and a small amount of second dopants causes an increase in the ionic conductivity and further doping decreases the conductivity due to its complex behaviour (Meng *et al.* 1988). The highest oxide ion conductivities are obtained for the systems with the lowest doping concentration which is needed to stabilise the  $\delta$  phase (Malavasi *et al.* 2010) which can be facilitated by the use of double stabilisers.

The study shows that tetravalent doping along with  $\text{Y}_2\text{O}_3$  in  $\text{Bi}_2\text{O}_3$  favours the cubic phase formation and at the same time, the divalent cations ( $\text{Ca}^{2+}$ ,  $\text{Sr}^{2+}$ ) transforms to rhombohedral at room temperature. The enhanced stability in tetravalent cation is due to the reduced cation interdiffusion (Fung and Virkar 1991). In addition to this recent studies have

shown that conductivities of the compositions are also improved with double trivalent doping (Polat *et al.* 2017).  $\text{WO}_3$  and  $\text{Dy}_2\text{O}_3$  doped  $\text{Bi}_2\text{O}_3$  were found to have maximum stability for the delta-phase, and this is due to the decreased concentration of  $\text{Dy}_2\text{O}_3$  to stabilise the  $\delta$  phase (Jung *et al.* 2016). In one of the recent study, the  $\text{Bi}_2\text{O}_3$  was stabilised using two trivalent cation  $\text{Gd}_2\text{O}_3$  and  $\text{Lu}_2\text{O}_3$  and the prepared compositions are found to be good oxide ion conductors (Polat *et al.* 2017). Thus these studies showed that double doping favours the stabilisation of  $\delta$ - $\text{Bi}_2\text{O}_3$  and causes increased ionic conductivity.

Earlier studies have shown that the  $\delta$ -phase exhibits higher ionic conductivity than other polymorphs of  $\text{Bi}_2\text{O}_3$ , but the stabilisation of the phase is hardly achieved. In this regard, the stabilisation of the  $\delta$ -phase of  $\text{Bi}_2\text{O}_3$  substituted with rare earth elements and  $\text{Mg}^{2+}$  is attempted in the compositions  $\text{MgBi}_{1.5}\text{RE}_{0.5}\text{O}_4$ , (RE = Nd, Sm, Gd, Dy, Y). The electrical properties of the compositions are also studied in detail. These compositions undergo a phase transformation from rhombohedral to fluorite structure. However, the effect of total dopant concentration and dopant ratio on structure and conductivity of these bismuth oxide-based electrolytes has still not been thoroughly investigated. In this study, different rare-earth dopants are selected to study the influence on the structure and electrical properties of these systems.

## 6.2 Experimental

Compositions with the general formula,  $\text{MgBi}_{1.5}\text{RE}_{0.5}\text{O}_4$ , (RE = Nd, Sm, Gd, Dy, Y) were prepared via solid-state reaction route. Commercially available  $\text{MgO}$ ,  $\text{Bi}_2\text{O}_3$ ,  $\text{Dy}_2\text{O}_3$ ,  $\text{Gd}_2\text{O}_3$  (Sigma Aldrich 99.999%),  $\text{Nd}_2\text{O}_3$ ,  $\text{Sm}_2\text{O}_3$  (Alfa Aesar 99.99%), and  $\text{Y}_2\text{O}_3$  (Sigma Aldrich 99.995%) were weighed stoichiometrically and were mixed thoroughly in an agate mortar in acetone medium with intermittent drying to attain maximum homogeneity in the mixture. The mixture was calcined at  $1000^\circ\text{C}$  for 6h. The powdered calcination product was pressed into a small cylindrical pellet of 10 mm diameter using a hydraulic press at a pressure of 25MPa and then sintered at a temperature  $1050^\circ\text{C}$  for 10h.

The phase purity of sintered samples at room temperature was analysed using an X-ray diffractometer (X'pert Pro, PANalytical) employing  $\text{Cu K}\alpha_1$  radiation with a wavelength of  $1.54060\text{\AA}$ . XRD data were recorded in the  $2\theta$  range from  $10^\circ$  to  $90^\circ$ . The morphology of the sample surface was analyzed using a Scanning Electron Microscope (SEM, Jeol JSM 5600LV). Thermal stability of the prepared samples was examined by differential thermal analysis (Thermogravimetry/ Differential thermal analyser, SII TG, DTA 6200) in the

temperature range from room temperature to 1273K. Electrical characterisation of the sintered pellets was carried out using an Impedance Spectrometer (Solartron SI 1260) with a Dielectric Interface (Solartron 1296). Electrodes were applied by painting silver paste over the flat polished surfaces of the cylindrical pellets. Silver wires were used to connect the samples to the Frequency Response Analyzer via the dielectric interface. The measurement was done in air atmosphere in the frequency range from 1Hz to 1MHz at various temperatures from 200 to 750°C.

### 6.3 Results and Discussion

$\text{MgBi}_{1.5}\text{RE}_{0.5}\text{O}_4$  (RE = Nd, Sm, Gd, Dy, Y) compositions were prepared via the conventional solid-state reaction route. The compositions thus prepared were characterised using powder X-ray diffraction, scanning electron microscopy and impedance spectroscopy. The samples are named MBRE for identification.

#### 6.3.1 Powder X-ray diffraction

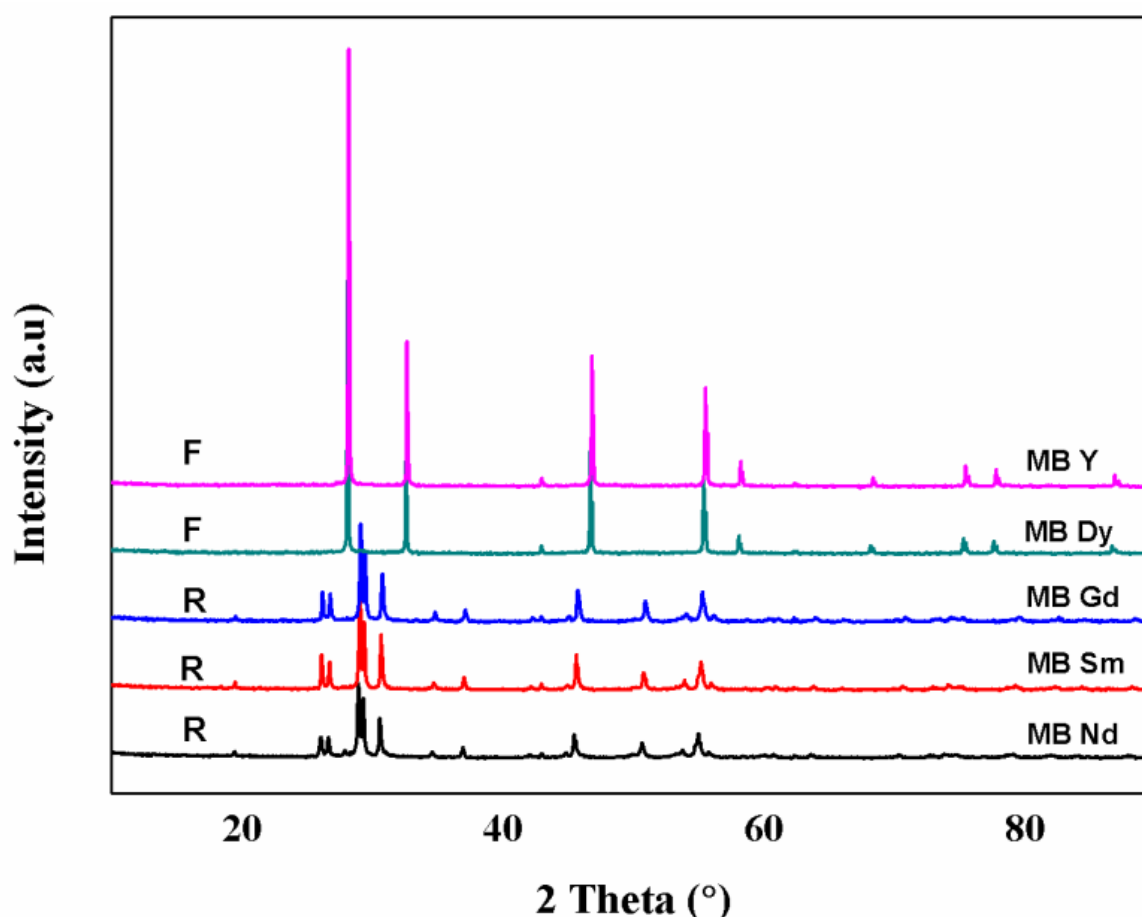
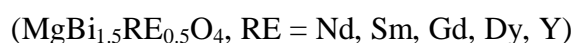


**Fig. 6.1** The X-ray powder diffraction patterns of the compositions



The X-ray powder diffraction patterns of the compositions are shown in Fig. 6.1. The set of diffraction patterns indicate that all the compositions were formed in a single phase. The compositions MBNd, MBSm and MBGd form in the rhombohedral (trigonal) crystal system with R-3m space group. The remaining compositions exhibit a cubic fluorite structure in a space group Fm3m space group. The formation of the trigonal or cubic crystal systems depends on the doped ionic species and composition (Jung *et al.* 2016). Doping Bi<sub>2</sub>O<sub>3</sub> with lanthanides having larger ionic radius such as Gd<sup>3+</sup> usually results in the formation of products with the rhombohedral structure (Jiang and Wachsman 1999; Takahashi *et al.* 1975). This is seen in this present work also. The compositions doped with Gd<sup>3+</sup> and other larger ionic radii lanthanides are exhibiting the rhombohedral structure.

In the rhombohedral structure, bismuth and oxygen ions occupy the Wyckoff positions 1a (0, 0, 0) and 2c (x, x, x). In most recent studies, on the rhombohedral structure, it shows at least three oxide ion sites are fully occupied, and two are partially occupied. The whole structure looks as follows: The structure is layered, consisting of neutral fluorites like sheets containing three layers of cations perpendicular to the c-axis and a van der Waals gap between the sheets. O(1) is located on the near the centre of the (M, Bi)<sub>3</sub>Bi tetrahedron and O(2) is located off centre in the Bi<sub>3</sub>(M, Bi) tetrahedron (M is the dopant cation) (Boivin and Thomas 1981). The lattice parameter and lattice volume is calculated using the following equations:

$$\frac{1}{d^2} = \frac{\{(h^2+k^2+l^2)\sin^2\alpha+2(hk+kl+lh)(\cos 2\alpha-\cos\alpha)\}}{a^2(1-3\cos 2\alpha+2\cos^3\alpha)} \quad (6.1)$$

$$\mathbf{Volume} = a^3 \sin \alpha \quad (6.2)$$

In the case of fluorite structured compositions, the cation occupies the 4c site, and the anions occupy the 8c and 32f Wyckoff positions. The lattice parameters are calculated:

$$\frac{1}{d^2} = \frac{(h^2+k^2+l^2)}{a^2} \quad (6.3)$$

$$\mathbf{Volume} = a^3 \quad (6.4)$$

The lattice parameter and the volume of the prepared compositions are listed in Table 6.1, which shows the variation in the lattice parameter and volume for various rare earth substitutions.

**Table 6.1** Lattice Parameter and Volume of the Compositions  $\text{MgBi}_{1.5}\text{RE}_{0.5}\text{O}_4$ , (RE = Nd, Sm, Gd, Dy, Y)

Composition	Lattice parameter (Å)	Angle $\alpha$ (degrees)	Volume (Å <sup>3</sup> )
MBNd	9.4011 (5)	24.6133 (30)	125.8953
MBSm	9.3828 (3)	24.5264 (21)	124.8086
MBGd	9.3735 (2)	24.5043 (46)	124.0758
MBDy	5.5001 (6)		166.375
MBY	5.4855 (2)		165.0626

### 6.3.2 Scanning electron microscopic studies

The surface morphology of the sintered pellets of the compositions was analysed using the scanning electron microscopy. The size and shape of the grains and the porosity analysis of the compositions can also be derived using these images. The cross-sectional images of the present compositions are shown in Fig. 6.2. The grain size shows a gradual increase from Nd to Dy samples. All the compositions show well-sintered grains, less porosity and perfect grain boundaries.

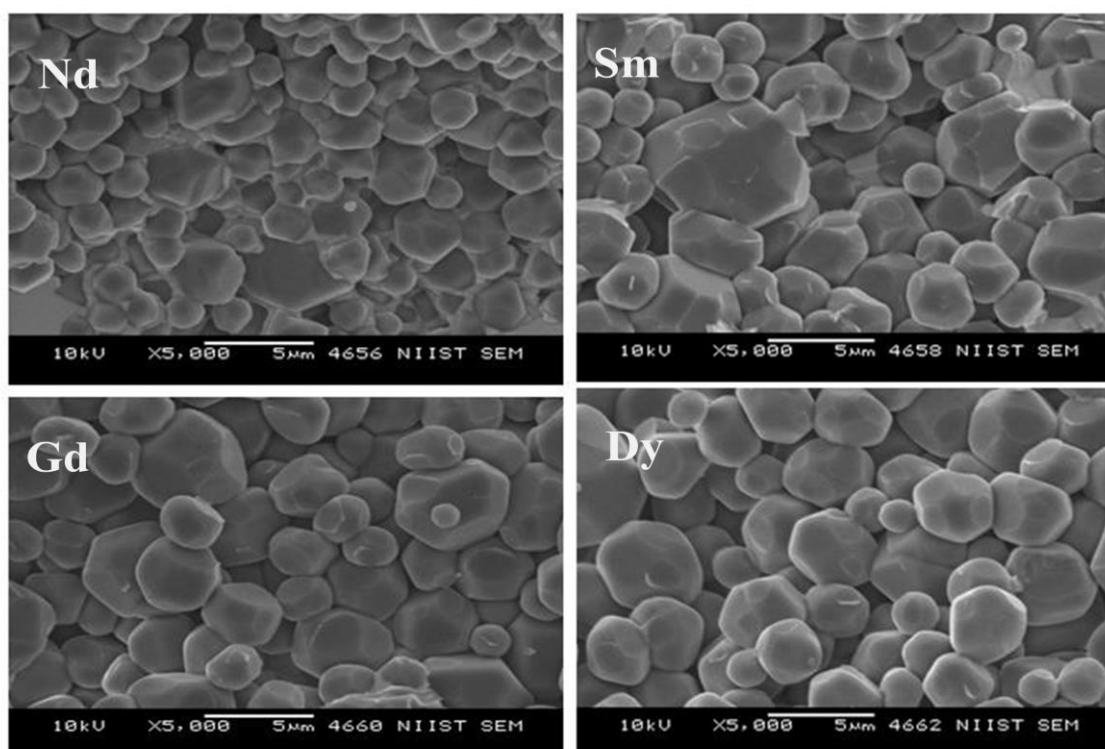


**Fig. 6.2** Cross-sectional SEM images of compositions  $\text{MgBi}_{1.5}\text{RE}_{0.5}\text{O}_4$ , RE = Nd, Sm, Gd, Dy



The chemical compositions are confirmed using the EDAX analysis. The results are in line with the proposed compositions. The homogeneity of the elements in the compositions is also established with elemental X-ray dot mapping. The EDAX analysis and X-ray dot mapping images of a representative sample (MBY) are shown in Fig. 6.3.

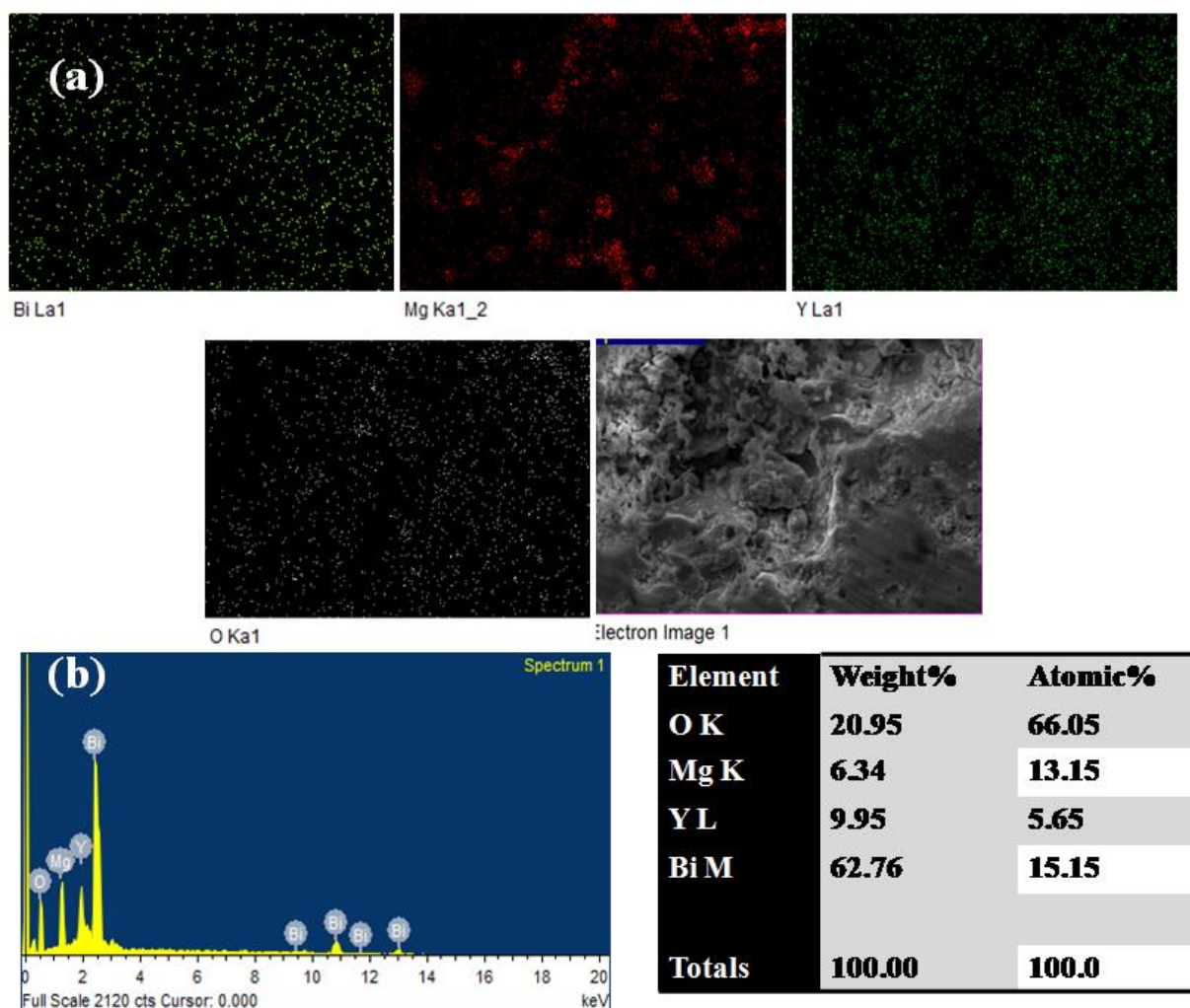


**Fig. 6.3** (a) Elemental dot mapping of the composition MBY. (b) EDAX results for composition MBY

### 6.3.3 Thermal stability studies.

The thermal stability and structural change during the heat treatment of the prepared MBY and MBdy samples were analysed using TG-DTA (Thermogravimetry- Differential Thermal Analysis) (Suzuki and Yoshikawa 2004). The DTA curves for the samples mentioned above are shown in Fig. 6.4. The DTA curve of the MBdy samples shows an endothermic peak at about 773K. The transformation from cubic to rhombohedral  $\text{Bi}_2\text{O}_3$

related systems is accompanied by an endothermic peak in the DTA curve (Chou, Liu, and Wei 2011b). This phase transformation in MBDy samples reduced the electrical conductivity as seen in the latter part of the text. Such a transformation is absent in the MBY sample.

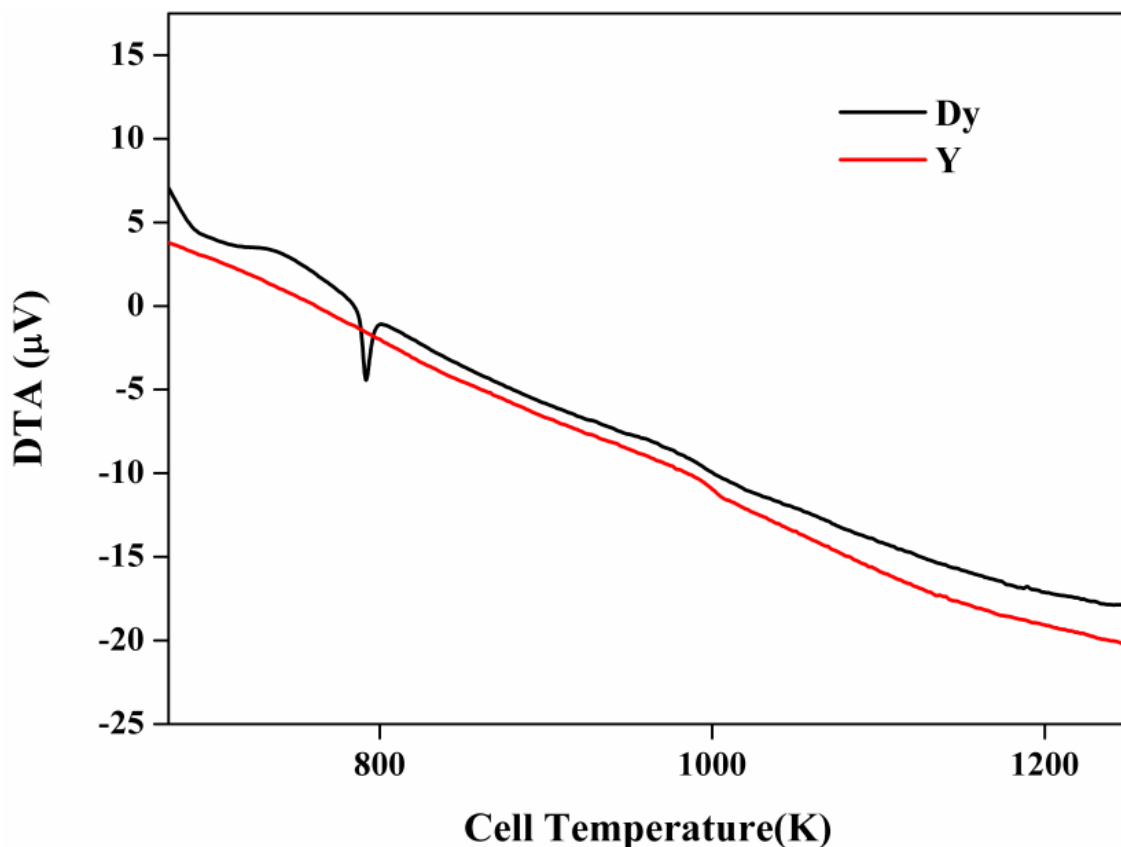


**Fig. 6.4** DTA curves of the samples MBDy and MBY

### 6.3.4 Conductivity Studies

A.C impedance spectroscopy is an essential tool for studying the ionic conductivity of the ceramic oxide and is an efficient tool for separating the grain, grain boundary and interfacial contribution to the bulk conductivity. The study of the conductivity is done over a wide range of frequencies (Lai 2007). In the present study, the conductivity of the samples in the frequency range from 1Hz to 1MHz within the temperature range of 573 to 1023K is measured with ac stimulus of 100mV.

The complex impedance spectra of the samples are shown in Fig. 6.5. The Cole-Cole plot of the imaginary part of ac impedance against its real part shows that semicircles are originated from the dielectric behaviour of the solid samples at various temperatures. The semicircles end up in a short spike at their low frequency ends. This shows an increase in capacitive reactance at the electrode-sample interface due to the accumulation of ions there

and is consistent with the conduction mechanism being predominantly ionic (Sibi *et al.* 2009). The intercept of the impedance arc with the real axis gives the resistance of the material. It can be seen from the figure that the radii of the impedance arcs diminish with increasing temperature, which indicates that the conduction is thermally activated.

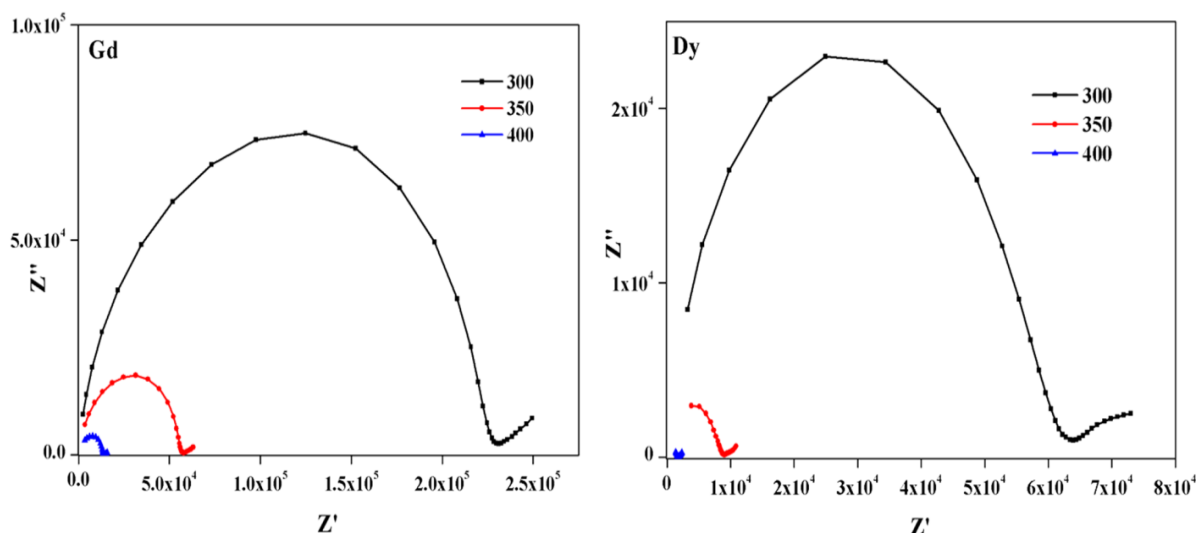


**Fig. 6.5** The complex impedance spectra of the representative samples of the compositions  $\text{MgBi}_{1.5}\text{RE}_{0.5}\text{O}_4$  (RE = Nd, Sm, Gd, Dy, Y)

The value of the total resistance from the impedance spectrum at various temperatures was determined from the point of intersection of the spectrum with the real axis. The ac conductivity of the sample can be calculated using the geometrical parameter and resistance of the sample as done elsewhere. The temperature dependence of the total conductivity is usually described by the Arrhenius equation, and the Arrhenius plot of the prepared composition is shown in Fig. 6.6. The values of activation energy were calculated from the slope of the straight line for each composition and summarised in Table 6.2. The activation energy increases with decreasing radius of the dopant ion. The increased activation energy is attributed to the decreased lattice volume. The studies of the Wakamura implies that the activation energy and lattice volume possess an inverse relation as  $E_a = A_v V^{-2/3}$ , where  $A_v$  is a constant (Wakamura 2009).

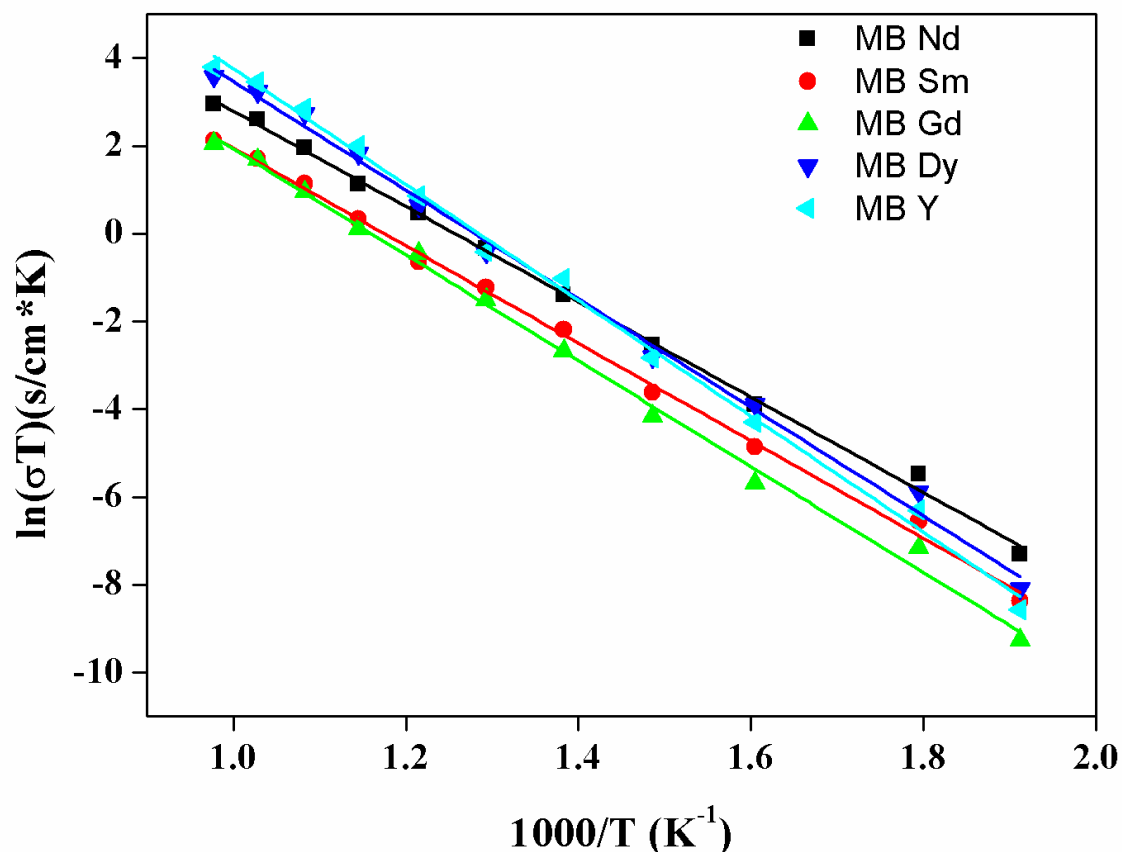


**Fig. 6.6** Arrhenius plot of the compositions  $\text{MgBi}_{1.5}\text{RE}_{0.5}\text{O}_4$ , (RE = Nd, Sm, Dy, Gd, Y)

**Table 6.2** The total conductivity at 1023K and activation energy of the compositions  $\text{MgBi}_{1.5}\text{RE}_{0.5}\text{O}_4$ , (RE = Nd, Sm, Dy, Gd, Y)

Compositions	Conductivity ( $\times 10^{-3}$ S/cm)	Activation Energy (eV)
MBNd	18.639	0.97
MBSm	8.1614	0.98
MBGd	7.6086	1.06
MBDy	32.793	1.08
MBY	43.675	1.16

The variation of total conductivity of the compositions with the rare earth is shown in Fig. 6.7. The conductivity of the rhombohedral structures  $\text{Bi}_2\text{O}_3$  based conductivity is one order of magnitude less conductive than that of the fluorite structured  $\text{Bi}_2\text{O}_3$  based ionic conductors (Wakamura 2009). The conductivity of the compositions at 1023K decreases for the rhombohedral compositions and then increases for the fluorite structured compositions.

The decrease in conductivity for the rhombohedral compositions is due to the decrease in lattice volume and increased activation energy. In addition to these changes in the structural changes, the whole conduction mechanism changes, and it goes from being a 3D conductor to a 2D conductor. After that, the conductivity of the fluorite structure compositions increases.

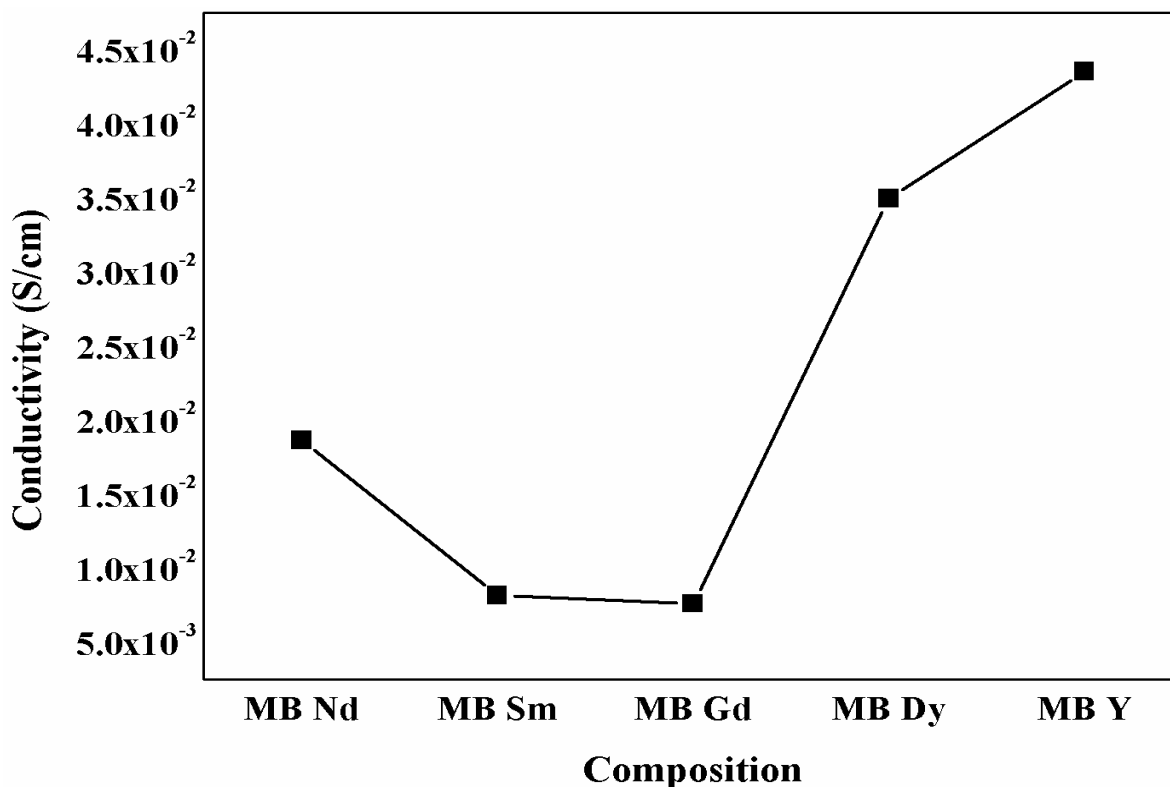


**Fig. 6.7** Variation of Total conductivity of the compositions  $\text{MgBi}_{1.5}\text{RE}_{0.5}\text{O}_4$ , (RE = Nd, Sm, Dy, Gd, Y) at 1023K

On close inspection, it is found that the conductivity of the MB Dy samples is high compared to that of MB Y in the low-temperature region below 773K. After heating the MB Dy samples above 773K, the conductivity is lowered compared to MB Y. The change in the conductivity of the MB Dy and MB Y compositions with temperature is shown in Fig. 6.8. The literature reviews show that the stabilised  $\delta\text{-Bi}_2\text{O}_3$  doped with rare earth transforms to the rhombohedral structure on heating at an intermediate temperature and thus causes conductivity to decrease, i.e. the fluorite structure MB Dy on heating to 773K transforms to the rhombohedral structure and thus its conductivity is lowered compared to that of MB Y (Omari *et al.* 1990; Takai *et al.* 1998). High-temperature XRD studies on the  $\text{Bi}_2\text{O}_3\text{-Y}_2\text{O}_3\text{-PbO}$  solid solution shows that in the temperature range 500-720°C a Bi-Sr-O type rhombohedral structure formed and is associated with a decrease in the ionic conductivity (Omari *et al.* 1990). Diffuse scattering techniques studies on the stabilised  $\delta\text{-Bi}_2\text{O}_3$  reveal that

the structure contains small, ordered microdomains of rhombohedral structure within the overall fluorite structure (Boivin and Thomas 1981). Thus the fluorite structure is locally destabilised and distorts locally to a lower symmetry with conductivity lower than that of  $\text{Bi}_2\text{O}_3$  (Verkerk *et al.* 1982). Literature reviews of the  $\text{Bi}_2\text{O}_3$  based oxygen ion conductors reveal that such a transformation also occurs for the  $\text{Y}_2\text{O}_3$  doped compositions, but in the present work, the MBY composition maintains its fluorite structure up to 1023K. That is the fluorite structured MBY that is having the maximum conductivity is stable up to 1023K.

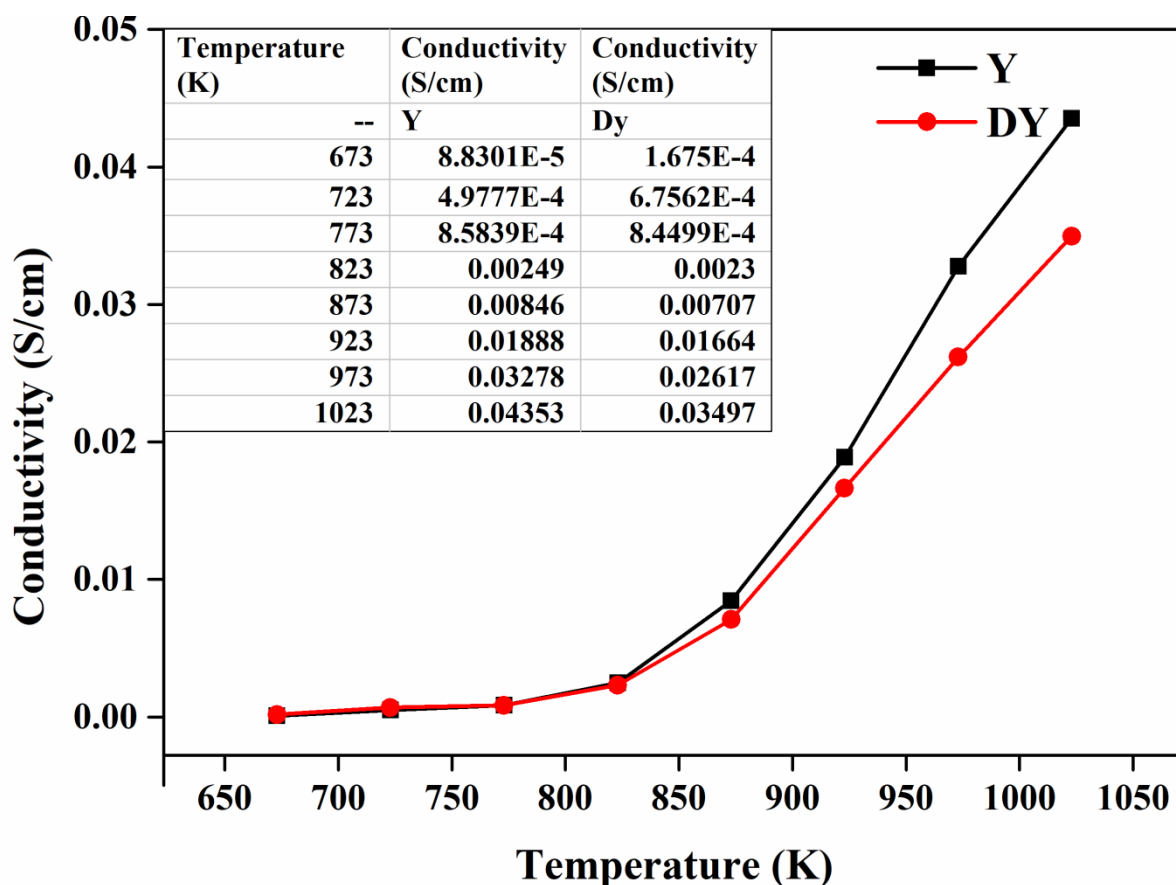


Fig. 6.8 The variation of conductivity of the compositions MBDy and MBY with the temperature

## 6.4 Conclusions

The  $\text{MgBi}_{1.5}\text{RE}_{0.5}\text{O}_4$ , (RE = Nd, Sm, Dy, Gd, Y) compositions were synthesised using conventional solid-state reaction route. The prepared compositions were characterised using powder X-ray diffraction, scanning electron microscopy, thermogravimetry analysis and impedance spectroscopy. All the prepared compositions are phase pure and the compositions exhibit a phase transformation from the rhombohedral (for larger rare-earth ions) to the cubic fluorite (for smaller ones) structures. The conductivity of the rhombohedral structured compositions is found to be less conductive compared to the fluorite structured ones, and the conductivity decreases as the lattice volume decreases and as the activation energy increases. In the case of fluorite structured compositions, despite having higher lattice volume and smaller activation energy, MBdy has smaller ionic conductivity at 1023K compared to MBY. The smaller ionic conductivity is due to the phase transformation from fluorite to rhombohedral at a temperature of about 773K. The composition MBY continues to be in the fluorite structure up to 1023K.





# Chapter 7

## Conclusions and Future Scope

---

---

The present chapter summarises the conclusions drawn from the investigation carried out in the present research work. Some general conclusions derived from the study are also listed in the chapter. A comparison of the present research work with the existing literature survey is made. On the last part of the chapter, the future aspects of the present work are also discussed.

---

---



## 7.1 Conclusion

The present research work is an attempt to study the structural factors affecting the ionic conductivity of the rare earth mixed oxides. The work is mainly concentrated on the pyrochlore type composition, and the last part of the thesis is an attempt to stabilise the  $\delta$ - $\text{Bi}_2\text{O}_3$  with aliovalent and isovalent substitutions. The study is a fundamental one that can be considered as the guidelines on designing of new oxide ion conductors. The study explores the correlation between the oxide ion conductivity, crystallography and chemical nature of the atoms. The conclusions drawn from the study are listed below:

- Influence of phase transition and Phillips ionicity on the thermal expansion coefficient and oxide ion conductivity of pyrochlore type compositions with multivalent cations on the B-site is studied by preparing a new series of composition  $\text{RE}_2\text{Y}_{2/3}\text{Zr}_{2/3}\text{Nb}_{2/3}\text{O}_7$  (RE = La, Nd, Sm, Gd, Dy and Y). The series of composition were prepared via solid-state reaction method.
- The series exhibits a phase transition from pyrochlore to fluorite based on the radius ratio of the A and B cation. The composition with RE = La, Nd and Sm have pyrochlore structure and the remaining ones with Gd, Dy and Y have fluorite structure. As the ionic radius of the lanthanide ions in the composition decreases the intensity of the superlattice peaks decreases.
- The lattice parameter of the composition decreases as the ionic radius of the lanthanide ions decreases. Raman spectroscopy studies also confirm the structural transition and the lattice parameter decrease.
- The crystal chemistry of the pyrochlore type oxides with multivalent cation is analysed using the Phillips and Van Vechten theory. Most of the physical properties of the crystal systems depend on the chemical nature of the bond in the system. In the case of complex crystal structure, each bond is characterised an energy gap  $E_g$  which arises from the bonding and antibonding of hybridised molecular orbitals resulting in two types of energy gap: namely homopolar energy ( $E_h^h$ ) and heteropolar energy ( $C^h$ ). These energy gaps result in the ionic and covalent character in the bonds. The square of the ratio of homopolar or heteropolar energy to the total energy gap is termed as fractional covalency or ionicity. The calculation of the fractional ionic and covalent behaviour can

provide a lot of qualitative and quantitative explanations based on the coordination number, nearest neighbour distances, active number of valence electrons on the cation and anion.

- The fractional ionicity of the A-O and B-O bonds was calculated, and as in the literature survey, the B-O bond has higher strength, and thus B-O has higher covalency. The ionicity of the A-O bond decrease as the ionic radius of the lanthanide ion decreases except for  $\text{Nd}^{3+}$ . The polarizability value of the  $\text{Nd}^{3+}$  is very high, so that the covalency of the bond increases.
- The thermal expansion coefficient of the pyrochlore structured composition mainly depends on the A-O bond, and that of the fluorite structured compositions depends on the difference in ionicity. In the case of the pyrochlore structured composition the A-O bond expands more rapidly than the B-O bond, and thus TEC goes hand in hand with the A-O bond whereas in fluorite structured composition when the difference in the ionicity decreases the oxygen position becomes unstable and the thermal expansion coefficient increases with the decrease in the difference in ionicity.
- The oxide ion conductivity also depends on the ionicity. When the difference in ionicity is small, the oxygen position becomes unstable and thus the pre-exponential factor, which is a measure for the charge carriers present in the system increases. The activation energy for the pyrochlore structured composition increases as the ionicity increases and that of the fluorite structured composition increases with the decrease in the difference in ionicity. The total conductivity of the composition is the competing effect of the pre-exponential factor and the activation energy.
- Analysis of the thermal expansion coefficient, ionicity and oxide ionic conductivity of the system indicates an interrelationship among these parameters with structural dependence
- The effects of the anion disorder in  $\text{Sm}_2\text{Zr}_2\text{O}_7$  by aliovalent cation substitution, keeping the oxygen stoichiometry same is studied in detail in chapter 2.
- A new series of composition  $\text{Sm}_2\text{Zr}_{2-x}(\text{YNb})_{x/2}\text{O}_7$  ( $x = 0, 0.25, 0.5, 0.75, 1$ ) were prepared via conventional solid-state reaction method. All the composition falls

in the pyrochlore structure. As the substitution of Y and Nb increases the intensity of the superlattice peaks decreases and the lattice parameter increases. The increase in the lattice parameter is due to the increased effective ionic radius of the Y and Nb on the B site of the pyrochlore type composition.

- The bond length A-O<sub>1</sub>, A-O<sub>2</sub> and B-O<sub>1</sub> were obtained from the structural refinement. These bond length and oxygen x-parameter show some abnormal variation as the substitution increases. The A-O<sub>2</sub> depends on the lattice parameter and the bond lengths A-O<sub>1</sub>, and B-O<sub>1</sub> varies following the x-parameter of the 48f oxygen.
- The x-parameter of the O<sub>48f</sub> determines the shape of the AO<sub>8</sub> and BO<sub>6</sub> polyhedra. When  $x = 0.3125$ , BO<sub>6</sub> polyhedra become perfect octahedra and when  $x=0.375$  the coordination of A cation is a perfect cubic, and an intermediate value is for distortion on both polyhedra. In pyrochlore structured composition the major part of the distortion of the whole crystal system arises from the AO<sub>8</sub> polyhedra since the bond length A-O<sub>1</sub> and A-O<sub>2</sub> are different
- For the composition  $x = 0.25$ , the difference between the A-O<sub>1</sub> and A-O<sub>2</sub> bond length decreases and thus distortion AO<sub>8</sub> decreases which causes an increase in the x-parameter. It implies that BO<sub>6</sub> octahedra get more distorted than AO<sub>8</sub>.
- The literature survey on the Y and Nb substitution on the ZrO<sub>2</sub> show that at a lower concentration of Y and Nb, ZrO<sub>2</sub> destabilises and at higher concentration it stabilises the ZrO<sub>2</sub> and causes severe distortion in the surrounding cation networks. Such a phenomenon occurs here too when the doping concentration becomes  $x = 0.5$  the distortion of the AO<sub>8</sub> polyhedra increases and the x-parameter decreases.
- The lattice strain is calculated from the W-H plot and the strain calculated depends on the AO<sub>8</sub> polyhedra.
- The ratio of the intensity of the E<sub>g</sub> Raman mode at  $\approx 300 \text{ cm}^{-1}$  and T<sub>2g</sub> mode at  $800 \text{ cm}^{-1}$  goes in line with the oxygen x-parameter, and the ratio is a qualitative measure of the anion disorder. The anion disorder increases the charge carriers available for the conduction and thus the pre-exponential factor.

- The increased lattice parameter causes a decrease in the activation energy, and it is explained by the additional driving force caused by the strain for ion migration because the ion migration process relaxes the lattice strain and thus reduces the free energy of the system
- The conductivity of  $\text{Sm}_2\text{Zr}_2\text{O}_7$  can be primarily influenced by the simultaneous aliovalent cation substitution on the B site through anion disorder and lattice strain.
- A new series of anion deficient pyrochlore type compositions  $\text{RE}_3\text{Zr}_{0.5}\text{Nb}_{0.5}\text{O}_{6.75}$  (RE = Nd, Sm, Gd, Dy and Y) were prepared via a solid-state reaction method. All the compositions are in fluorite structure. Lattice parameter decreases with the decrease in the ionic radius of the lanthanide ions. Raman spectroscopic studies also confirmed the formation of defect fluorite structure.
- The conductivity studies on the series show that the conductivity decreases rapidly as the ionic radius of the lanthanide ion increases.
- When the number of charge carriers in the system increases the cooperative behaviour among the ions increases, and the effect is enhanced when the lattice volume decreases. Thus the activation energy increases exponentially with a decrease in the lattice volume.
- Thus the study reveals that in addition to the number of oxygen vacancies and activation energy, the cooperative behaviours of the oxide ion also plays a crucial role in determining the ionic conductivity. The effect of the induced oxygen vacancies on the ionic conductivity is maximum only when the lattice volume is also maximum on which the ion-ion interaction is minimum.
- The displacive pyrochlore was examined for the ionic conductivity which is not done in detail yet. The series exhibits a transition from the cubic pyrochlore to monoclinic pyrochlore depending on the ionicity of the B-O bond.
- The ionic conductivity reported for the current series of composition is an order of magnitude higher than the reported values for the same structure, and the maximum conductivity is obtained for the cubic pyrochlore  $\text{Ca}_3\text{Ti}_3\text{Nb}_2\text{O}_{14}$ .

- In the last chapter of the thesis, an attempt to stabilise  $\delta$ -Bi<sub>2</sub>O<sub>3</sub> is done. The series of compositions MgBi<sub>1.5</sub>RE<sub>0.5</sub>O<sub>4</sub> (RE = Nd, Sm, Gd, Dy, Y) exhibit a phase transition from rhombohedral to fluorite
- The conductivity of the compositions shows abrupt change as the structure changes from rhombohedral to fluorite structure.
- The activation energy increases with a decrease in the radius of the dopant ion decreases. The conductivity of the rhombohedral structure decreases due to the lesser lattice volume and increased activation energy
- The lower activation energy and high lattice volume in MgBi<sub>1.5</sub>Dy<sub>0.5</sub>O<sub>4</sub> does not favour the ionic conductivity at 1023K due to the phase transformation from fluorite to rhombohedral at a temperature of about 773K
- Thus the concentration of the dopant influence the ionic conductivity and the phase stability of the Bismuth based oxide ion conductors

In the present work, some of new oxide ion conductors were developed which have the potential to develop as the solid oxide electrolyte. The best conductivity obtained on the present study is for the anion deficient Nd<sub>3</sub>Zr<sub>0.5</sub>Nb<sub>0.5</sub>O<sub>6.75</sub> composition. However, the conductivity value is low compared to the one used for the practical application. However, the study of these compositions as in the real-time SOFC application is not done. In the case of bismuth-based composition, the best conductivity of the order of 10<sup>-2</sup> S/cm (at 750°C) and better stability is obtained for MgBi<sub>1.5</sub>Y<sub>0.5</sub>O<sub>4</sub> composition which is of the same order as that of the YSZ at 1000°C. The present research work reveals some of the structural factors that can be used in designing new oxide ion conductors and some of the general results that can be drawn from the study are listed below.

- Phillips ionicity is a crucial factor that determines the thermal expansion coefficient and oxide ion conductivity of the pyrochlore and fluorite structured oxides. In the pyrochlore structured oxides, the individual bonds play its role in determining the properties of the composition, but in the case of the fluorite structured oxides, the cumulative effect of the bonds take part in this.
- Lattice strain became an essential parameter in determining the activation energy of the pyrochlore structured composition and qualitative measurement of the anion disorder in the pyrochlore type composition can be done by measuring the

ratio of the intensity of the  $E_g$  Raman mode at  $\approx 300 \text{ cm}^{-1}$  and  $T_{2g}$  mode at  $800 \text{ cm}^{-1}$

- When the number of oxide vacancies is increased in the composition, the cooperative behaviour among the charge carriers increases, and it is further enhanced when the lattice volume decreases. Therefore in order to enhance the oxide ion conductivity via the introduction of oxide ion vacancies, the lattice volume should be concerned
- In the case of the displaced pyrochlore since the  $B_2O_6$  is rigid network in its ionicity plays a vital role in determining whether the formed structure is cubic or monoclinic and high conductivity is observed for the cubic displaced pyrochlore
- The stabilisation of the  $\delta\text{-Bi}_2\text{O}_3$  depends on the type of the dopant and the amount of the dopant

### 7.2 Future Scope

The upward trend in the global oil price, fall in the discovery of new oil wells and the depletion of current oil well demand the development and implementation of fuel cell technology. The concern for the environmental damage and pollution from the emission while burning fossil fuels also catalyses the development of the fuel cells. In the case of the SOFC, the electrolyte is termed as the heart of the solid oxide fuel cell. Hence the development of new solid oxide materials are that have ionic conductivity is essential. The present research work is only the initial stage in understanding the structural factor affecting the oxide ionic conductivity of the solid oxide electrolyte.

The present study is concentrated on the correlation between the structural parameters and the electrical conductivities of the rare earth mixed oxides. The microstructural optimisation is not done in the present since all the compositions in the present work were prepared via conventional solid-state reaction route followed by high-temperature calcination and sintering. In order to obtain the microstructural optimisation, low-temperature soft chemical methods to prepare the compounds can be used and using the soft chemical methods, the sintering temperature of the pellets can be reduced. The use of the sintering aide can also reduce the sintering temperature. Thus such a study in which different synthesis is used can help to study the effect of the microstructure on the oxide ion conductivity



In addition to this, improved characterisation techniques can give a lot more information about the oxide ion conduction mechanism. In the present work, the frequency range used is 1Hz to 1MHz. Expanding the frequency range above and below this frequency range will be helpful to understand the bulk, grain boundary and sample electron interface contribution and its variation with temperature and composition. Also, in order to measure the transference number, (the ratio of the oxide ion conductivity to the total conductivity of the system) the conductivity should be measured with different environments such as varied oxygen partial pressure, different gases such as H<sub>2</sub> and N<sub>2</sub>. The chemical stability of the samples can also be checked via using different atmosphere.

In addition to all these efforts, as the development and study of these compositions were done to make use of these materials in the SOFC, the cell fabrication should be done, and the cell performance should be checked with a fuel cell work station with load and no-load conditions.



## REFERENCES

- Abdalla A. M., Hossain S., Azad A. T., and Petra P. M. I., "Nanomaterials for Solid Oxide Fuel Cells : A Review", *Renewable and Sustainable Energy Reviews* 82 (2018) 353–368.
- Abram, E. J., Sinclair D. C., and West A. R., "Electrode-Contact Spreading Resistance Phenomena in Doped-Lanthanum Gallate Ceramics", *Journal of Electroceramics* 7 (2001) 179–188.
- Advances in Solid Oxide Fuel Cells VI* ® WILEY (2010).
- Aleshin E., and Roy R., "Crystal Chemistry of Pyrochlore", *Journal of the American Ceramic Society* 45 (1962) 18–25.
- Anithakumari P., Grover V., Nandi C., Bhattacharyya K., Tyagi A. K., "Utilizing Non-Stoichiometry in  $\text{Nd}_2\text{Zr}_2\text{O}_7$  Pyrochlore: Exploring Superior Ionic Conductors", *RSC Advances* 6 (2016) 97566–97579.
- Ashbrook S. E., Mitchell M. R., Sneddon S., Moran R. F., de los Reyes M., Lumpkin G. R., Whittle K. R., "New Insights into Phase Distribution, Phase Composition and Disorder in  $\text{Y}_2(\text{Zr},\text{Sn})_2\text{O}_7$  Ceramics from NMR Spectroscopy", *Physical Chemistry Chemical Physics* 17 (2015) 9049–9059.
- Avdeev M., Haas M. K., Jorgensen J. D., Cava R. J., "Static Disorder from Lone-Pair Electrons in  $\text{Bi}_{2-x}\text{M}_x\text{Ru}_2\text{O}_{7-y}$  (M = Cu, Co; x = 0, 0.4) Pyrochlores", *Journal of Solid State Chemistry* 169 (2002) 24–34.
- Badwal S.P.S., Ciacchi F. T., and Milosevic D., "Scandia-Zirconia Electrolytes For Intermediate Temperature Solid Oxide Fuel Cell Operation", *Solid State Ionics* 136–137 (2000) 91–99.
- Badwal S.P.S., and Foger K., "Solid Oxide Electrolyte Fuel Cell Review", *Ceramics International* 22 (1996) 257–265.
- Barsoukov E., and Macdonald J. R., "Impedance Spectroscopy Theory, Experiment, And Applications", *John Wiley & Sons Inc, Hoboken* (2005)
- Bazuev G. V., and Chupakhina T. I., "Magnetic Properties of  $\text{Er}_2\text{Mn}_{2/3}\text{Re}_{4/3}\text{O}_7$ , a New Zirkelite-Structure Oxide ", *Inorganic Materials* 45 (2009) 409–413.

## References

---

- Begg B. D., Hess N. J., McCready D. E., Thevuthasan S., Weber W. J., "Heavy-Ion Irradiation Effects in  $\text{Gd}_2(\text{Ti}_{2-x}\text{Zr}_x)\text{O}_7$  Pyrochlores", *Journal of Nuclear Materials* 289 (2001) 188–193.
- Blanchard P. E. R., Clements R., Kennedy B. J., Ling C. D., Reynolds E., Avdeev M., Stampfl A. P. J., Zhang Z., Jang Y. L., "Does Local Disorder Occur in the Pyrochlore Zirconates?", *Inorganic Chemistry* 51 (2012) 13237–13244.
- Boivin J.C., and Thomas D. J., "Structural Investigation on Bismuth Based Mixed Oxides", *Solid State Ionics* 4 (1981) 457–462.
- Boivin J. C., and Mairesse G., "Recent Material Developments in Fast Oxide Ion Conductors", *Chemistry of Materials* 10 (1998) 2870–2888.
- Boivin J. C., "Structural and Electrochemical Features of Fast Oxide Ion Conductors", *International Journal of Inorganic Materials* 3 (2001) 1261–1266.
- Bolech M., Cordfunke E. H. P., Van Genderen A. C. G., Van Der Laan R. R., Janssen F. J. J. G., Van Miltenburg J. C., "The Heat Capacity and Derived Thermodynamic Functions of  $\text{La}_2\text{Zr}_2\text{O}_7$  and  $\text{Ce}_2\text{Zr}_2\text{O}_7$  from 4 to 1000K", *Journal of Physics and Chemistry of Solids* 58 (1997) 433–439.
- Bove R., "Solid Oxide Fuel Cells: Principles, Designs and State-of-the-Art in Industries", *Recent Trends in Fuel Cell Science and Technology* (2007) 267–285.
- Brett D. J. L., Atkinson A., Brandon N. P., and Skinner S. J., "Intermediate Temperature Solid Oxide Fuel Cells", *Chemical Society Reviews* 37 (2008) 1568–1578.
- Brugnoni C., Ducati U., and Scagliotto M., "SOFC Cathode/Electrolyte Interface. Part I: Reactivity between  $\text{La}_{0.85}\text{Sr}_{0.15}\text{MnO}_3$  and  $\text{ZrO}_2\text{-Y}_2\text{O}_3$ ", *Solid State Ionics* 76 (1995) 177–182.
- Callister W. D., *Fundamentals Of Materials Science and Engineering* (2001)
- Chadwick A. V., "Solid Progress in Ion Conduction", *Nature* 408 (2000) 925–926.
- Chakoumakos B. C., "Systematics of the Pyrochlore Structure Type, Ideal  $\text{A}_2\text{B}_2\text{X}_6\text{Y}$ ", *Journal of Solid State Chemistry* 53 (1984) 120–129.
- Chen M., Tanner D. B., and Nino J. C., "Infrared Study of the Phonon Modes in Bismuth Pyrochlores", *Physical Review B* 72 (2005) 054303(1-80).
- Chiodelli G., and Scagliotti M., "Electrical Characterization of Lanthanum Zirconate

- Reaction Layers by Impedance Spectroscopy", *Solid State Ionics* 73 (1994) 265–271.
- Chou T., Liu L. D., and Wei W. C. J., "Phase Stability and Electric Conductivity of Er<sub>2</sub>O<sub>3</sub>-Nb<sub>2</sub>O<sub>5</sub> Co-Doped Bi<sub>2</sub>O<sub>3</sub> Electrolyte", *Journal of the European Ceramic Society* 31 (2011) 3087–3094.
- Chronos A., Parfitt D., Kilner J. A., and Grimes R. W., "Anisotropic Oxygen Diffusion in Tetragonal La<sub>2</sub>NiO<sub>4+δ</sub>: Molecular Dynamics Calculation", *Journal of Material Chemistry* 20 (2010) 266–270.
- Conflant P., Boivin J. C., and Thomas D., "Le Diagramme Des Phases Solides Du Systeme Bi<sub>2</sub>O<sub>3</sub>-CaO", *Journal of Solid State Chemistry* 18 (1976) 133–140.
- Dickson F.J., Hawkins K. D., and White T. J., "Calcium Uranium Titanate—A New Pyrochlore", *Journal of Solid State Chemistry* 82 (1989) 146–150.
- van Dijk M. P., Burggraaf A. J., Cormack A. N., and Catlow C. R. A., "Defect Structures and Migration Mechanisms in Oxide Pyrochlores", *Solid State Ionics* 17 (1985) 159–167.
- Dinnebier R., *Commission on Powder Diffraction* 26 (2001).
- Evans I. R., Howard J. A. K., Evans J. S. O., "The Crystal Structure of R-La<sub>2</sub>Mo<sub>2</sub>O<sub>9</sub> and the Structural Origin of the Oxide Ion Migration Pathway." *Chemistry of Materials* 17 (2005) 4074–4077.
- Ewing R. C., Weber W. J., and Lian J., "Nuclear Waste Disposal-Pyrochlore (A<sub>2</sub>B<sub>2</sub>O<sub>7</sub>): Nuclear Waste Form for the Immobilization of Plutonium and "Minor" Actinides", *Journal of Applied Physics* 95 (2004) 5949–5971.
- Feng J., Xiao B., Zhou R., and Pan W., "Thermal Expansions of Ln<sub>2</sub>Zr<sub>2</sub>O<sub>7</sub> (Ln = La, Nd, Sm, and Gd) Pyrochlore." *Journal of Applied Physics* 111 (2012) 103535 (1-4).
- Ferrara C., Eames C., Islam M. S., and Tealdi C., "Lattice Strain Effects on Doping, Hydration and Proton Transport in Scheelite-Type Electrolytes for Solid Oxide Fuel Cells", *Physical Chemistry Chemical Physics* 18 (2016) 29330–29336.
- Finnerty C. M., and Ormerod R. M., "Internal Reforming over Nickel/Zirconia Anodes in SOFCs Operating on Methane: Influence of Anode Formulation, Pre-Treatment and Operating Conditions", *Journal of Power Sources* 86 (2000) 390–394.
- Fung K. Z., Baek H. D., and Virkar A.V., "Thermodynamic and Kinetic Considerations for Bi<sub>2</sub>O<sub>3</sub>-Based Electrolytes ", *Solid State Ionics* 52 (1992) 199–211.

## References

---

- Fung K. Z., and Virkar A. V., "Phase Stability, Phase Transformation Kinetics, and Conductivity of  $\text{Y}_2\text{O}_3\text{-Bi}_2\text{O}_3$  Solid Electrolytes Containing Aliovalent Dopants", *Journal of American Ceramic Society* 74 (1991) 1970–1980.
- Gardner J. S., Gingras M. J. P., and Greedan J. E., "Magnetic Pyrochlore Oxides", *Reviews of Modern Physics* 82 (2010) 53–107.
- Georges S., Goutenoire F., Altorfer F., Sheptyakov D., Fauth F., Suard E., Lacorre P., "Thermal, Structural and Transport Properties of the Fast Oxide-Ion Conductors  $\text{La}_{2-x}\text{R}_x\text{Mo}_2\text{O}_9$  (R=Nd, Gd, Y)", *Solid State Ionics* 161 (2003) 231–241.
- Ghosh D. C., and Biswas R., "Theoretical Calculation of Absolute Radii of Atoms and Ions. Part 1. The atomic Radii", *International Journal of Molecular Sciences* 3 (2002) 87–113.
- Glerup M., Nielsen O. F., and Poulsen F. W., "The Structural Transformation from the Pyrochlore Structure,  $\text{A}_2\text{B}_2\text{O}_7$ , to the Fluorite Structure,  $\text{AO}_2$ , Studied by Raman Spectroscopy and Defect Chemistry Modeling", *Journal of Solid State Chemistry* 160 (2001) 25–32.
- Gomez-Perez A., Prado-Gonjal J., Munoz-Gil D., Andrada-Chacon A., Sanchez-Benitez J., Moran E., Teresa Azcondo M., Amador U., Schmidt R., "Anti-Site Disorder and Physical Properties in Microwave Synthesized  $\text{RE}_2\text{Ti}_2\text{O}_7$  (RE=Gd, Ho) Pyrochlore", *RSC Advances* 7 (2015) 85229–85241.
- Goodenough J. B., "Oxide-Ion Conductors by Design", *Nature* 404 (2000) 821–822.
- Goutenoire F., Isnard O., Suard E., Bohnke O., Lalignant Y., Retoux R., Lacorre P., "Structural and Transport Characteristics of the LAMOX Family of Fast Oxide-Ion Conductors, Based on Lanthanum Molybdenum Oxide  $\text{La}_2\text{Mo}_2\text{O}_9$ ", *Journal of Materials Chemistry* 11 (2001) 119–124.
- Goutenoire F., Retoux R., Suard E., and Lacorre P., "Ab Initio Determination of the Novel Perovskite-Related Structure of  $\text{La}_7\text{Mo}_7\text{O}_{30}$  from Powder Diffraction", *Journal of Solid State Chemistry* 142 (1999) 228–35.
- Govindan Kutty K.V., Mathews C. K., Rao T. N., and Varadaraju U. V., "Oxide Ion Conductivity in Some Substituted Rare Earth Pyrochlores", *Solid State Ionics* 22 (1995) 99–110.

- Gunn D. S. D., Allan N. L., Foxhall H., Harding J. H., Purton J. A., Smith W., Stein M. J., Todorov I. T., Travis K. P., "Novel Potentials for Modelling Defect Formation and Oxygen Vacancy Migration in  $\text{Gd}_2\text{Ti}_2\text{O}_7$  and  $\text{Gd}_2\text{Zr}_2\text{O}_7$  Pyrochlores." *Journal of Materials Chemistry* 22 (2012) 4675-4680.
- Hayashi H., Inaba H., Matsuyama M., Lan N. G., Dokiya M., Tagawa H., "Structural Consideration on the Ionic Conductivity of Perovskite-Type Oxides", *Solid State Ionics* 122 (1999) 1–15.
- Hector A. L., and Wiggin S. W., "Synthesis and Structural Study of Stoichiometric  $\text{Bi}_2\text{Ti}_2\text{O}_7$  Pyrochlore." *Journal of Solid State Chemistry* 177 (2004) 139–145.
- Heremans C., Wuensch B. J., Stalick J. K., and Prince E., "Fast-Ion Conducting  $\text{Y}_2(\text{Zr}_y\text{Ti}_{1-y})_2\text{O}_7$  Pyrochlores: Neutron Rietveld Analysis of Disorder Induced by Zr Substitution", *Journal of Solid State Chemistry* 117 (1995) 108–121.
- Hinojosa B. B., Nino J. C., and Asthagiri A., "First-Principles Study of Cubic Bi Pyrochlores", *Physical Review B* 77 (2008) 104123 (1-14).
- Hoda S. N., and Chang L. L. Y., "Phase Relations in the System  $\text{Bi}_2\text{O}_3\text{-WO}_3$ ", *Journal of the American Ceramic Society* 57 (1974) 323–326.
- Hong S. J., Mehta K., and Virkar A. V., "Effect of Microstructure and Composition on Ionic Conductivity", *Journal of electrochemical society* 145 (1998) 638–647.
- Ishihara Y., Kilner J. A., Honda M., Sakai N., Yokokawa H., Takita Y., "Oxygen Surface Exchange and Diffusion in  $\text{LaGaO}_3$  Based Perovskite Type Oxides." *Solid State Ionics* 113–115 (1998) 593–600.
- Ishihara T., Enoki M., Yan J. W., and Matsumoto H., "Power Generating Property of SOFC Using  $\text{La}(\text{Sr})\text{Ga}(\text{Mg},\text{Fe})\text{O}_3$  Electrolyte Coated with  $\text{LaGaO}_3$  Film", *Proceedings of the Electrochemical Society PV 2005-07* (2005) 1117–1126.
- Ishihara T., Matsuda H., and Takita Y., "Perovskite Type Oxide as a New Oxide Ionic Conductor", *Journal of American Ceramic Society* 116 (1994) 3801–3803.
- Ishihara T., Matsuda H., and Takita Y., "Effects of Rare Earth Cations Doped for La Site on the Oxide Ionic Conductivity of  $\text{LaGaO}_3$ -Based Perovskite Type Oxide ", *Solid State Ionics* 79 (1995) 147–151.
- Islam M. S., and Slater P. R., "Solid-State Materials for Clean Energy : Insights from Atomic-

## References

---

- Scale Modeling". *MRS Bulletin* 34 (2009) 935–941.
- Jiang N., and Wachsman E. D., "Structural Stability and Conductivity of Phase-Stabilized Cubic Bismuth Oxides", *Journal of American Ceramic Society* 82 (1999) 3057–3064.
- Jung D. W., Lee K. T., and Wachsman E. D., "Dysprosium and Gadolinium Double Doped Bismuth Oxide Electrolytes for Low-Temperature Solid Oxide Fuel Cells", *Journal of The Electrochemical Society* 163 (2016) 411–415.
- Kajitani M., Matsuda M., Hoshikawa A., Harjo S., Kamiyama T., Ishigaki T., Izumi F., Miyake M., "In Situ Neutron Diffraction Study on Fast Oxide Ion Conductor LaGaO<sub>3</sub> - Based Perovskite Compounds", *Chemistry of Materials* 17 (2005) 4235–4243.
- Kendrick E., Islam M. S., and Slater P. R., "Developing Apatites for Solid Oxide Fuel Cells: Insight into Structural, Transport and Doping Properties", *Journal of Materials Chemistry* 17 (2007) 3104–3111.
- Kendrick E., Islam M. S., and Slater P. R., "Atomic-Scale Mechanistic Features of Oxide Ion Conduction in Apatite-Type Germanates", *Chemical Communications* 33 (2008) 715–717.
- Kendrick E., Orera A., and Slater P. R., "Neutron Diffraction Structural Study of the Apatite-Type Oxide Ion Conductor, La<sub>8</sub>Y<sub>2</sub>Ge<sub>6</sub>O<sub>27</sub>: Location of the Interstitial Oxide Ion Site." *Journal of Materials Chemistry* 19 (2009) 7955–7958.
- Kennedy B. J., Hunter B. A., and Howard C. J., "Structural and Bonding Trends in Tin Pyrochlore Oxides", *Journal of Solid State Chemistry* 130 (1997) 58–65.
- Keramidas V.G., and White W. B., "Raman Spectra of Oxides with the Fluorite Structure", *The Journal of Chemical Physics* 59 (1973) 1561–1562.
- Kertesz M., Riess I., Tannhauser S., Langpape R., Rohr F. J., "Structure and Electrical Conductivity of La<sub>0.84</sub>Sr<sub>0.16</sub>MO<sub>3</sub>", *Journal of Solid State Chemistry* 129 (1982) 125–129.
- Kharton V. V., Marques F. M. B., and Atkinson A., "Transport Properties of Solid Oxide Electrolyte Ceramics: A Brief Review", *Solid State Ionics* 174 (2004) 135–149.
- Kilner J. A., "Fast Oxygen Transport in Acceptor Doped Oxides", *Solid State Ionics* 129 (2000) 13–23.
- Kiruthika G. V. M., Govindan Kutty K. V., and Varadarju U. V., "Effect of Aliovalent Ion



- Substitution on the Oxide Ion Conductivity in Rare-Earth Pyrohafnates  $\text{RE}_{2-x}\text{Sr}_x\text{Hf}_2\text{O}_{7-\delta}$  and  $\text{RE}_2\text{Hf}_{2-x}\text{Al}_x\text{O}_{7-\delta}$  (RE = Gd and Nd;  $x = 0, 0.1$  and  $0.2$ ), *Solid State Ionics* 110 (1998) 335–340.
- Kramer S., "A Novel Titanate-Based Oxygen Ion Conductor:  $\text{Gd}_2\text{Ti}_2\text{O}_7$ ", *Solid State Ionics* 82 (1995) 15–23.
- Kramer S., Spears M., and Tuller H., "Conduction in Titanate Pyrochlores: Role of Dopants", *Solid State Ionics* 72 (1994) 59–66.
- Kushima A., and Yildiz B., "Oxygen Ion Diffusivity in Strained Yttria Stabilized Zirconia : Where Is the Fastest Strain ?", *Journal of Materials Chemistry* 20 (2010) 4809–4819.
- Kutty G. K.V., Rajagopalan S., and Mathews C. K., "Thermal Expansion Behaviour of Some Rare Earth Oxide Pyrochlores", *Materials Chemistry and Physics* 29 (1994) 759–766.
- Lacerda M., Irvine J. T. S., Glasser F. P., and West A. R., "High Oxide Ion Conductivity in  $\text{Ca}_{12}\text{Al}_{14}\text{O}_{33}$ ", *Nature* 332 (1988) 525–526.
- Lacorre P., Goutenoire E., Bohnke O., Retoux R., Laligant Y., "Designing Fast Oxide-Ion Conductors Based on  $\text{La}_2\text{Mo}_2\text{O}_9$ ", *Nature* 404 (2000) 9–11.
- Lai W., "Impedance Spectroscopy as a Tool for the Electrochemical Study of Mixed Conducting Ceria", *Thesis* (2007)
- Levin E. M., and Roth R. S., "Polymorphism of Bismuth Sesquioxide. II. Effect of Oxide Additions on the Polymorphism of  $\text{Bi}_2\text{O}_3$ ", *Journal of Research of the National Bureau of Standards Section A: Physics and Chemistry* 68A (1964) 197.
- Levin I., Amos T. G., Nino J. C., Vanderah T. A., Randall C. A., Lanagan M. T., "Structural Study of an Unusual Cubic Pyrochlore  $\text{Bi}_{1.5}\text{Zn}_{0.92}\text{Nb}_{1.5}\text{O}_{6.92}$ ", *Journal of Solid State Chemistry* 168 (2002) 69–75.
- Levin I., Amos T. G., Nino J. C., Vanderah T. A., Reaney I. M., Randall C. A., Lanagan M. T., "Crystal Structure of the Compound  $\text{Bi}_2\text{Zn}_{2/3}\text{Nb}_{4/3}\text{O}_7$ ", *Journal of Materials Research* 17 (2002) 1406–1411.
- Levine B. F., "D-Electron Effects on Bond Susceptibilities and Ionicities", *Physical Review B* 7 (1973) 2591–2600.
- Li P., Chen I., and Penner-Hahn J. E., "Effect of Dopants on Zirconia Stabilization-An X-ray Absorption Study: III, Charge-Compensating Dopants", *Journal of American Ceramic*

## References

---

- Society* 77 (1974) 1289–1295.
- Li S., and Bergman B., "Doping Effect on Secondary Phases, Microstructure and Electrical Conductivities of LaGaO<sub>3</sub> Based Perovskites", *Journal of the European Ceramic Society* 29 (2009) 1139–1146.
- Linus P., "The Nature of the Chemical Bond, An Introduction to Modern Structural Chemistry", (1960)
- Liu Z. G., Ouyang J. H., Zhou Y., and Xia X. L., "Electrical Conductivity of Samarium-Ytterbium Zirconate Ceramics", *Electrochimica Acta* 54 (2009) 3968–3971.
- Maczka M., Cepeda-sa N. M., Fuentes A. F., Amador U., "Cations Size Mismatch versus Bonding Characteristics: Synthesis, Structure and Oxygen Ion Conducting Properties of Pyrochlore-Type Lanthanide Hafnates", *Journal of Materials Research* 53 (2018) 13513–13529.
- Mahato N., Banerjee A., Gupta A., Omar S., Balani K., "Progress in Material Selection for Solid Oxide Fuel Cell Technology: A Review", *Progress in Materials Science* 72 (2015) 141–337.
- Mairesse G., "Bismuth-Based Oxide Conductors Novel Structural and Electrical Features", *Fast Ion Transport in Solids*, (1993) 271–290.
- Malavasi L., Kim H. J., Billinge S. J. L., Proffen T., Tealdi C., Flor G., "Nature of the Monoclinic to Cubic Phase Transition in the Fast Oxygen Ion Conductor La<sub>2</sub>Mo<sub>2</sub>O<sub>9</sub> (LAMOXY)", *Journal of the American Chemical Society* 129 (2007) 6903–6907.
- Malavasi L., Fisher C. A. J., and Islam M. S. "Oxide-Ion and Proton Conducting Electrolyte Materials for Clean Energy Applications: Structural and Mechanistic Features", *Chemical Society Reviews* 39 (2010) 4370–4387.
- Mandal B. P., Banerji A., Sathe V., Deb S. K., Tyagi, A. K., "Order-Disorder Transition in Nd<sub>2-y</sub>Gd<sub>y</sub>Zr<sub>2</sub>O<sub>7</sub> Pyrochlore Solid Solution: An X-ray Diffraction and Raman Spectroscopic Study", *Journal of Solid State Chemistry* 180 (2007) 2643–2648.
- Mandal B. P., Krishna P. S. R., and Tyagi A. K., "Order-Disorder Transition in the Nd<sub>2-y</sub>Y<sub>y</sub>Zr<sub>2</sub>O<sub>7</sub> System: Probed by X-ray Diffraction and Raman Spectroscopy", *Journal of Solid State Chemistry* 183 (2010) 41–45.
- McCauley R. A., "Structural Characteristics of Pyrochlore Formation", *Journal of Applied*

- Physics* 51 (1980) 290–294.
- Medernach J. W., and Snyder R. L., "Powder Diffraction Patterns and Structures of the Bismuth Oxides", *Journal of the American Ceramic Society* 61 (1978) 494–497.
- Meng G., Chen C., Han X., Yang P., Peng D., "Conductivity of Bi<sub>2</sub>O<sub>3</sub>-Based Oxide Ion Conductors with Double Stabilizers", *Solid State Ionics* 28 (1988) 0–5.
- Michel D., Jorba M. P. Y., and Collongues R., "Etude de La Transformation Ordre-Desordre de La Structure a La Structure Pyrochlore Pour Des Phases (1-x)ZrO<sub>2</sub>-xLn<sub>2</sub>O<sub>3</sub>", *Materials Research Bulletin* 9 (1974) 1457–1468.
- Minervini L., Grimes R. W., and Sickafus K. E., "Disorder in Pyrochlore Oxides", *Journal of the American Ceramic Society* 83 (2000) 1873–1878.
- Minh N. Q., "Ceramic Fuel Cells", *Journal of the American Ceramic Society* 76 (1993) 563–588.
- Mobius H., "On the History of Solid Electrolyte Fuel Cells", *Journal of Solid State Electrochemistry* 1 (1997) 2–16.
- Mond L., and Langer C., "A New Form of Gas Battery", *Proceeding of the Royal Society of London* 46 (1890) 296–304.
- Moreno K. J., Mendoza-Suarez G., Fuentes A. F., García-Barriocanal J., Leon C., Santamaría J., "Cooperative Oxygen Ion Dynamics in Gd<sub>2</sub>Ti<sub>2-y</sub>Zr<sub>y</sub>O<sub>7</sub>", *Physical Review B* 71 (2005) 132301 (1-4).
- Moreno K. J., Fuentes A. F., Santamaría J., and León C., "Dynamics of Mobile Oxygen Ions in Disordered Pyrochlore-Type Oxide- Ion Conductors", *Defect and Diffusion Forum* 289–292 (2009) 347–354.
- Moreno K. J., Fuentes A. F., Maczka M., Hanuza J., Amador U., Santamaría J., León C., "Influence of Thermally Induced Oxygen Order on Mobile Ion Dynamics in Gd<sub>2</sub>(Ti<sub>0.65</sub>Zr<sub>0.35</sub>)<sub>2</sub>O<sub>7</sub>", *Physical Review B - Condensed Matter and Materials Physics* 75 (2007) 1–8.
- Moriga T., Emura S., Yoshiasa A., Kikkawa S., Kanamaru F., Koto K., "X-Ray and Raman Study on Coordination States of Fluorite- and Pyrochlore-Type Compounds in the System ZrO<sub>2</sub>-Gd<sub>2</sub>O<sub>3</sub>", *Solid State Ionics* 40–41 (1990) 357–361.

## References

---

- Morris D. J. P., Tennant D. A., Grigera S. A., Klemke B., Castelnovo C., Moessner R., Czternasty C., Meissner M., Rule K. C., Hoffmann J. U., Kiefer K., Gerischer S., Slobinsky D., Perry R. S., "Dirac Strings and Magnetic Monopoles in the Spin Ice  $\text{Dy}_2\text{Ti}_2\text{O}_7$ ", *Science* 326 (2009) 411–414.
- Mouta R., Silva R. X., and Paschoal C. W. A., "Tolerance Factor for Pyrochlores and Related Structures", *Acta Crystallographica Section B* 69 (2013) 439–445.
- Munshi M. Z. A., "Handbook of Solid State Batteries & Capacitors" (1995).
- Nakayama S., Aono H., and Sadaoka Y., "Ionic Conductivity of  $\text{Ln}_{10}(\text{SiO}_4)_6\text{O}_3$  (Ln = La, Nd, Sm, Gd and Dy)", *Chemistry Letters* 24 (1995) 431–432.
- Nakayama S., Kageyama T., and Sadaoka Y., "Ionic Conductivity of Lanthoid Silicates  $\text{Ln}_{10}(\text{SiO}_4)_6\text{O}_3$  (Ln=La, Nd, Sm, Dy, Y, Ho, Er and Yb)", *Journal of Material Chemistry* 5 (1995) 1801–1805.
- Navas C., and Zur Loye H. C., "Conductivity Studies on Oxygen-Deficient Ruddlesden-Popper Phases", *Solid State Ionics* 93 (1996) 171–176.
- Navrotsky A., "Thermodynamics of Solid Electrolytes and Related Oxide Ceramics Based on the Fluorite Structure", *Journal of Materials Chemistry* 20 (2010) 10577–10587.
- Neogy S., Savalia R. T., Tewari R., Srivastava D., Dey G. K. "Transmission Electron Microscopy of Nanomaterials", *Indian Journal of Pure and Applied Physics* 2 (2006) 119–124.
- Nernst W., "No Title", *Z. Elektrochem* 6 (1899) 41-43.
- Ngai K. L., and Leon C., "Cage Decay, Near Constant Loss, and Crossover to Cooperative Ion Motion in Ionic Conductors: Insight from Experimental Data", *Physical Review B* 66 (2002) 064308(1-11).
- Ngai K. L., and León C., "A Quantitative Explanation of the Difference between Nuclear Spin Relaxation and Ionic Conductivity Relaxation in Superionic Glasses", *Journal of Non-Crystalline Solids* 315 (2003) 124–133.
- Ngai K. L., and Tsang K. Y., "Similarity of Relaxation in Supercooled Liquids and Interacting Arrays of Oscillators", *Physical Review E* 60 (1997) 4511–4517.
- Nishino H., Yamamura H., Arai T., Kakinuma K., Nomura K., "Effect of Cation Radius Ratio and Unit Cell Free Volume on Oxide-Ion Conductivity in Oxide Systems with

- Pyrochlore-Type Composition", *Journal of the Ceramic Society of Japan* 112 (2004) 541–546.
- Norberg S. T., Ahmed I., Hull S., Marrocchelli D., Madden P. A., "Local Structure and Ionic Conductivity in the  $Zr_2Y_2O_7$ - $Y_3NbO_7$  System ", *Journal of physics. Condensed matter : an Institute of Physics journal* 21 (2009) 215401(1-11).
- Ohno Y., Nagata S., and Sato H., "Effect of Electrode Materials on the Properties of High-Temperature Solid Electrolyte Fuel Cells", *Solid State Ionics* 3–4 (1981) 439–442.
- Omari M., Drache M., Conflant P., and Boivin J. C., "Anionic Conduction Properties of the Fluorite -Type Phase in the  $Bi_2O_3$ -  $Y_2O_3$ -  $PbO$  System", *Solid State Ionics* 40–41 (1990) 929–933.
- Ormerod R. M., "Solid Oxide Fuel Cells", *Chemical Society Reviews* 32 (2003) 17–28.
- Padmasree K. P., Kanchan D. K., and Kulkarni A. R., "Impedance and Modulus Studies of the Solid Electrolyte System  $20CdI_2$ - $80[xAg_2O$ - $y(0.7V_2O_5$ - $0.3B_2O_3)]$ , Where  $1 \leq x/y \leq 3$ ", *Solid State Ionics* 177 (2003) 475–482.
- Pandey J., Shrivastava V., and Nagarajan R., "Metastable  $Bi_2Zr_2O_7$  with Pyrochlore-like Structure: Stabilization, Oxygen Ion Conductivity, and Catalytic Properties", *Inorganic Chemistry* 57 (2018) 13667–13678.
- Panwar N. L., Kaushik S. C., and Kothari S., "Role of Renewable Energy Sources in Environmental Protection: A Review", *Renewable and Sustainable Energy Reviews* 15 (2011) 1513–1524.
- Petri A., and Huang P., "Oxygen Conductivity of  $Nd(Sr/Ca)Ga(Mg)O_{3-\delta}$  Perovskites", *Solid State Ionics* 92 (1996) 113–117.
- Phillips J. C., "Ionicity of the Chemical Bond in Crystals", *Reviews of Modern Physics* 42 (1970) 317–356.
- Pirzada M., Grimes R. W., and Maguire J. F., "Incorporation of Divalent Ions in  $A_2B_2O_7$  Pyrochlores." *Solid State Ionics* 161 (2003) 81–91.
- Pirzada M., Grimes R.W., Minervini L., Maguire J. F., Sickafus K. E., "Oxygen Migration in  $A_2B_2O_7$  Pyrochlores", *Solid State Ionics* 140 (2001) 201–208.
- Polat Y., Akalan H., and Arı M., "Thermo-Electrical and Structural Properties of  $Gd_2O_3$  and  $Lu_2O_3$  Double-Doped  $Bi_2O_3$ ", *International Journal of Hydrogen Energy* 42 (2017)

## References

---

- 614–622.
- Qu Z., Wan C., and Pan W., "Thermal Expansion and Defect Chemistry of MgO-Doped  $\text{Sm}_2\text{Zr}_2\text{O}_7$ ", *Chemistry of Materials* 19 (2007) 4913–4918.
- Radhakrishnan A. N., Rao P. P., Linsa K. S. M., Deepa M., Koshy P., "Influence of Disorder-to-Order Transition on Lattice Thermal Expansion and Oxide Ion Conductivity in  $(\text{Ca}_x\text{Gd}_{1-x})_2(\text{Zr}_{1-x}\text{M}_x)_2\text{O}_7$  Pyrochlore Solid Solutions", *Dalton Transactions* 40 (2011) 3839–3848.
- Radhakrishnan A. N., Rao P. P., Linsa K. S. M., Deepa M., Koshy P., "Role of Bond Strength on the Lattice Thermal Expansion and Oxide Ion Conductivity in Quaternary Pyrochlore Solid Solutions", *Inorganic Chemistry* 51 (2012) 2409–2419.
- Radhakrishnan A. N., Prabhakar Rao P., Sibi K. S., Deepa M., Koshy P., "Order-Disorder Phase Transformations in Quaternary Pyrochlore Oxide System: Investigated by X-ray Diffraction, Transmission Electron Microscopy and Raman Spectroscopic Techniques", *Journal of Solid State Chemistry* 182 (2009) 2312–2318.
- Radosavljevic I., Evans J. S.O., and Sleight A. W., "Synthesis and Structure of Pyrochlore-Type Bismuth Titanate", *Journal of Solid State Chemistry* 136 (1998) 63–66.
- Reau J. M., Rossignol S., Tanguy B., Rojo J. M., Herrero P., Rojas R. M., Sanz J., "Conductivity Relaxation Parameters of Some  $\text{Ag}^+$  Conducting Tellurite Glasses Containing  $\text{AgI}$  or the  $(\text{AgI})_{0.75}(\text{TlI})_{0.25}$  Eutectic Mixture", *Solid State Ionics* 74 (1994) 65–73.
- Renju U. A., Rao P. P., and Vaisakhan Thampi D. S., "Influence of Phase Transition from Order to Disorder and Philip's Ionicity on the Thermal Expansion Coefficient of Pyrochlore Type Compositions with a Multivalent Environment", *New Journal of Chemistry* 41 (2017) 245–255.
- Rittman D. R., Turner K. M., Park S., Fuentes A. F., Yan J., Ewing R. C., Mao W. L., "High-Pressure Behavior of  $\text{A}_2\text{B}_2\text{O}_7$  Pyrochlore (A=Eu, Dy; B=Ti, Zr)", *Journal of Applied Physics* 121 (2017) 045902 (1-6)
- Rittman D. R., Turner K. M., Park S., Fuentes A. F., Ewing R. C., Mao W. L., "Strain Engineered Pyrochlore at High Pressure", *Scientific Reports* 7 (2017) 1–10.

- Roth R. S., Vanderah T. A., Bordet P., Grey I. E., Mumme W. G., Cai L., Nino J. C., "Pyrochlore Formation, Phase Relations, and Properties in the CaO–TiO<sub>2</sub>–(Nb,Ta)<sub>2</sub>O<sub>5</sub> Systems", *Journal of Solid State Chemistry* 181 (2008) 406–414.
- Rousseau D. L., Bauman R. P., and Porto S. P. S., "Normal Mode Determination in Crystals", *Journal of Raman Spectroscopy* 10 (1981) 253–290.
- Sammells A. F., Cook R. L., White J. H., Osborne J. J., MacDuff R. C., "Rational Selection of Advanced Solid Electrolytes for Intermediate Temperature Fuel Cells", *Solid State Ionics* 52 (1992) 111–123.
- Sammes N. M., Tompsett G. A., Näfe H., and Aldinger F., "Bismuth Based Oxide Electrolytes - Structure and Ionic Conductivity", *Journal of the European Ceramic Society* 19 (1999) 1801–1826.
- Sansom J. E. H., Richings D., and Slater P. R., "Powder Neutron Diffraction Study of the Oxide-Ion-Conducting Apatite-Type Phases, La<sub>9.33</sub>Si<sub>6</sub>O<sub>26</sub> and La<sub>8</sub>Sr<sub>2</sub>Si<sub>6</sub>O<sub>26</sub>", *Solid State Ionics* 139 (2001) 205–210.
- Sayed F. N., Jain D., Mandal B. P., Pillai C. G. S., Tyagi A. K., "Tunability of Structure from Ordered to Disordered and Its Impact on Ionic Conductivity Behavior in the Nd<sub>2-y</sub>Ho<sub>y</sub>Zr<sub>2</sub>O<sub>7</sub> (0.0 ≤ y ≤ 2.0) System", *RSC Advances* 2 (2012) 8341–8351.
- Sayed F. N., Mandal B. P., Jain D., Pillai C. G., Nair S., Tyagi A. K., "Improved Ionic Conductivity in NdGdZr<sub>2</sub>O<sub>7</sub>: Influence of Sc<sup>3+</sup> Substitution", *Journal of the European Ceramic Society* 32 (2012) 3221–3228.
- Scheetz B. E., and White W. B., "Characterization of Anion Disorder in Zirconate A<sub>2</sub>B<sub>2</sub>O<sub>7</sub> Compounds By Raman Spectroscopy", *Journal of the American Ceramic Society* 62 (1979) 468–470.
- Schelling P. K., Phillpot S. R., and Grimes R. W., "Optimum Pyrochlore Compositions for Low Thermal Conductivity", *Philosophical Magazine Letters* 84 (2004) 127–137.
- Scott H.G., "Phase Relationships in the Zirconia-Yttria System", *Journal of Materials Science* 10 (1975) 1527–1528.
- Scott P. M. B., "An Investigation of Solid Oxide Fuel Cell Chemistry: A Spectroscopic Approach", University of Maryland (2007)



## References

---

- Seo D. J., Ryu K. O., Park S. B., Kim K. Y., Song R. H., "Synthesis and Properties of  $Ce_{1-x}Gd_xO_{2-x/2}$  Solid Solution Prepared by Flame Spray Pyrolysis", *Materials Research Bulletin* 41 (2006) 359–366.
- Shabana E. I., and Misak N. Z., "Self-Diffusion and Trace Component Diffusion of Cesium Ion in Hydrrous Stannic Oxide", *Solid State Ionics* 44 (1990) 41–46.
- Shannon R. D., "Revised Effective Ionic Radii and Systematic Studies of Interatomic Distances in Halides and Chalcogenides", *Acta Crystallographica Section A* 32 (1976) 751–767.
- Shannon R. D., Bierlein J. D., Gillson J. L., Jon G. A., Sleight A. W., "Polymorphism in  $Bi_2Sn_2O_7$ ", *Journal of Physics and Chemistry of Solids* 41(1978) 117–122.
- Shinozaki K., Miyauchi M., Kuroda K., Sakurai O., Mizutani N., Kato M., "Oxygen-Ion Conduction in the  $Sm_2Zr_2O_7$  Pyrochlore Phase", *Journal of the American Ceramic Society-Discussion and Notes* 62 (1979) 538–539.
- Shlyakhtina A. V., Pigalskiy K. S., Belov D. A., Lyskov N. V., Kharitonova E. P., Kolbanev I. V., Borunova A. B., Karyagina O. K., Sadovskaya E. M., Sadykov V. A., Ereemeev N. F., "Proton and Oxygen Ion Conductivity in the Pyrochlore/Fluorite Family of  $Ln_{2-x}Ca_xScMO_{7-\delta}$  (Ln = La, Sm, Ho, Yb; M = Nb, Ta; X = 0, 0.05, 0.1) Niobates and Tantalates", *Dalton Transactions* 47 (2018) 2376–2392.
- Shlyakhtina A. V., Pigalskiy K. S., Belov D. A., Lyskov N. V., Kharitonova E. P., Kolbanev I. V., Borunova A. B., Karyagina O. K., Sadovskaya E. M., Sadykov V. A., Ereemeev N. F., "Ionic Conductivity of  $Ln_{2+x}Zr_{2-x}O_{7-x/2}$  (Ln = Sm–Gd) Solid Solutions", *Inorganic Materials* 41 (2005) 975–984.
- Shlyakhtina A. V., Pigalskiy K. S., Belov D. A., Lyskov N. V., Kharitonova E. P., Kolbanev I. V., Borunova A. B., Karyagina O. K., Sadovskaya E. M., Sadykov V. A., Ereemeev N. F., "Interstitial Oxide Ion Conduction in  $(Sm_{2-x}Zr_x)Zr_2O_{7+\delta}$ ", *Solid State Ionics* 262 (2014) 543–547.
- Sibi K.S., Radhakrishnan A.N., Deepa M., Prabhakar Rao P., Koshy P., "Oxide Ion Conductivity and Relaxation in  $CaREZrNbO_7$  (RE=La, Nd, Sm, Gd, and Y) System", *Solid State Ionics* 180 (2009) 1164–1172.
- Sillén L. G., and Aurivillius B., "Oxide Phases with a Defect Oxygen Lattice", *Zeitschrift für Kristallographie - Crystalline Materials* 101 (2014) 483–495.



- Singh S., Saha S., Dhar S. K., Suryanarayanan R., Sood A. K., Revcolevschi A., "Manifestation of Geometric Frustration on Magnetic and Thermodynamic Properties of the Pyrochlores  $\text{Sm}_2\text{X}_2\text{O}_7$ , ( $\text{X} = \text{Ti}, \text{Zr}$ )", *Physical Review B* 77 (2008) 054408(1-7).
- Singhal S. C., "Advances in Solid Oxide Fuel Cell Technology", *Solid State Ionics* 135 (2000) 305–313.
- Sinha A., Näfe H., Sharma B. P., and Gopalan P., "Study on Ionic and Electronic Transport Properties of Calcium-Doped  $\text{GdAlO}_3$ ", *Journal of The Electrochemical Society* 155 (2008) B309–314.
- Skinner S. J., and Kilner J. A., "Oxygen Ion Conductors", *Materialstoday* 6 (2003) 30–37.
- Solomon S., George A., Thomas J. K., and John A., "Preparation, Characterization, and Ionic Transport Properties of Nanoscale  $\text{Ln}_2\text{Zr}_2\text{O}_7$  ( $\text{Ln} = \text{Ce}, \text{Pr}, \text{Nd}, \text{Sm}, \text{Gd}, \text{Dy}, \text{Er}, \text{and Yb}$ ) Energy Materials", *Journal of Electronic Materials* 44 (2005) 28–37.
- Sreena T. S., Prabhakar Rao P., Francis L. T., Raj A. K. V., Babu P. S., "Structural and Photoluminescence Properties of Stannate Based Displaced Pyrochlore-Type Red Phosphors:  $\text{Ca}_{3-x}\text{Sn}_3\text{Nb}_2\text{O}_{14}:x\text{Eu}^{3+}$ ", *Dalton Transactions* 44 (2015) 8718–8728.
- Sreena T. S., Prabhakar Rao P., Raj A. K. V., Babu P. S., "Influence of Structural Disorder on the Photoluminescence Properties of  $\text{Eu}^{3+}$  Doped Red Phosphors:  $\text{Ca}_2\text{Y}_{3-x}\text{Nb}_3\text{O}_{14}:x\text{Eu}^{3+}$ ", *Chemistry Select* 1 (2016) 3413–3422.
- Srinivasan N., and Kiruthika G.V.M., "Conductivity Studies on the Substituted Stannate Pyrochlore System  $\text{Gd}_2\text{Sn}_{2-x-y}\text{M}_x\text{A}_y\text{O}_7$  ( $\text{M} = \text{Ti}$  and  $\text{A} = \text{Ru}$ ;  $x = 0.5, 1.0$  and  $1.5$ ;  $y = 0.2$ )", *Solid State Sciences* 96 (2019) 105957.
- Srivastava V. K., and Fermi V. E., "Ionic and Covalent Energy Gaps of CsCl Crystals", *Physics Letters* 102 (1984) 127–129.
- Stambouli A. B., and Traversa E., "Solid Oxide Fuel Cells (SOFCs): A Review of an Environmentally Clean and Efficient Source of Energy", *Renewable and Sustainable Energy Reviews* 6 (2002) 433–455.
- Steele B. C. H., and Heinzl A., "Materials for Fuel-Cell Technologies", *Nature* 414 (2001) 345–352.
- Subramanian M. A., Aravamudan G., and Subba Rao G. V., "Oxide Pyrochlores — A Review", *Progress in Solid State Chemistry* 15 (1983) 55–143.

## References

---

- Suda E., Pacaud B., and Mori M., "Sintering Characteristics, Electrical Conductivity and Thermal Properties of La-doped Ceria Powders", *Journal of Alloys and Compounds* 408–412 (2006) 1161–1164.
- Sun Y., Wu Q., and Shi G., "Graphene Based New Energy Materials", *Energy and Environmental Science* 4 (2011) 1113–1132.
- Suzuki Y., and Yoshikawa S., "Synthesis and Thermal Analyses of TiO<sub>2</sub>-Derived Nanotubes Prepared by the Hydrothermal Method", *Journal of Materials Research* 19 (2004) 982–985.
- Taimatsu H., Wada K., Kaneko H., and Yamamura H., "Mechanism of Reaction between Lanthanum Manganite and Ytria-Stabilized Zirconia", *Journal of the American Ceramic Society* 75 (1992) 401–405.
- Takahashi T., Esaka T., and Iwahara H., "High Oxide Ion Conduction in the Sintered Oxides of the System Bi<sub>2</sub>O<sub>3</sub>- Gd<sub>2</sub>O<sub>3</sub>", *Journal of Applied Electrochemistry* 5 (1975) 197–202.
- Takahashi T., and Iwahara H., "Ionic Conduction in Perovskite-Type Oxide Solid Solution and Its Application to the Solid Electrolyte Fuel Cell", *Energy Conversion* 11 (1971) 105–111.
- Takahashi T., Iwahara H., and Nagai Y., "High Oxide Ion Conduction in Sintered Bi<sub>2</sub>O<sub>3</sub> Containing SrO, CaO or La<sub>2</sub>O<sub>3</sub>", *Journal of Applied Electrochemistry* 2 (1972) 97–104.
- Takahashi T., and Iwahara H., "High Oxide Ion Conduction in Sintered Oxides of the System Bi<sub>2</sub>O<sub>3</sub> - WO<sub>3</sub>", *Journal of Applied Electrochemistry* 3 (1973) 65–72.
- Takahashi T., and Iwahara H., "Oxide Ion Conductors Based on Bismuthsesuioxide", *Materials Research Bulletin* 13 (1978) 1447–1453.
- Takahashi T., Iwahara H., and Esaka T., "High Oxide Ion Conduction in Sintered Oxide of the System Bi<sub>2</sub>O<sub>3</sub>-M<sub>2</sub>O<sub>5</sub>", *Journal of the Electrochemical Society* 124 (1977) 1563–1569.
- Takai S., Kohno N., and Esaka T., "Conductivity Relaxation Study on (Bi<sub>2</sub>O<sub>3</sub>)<sub>1-x</sub>(Y<sub>2</sub>O<sub>3</sub>)<sub>x</sub> and (Bi<sub>2</sub>O<sub>3</sub>)<sub>1-x</sub>(Gd<sub>2</sub>O<sub>3</sub>)<sub>x</sub> with the Defect Fluorite Structure", *Materials Research Bulletin* 33 (1998) 945–953.
- Taniguchi S., and Aniya M., "Relationship Between Thermal Expansion Coefficient and

- Ionic Conduction in Perovskite Type Oxides", *Journal of Physical Society of Japan* 53 (2010) 106–108.
- Taniguchi S., and Aniya M., "A Chemical Bonding Approach to Ionic Conduction and Thermal Expansion in Oxide Ion Conductors", *Advances in Science and Technology* 72 (2010) 343–347.
- Torres-Martínez L. M., Ruiz-Gómez M. A., Figueroa-Torres M. Z., Juárez-Ramírez I., Moctezuma E., Cuéllar E. L., "Synthesis by Two Methods and Crystal Structure Determination of a New Pyrochlore-Related Compound  $\text{Sm}_2\text{FeTaO}_7$ ", *Materials Chemistry and Physics* 133 (2012) 839–844.
- Tsai T., and Barnett S. A., "Effect of Mixed-Conducting Interfacial Layers on Solid Oxide Fuel Cell Anode Performance", *Journal of the Electrochemical Society* 145 (1998) 1696–1701.
- Tuller H., "Ionic Conduction and Applications", *Springer Handbook of Electronic and Photonic Materials* (2017) 247–267.
- Tuller H., "Oxygen Ion Conduction and Structural Disorder in Conductive Oxides", *Journal of Physics and Chemistry of Solids* 55 (1994) 1393–1404.
- Turrillas X., Sellars A.P., and Steele B. C. H., "Oxygen Ion Conductivity in Selected Ceramic Oxide Materials", *Solid State Ionics* 20–30 (1988) 465–469.
- Ubic R., Abrahams I., and Hu Y., "Oxide Ion Disorder in  $\text{Nd}_2\text{Hf}_2\text{O}_7$ ", *Journal of the American Ceramic Society* 91 (2008) 235–239.
- Uchida H., Suzuki H., and Watanabe M., "High-Performance Electrode for Medium-Temperature Solid Oxide Fuel Cells Effects of Composition and Microstructure on Performance of Ceria Based Anodes", *Journal of electrochemical society* 145 (1998) 615–620.
- Vaisakhan Thampi D. S., Prabhakar Rao P., and Radhakrishnan A. N., "Influence of Ce Substitution on the Order-to-Disorder Structural Transition, Thermal Expansion and Electrical Properties in  $\text{Sm}_2\text{Zr}_{2-x}\text{Ce}_x\text{O}_7$  System", *RSC Advances* 4 (2014) 12321–12329.
- Vaisakhan Thampi D. S., Prabhakar Rao P., and Renju U. A., "Studies on Order-Disorder Transition, Lattice Expansion and Ionic Conductivity in Aliovalent Cation Substituted  $\text{Sm}_2\text{Zr}_2\text{O}_7$  System", *Journal of Solid State Chemistry* 255 (2017) 121–128.

## References

---

- Vaisakhan Thampi D. S., Prabhakar Rao P., and Renju U. A., "Influence of Aliovalent Cation Substitution on Structural and Electrical Properties of  $Gd_2(Zr_{1-x}M_x)_2O_{7-\delta}$  (M = Sc, Y) Systems", *RSC Advances* 5 (2015) 88675–88685.
- Vandenborre M. T., Husson E., Chatry J. P., and Michel D., "Rare-Earth Titanates and Stannates of Pyrochlore Structure; Vibrational Spectra and Force Fields", *Journal of Raman Spectroscopy* 14 (1983) 63–71.
- Vanderah T. A., Levin I., and Lufaso M. W., "An Unexpected Crystal-Chemical Principle for the Pyrochlore Structure", *European Journal of Inorganic Chemistry* 2005 (2005) 2895–2901.
- Vegard L., "The Constitution of the Mixed Crystals and the Space Filling of the Atoms", *Magazine for Physics* 5 (1921) 17–26.
- Verkerk M. J., van de Velde G. M. H., Burggraaf A. J., and Helmholtz R. B., "Structure and Ionic Conductivity of  $Bi_2O_3$  substituted with Lanthanide Oxides", *Journal of Physics and Chemistry of Solids* 43 (1982) 1129–1136.
- Verkerk M. J., Keizer K., and Burggraaf A. J., "High Oxygen Ion Conduction in Sintered Oxides of the  $Bi_2O_3$ - $Er_2O_3$  System", *Journal of Applied Electrochemistry* 10 (1980) 81–90.
- Vetter G., "Preparation, Stabilite Et Etude Cristallographique Preliminaire Du Compose  $Bi_2Sn_2O_7$ ", *Materials Research Bulletin* 13 (1978) 211–216.
- Vilarinho P. M., "Functional Materials : Properties, Processing and Applications", (2005)
- Virkar A. V., Chen J., Tanner C. W., and Kim J. W., "Role of Electrode Microstructure on Activation and Concentration Polarizations in Solid Oxide Fuel Cells", *Solid State Ionics* 131 (2000) 189–198.
- Wakamura K., "Ion Conduction in Proton- and Related Defect ( Super ) Ionic Conductors : Mechanical, Electronic and Structure Parameters", *Solid State Ionics* 180 (2009) 1343–1349.
- Wan C., Qu Z., Du A., and Pan W., "Order-Disorder Transition and Unconventional Thermal Conductivities of the  $(Sm_{1-x}Yb_x)_2Zr_2O_7$  Series", *Journal of the American Ceramic Society* 94 (2011) 592–596.
- Wang S., Hsu Y., Tsai W., and Lu H., "The Phase Stability and Electrical Conductivity of

- Bi<sub>2</sub>O<sub>3</sub> Ceramics Stabilized By Co-dopants", *Journal of Power Sources* 218 (2012) 106–112.
- Wang S., Inaba H., Tagawa H., and Hashimoto T., "Nonstoichiometry of Ce<sub>0.8</sub>Gd<sub>0.2</sub>O<sub>1.9-x</sub>", *Journal of the Electrochemical Society* 144 (1997) 4076–4080.
- Wang X. P., Cheng Z. J., and Fang Q. F., "Influence of Potassium Doping on the Oxygen-Ion Diffusion and Ionic Conduction in the La<sub>2</sub>Mo<sub>2</sub>O<sub>9</sub> Oxide-Ion Conductors", *Solid State Ionics* 176 (2005) 761–765.
- Wang X. P., and Fang Q. F., "Mechanical and Dielectric Relaxation Studies on the Mechanism of Oxygen Ion Diffusion in La<sub>2</sub>Mo<sub>2</sub>O<sub>9</sub>", *Physical Review B - Condensed Matter and Materials Physics* 65 (2002) 1–6.
- Wang X., Wang H., and Yao X., "Structures, Phase Transformations, and Dielectric Properties of Pyrochlores Containing Bismuth", *Journal of the American Ceramic Society* 80 (2005) 2745–2748.
- Webster N. A. S., Ling C. D., Raston C. L., and Lincoln F. J., "The Structure and Conductivity of New Fluorite-Type Bi<sub>2</sub>O<sub>3</sub>–Er<sub>2</sub>O<sub>3</sub>–PbO Materials", *Solid State Ionics* 178 (2007) 1451–1457.
- West A. R., Sinclair D. C., and Hirose N., "Characterization of Electrical Materials, Especially Ferroelectrics, by Impedance Spectroscopy", *Journal of Electroceramics* 1 (1997) 65–71.
- Whittle K. R., Cranswick L. M. D., Redfern S. A. T., Swainson I. P., Lumpkin G. R., "Lanthanum Pyrochlores and the Effect of Yttrium Addition in the Systems La<sub>2-x</sub>Y<sub>x</sub>Zr<sub>2</sub>O<sub>7</sub> and La<sub>2-x</sub>Y<sub>x</sub>Hf<sub>2</sub>O<sub>7</sub>", *Journal of Solid State Chemistry* 182 (2009) 442–450.
- Wilde P., "Defects and Diffusion in Pyrochlore Structured Oxides." *Solid State Ionics* 112 (1998) 173–183.
- Withers R. L., Welberry T. R., Larsson A. K., Liu Y., Norén L., Rundlöf H., Brink F. J., "Local Crystal Chemistry, Induced Strain and Short Range Order in the Cubic Pyrochlore (Bi<sub>1.5-α</sub>Zn<sub>0.5-β</sub>)(Zn<sub>0.5-γ</sub>Nb<sub>1.5-δ</sub>)O<sub>(7-1.5α-β-γ-2.5δ)</sub> (BZN)", *Journal of Solid State Chemistry* 177 (2004) 231–244.
- Wu Z. J., and Zhang S. Y., "Semiempirical Method for the Evaluation of Bond Covalency in Complex Crystals", *The Journal of Physical Chemistry A* 103 (1999) 4270–4274.

## References

---

- Wuensch B. J., Eberman K. W., "Order-Disorder Phenomena in  $A_2B_2O_7$  Pyrochlore Oxides", *Alloy Science* (2000) 19–21.
- Wuensch B. J., Eberman K. W., Heremans C., Ku E. M., Onnerud P., Yeo E. M. E., Haile S. M., Stalick J. K., Jorgensen J. D. "Connection between Oxygen-Ion Conductivity of Pyrochlore Fuel-Cell Materials and Structural Change with Composition and Temperature", *Solid State Ionics* 129 (2000) 111–133.
- Xia X. L., Gao S., Liu Z. G., and Ouyang J. H., "The Influence of Pentavalent Nb Substitution for Zr on Electrical Property of Oxide-Ion Conductor  $Gd_2Zr_2O_7$ ", *Electrochimica Acta* 55 (2010) 5301–5306.
- Xia X. L., Ouyang J. H., and Liu Z. G., "Influence of CaO on Structure and Electrical Conductivity of Pyrochlore-Type  $Sm_2Zr_2O_7$ ", *Journal of Power Sources* 189 (2009) 888–893.
- Xia X. L., Ouyang J. H., Liu Z. G., Li S., "Effect of MgO on the Electrical Conductivity of the Pyrochlore Type  $Sm_2Zr_2O_7$ ", *Science of Advanced Materials* 2 (2010) 497–502.
- Yahiro H., Eguchi K., and Arai H., "Electrical Properties and Reducibilities of Ceria-Rare Earth Oxide Systems and Their Application to Solid Oxide Fuel Cell", *Solid State Ionics* 36 (1989) 71–75.
- Yahiro H., Eguchi Y., Eguchi K., and Arai H., "Oxygen Ion Conductivity of the Ceria-Samarium Oxide System with Fluorite Structure", *Journal of Applied Electrochemistry* 18 (1988) 527–531.
- Yamamoto O., Takeda R., Kanno Y., and Noda M., "Perovskite Oxides as Oxygen Electrodes for High-Temperature Oxide Fuel Cells", *Solid State Ionics* 22 (1987) 241–246.
- Yamamura H., Nishino H., Kakinuma K., and Nomura K., "Electrical Conductivity Anomaly around Fluorite – Pyrochlore Phase Boundary", *Solid State Ionics* 158 (2003) 359–365.
- Yang F., Wang Y., Zhao X., and Xiao P., "Enhanced Ionic Conductivity in Pyrochlore and Fluorite Mixed Phase Yttrium-Doped Lanthanum Zirconate", *Journal of Power Sources* 273 (2015) 290–297.
- Yashiro K., Suzuki T., Kaimai A., Matsumoto H., Nigara Y., Kawada T., Mizusaki J., Sfeir J., Van Herle J., "Electrical Properties and Defect Structure of Niobia-Doped Ceria", *Solid State Ionics* 175 (2004) 341–344.

- Yeh T. H., and Chou C. C., "Development of Ceria-Doped Zirconia Electrolytes with High Toughness and Ionic Conductivity", *Solid State Ionics* 180 (2009) 1529–1533.
- Yilmaz S., Turkoglu O., Ari M., and Belenli I., "Electrical Conductivity of the Ionic Conductor Tetragonal  $(\text{Bi}_2\text{O}_3)_{1-x}(\text{Eu}_2\text{O}_3)_x$ ", *Ceramica* 57 (2011) 185–192.
- Yu T. H., "Electrical Properties and Structural Disorder in Stannate Pyrochlores", *Thesis* (1996)
- Zhang S., Zhang H. B., Zhao F. A., Jiang M., Xiao H. Y., Liu Z. J., Zu X. T., "Impact of Isovalent and Aliovalent Substitution on the Mechanical and Thermal Properties of  $\text{Gd}_2\text{Zr}_2\text{O}_7$ ", *Scientific Reports* 7 (2017) 1–13.
- Zhao J., Deng Y., Wei H., Zheng X., Yu Z., Shao Y., Shield J. E., Huang J., "Strained Hybrid Perovskite Thin Films and Their Impact on the Intrinsic Stability of Perovskite Solar Cells", *Science Advances* 3 (2017) 1–8.
- Zhao Y., and Zhang J., "Microstrain and Grain-Size Analysis from Diffraction Peak Width and Graphical Derivation of High- Pressure Thermomechanics", *Journal of Applied Crystallography* 41 (2008) 1095–1108.
- Zhou L., Huang Z., Qi J., Feng Z., Wu D., Zhang W., Yu X., Guan Y., Chen X., Xie L., Sun Kai., Lu T., "Thermal-Driven Fluorite–Pyrochlore–Fluorite Phase Transitions of  $\text{Gd}_2\text{Zr}_2\text{O}_7$  Ceramics Probed in Large Range of Sintering Temperature", *Metallurgical and Materials Transactions A* 47 (2016) 623–630.
- Zhu B., "Solid Oxide Fuel Cell ( SOFC ) Technical Challenges and Solutions from Nano-Aspects", *International Journal of Energy Research* 33 (2009) 1126–1137.





## LIST OF PUBLICATIONS

### SCI JOURNALS

1. **U.A Renju**, P. Prabhakar Rao and Vaishakan Thampi D.S, Influence of phase transition from order to disorder and Philip's ionicity on the thermal expansion coefficient of pyrochlore type compositions with a multivalent environment, **New Journal of Chemistry**, (2017)41,245-255
2. **U.A Renju**, and P. Prabhakar Rao, Contrasting anion disorder behaviour in  $\text{Sm}_2\text{Zr}_2\text{O}_7$  by simultaneous aliovalent cation substitutions and its structural and electrical properties, **Journal of Applied Physics**, (2019)126, 045110 (1-9)
3. **U.A Renju**, and P. Prabhakar Rao, Structural stabilisation of  $\delta$ -phase  $\text{Bi}_2\text{O}_3$  in  $\text{MgBi}_{1.5}\text{RE}_{0.5}\text{O}_4$  system through rare-earth substitution for improved ionic conductivity, (communicated)
4. Vaishakan Thampi D.S, P. Prabhakar Rao, **Renju U A**, Studies on Order - disorder transition, Lattice expansion and Ionic conductivity in Aliovalent cation substituted  $\text{Sm}_2\text{Zr}_2\text{O}_7$  System, **Journal of Solid State Chemistry**, (2017)255,121-128
5. Vaisakhan Thampi D.S, P.Prabhakar Rao, **Renju U A** Influence of aliovalent cation substitution on structural and electrical properties of  $\text{Gd}_2(\text{Zr}_{1-x}\text{M}_x)_2\text{O}_{7-\delta}$  (M = Sc, Y) system, **RSC Advances**, (2015)5,88675 – 88685
6. Athira K. V Raj, P Prabhakar Rao, T. S Sreena, S Sameera, Vineetha James, **U. A Renju**, Remarkable changes in the photoluminescent properties of  $\text{Y}_2\text{Ce}_2\text{O}_7$ :  $\text{Eu}^{3+}$  red phosphors through modification of the cerium oxidation states and oxygen vacancy ordering, **Physical Chemistry Chemical Physics**, (2014)16,23699-23710

### INTERNATIONAL/NATIONAL CONFERENCES ORAL/POSTER PRESENTATIONS

1. **Renju U A**, P. Prabhakar Rao, and Vaisakhan Thampi D S, Electrical properties of  $\text{Gd}_2\text{Zr}_2\text{O}_7$ - $\text{CaTiO}_3$  solid solutions for fuel cell applications, Presented at National Conference on Advanced Technologies for Materials Processing and Diagnostics (ISAS 2014) held at Kochi on September 18-24, 2014.
2. **Renju.U.A**, P. Prabhakar Rao, and Vaisakhan Thampi D.S, Structure Transition of Rare Earth Zirconates with Aliovalent substitution at the B site of Pyrochlore type Compositions, International Conference on Science, Technology and Application of Rare Earths ICSTAR 2015, Kovalam, Kerala, India

## ***List of Publications***

---

3. **Renju U A**, Padala Prabhakar Rao, Vaisakhan Thampi D. S., Influence of phase transition from order to disorder and Philip's ionicity on the thermal expansion coefficient of pyrochlore type compositions with a multivalent environment; National Conference on Critical and Strategic Materials for Advanced Technologies CSMAT 2017, Munnar, Kerala, India
4. **Renju.U.A**, P.Prabhakar Rao, Study of structural and electrical properties of pyrochlore type compositions with multivalent environment; International Conference on Science, Technology and Application of Rare Earths ICSTAR 2018, Tirupati, Andhra Pradesh, India
5. **Renju.U.A**, P.Prabhakar Rao, Structural and Electrical Studies of Bismuth Oxides Doped with Aliovalent and Isovalent Cations ( $\text{MgBi}_{1.5}\text{RE}_{0.5}\text{O}_4$ ; RE = Nd, Sm, Dy, Gd, Y), National Conference on Emerging Trends in Science, Technology and Application of Electron Microscopy STEAM 2018, Trivandrum, Kerala, India